

See discussions, stats, and author profiles for this publication at: <https://www.researchgate.net/publication/265437984>

Stability of Transfermium Elements at High Spin: Measuring the Fission Barrier of ^{254}No

Article · September 2012

CITATIONS

3

READS

2,472

1 author:



Greg Henning

Institut Pluridisciplinaire Hubert Curien

66 PUBLICATIONS 273 CITATIONS

SEE PROFILE



Stability of Transfermium Elements at High Spin : Measuring the Fission Barrier of ^{254}No

Gregoire Henning

► To cite this version:

Gregoire Henning. Stability of Transfermium Elements at High Spin : Measuring the Fission Barrier of ^{254}No . Other. Université Paris Sud - Paris XI, 2012. English. <NNT : 2012PA112143>. <tel-00745915>

HAL Id: tel-00745915

<https://tel.archives-ouvertes.fr/tel-00745915>

Submitted on 26 Oct 2012

HAL is a multi-disciplinary open access archive for the deposit and dissemination of scientific research documents, whether they are published or not. The documents may come from teaching and research institutions in France or abroad, or from public or private research centers.

L'archive ouverte pluridisciplinaire **HAL**, est destinée au dépôt et à la diffusion de documents scientifiques de niveau recherche, publiés ou non, émanant des établissements d'enseignement et de recherche français ou étrangers, des laboratoires publics ou privés.

UNIVERSITE PARIS-SUD

ÉCOLE DOCTORALE : *Particules, Noyaux et Cosmos*

Laboratoire : Centre de Spectrométrie Nucléaire et de Spectrométrie de Masse

DISCIPLINE : Physique Nucléaire

THÈSE DE DOCTORAT

soutenue le 20 Septembre 2012

par

Greg HENNING

Stability of Transfermium Elements at High Spin: Measuring the Fission Barrier of ^{254}No

Directeur de thèse :

Co-directeur de thèse :

Araceli Lopez-Martens Chargée de recherche (CSNSM)

Teng-Lek Khoo

Directeur de recherche (*Argonne National Lab.*)

Composition du jury :

Président du jury :

Rapporteurs :

Elias KHAN

Silvia Leoni

Professeur (IPN Orsay)

Professeure (Dipartimento di Fisica,
Università di Milano)

Peter Rieter

Professeur (Institut fuer Kernphysik,
Universitaet zu Koeln)

Examinateur :

Philippe QUENTIN

Professeur Émérite (CENBG)

Abstract

Super heavy nuclei provide opportunities to study nuclear structure near three simultaneous limits: in charge Z , spin I and excitation energy E^* . These nuclei exist only because of a fission barrier, created by shell effects. It is therefore important to determine the fission barrier and its spin dependence $B_f(I)$, which gives information on the shell energy $E_{\text{shell}}(I)$. Theoretical calculations predict different fission barrier heights from $B_f(I = 0) = 6.8$ MeV for a macro-microscopic model [1, 2] to 8.7 MeV for Density Functional Theory calculations using the Gogny or Skyrme interactions [3–5]. Hence, a measurement of B_f provides a test for theories.

To investigate the fission barrier, an established method is to measure the rise of fission with excitation energy, characterised by the ratio of decay widths $\Gamma_{\text{fission}}/\Gamma_{\text{total}}$, using transfer reactions [6, 7]. However, for heavy elements such as ^{254}No , there is no suitable target for a transfer reaction. We therefore rely on the complementary decay widths ratio $\Gamma_\gamma/\Gamma_{\text{fission}}$ and its spin dependence, deduced from the entry distribution (I, E^*) .

Measurements of the gamma-ray multiplicity and total energy for ^{254}No have been performed with beam energies of 219 and 223 MeV in the reaction $^{208}\text{Pb} (^{48}\text{Ca}, 2n)$ at ATLAS (Argonne Tandem Linac Accelerator System). The ^{254}No gamma rays were detected using the Gammasphere array as a calorimeter – as well as the usual high-resolution γ -ray detector. Coincidences with evaporation residues at the Fragment Mass Analyzer focal plane separated ^{254}No gamma rays from those from fission fragments, which are $> 10^6$ more intense. From this measurement, the entry distribution – i.e. the initial distribution of I and E^* – is constructed. Each point (I, E^*) of the entry distribution is a point where gamma decay wins over

fission and, therefore, gives information on the fission barrier.

The measured entry distributions show an increase in the maximum spin and excitation energy from 219 to 223 MeV of beam energy. The distributions show a saturation of E^* for high spins. The saturation is attributed to the fact that, as E^* increases above the saddle, Γ_{fission} rapidly dominates. The resulting truncation of the entry distribution at high E^* allows a determination of the fission barrier height.

The experimental entry distributions are also compared with entry distributions calculated with decay cascade codes which take into account the full nucleus formation process, including the capture process and the subsequent survival probability as a function of E^* and I . We used the KEWPIE2 [8] and NRV [9] codes to simulate the entry distribution.

Stabilité des Éléments Trans-fermium à Haut Spin : Mesure de la Barrière de Fission de ^{254}No

Les noyaux super lourds offrent la possibilité d'étudier la structure nucléaire à trois limites simultanément: en charge Z, spin I et énergie d'excitation E^* . Ces noyaux existent seulement grâce à une barrière de fission créée par les effets de couche. Il est donc important de déterminer cette barrière de fission et sa dépendance en spin $B_f(I)$, qui nous renseigne sur l'énergie de couche $E_{\text{shell}}(I)$. Les théories prédisent des valeurs différentes pour la hauteur de la barrière de fission, allant de $B_f(I = 0) = 6.8$ MeV dans un modèle macro-microscopique [1, 2] à 8.7 MeV pour des calculs de la théorie de la fonctionnelle de la densité utilisant l'interaction Gogny ou Skyrme [3–5]. Une mesure de B_f fournit donc un test des théories.

Pour étudier la barrière de fission, la méthode établie est de mesurer, par réaction de transfert, l'augmentation de la fission avec l'énergie d'excitation, caractérisée par le rapport des largeurs de décroissance $\Gamma_{\text{fission}}/\Gamma_{\text{total}}$, [6, 7]. Cependant, pour les éléments lourds comme ^{254}No , il n'existe pas de cible appropriée pour une réaction de transfert. Il faut s'en remettre à un rapport de largeur de décroissance complémentaire: $\Gamma_\gamma/\Gamma_{\text{fission}}$ et sa dépendance en spin, déduite de la distribution d'entrée (I, E^*).

Des mesures de la multiplicité et l'énergie totale des rayons γ de ^{254}No ont été faites aux énergies de faisceau 219 et 223 MeV pour la réaction $^{208}\text{Pb} (^{48}\text{Ca}, 2n)$ à ATLAS (Argonne Tandem Linac Accelerator System). Les rayons γ du ^{254}No ont été détectés par le multi-détecteur Gammasphere utilisé comme calorimètre – et aussi

comme détecteur de rayons γ de haute résolution. Les coïncidences avec les résidus d'évaporation au plan focal du Fragment Mass Analyzer ont permis de séparer les rayons γ du ^{254}No de ceux issus de la fission, qui sont $> 10^6$ fois plus intenses. De ces mesures, la distribution d'entrée – c'est-à-dire la distribution initiale en I et E^* – est reconstruite. Chaque point (I, E^*) de la distribution d'entrée est un point où la décroissance γ l'a emporté sur la fission, et ainsi, contient une information sur la barrière de fission.

La distribution d'entrée mesurée montre une augmentation du spin maximal et de l'énergie d'excitation entre les énergies de faisceau 219 et 223 MeV. La distribution présente une saturation de E^* à hauts spins. Cette saturation est attribuée au fait que, lorsque E^* augmente au-dessus de la barrière, Γ_{fission} domine rapidement. Il en résulte une troncation de la distribution d'entrée à haute énergie qui permet la détermination de la hauteur de la barrière de fission.

La mesure expérimentale de la distribution d'entrée est également comparée avec des distributions d'entrée calculées par des simulations de cascades de décroissance qui prennent en compte le processus de formation du noyau, incluant la capture et la survie, en fonction de E^* et I . Dans ce travail, nous avons utilisé les codes KEWPIE2 [8] et NRV [9] pour simuler les distributions d'entrée.

*On a qu'à parler avec une robe et un bonnet, tout galimatias
devient savant, et toute sottise devient raison.*

Molière
Le Malade imaginaire, Acte III, Scène 14.

Foreword

Reaching the end of those three years of work, I can say that I met a lot of great people. I enjoyed working with them and in the process, gained colleagues and, dare I say, friends.

I first want to give the biggest thanks to my supervisors: Waely and Teng Lek. I could not have dreamed of anybody better to help me during those three years. They let me all the autonomy I needed to work while guiding me and being available for all my questions.

Thank you to Silvia Leoni and Peter Reiter for accepting to review my (long) manuscript during the summer. Thanks to Philippe Quentin for being part of the defense jury and to Elias Khan for presiding it. I am grateful to all the jury members who asked challenging questions and provided insightful comments that will help move the analysis to even more significant results.

Thanks to David Potterveld for helping with the experiment data that would have been lost without him. Thank you to Darek Seweryniak, Mike Carpente, Torben Lauritsen and Shaofei Zhu for their support and involvement in the experiment and the analysis. Thank you to Neil Rowley and David Boiley for their interest in my work and fruitful discussions. Thank you to Peter Reiter for providing many information on the previous experiment. Thanks to Andreas Heinz, with whom I learnt a lot about nuclear physics, and who provided comments and encouragement.

I thank all my colleagues at Argonne National Lab.: Andrew, Ben, Birger, Calem, Chris, Chitra, Darek, David, Filip, Gulam, Kim, Libby, Martin, Mike, Peter, Robert and Shaofei, and at CSNSM: Carole, Catherine, Dave, Georges, Georgi, Joa, Karl, Pierre and Stephanie and specially my office-mates and fellow *thésards*: Asenath, Asli, Cédric, Christophe, Meng. Thank you to the administrative staff: Annie, Christine, Patricia, Réjane and Sonia in Orsay and Coleen, Barbara and Janet at Argonne, for their essential support.

I can't forget the other student from NPAC 2009 class, in particular, the happy few nuclear physicists among them: Aurore and Fabien.

Last but certainly not least, from the bottom of my heart, I thank Corinne for all she did for me.

Collaborators

This work was possible with the help of : T. L. Khoo¹, A. Lopez-Martens², D. Seweryniak¹, M. Alcorta¹, M. Asai³, B. B. Back¹, P. Bertone¹, D. Boiley⁴, M. P. Carpenter¹, C. J. Chiara^{1,5}, P. Chowdhury⁶, B. Gall⁷, P. T. Greenlees⁸, G. Gurdal⁹, K. Hauschild², A. Heinz¹⁰, C. R. Hoffman¹, R. V. F. Janssens¹, A. V. Karpov¹¹, B. P. Kay¹, F. G. Kondev¹, S. Lakshmi⁶, T. Lauritsen¹, C. J. Lister⁶, E. A. McCutchan¹², C. Nair¹, J. Piot⁴, D. Potterveld¹, P. Reiter¹³, N. Rowley¹⁴, A. M. Rogers¹ and S. Zhu¹.

¹ Argonne National Laboratory, Argonne, IL, USA

² CSNSM, IN2P3-CNRS, Orsay, France

³ Japan Atomic Energy Agency (JAEA), Japan

⁴ GANIL, CEA-DSM and IN2P3-CNRS, B.P. 55027, F-14076 Caen Cedex, France

⁵ University of Maryland, College Park, MD, USA

⁶ University of Massachusetts Lowell, Lowell, MA, USA

⁷ IPHC, IN2P3-CNRS and Universite Louis Pasteur, F-67037 Strasbourg Cedex 2, France

⁸ University of Jyväskylä, Finland

⁹ DePaul University, Chicago, IL

¹⁰ Fundamental Fysik, Chalmers Tekniska Hogskola, 412 96 Goteborg, Sweden

¹¹ Flerov Laboratory of Nuclear Reactions, JINR, Dubna, Moscow Region, Russia

¹² Brookhaven National Lab., Brookhaven, NY

¹³ Universität zu Köln, Germany

¹⁴ IPNO, CNRS/IN2P3, Université Paris-Sud 11, F-91406 Orsay Cedex, France

This work is supported by the U.S. Department of Energy, under Contract Nos. DE-AC02-06CH11357, DE-FG02-91ER-40609 and DE-FG02-94ER40848

Contents

1	Introduction	21
1.1	Nuclear Landscape: toward the Island of stability	21
1.1.1	Discovering the nucleus	21
1.1.2	The nuclear landscape today	24
1.1.3	From magic numbers to Super Heavy Elements	28
1.1.4	Story of a very heavy nucleus: ^{254}No	29
1.1.5	Motivation for measuring the fission barrier of ^{254}No	29
1.2	Nuclear properties	30
1.2.1	Macroscopic and ground state properties	30
1.2.2	Excited states in the nuclei	33
1.2.3	Decay modes	35
2	Synthesis of Super Heavy Elements	39
2.1	Fusion Evaporation Reactions	39
2.1.1	Capture	40
2.1.2	Compound Nucleus: Fusion and Formation	42
2.1.3	Evaporation	43
2.1.4	Evaporation residue formation	49

2.2	Hot and Cold Fusion	49
2.2.1	Cold fusion	49
2.2.2	Hot fusion	50
2.2.3	The case of ^{254}No	50
2.3	The importance of Fission	52
2.3.1	The fission process	52
2.3.2	B_f dependence on I	53
2.3.3	Probing the fission barrier	53
3	Theoretical calculations	57
3.1	Theoretical predictions of the fission barrier height and spin dependence . .	57
3.2	Entry distribution calculation	59
3.2.1	Analytic width calculations	59
3.2.2	evapOR calculation	59
3.2.3	KEWPIE2	59
3.2.4	NRV calculation	61
3.2.5	Calculations of entry distribution: results	66
3.3	Conclusion on calculations	72
4	Experimental measurement of Fission Barrier	73
4.1	Experimental setup	73
4.1.1	Reaction	73
4.1.2	Beam structure	75
4.1.3	Beam spot	77
4.1.4	Target	77

4.1.5	Reset foil	77
4.1.6	Gammasphere	79
4.1.7	Fragment Mass Analyzer	82
4.1.8	Focal plane detectors	83
4.1.9	Trigger	84
4.2	Recoil and recoil decay tagging	87
4.3	Calorimetric measurement	88
4.3.1	Principle of measurement	88
4.3.2	Partial loss of BGO and Ge signals	91
5	Data analysis	95
5.1	Calibration of detectors	95
5.1.1	Gammasphere	95
5.1.2	DSSD calibration	102
5.2	Recoil selection at the focal plane	106
5.2.1	Contaminants	106
5.2.2	^{254}No recoils	107
5.2.3	Cuts and Selections	107
5.3	Test reaction: $^{176}\text{Yb} (^{48}\text{Ca}, 4 - 5n)^{220,219}\text{Th}$	112
5.3.1	Reaction and production cross section	112
5.3.2	γ and decay spectroscopy of ^{220}Th	112
5.4	Cross section	116
5.5	Prompt γ spectroscopy	117
5.6	Alpha spectroscopy	120

5.6.1	Decay chain	120
5.6.2	Decay energy and time	122
5.7	Isomer decays	125
5.8	Principle of calorimetric measurement and calibration	127
5.8.1	Measured quantities	127
5.8.2	Fold and Energy calibration	127
5.8.3	Response characteristics	133
5.9	The unfolding procedure	135
5.9.1	Principle of the unfolding	136
5.9.2	Formal description of the unfolding	136
5.9.3	Validation of the unfolding	138
5.10	Experimental Calorimetric measurements	153
5.10.1	(k, H) distribution	153
5.10.2	Unfolding	155
5.10.3	Multiplicity to Spin and E_{Sum} to E^* conversion	155
5.11	Entry distribution	160
5.11.1	Comparison with previous measurement	160
6	Entry distribution and fission barrier of ^{254}No	165
6.1	Entry distribution: measurement and analysis	165
6.1.1	Measured unfolded distributions	165
6.1.2	Analysis of the Entry Distribution	167
6.2	Extraction of the saddle energy	175
6.2.1	Fit on $E_{1/2}$	175

6.2.2	Mapping the best parameters	175
6.3	Conclusions on the Fission barrier	179
6.3.1	Agreement with $\Delta(I)$	179
6.3.2	Agreement with calculation	180
7	Perspectives	183
7.1	Measurement improvement: digital electronics	183
7.2	Neutron effect	183
7.3	Complementary measurements	184
7.3.1	Prompt electron spectroscopy	184
7.3.2	Formation of ^{254}No by other reactions	184
7.3.3	Measure of partial fusion cross section	185
7.3.4	Improvement of cascade code and simulations	185
7.3.5	Systematic spin measurement in other facilities	185
7.3.6	Measurement of ^{255}Lr entry distribution	187
7.3.7	Insight on the reaction mechanism from the entry distribution	187
A	Effect of neutrons	189
A.1	GEANT4 Simulation of the neutron contribution	189
A.2	Correction of the neutron contribution	192
A.3	Caveat	192
B	New and upgraded facilities for the study of SHN	195
B.1	Digital Gammasphere and FMA	195
B.2	Gretina	195

B.3	Jurogam, Ritu, GREAT	196
B.4	JINR	198
B.5	S ³	199
C	^{220}Th entry distribution	201
C.1	Data	201
C.2	Multiplicity to spin transformation	203
C.3	Results	203
C.4	Conclusions	207
D	Damping of shell effects	209
D.1	Expected consequences for fission width	209
D.2	Simple proof of principle calculation	210
D.3	Conclusions:	213
E	Random selection of value from a probability distribution	215
E.1	Probability and cumulative probability distribution	215
E.2	Computer random number generator	216
E.3	Choosing a value from the probability distribution	217
F	Determining the half maximum point in a distribution	219
F.1	Procedure	219
F.2	Uncertainty on $x_{1/2}$	220
	F.2.1 Uncertainty from bin width	220
	F.2.2 Uncertainty from bin count	220
F.3	Case of multiple half maxima	221

Chapter 1

Introduction

1.1 Nuclear Landscape: toward the Island of stability

1.1.1 Discovering the nucleus

The story of nuclear physics started a long time ago, already in the antiquity, the Greek philosophers imagined that matter is made of very small blocks that Democritus called *atomos* ($\alpha\tauομος$), which means "uncuttable". Later in the Middle Ages and the 16 and 17th centuries, alchemists introduced the idea of chemical elements that can be separated. In 1815, William Prout observed that the measured atomic weights were multiples of the atomic weight of hydrogen. He presented the hypothesis that elements were composed of hydrogen atoms which he called *prolyte* (a name that E. Rutherford made evolved to *protons* in 1920) [10, 11]. In 1869, Dmitri Mendeleïev presented a periodic table of the elements classifying them according to their chemical properties [12]. At the turn of the 19th century, in 1896, Becquerel discovered the natural radioactivity of Uranium ore [13]. Two years later, Thomson discovered the electron and suggested that the atom has an internal structure [14, 15]. One hundred years ago, in 1911, Rutherford presented his model of the atom with a central nucleus [16]. As quantum physics developed and the experimental techniques improved, in 1932, Chadwick discovered the neutron and opened the way for a description of the nucleus as we know it today.

From that point, the knowledge of nuclear physics expanded and models were developed to describe and explain the new experimental measurements. George Gamow, proposed to treat the nucleus as a drop of incompressible nuclear fluid; later Niels Bohr and John Archibald Wheeler used this model to describe fission. Following the liquid drop idea, in

1935, Carl Friedrich von Weizsaecker introduced a semi-empirical formula giving the mass of the nucleus according to its number of protons (Z) and neutrons (N , the total number of nucleons is $A = Z + N$). The mass is often given in terms of binding energy, E_B , which is the difference between the mass $M(Z, N)$ of the nucleus and the sum of the masses of its constituents $Z \times m_p$ and $N \times m_n$, calculated by equation 1.1. The formula was completed by Hans Bethe and is known as the Bethe-Weizsäcker formula (equation 1.2).

$$E_B = Z \cdot m_p + N \cdot m_n - M(Z, N) \quad (1.1)$$

$$E_B = a_V A - a_S A^{2/3} - a_C \frac{Z(Z-1)}{A^{1/3}} - a_A \frac{(A-2Z)^2}{A} + \delta(A, Z) \quad (1.2)$$

In equation 1.2, the different terms are : a_V is the volume term, $\approx 14 - 16 \text{ MeV}$, a_S is the surface term; $a_S \approx 13 - 18 \text{ MeV}$, a_C is the Coulomb term $\approx 0.6 - 0.7 \text{ MeV}$ and reflects the Coulomb repulsion between the electrically charged protons – the three first terms are linked to the liquid drop model; a_A is the asymmetry term $\approx 19 - 24 \text{ MeV}$, present because the nuclear liquid is a mixture of protons and neutrons and δ is the pairing term, a first step of treating the quantum nature of nucleons, equal to $-11 - 33 \text{ MeV}$ for even-even nuclei, to $+|\delta|$ for odd-odd nuclei and to 0 MeV for odd-even nuclei.

The liquid drop model described by N. Bohr was successful at describing the capture cross-sections and later the fission phenomena.

However, the liquid drop model failed to explain simple experimental observations such as the natural abundance of elements in nature, which shows peaks for specific numbers of neutrons or protons; similar peaks are observed in the binding energy of elements or other macroscopic properties. As early as 1932, the idea of a shell structure in the nucleus was introduced by W. Heinsenberg and J. H. Barlett. The so-called *magic numbers* arise from experimental evidence, but the theory was, at first, unable to explain them. The consensus was that nucleons behave in the nucleus like electrons in the atom and are organised in quantum levels. The spacing of the levels creates *gaps* leading to the observed magic numbers: **2, 8, 20, 28, 50, 82, 126**. Physicists failed to find an energy potential that would reproduce all the magic numbers, until 1948, when Maria Goeppert-Mayer (following a suggestion by Enrico Fermi) and independently J. Hans D. Jensen introduced a spin-orbit coupling in the calculation of energy levels and reproduced the magic numbers perfectly [17] – see figure 1.1. M. Goeppert-Mayer and J. H. D. Jensen shared the 1963 Nobel Prize in Physics with E. P. Wigner, for their contributions to theoretical nuclear physics.

After the 1960s, more complex models will be developed: self-consistent approaches with

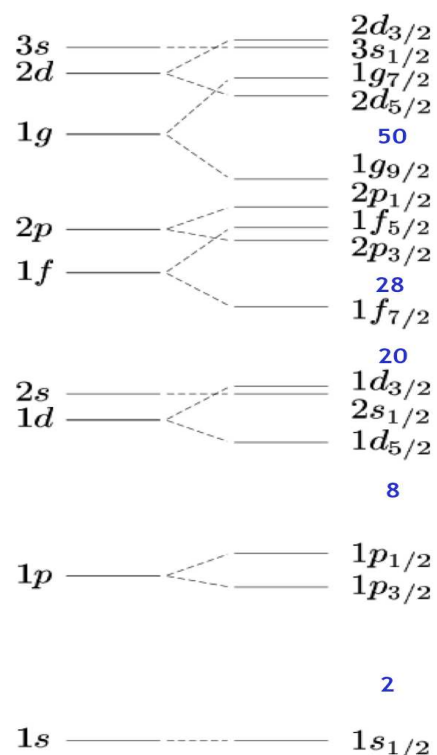


Figure 1.1: Representation of the shell model and energy splitting introduced by the spin-orbit term. On the left are the energy levels for a harmonic oscillator plus an orbital term (ℓ^2). On the right, levels with spin-orbit splitting. The energy gaps between the level groups lead to the magic number 2, 8, 20, 28, 50, 82, 126. The first magic numbers are noted in blue.

Hartree-Fock calculations, relativistic mean field approaches and *ab-initio* calculation with effective interactions like *Argonne v₁₈*.

1.1.2 The nuclear landscape today

Today, the landscape of nuclear physics has expanded both in theoretical understanding and in experimental techniques. There are 118 elements (characterised by the number of protons Z) known and more than 3000 isotopes (characterised by their mass A and charge Z). Only about 100 isotopes are stable and 300 found in nature. Among the *unstable* elements, about 20 have a half life of the order of the age of the Universe (10^{17} s).

The valley of stability

Along the centre of the nuclear landscape lies the valley of stability. Nuclei in the valley are stable, whereas those on the edges are not and decay, mostly by β decay for light nuclei and α decay for the heaviest – see figure 1.2. A parametrization of the position of the stability valley can be derived from the Bethe-Weizsäcker equation (1.2) by maximizing the binding energy at a given A:

$$Z \approx \frac{1}{2} \frac{A}{1 + A^{2/3} \frac{a_C}{4a_A}} \quad (1.3)$$

One notes that the valley connects the elements with N and Z equal to magic numbers.

Shell model and shell induced stability

On top of the liquid drop model, in which one considers the nucleus from a macroscopic point of view, quantum effects exist, giving rise to shell structure. In the shell model, the nucleons occupy quantum levels in the collective energy potential created by the nuclear matter (*mean field*). The existence of energy gaps between levels creates extra stability (manifesting by additional binding energy) [18]. Figure 1.3 shows the stabilisation of the heaviest nuclei by the shell effects.

Nuclei at the limit(s)

Stable nuclei have been studied for years and are well known. In particular the shell model is strongly verified around the magic numbers. However, the limits of the nuclear chart

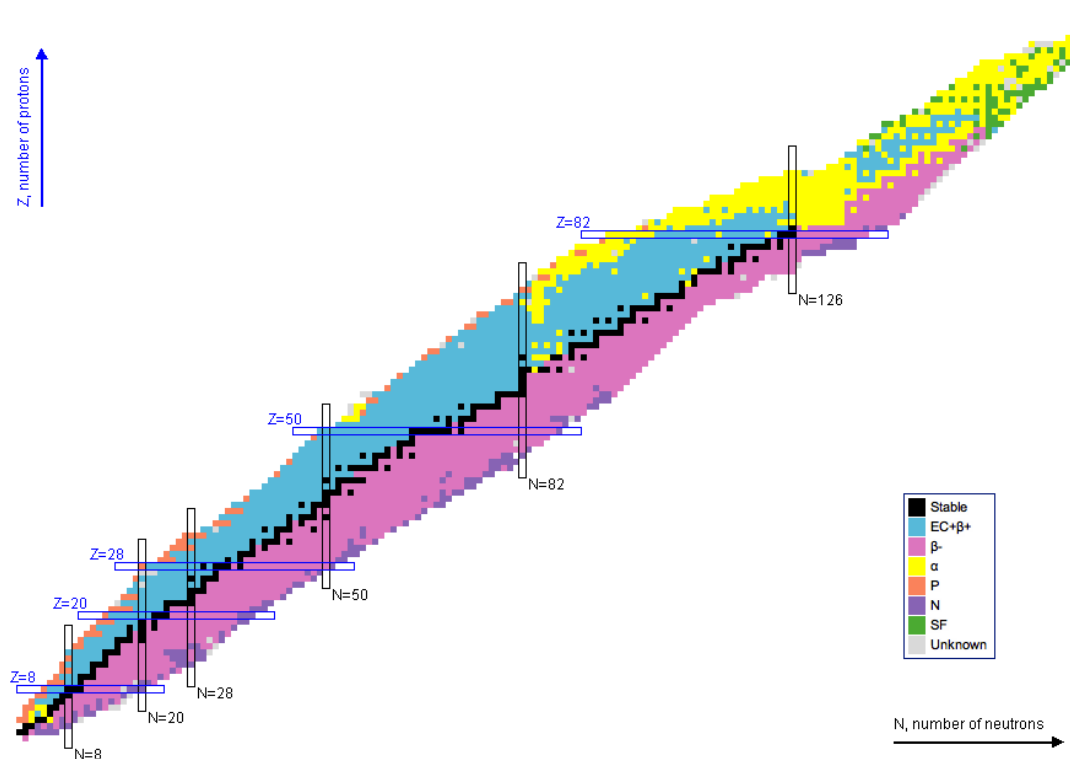


Figure 1.2: Chart of nuclei, arranged according to their number of protons Z and neutrons N . The colour code indicates the decay mode. Magic numbers in N and Z are marked. (From National Nuclear Data Center, Brookhaven National Laboratory).

are still *terra incognita* and under intense investigation today.

On each side of the nuclear chart are the drip lines. The drip line represents the furthest in terms of Z (protons) or N (neutrons) elements are bound and are the boundaries of nuclear existence. The proton drip line is well established, up to $Z \approx 90$. The neutron drip line is known only up to oxygen, with ^{24}O the heaviest possible oxygen isotope.

Other phenomena exist: halo nuclei [19], neutron skin [20], disappearance of magic numbers [21, 22], ... The nuclear landscape is still full of puzzles.

At the highest values of Z and N there is another limit of stability: the liquid drop model predicts life times much shorter than the experimental observations for $Z \approx 100$ and the binding energy drops to and below zero around $Z \gtrsim 104$. For the highest Z, the Coulomb repulsion between protons prevails over the surface energy. This can be expressed, following equation 1.2, with the *fissility* x :

$$x = \frac{E_{\text{Coulomb}}}{2E_{\text{surface}}} = \frac{a_C}{2a_S} \frac{Z(Z-1)}{A^{1/3}} \frac{1}{A^{2/3}} \approx 0.019 \frac{Z^2}{A} \quad (1.4)$$

The fissility is widely used to characterise the tendency of elements to fission. The heavy nuclei exist only because shell effects create gaps in the density of single particle states and stabilise the nucleus against the liquid drop fission process: The potential energy surface is modified and a minimum appears, where the nucleus can exist at a finite deformation, protected from fission by a *fission barrier* whose height is noted B_f and which characterises the stability of very high elements against fission. The elements above $Z \approx 100$ are generally called *Super Heavy Elements* (SHE) and the search for those is a *hot* topic in nuclear physics today and laboratories around the world are working on the synthesis and study of the heaviest elements [23, 24].

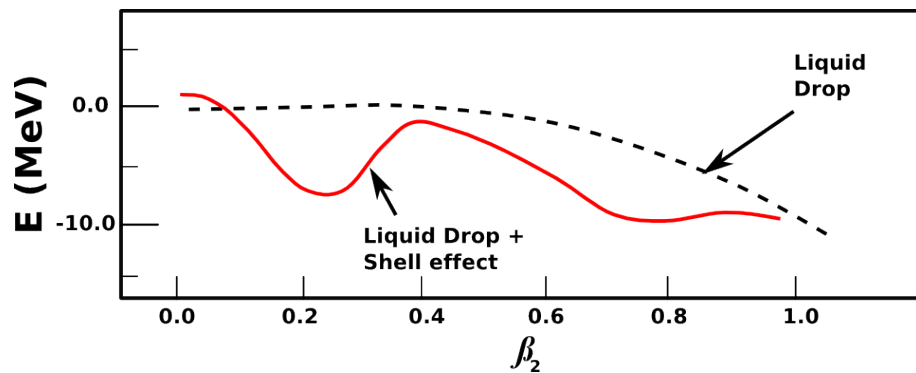


Figure 1.3: Illustration of shell effects on the potential energy surface against deformation, calculated for $^{264}\text{108}$. With only the liquid drop approach (dotted line) there is no minimum and the nucleus is unbound. When including the shell effects (full line), minima appear making the existence of the nucleus possible.

1.1.3 From magic numbers to Super Heavy Elements

The theoretical justification of magic numbers is the formation of gaps in the density of single particle states. In this picture, the series of magic number should go beyond ^{208}Pb — although with the density of levels increasing, the size of the gaps would diminish. In the liquid drop model, stability significantly decreases above Pb, but the shell stabilisation keeps the nuclei bound. Hence, specific combinations of Z and N should show a strong stability above the heaviest known *magic nucleus*, ^{208}Pb . The hypothetical region of spherical stability in the region of $Z \approx 120$ is called *island of stability*. The position of the island (determined by the next *magic numbers*) is not precisely predicted as different theories give different values: $N = 172$ or 184 , $Z = 114$, 120 or 126 . In addition to the spherical island of stability, theories predict a region where nuclei are stabilised by deformation, which modifies the orbitals order and spacing (see later section 1.2.1) and creates new gaps, around $Z \approx 100 - 102$ and $N \approx 152$. Figure 1.4 shows the region of the heaviest known nuclei, that we will call Very and Super Heavy Elements (V&SHE).

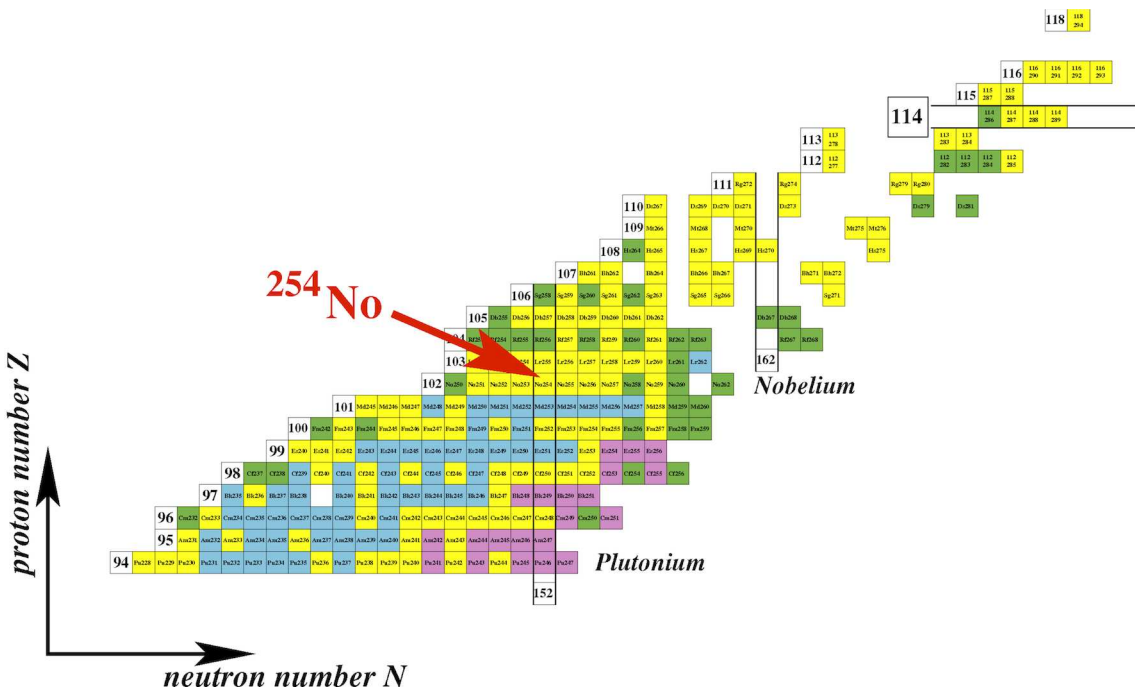


Figure 1.4: Nuclear chart: section of the heaviest element, for Z above 94. The position of ^{254}No is marked. Element $Z=117$ is missing from this chart but has been discovered since. (From AME2003)

SHE are stable **only** thanks to shell effects creating a fission barrier, as illustrated in figure 1.3. Therefore, studying the fission barrier of such nuclei is key to understanding

their stability.

1.1.4 Story of a very heavy nucleus: ^{254}No

The first announcement of the observation of element Z=102 was made from the Nobel Institute in Sweden in 1957; but the claim was later retracted. Between 1958 and 1961 a team led by A. Ghiorso and G.T. Seaborg in UC Berkeley adopted the name *Nobelium* for the element Z=102 formed in $Cm + C$ reactions. Later, in 1966, the decay of ^{254}No was observed at FNLR, Dubna. The chemical properties of the element were studied there, three years later.

Between 1961 and 1971, American teams in Berkeley and Oak Ridge confirmed the discovery of the element and in 1992 IUPAC-IUPAP officially recognised the Dubna team as discoverers of element Z=102. Two years later, IUPAC adopted the name *Nobelium* for this element.

As of today, isotopes of Nobelium have been synthesised from A=250 to A=262. *Prompt* spectroscopy of ^{254}No was performed for the first time in 1998 at Argonne National Laboratory, and shortly after confirmed at Jyväskylä. The measurements established the rotational band and hence the deformed nature of this nucleus [25, 26].

1.1.5 Motivation for measuring the fission barrier of ^{254}No

The fission barrier of very heavy elements like ^{254}No is a direct manifestation of shell effects stabilising the nucleus. The measurement of the barrier height B_f is a way to investigate the strength of shell effects in the heaviest nuclei. Furthermore, the V&SHE are produced at high spin, hence the knowledge of the fission barrier at high spin is essential to understand the synthesis of the heaviest nuclei.

Theoretical calculations give predictions for the fission barrier height at spin 0, but do not agree: the microscopic-macroscopic method predicts $B_f = 6.76$ MeV [1] and the HFB calculation predicts $B_f = 8.66$ MeV [3].

As of today, there was no experimental measurement of a fission barrier above ^{253}Cf [27]. Our measurement is giving the first experimental information in the V&SHE region. A previous measurement was conducted at Argonne National Laboratory and established that $B_f \geq 5$ MeV; which does not distinguish between the two theories. Our goal in the

experiment presented in this thesis is to measure the fission barrier height and its spin dependence.

1.2 Nuclear properties

1.2.1 Macroscopic and ground state properties

Nucleus mass

The primary property of the nucleus is its mass, or more precisely its binding energy (see equation 1.1). The larger the binding energy, the more stable the nucleus. The Bethe-Weizsäcker equation (equation 1.2) describes the binding energy in the macroscopic way. Extra binding energy can be obtained from shell effects. Hence a lighter mass than the one predicted by the liquid drop model reveals the shell structure of the nuclei.

Nucleus shape

While the liquid drop model first assumed a completely spherical nucleus, it is natural today to expand the concept to a deformed nucleus. This was not obvious in the early times of nuclear physics, J Rainwater proposed the idea of deformed nuclei in 1950 [28] and was awarded the 1975 Nobel Prize for his contribution. In general, the deformation can be expressed in terms of spherical harmonics, with the radius at a given angle given by

$$R(\theta, \varphi) = R_0 \left(1 + \sum_{\ell=1}^{\infty} \sum_{m=-\ell}^{\ell} \alpha_{\ell,m} Y_{\ell,m}(\theta, \varphi) \right) \quad (1.5)$$

with ℓ the multipole and m the order of the deformation. The 0th and 1st multipoles do not contribute since they are not deformations ($\ell = 0$ is an expansion or contraction of the sphere, $\ell = 1$ is a translation). The first significant multipole is $\ell = 2$, which is quadrupolar. Assuming an axial symmetry, the simplest deformation can be expressed as $R(\theta, \varphi) = R_0(1 + \beta Y_{2,0}(\theta, \varphi))$ – see figure 1.5 for axis definition – which is an ellipsoid, characterised by the deformation parameter β . The deformation can be parametrized in different ways. The two most commons are β (as described above) and ε which is a measure of the relative deviation from sphericity. If a and b are the semi-axis of the ellipsoid (as described in figure 1.5), then $\varepsilon = \frac{b-a}{(b+a)/2}$. ε is related to β as $\varepsilon \approx \frac{3}{4}\sqrt{\frac{5}{\pi}}\beta - \frac{15}{16\pi}\beta^2$. For

$\beta > 0$ the nucleus is *prolate*, the major axis of the ellipsoid is along the symmetry axis, for $\beta < 0$, the nucleus is *oblate* with the minor axis of the ellipsoid along the symmetry axis.

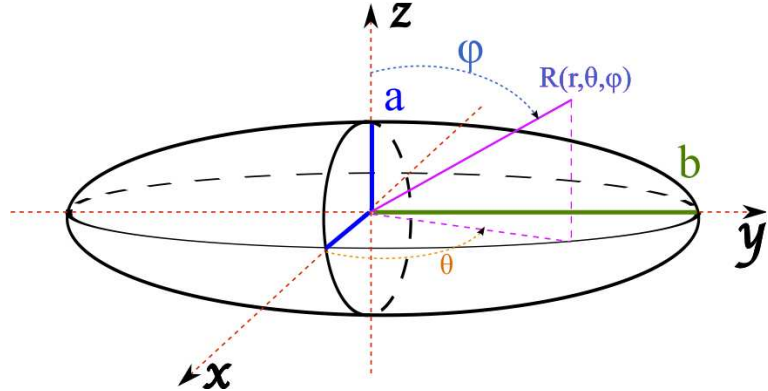


Figure 1.5: Visualisation of a deformed, axially symmetric nucleus. The ellipsoid semi-axis a and b are marked in colour (blue and green). The angle parameters θ and φ are also represented.

The deformation affects the electric moment of the nucleus Q_0 which is a measure of the charge distribution in the nucleus, Q_0 is calculated by integrating the distribution of charges in the nucleus: $Q_0 = e \int \rho (3z^2 - r^2) dV$. For an ellipsoidally deformed nucleus, Q_0 is related to β as $Q_0 = \frac{3}{\sqrt{5}\pi} Z R^2 \beta (1 + 0.36\beta)$. Experimentally, it is the expectation value of Q_0 that is measured Q_s . The two quantities are related by $Q_s = f(I)Q_0$ with $f(I)$ a function of the spin of the nucleus.

Ground state spin and parity

The properties of nuclear states depend on the number of protons and neutrons and the filling of the quantum levels in the nucleus.

For even-even nuclei: The ground state of an even-even nucleus always has a spin-parity of 0^+ , as symmetry and pairing interactions between nucleons will favour this configuration [29].

For odd-even nuclei: The ground state of an odd-even nucleus is determined by the single particle level occupied by the last unpaired nucleon. For spherical nuclei, the shell model developed by GopPERT-MAYER and Jensen gives the orbital order and grouping. For

deformed nuclei, the symmetry breaking lifts the energy degeneracy in the orbitals according to Ω , the projection of the spin \vec{J} on the symmetry axis. This energy splitting leads to a reorganisation of shell levels with deformation and a change in energy gaps. Orbitals of lower Ω are more bound for prolate nuclei – respectively, orbitals of high Ω have lower energy for oblate nuclei. This degeneracy lifting has been introduced by S.G. Nilsson and explains the stability, ground state and low lying excitation properties of deformed nuclei [30]. Nilsson proposed to classify the orbitals in a deformed nucleus according to the numbers $\Omega[Nn_z\Lambda]$ with N the main quantum number of the spherical shell (which determines the parity), n_z the number of excitation quanta on the symmetry axis and Λ the projection of the angular momentum ℓ on the symmetry axis. Figure 1.6 shows the Nilsson-orbitals calculated with a wood-saxon potential for SHE.

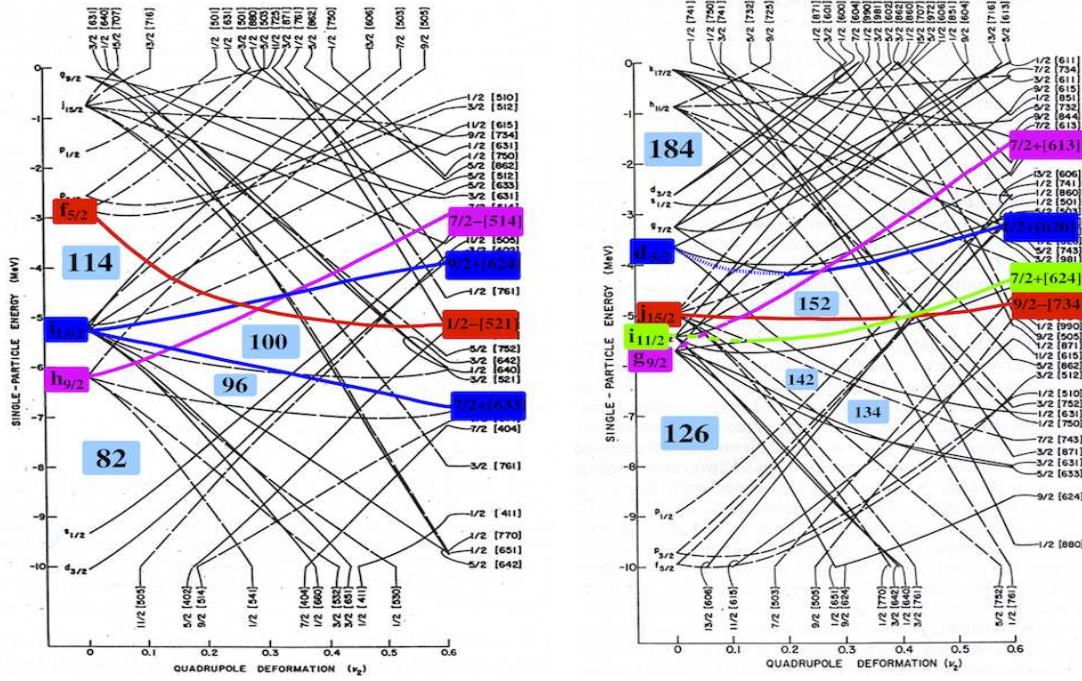


Figure 1.6: Nilsson orbitals for protons $82 \leq Z \leq 114$ (left) and neutrons $N \geq 126$ (right) as a function of the deformation (parametrized by ε). There are gaps at finite deformation that stabilise the deformed nuclei. The position of the gaps and orbitals relevant for ^{254}No at $Z = 102$ and $N = 152$ are marked. (From [31])

1.2.2 Excited states in the nuclei

Rotational excitation

Deformed nuclei gain an extra degree of freedom and can rotate, the axis of rotation being different from the symmetry axis. On figure 1.5 or 1.7 the rotation axis would be z .

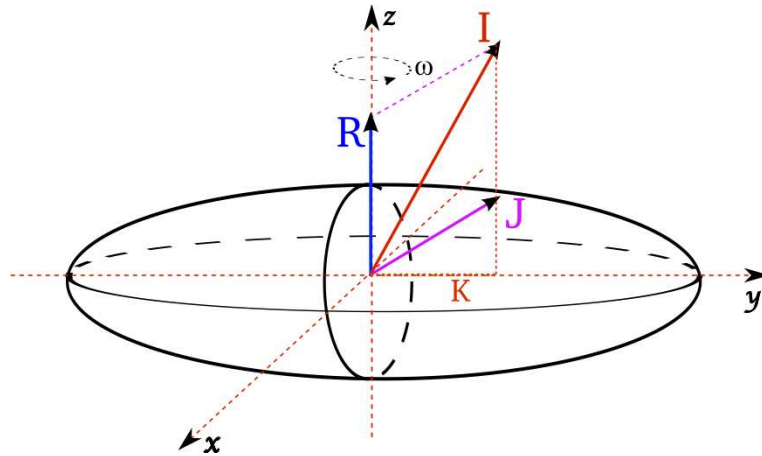


Figure 1.7: Schematic drawing of a deformed rotating nucleus. The nucleus rotates along the z axis, perpendicular to the symmetry axis (y). The total spin of the nucleus is $\vec{I} = \vec{R} + \vec{J}$ with \vec{R} the rotation vector and \vec{J} the intrinsic excitation spin.

The energy associated with the rotation is $E_{\text{rot}} = \frac{\vec{R}^2}{2\mathcal{J}}$ with \vec{R} the global rotation vector (similar to a classical body rotation) and \mathcal{J} the moment of inertia of the nucleus. For a rigid-body rotation, the moment of inertia is derived from the classical value, and for a sphere is $\mathcal{J}_{\text{sphere}} = 2/5 M R^2$. For an axially deformed nucleus, the moment of inertia along the Z axis would be :

$$\mathcal{J} = 2/5 M R^2 (1 + \beta/3) (\hbar^2/\text{MeV}) \quad (1.6)$$

The moment of inertia of the nucleus is generally reduced with respect to the rigid-body values given above by the super-fluidity of the nuclear matter. The effective moment of inertia of a nucleus is $\mathcal{J} = k\mathcal{J}_{\text{rigid}}$ with $k \approx 0.4 - 0.5$ [32]. Moreover, \mathcal{J} is not constant over the all range of excitation and spin of the nucleus: particle alignment, orbital crossing or change in deformation will modify the moment of inertia. That is why we define spin

dependent kinematic $\mathcal{J}^{(1)}$ and dynamic $\mathcal{J}^{(2)}$ moment of inertias:

$$\begin{aligned}\mathcal{J}^{(1)} &= I \left(\frac{dE(I)}{dI} \right)^{-1} \\ \mathcal{J}^{(2)} &= \left(\frac{d^2E(I)}{dI^2} \right)^{-1}\end{aligned}\tag{1.7}$$

Because of the necessary symmetry of the nuclear wave function, for even-even nucleus only even I values are allowed. Therefore the sequence of energy levels follows $E(I) = \frac{I(I+1)}{2\mathcal{J}}$ with $I = 0, 2, 4, 6, \dots$. This sequence of energy is a signature of rotational motion. The rotational states with the lowest energy at a given spin is called the *yrast* line.

Intrinsic excitations

Rotation can be built on top of the ground-state and also on top of excited states. Such excitations occur when one or more nucleons are excited to higher single particle levels within a shell (or even across a shell gap). These excitations may change the nuclei shape, spin and parity.

K quantum number

The global spin \vec{I} of the nucleus has two components: the first is the global rotational angular momentum \vec{R} , along the rotational axis, the second is the spin of the intrinsic excitation in the nucleus \vec{J} ; $\vec{I} = \vec{R} + \vec{J}$. One notes that, by definition and for an axially deformed nucleus, the rotation axis is different (often perpendicular) than the axis of symmetry. The projection of the total spin on the symmetry axis is noted K and is a good quantum number for axially deformed nuclei, as strict selection rules exist for transitions. For an even-even nucleus rotating along an axis perpendicular to the symmetry axis without intrinsic excitation $K = 0$.

K isomers

When K is a conserved quantum number, transitions in the nucleus between states of different K will be disfavoured. One can visualise the transition as a potential energy with multiple minima at different values of K . The difference in K between the two minima implies a small probability of electromagnetic transition. Hence, the high K states have a long life-time and constitute isomers. The trans-uranium elements display such long lived high K states [33]. Figure 1.6 shows the Nilsson orbitals and highlights the gaps for

^{254}No : the orbitals at the Fermi level have a large projection of angular momentum on the symmetry axis, leading to the formation of high- K states and isomers.

1.2.3 Decay modes

Gamma decay

The decay of an excited nucleus by electromagnetic transition is associated with the emission of a photon (electro-magnetic radiation). This process does not change the mass or charge of the emitting nucleus; however it reduces its excitation energy and the spin is changed.

The angular momentum carried by the photon is determined by its multipolarity L . The relation between the initial and final states spin I_i and I_f is $\vec{L} = \vec{I}_i + \vec{I}_f$, or :

$$|I_i - I_f| \leq L \leq I_i + I_f$$

Furthermore, the parity change $\Delta\pi = \pi_i \cdot \pi_f$ is equal to $+1$ or -1 . The transition is called *electric* if $\Delta\pi = (-1)^L$ and *magnetic* is $\Delta\pi = (-1)^{L+1}$; the table 1.1 summarises the different transitions and their characteristics. Between two levels, the favoured transition is the one with the lowest multipolarity.

Transition	J	$\Delta\pi$
E1	1	-1
M1	1	1
E2	2	1
M2	2	-1
E3	3	-1
M3	3	1

Table 1.1: Characteristics of electro-magnetic transitions (angular momentum carried and parity change), according to their names.

The selection rules in the transition come from the underlying quantum process: the reduced transition probability for a σL transition (with σ the type of transition, electric or magnetic and L the angular momentum carried by the γ -ray) is $B(\sigma L) = \frac{1}{2I_i} |\langle I_f | \mathcal{M}(\sigma L) | I_i \rangle|^2$ with $\mathcal{M}(\sigma L)$ the matrix element for the transition. Within a rotational band, M1 and E2

transition probabilities are:

$$B(M1) = \frac{3}{4\pi} (g_K - g_R)^2 K^2 |\langle I_i K 10 | I_f K \rangle|^2 \mu_N^2 \quad (1.8)$$

$$B(E2) = \frac{5}{16\pi} Q_0^2 K^2 |\langle I_i K 20 | I_f K \rangle|^2 (eb)^2 \quad (1.9)$$

Here g_R is the collective magnetic moment of the nucleus – independent on the intrinsic excitation, g_K the configuration magnetic moment which depends on the orbitals occupied by the nucleons, and Q_0 the quadrupole moment of the nucleus. The transition probabilities are strongly dependent on the configurations of the initial and final levels. Transitions between two $I = 0$ states are not possible with γ emission, as a photon must carry angular momentum, but internal conversion is possible for $0 \rightarrow 0$ transitions.

Internal conversion

Internal conversion manifests itself by the emission of an electron. The process is a case of electro-magnetic transition, even if it is not associated with the emission of a photon. Internal conversion happens when the electro-magnetic transition energy is transmitted to an electron of the atom which is removed from the electronic cloud and gains kinetic energy. The process is in competition with γ emission, except for $0 \rightarrow 0$ transitions. The internal conversion process is favoured when: Z is large, the γ transition energy is small and the electron wave function has a higher probability to be *inside* the nucleus (it is the case for K electron shells). The multipolarity of the γ transition and the wave function of the electron also play a role in the conversion process. When an electron of binding energy W_B is ejected by internal conversion, the energy of the electron is $E_{e^-} = E_\gamma - W_B$.

The ratio of the number of internal conversion electrons emitted over the number of γ -rays emitted is $\alpha = \frac{N_e}{N_\gamma}$ and is called the internal conversion coefficient. It is established that $\alpha \propto \frac{Z^3}{E_\gamma}$. The internal conversion coefficients are tabulated or can be calculated [34]. For the ground state bands in ^{254}No , the conversion coefficients for E2 transition can be as large as 1545 at the lowest energy (44 keV). Table 1.2 gives the conversion coefficients for the main known ^{254}No transitions.

Following an internal conversion, the hole in the electronic shell is filled by electrons from higher shells in the electronic cloud. This process is accompanied by X-rays emission and ejection of low-energy electrons (called Auger electrons), leading to multiple ionized atoms. The probability of emitting a X-ray is determined by the fluorescence yield ω which differs depending on the electronic shells. For ^{254}No , the $\omega_K \approx 1$.

E_γ (keV)	α
44	1545
102	28.8
159	4
214	1.2
267	0.54
318	0.3
366	0.2
412	0.14
456	0.11
498	0.09
536	0.07
570	0.06

Table 1.2: Internal conversion coefficients for known ^{254}No yrast E2 transitions. The α coefficient decreases with E_γ .

β decay, Electron capture

β decay is the process in which the nucleus changes its charge by 1 unit; this is the primary process in which a nucleus decays along an isobaric chain to a more stable element. The weak interaction is responsible for the reaction $n \rightarrow p + e^- + \bar{\nu}_e$ for β^- decay, or $p \rightarrow n + e^+ + \nu_e$ for β^+ decay. The transition from ^ZA to ^{Z-1}A can also occur via *electron capture*, a process during which a proton is converted into a neutron via the capture of an electron from the atomic electron cloud : $p + e^- \rightarrow n + \nu_e$ [35, 36].

Alpha decay

Heavy elements ($Z \gtrsim 50$) can decay by emitting an α particle, i.e. a ^4He nucleus.

The process of emitting an α particle from the nucleus is characterised by the Q -value $Q = M(A, Z) - M(A - 4, Z - 2) - M_{^4\text{He}}$. The α particle energy can be approximated as: $K_\alpha \approx \frac{A-4}{A}Q$. For elements with $A \approx 250$, $K_\alpha \gtrsim 95\%$ of Q . Furthermore, the problem of α decay can be treated, in a very simplistic approximation, as a barrier penetration with the α particle escaping across a potential barrier. The transmission is $\propto e^{-2\Delta\sqrt{2M_\alpha|V-K_\alpha|/\hbar}}$ with Δ the barrier width. In fact, in addition to the nuclear potential well from which the α particle has to escape, there is a Coulomb and a centrifugal barrier. The alpha decay problem, when solved, leads a relation between Q and the half-life of the nucleus $T_{1/2} = \frac{\ln 2}{\lambda_\alpha}$

with $T_{1/2} \propto \frac{Z}{\sqrt{Q}}$. The combination of the E_α and $T_{1/2}$ can be used to identify the parent nucleus – See figure 1.8 and reference [37, 38].

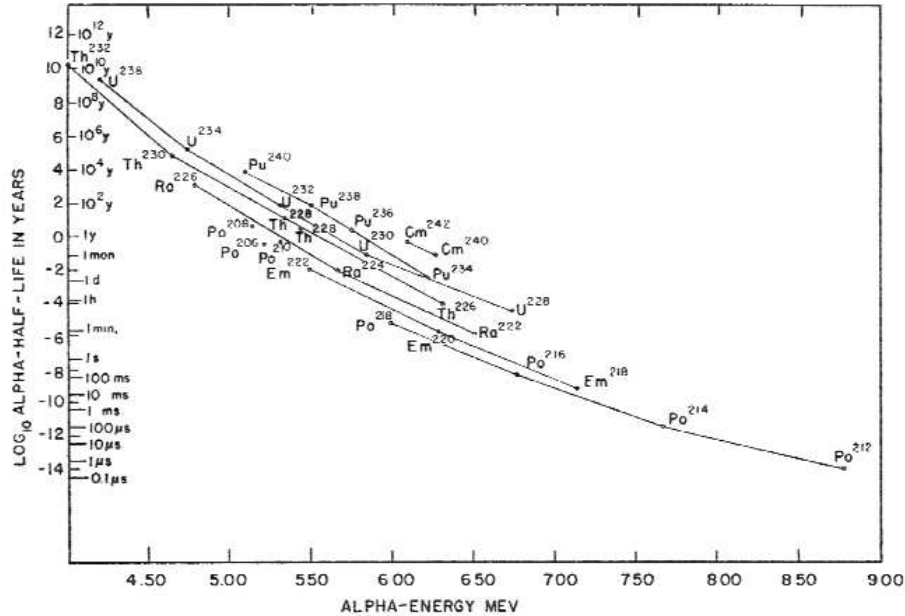


Figure 1.8: Plot of $\log(\text{half life})$ vs. α energy for even-even heavy nuclei – from [37].

Spontaneous fission

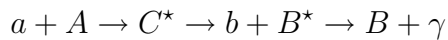
Spontaneous fission is a decay process in which the nucleus breaks up in two fragments. One has to separate spontaneous fission from induced fission and fission during a reaction process when the excitation energy causes the nucleus to fission. Spontaneous fission is characterised by the fissility x which is greater than 1 for elements with $Z^2/A \gtrsim 47$.

Chapter 2

Synthesis of Super Heavy Elements

2.1 Fusion Evaporation Reactions

V&SHE are not found in nature – yet [39] – and must be produced in the laboratory. Moreover their limited stability makes them short lived. Therefore, one needs to produce them just beforehand and *on location* for study. Production of such elements is done either by deep inelastic reaction [40] or by a type of reaction called “**fusion-evaporation**” which is, as the name suggest, a multi-step process. Fusion-Evaporation is a reaction where a projectile nucleus a collides with a target nucleus A to form a compound nucleus (CN) C^* that will evaporate light particles b to produce the nucleus of interest B , following the equation :



As the equation suggests, fusion-evaporation can be described in different steps [32]– see also fig. 2.1 :

- Contact and capture between projectile and target
- Formation of the Compound Nucleus (fusion)
- Evaporation of particles to form the nucleus of interest.
- Emission of γ -rays in the decay to the ground state.

2.1.1 Capture

The first step of fusion-evaporation is the **capture**: the two nuclei a and A have to *touch* in order to form the compound nucleus – figure 2.1. In addition to obvious geometric considerations to this phase of the reaction, there are conditions in terms of energy and angular momentum that need to be met to get capture between the two nuclei. There is a *barrier* that must be overcome: mainly from the Coulomb repulsion between the two charged nuclei, plus a kinetic component: at low angular momentum ℓ , the phase space is small and makes it harder for the two nuclei to be in contact, whereas for very large angular momentum the corresponding large impact parameter disfavours the contact. The contact phase is characterised by a probability $P_{\text{contact}}^{a,A}(E_a, \ell)$ where E_a is the kinetic energy of the projectile and ℓ is the angular momentum in the system.

The characteristic values of importance in the contact phase are :

Size of the nuclei With the radius of a nucleus given by $R = r_0 A^{1/3}$ ($r_0 = 1.2$ fm), the distance between the two centres at contact is $b_{\text{contact}} = R_a + R_A + d_{\text{interaction}}$ (R_a and R_A are the radii of the nuclei a and A), with $d_{\text{interaction}} \approx 2 - 3$ fm the distance of interaction of the two nuclei. The impact parameter must therefore be smaller than this value, otherwise the nuclei can not touch.

Angular Momentum The transferred angular momentum in the reaction is given by $\sqrt{\ell(\ell+1)} = \frac{1}{\hbar} \mu v b$, where ℓ is the angular momentum, μ is the reduced mass of the system ($\mu = \frac{m_a m_A}{m_a + m_A}$, m_a and m_A are the masses of the nuclei), v the speed of the projectile (in the centre of mass frame) and b the impact parameter.

Coulomb barrier The Coulomb barrier is proportional to $\frac{Z_a Z_A}{A_a^{1/3} + A_A^{1/3}}$ (Z_a, A_a and Z_A, A_A are the charge and mass number of the nuclei) ; the energy in the centre of mass must be above this value for the two nuclei a and A to get in contact.

R. Bass described the fusion process in a classical liquid drop potential model with no deformation and showed that the interaction (*contact*) cross-section can be expressed in terms of a one-dimensional barrier [41, 42], with $\sigma_R = \pi R_{\text{int}}^2 \left(1 - \frac{V(R_{\text{int}})}{E}\right)$, with $R_{\text{int}} = R_a + R_A + d_{\text{interaction}}$ and $V(R_{\text{int}}) = 1.44 \text{ MeV} \frac{Z_a Z_A}{R_{\text{int}}} - b \frac{R_a R_A}{R_a + R_A}$ ($b \approx 1 \text{ MeV}$). The potential $V(R)$ reflects the competition between Coulomb repulsion ($\propto Z_a Z_A / R$) and the surface tension energy ($\propto R_a R_A / (R_a + R_A)$).

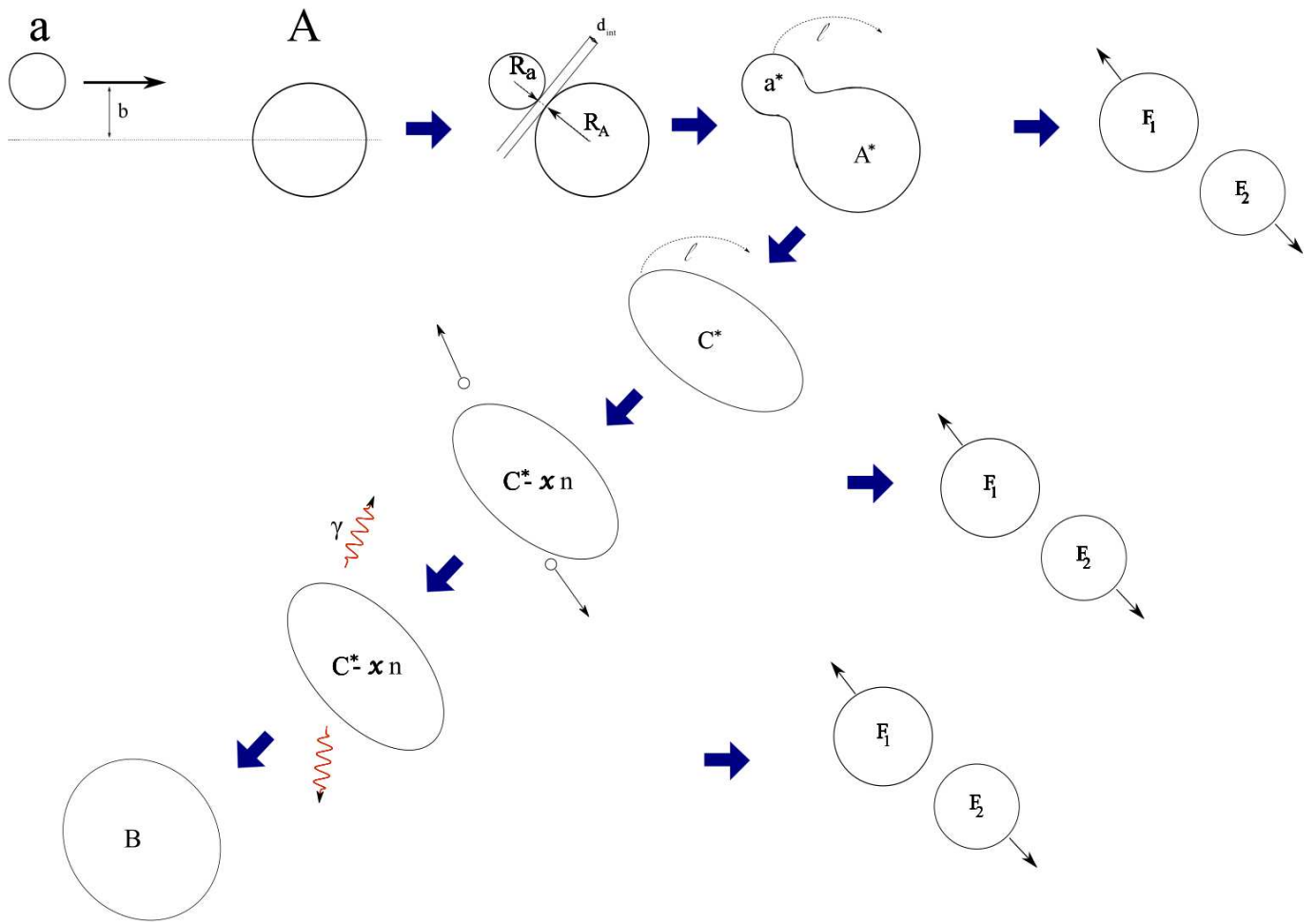


Figure 2.1: Schematic view of the fusion-evaporation reactions process. The projectile a impacts the target nucleus A with the impact parameter b . The pre-fusion system is characterised by the interaction distance $d_{\text{interaction}}$. At each step of the process, the system can fission, before forming the compound nucleus, or evolving to form the CN C^* , which will evaporate neutrons and γ -rays to loose excitation energy and form the evaporation residue B .

2.1.2 Compound Nucleus: Fusion and Formation

The second step in a fusion-evaporation reaction is the formation of the CN; i.e. the passage from 2 nuclei in contact into one excited nucleus at thermal equilibrium (C^*). The CN formation implies a change of the shape (see figure 2.1) often characterised by a barrier the system needs to pass in order to make the transition. The transition to the CN must happen on a time scale of the order of the time needed for the bombarding particles to travel across the target nucleus (i.e. approximately 10^{-21} s) [43]. The reaction energy is shared among all the CN nucleons, leading to a nucleus with an excitation energy E^* equal to the total energy in the system plus the Q -value (negative) to form the CN. The CN exists over a time scale of the order of 10^{-19} to 10^{-16} s. The formation of the CN will depend on the beam energy E , the angular momentum ℓ and the entrance channel. The probability to form the compound nucleus is given by $P_{\text{CN}}^{A+a \rightarrow C^*}(E, \ell)$ [44]. If the formation of the CN fails, the pre-compound system $a + A$ splits into target-like and projectile-like fragments; this process is called *quasi-fission* – see figure 2.1.

Deformed nuclei barrier

The barrier described above considers only spherical nuclei. For a deformed nucleus, the barrier, which depends on the interaction distance, cannot be expressed as simply for deformed nuclei, it depends on the relative orientation η of the nuclei: $R_{\text{int}}(\eta) = R_a + R_A + d_{\text{interaction}}(\eta)$. As the orientation η is not controlled, there is a distribution of barriers spread over all the possible η configurations.

Coupled channel

To the simple geometrical approach, one must add the refinement of quantum mechanics. During the reaction process, the nuclei can be excited to their internal excited levels [45]. The coupling between the internal excitation configurations will enhance or reduce the fusion probability depending on the configuration, possible shape changes in excited states, ... This modifies the barrier distribution as a function of reaction energy.

For the ^{48}Ca on ^{208}Pb reaction, coupled channels calculations are necessary to reproduce the experimental capture cross-sections below and around the fusion barrier. Without coupling, there is only one barrier. Coupling to 1-phonon excitations in the nuclei makes additional barriers appear and higher-order coupling lowers the secondary barriers, making them reachable in experiment. Figure 2.2 shows an example of barrier distributions for

^{254}No . Therefore coupling creates a secondary maximum in partial fusion transmission at lower angular momentum. Figure 2.3 shows calculations from [46].

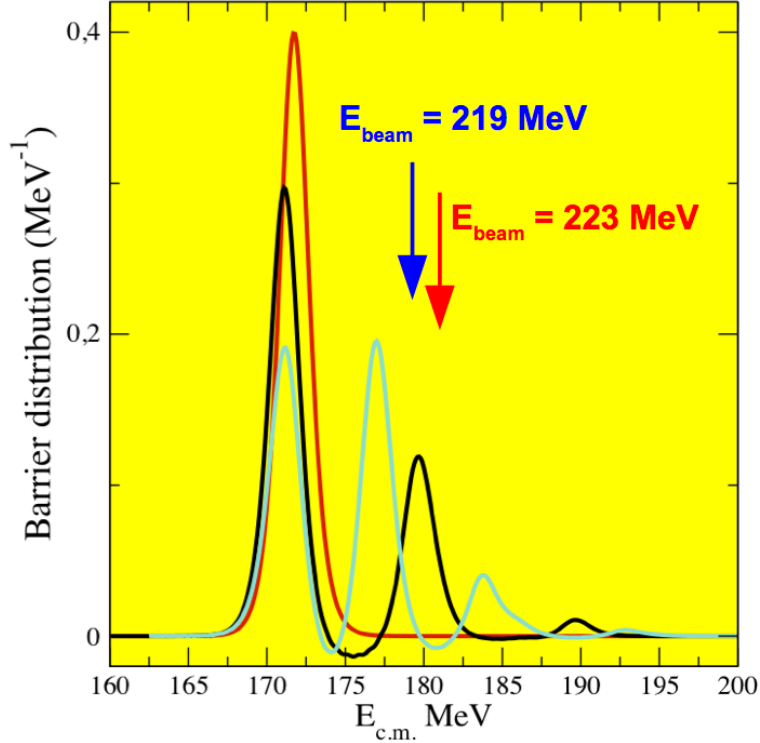


Figure 2.2: Calculation of the barrier distribution as a function of centre of mass energy for ^{254}No in the reaction $^{208}\text{Pb}(^{48}\text{Ca},2\text{n})^{254}\text{No}$ with no coupling (red), excitation of one (black) and excitation of two (blue) phonons in the target and projectile nuclei. The blue arrow shows the centre of mass energy in our experiment at $E_{\text{Beam}} = 219$ MeV and the red arrow at $E_{\text{Beam}} = 223$ MeV, which is below the second barrier with only one phonon coupling but above it when coupling two phonons. From [46].

2.1.3 Evaporation

The last step of the fusion-evaporation reaction is the evaporation by the CN of light particles (protons, neutrons, α particles) or emission of γ -rays to form evaporation residues. When formed, the CN has an excitation energy $E^* = E_{\text{cm}} + Q$, where E_{cm} is the total energy available in the centre-of-mass frame ($E_{\text{cm}} \sim K + A_A + A_a$, with K the kinetic energy of the projectile in the centre-of-mass frame) and Q the Q -value for forming the CN ($Q = BE_{\text{CN}} - (BE_a + BE_A)$), Q being negative for typical reactions in the formation of heavy nuclei.

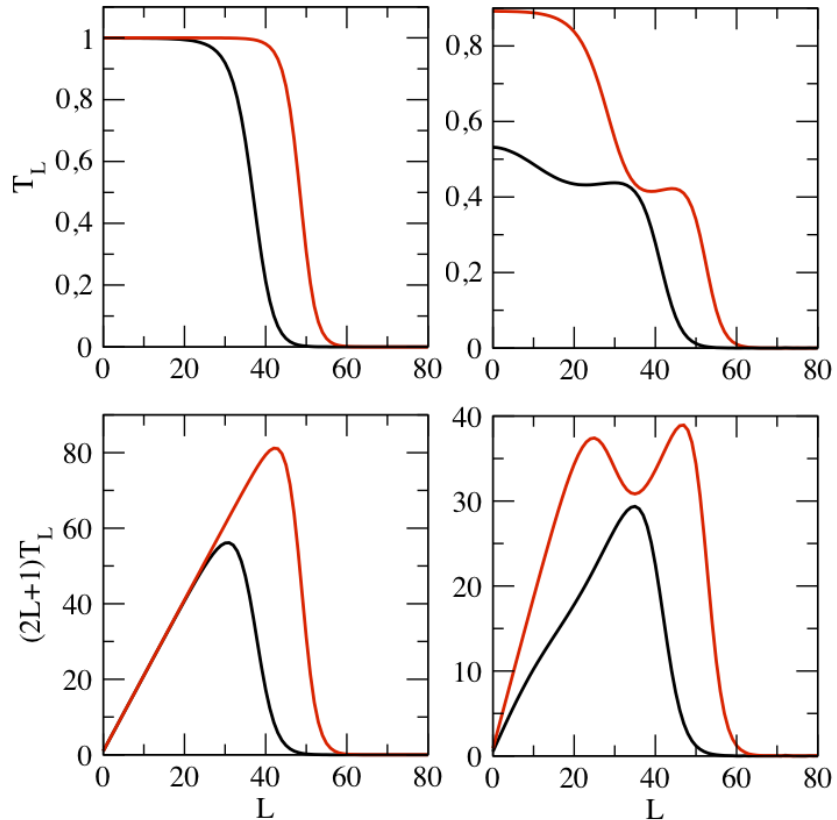


Figure 2.3: Partial transmission coefficient for the fusion of ^{48}Ca with ^{208}Pb at projectile energy of 219 MeV (black) and 223 MeV (red) calculated without (left) and with (right) coupled channels. The channel coupling creates a secondary peak from the higher barrier, following $L_{\max} \propto \sqrt{E_{CN} - B}$ (with E_{CN} the excitation energy of the compound nucleus and B the fusion barrier height). From [46].

The evaporation process happens on a *long* time scale (as long as 10^{-15} s, compared to the typical orbit time of a nucleon in the nucleus: 10^{-21} s). The process is statistical and the evaporation channels are independent. Evaporation of neutrons is strongly favoured since it is not hindered by the Coulomb barrier. Protons and α particles evaporation is usually not observed from heavy CN, although it is theoretically possible. Fission will compete with particle and γ emission.

Neutrons (or more generally particle) evaporation reduces the CN excitation energy by the separation energy and the kinetic energy of the evaporated particle. However, evaporation does not affect the angular momentum very much. Particles will be evaporated as long as E^* is above the particle separation energy. When $E^* < S_{\text{particle}}$ for any particle, the CN will emit statistical γ -rays, mainly of E1 multipolarity, carrying energy and very little angular momentum, bringing the nucleus closer to *yраст* and other excited rotational bands constituting the *normal* γ -decay path – see figure 2.1. The evaporation to a given evaporation residue (ER) is characterised by the probability $P_{\text{ER}}^{C*}(E^*, \ell)$.

Decay widths

The decay of the compound nucleus by emission of neutrons and other particles, γ -rays or by fissionning is governed by the associated decay widths [47]. According to Fermi's golden rule, the width for a decay is $\Gamma = \frac{2\pi}{\hbar} |M|^2 \rho$ – where M is the transition matrix element and ρ the phase space factor, measuring the density of final states. In terms of global quantities, the width can be expressed as the ratio of the number of available final states N over the level density at the initial state ρ : $\Gamma = \frac{N}{2\pi\rho}$. The number of available final states is obtained by integrating the level density of the final states over the available energy range.

Level Density The level density is a key parameter for the calculation of decay widths. It is not an easy quantity to measure at intermediate energies and is parametrized from theory [48]. A classical parametrization is [8, 48–51]:

$$\rho(E^*, J) = \frac{2J+1}{24\sqrt{2}a^{1/4}(E^* - E_{\text{rot}}(J) - \Delta)^{5/4}\sigma^3} \exp\left(2\sqrt{a(E^* - E_{\text{rot}}(J) - \Delta)} - \frac{(J + 1/2)^2}{2\sigma^2}\right) \text{ MeV}^{-1} \quad (2.1)$$

Here a is the level density parameter, of the order of $A/8$, $E_{\text{rot}}(J)$ the rotational energy $= \frac{J(J+1)}{2\mathcal{J}_{g.s.}}$, Δ is the pairing gap, of the order of $24/\sqrt{A}$ for even-even nuclei, equal to 0 in other cases and σ is the spin cut-off parameter: $\sigma = \frac{\mathcal{J}_{\text{rigid}}T}{\hbar}$ where $\mathcal{J}_{\text{rigid}}$ is the rigid body moment of inertia and T the temperature of the system.

More complex factors affect the level density: There is an enhancement of the level density by collective excitations ($\rho_{\text{enhanced}}(E^*, I) = K_{\text{collective}}(E^*, I)\rho(E^*, I)$ [52, 53]). In addition, damping of shell effects with excitation energy [8, 48], needs to be taken into account, by using $a_{\text{damped}} = a[1 + \delta \frac{1 - \exp(-\gamma_D E^*)}{E^*}]$ with δ the shell correction and γ_D the damping parameter [50]. The way to implement such damping in the calculation is currently under discussion, see appendix D.

Fission Potential Even if fission eventually leads to a gain in energy (the binding energy of the two fragments is higher than the one of the initial nucleus) during the process, the system has to overcome the *fission barrier*, noted B_f .

An easy way to represent the fission process is having the system moving along the energy potential V as a function of deformation β . During the fission, the nucleus undergoes a transition from inside the potential well, around $\beta_{\text{g.s.}}$, to a higher deformation β . In order to get over the saddle at β_{saddle} (the deformation “threshold” over which the nucleus becomes unbound and fissions) the system must go over $B_f = E_{\text{saddle}} - E_{\text{g.s.}}$ – see figure 2.4. The saddle energy can be parametrized by $E_{\text{saddle}} = B_f(0) + \frac{\hbar^2 I(I+1)}{2\mathcal{J}_{\text{saddle}}}$, with $B_f(0)$ the height of the fission barrier at spin 0, and $\mathcal{J}_{\text{saddle}}$ the moment of inertia of the saddle, assuming a rotor behaviour, with $\mathcal{J}_{\text{saddle}}$ linked to the saddle deformation β_{saddle} .

The quantum nature of the system implies that a tunnelling of the wave function through the potential is possible when $E^* < E_{\text{saddle}}$. Therefore, the transition from a non fissionning nucleus to fission with increasing E^* is not sharp but smooth; depending on how strong the tunnelling is and the competition with other decay modes (given by $\Gamma_{\text{fission}}/\Gamma_{\text{total}}$).

The fission barrier B_f is a framework of calculation used to model the fission process and is not directly observable. However, the fission barrier is computed and is used in all calculations. Furthermore, the quantity B_f is linked to very experimental observables like the maximum excitation energy one can *put* in the nucleus before it fissions, spontaneous fission half-lives, fission probability in reactions, etc. Hence it is a parameter that can be deduced from experimental data.

Fission decay width For the fission decay, the number of final states is given by integrating the level density above the saddle point energy up to the excitation energy. In practice, due to the barrier penetration in the fission process, the integration goes from 0 to E^* with a tunnelling factor, characterised by the energy $\hbar\omega$. The tunnelling parameter $\hbar\omega$ is linked to the curvature of the potential (supposed parabolic) around the saddle and usually taken to be ≈ 1 MeV. The fission width grows rapidly above the threshold energy

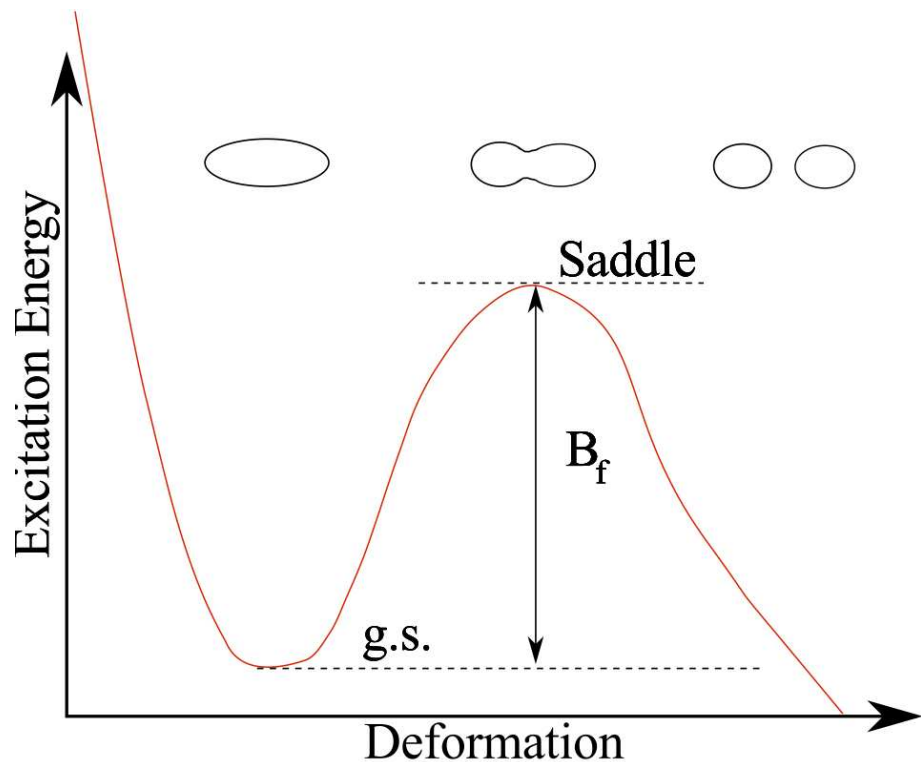


Figure 2.4: Schematic potential energy for fission against the deformation parameter (β). The ground state, located at a finite deformation and the saddle point at higher deformation define the fission barrier B_f . A schematic view of the shape of the nucleus is represented above the potential.

B_f and can be expressed as [54–56]:

$$\Gamma_{\text{fission}} = \frac{1}{2\pi\rho_{g.s.}(E^*)} \int_0^{E^*} \frac{\rho_{\text{saddle}}(E^* - \varepsilon)}{1 + \exp\left(-\frac{2\pi(\varepsilon - B_f)}{\hbar\omega}\right)} d\varepsilon \text{ MeV} \quad (2.2)$$

In the formula, the denominator is the transmission through the barrier (tunnelling).

Neutron decay width For the neutron decay, Weisskopf calculates the widths in the frame of the equilibrium reaction ${}^A\text{Z} \rightleftharpoons n + {}^{A-1}\text{Z}$, following the transition state theory. One has to introduce the cross-section of the reverse reaction (neutron capture) in the calculation. The integration is done over the excitation energy above the neutron separation energy S_n and for the level density of the ${}^{A-1}\text{Z}$ nucleus. A pre-factor appears due to the kinematic degrees of freedom of the neutron and the spin degeneracy (g). There is no tunnelling for neutron emission. This leads to [8]:

$$\Gamma_{\text{neutron}} = \frac{gm}{\pi^2\hbar^2} \frac{1}{\rho_A(E^*)} \int_0^{E^*-S_n} \varepsilon \sigma_{\text{inverse}}(\varepsilon) \rho_{A-1}(E^* - S_n - \varepsilon) d\varepsilon \text{ MeV} \quad (2.3)$$

The Weisskopf approach does not depend on the spin of the initial and final state. To account for angular momentum and barrier penetration, the Hauser-Feshbach formalism is better suited and considers the angular momentum carried by the emitted neutron [8, 57].

γ decay width For γ decay, the width depends on the transition multipolarity and the strength function specific to a nucleus (in particular the deformation).

For an E1 multipolarity transition, the strength function has a Lorentzian form, following the Giant Dipole Resonance energy and width: $f_{\text{E1}}(E_\gamma) = C \frac{E_\gamma \Gamma_{\text{GDR}}}{(E_\gamma^2 - E_{\text{GDR}}^2)^2 + \Gamma_{\text{GDR}}^2 E_\gamma^2}$, with C a constant factor and Γ_{GDR} and E_{GDR} are the Giant Dipole Resonance width and energy. The strength function typically has a value of a few 10^{-6} MeV^{-1} . For axially deformed nuclei, the strength function depends on β , the quadrupole deformation parameter and has several maxima, compared to only one for spherical nuclei.

The γ decay width also depends on the γ energy to the power of $2L + 1$, with L the γ multipolarity. There is no threshold energy to emit a γ -ray. An E1 γ can carry one unit of spin and one has to sum over the different final possible spins.

This leads to an E1 γ decay width of [58, 59] :

$$\Gamma_\gamma^{\text{E1}} = \frac{1}{\rho(E, I)} \sum_{J=I-1}^{J=I+1} \int_0^E \varepsilon^3 f_{\text{E1}}(\varepsilon) \rho(E - \varepsilon) d\varepsilon \text{ MeV} \quad (2.4)$$

Decay probability The decay probability for a given decay channel is given, in term of width as $P_{\text{decay}} = \frac{\Gamma_{\text{decay}}}{\Gamma_{\text{total}}}$, with Γ_{total} the sum of all decay channel widths [60]. In the case of fusion-evaporation, the probability of fission is $P_{\text{fission}} = \frac{\Gamma_{\text{fission}}}{\Gamma_{\text{fission}} + \Gamma_{\text{neutron}} + \Gamma_{\gamma}}$. The probability to form an evaporation residue B by emitting two neutrons from the compound nucleus C^* will be given by: $P_{\text{ER}}^{C^* \rightarrow B} = \frac{\Gamma_n^{C^*}}{\Gamma_{\text{total}}^{C^*}} \times \frac{\Gamma_n^{C^* - n}}{\Gamma_{\text{total}}^{C^* - n}}$.

2.1.4 Evaporation residue formation

The total probability of formation of an ER at a given excitation energy from the $a + A$ reaction is therefore characterised by the cross section [50] :

$$\sigma_{\text{ER}}(E^*) = \frac{\pi \hbar^2}{2\mu E} \sum_{L=0}^{\infty} (2L+1) \cdot P_{\text{contact}}^{\text{a,A}}(E_a, L) \cdot P_{\text{CN}}^{A+a \rightarrow C^*}(E, L) \cdot P_{\text{ER}}^{C^*}(E^*, L) \quad (2.5)$$

μ is the reduced mass, as introduced in 2.1.1.

The fission barrier affects the term: $P_{\text{ER}}^{C^*}(E^*, L)$. Theoretical calculations, although they manage to give rather good predictions for the cross section σ_{ER} , fail to agree for the different terms and steps of the process. This is a big limitation of the calculation since the internal steps of calculation rely on complex process and hypotheses that cannot be individually verified experimentally and that are not unique in their modelisation.

2.2 Hot and Cold Fusion

Fusion-evaporation can be *hot* or *cold*, depending on the excitation energy of the CN. The choice of projectile-target combination determine which of the two regime happens.

2.2.1 Cold fusion

Cold fusion relies on magic or nearly-magic projectile and target (like ^{48}Ca and ^{208}Pb or ^{209}Bi). As a consequence, the reaction Q -value is very negative (the magicity gives a large binding energy and $Q = E_B(\text{CN}) - (E_B(a) + E_B(A))$ is therefore large and negative) and the CN excitation energy is low (around 10–20 MeV). The CN evaporates only one or two particles (predominantly neutrons).

In cold fusion, the capture is disfavoured by the high $Z_1 Z_2$ term in the potential energy; but the low excitation energy of the compound nucleus favour the survival of the evaporation residues.

2.2.2 Hot fusion

For hot fusion, heavier targets and more asymmetric projectile / target combinations are used (for example ^{244}Cm on ^{12}C to produce ^{254}No). The CN excitation energy is usually around 50 MeV and 4 or 5 neutrons are evaporated.

In hot fusion, the lower $Z_1 Z_2$ favours the contact between projectile and target nuclei; but the higher compound nucleus excitation energy reduces the survival probability of the ERs.

2.2.3 The case of ^{254}No

^{254}No can be produced via hot and cold fusion, the different beam-target combination give different Q-values and production cross section, as shown in table 2.1.

Reaction	Q-value (MeV)	CN E^* at max. σ (MeV)	Max. σ (μb)
$^{238}\text{U}(^{22}\text{Ne},6\text{n})$ [61]	-93.9	57	$15 \pm 7 \times 10^{-3}$
$^{208}\text{Pb}(^{48}\text{Ca},2\text{n})$ [61, 62]	-166.8	21	2

Table 2.1: Table of Q-values and production cross section for hot and cold fusion to produce ^{254}No . The compound nucleus excitation energy at the maximum of cross section is indicated. The difference between the hot and cold reactions are clearly visible in terms of the Q-values, E^* and σ .

Independently of the type of fusion-evaporation reaction, the production cross section in the region of V&SHE falls exponentially with the atomic number Z of the produced element. Figure 2.5 shows the evolution of production of SHE cross section with neutron number for hot or cold fusion.

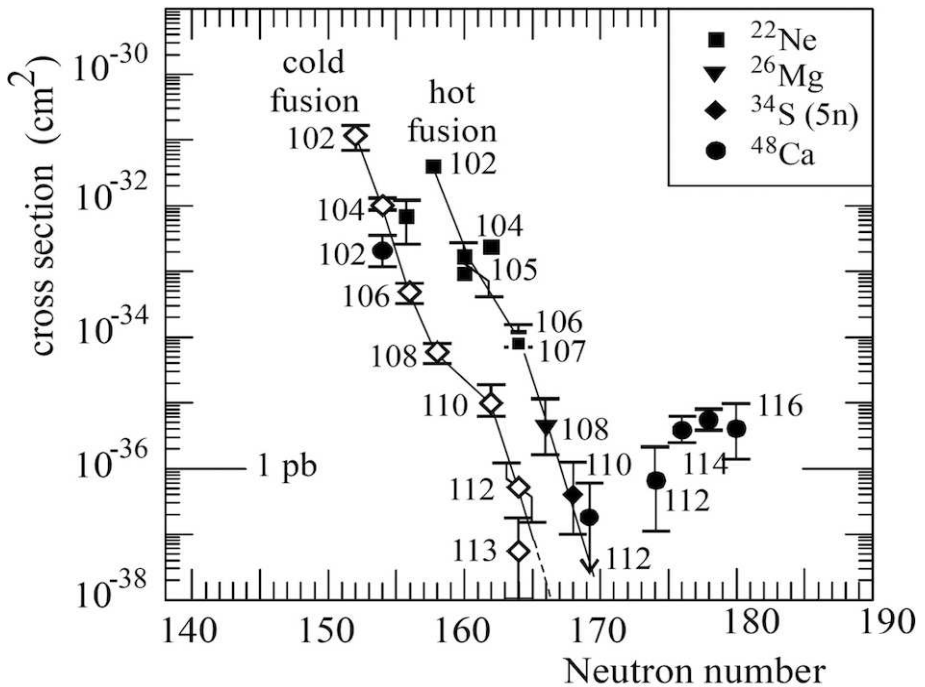


Figure 2.5: Plot of cross section for cold and hot fusion reactions, as a function of the compound nucleus neutron number (from [63]). The plot shows an exponential decrease in cross-section for both hot and cold fusion up to $N=170$, above which values there is an increase for ^{48}Ca induced reactions. This increase corresponds to higher B_f predicted in macroscopic-microscopic models (see chapter 3): Calculation predict $B_f \approx 7 - 8$ MeV for $N \gtrsim 170$ while the fission barrier is lower around $6 - 7$ MeV for N between 150 and 170 [1].

2.3 The importance of Fission

In fusion evaporation, fission is in competition with every steps of the ER formation process:

- The $a + A$ system can fission during the formation of the CN (quasi-fission).
- The excited CN C^* can fission.
- The excited ER $C - xn$ can fission.

For heavy elements, fission will be in strong competition with neutron evaporation and other decay channels (because of the strong Coulomb repulsion in the large system). Hence, the production of the ER will be weak and have very small cross sections, of the order of μbarn or less. In fact, the evaporation residues cross-section is about 4 orders of magnitude smaller than the capture; as shown in figure 2.6.

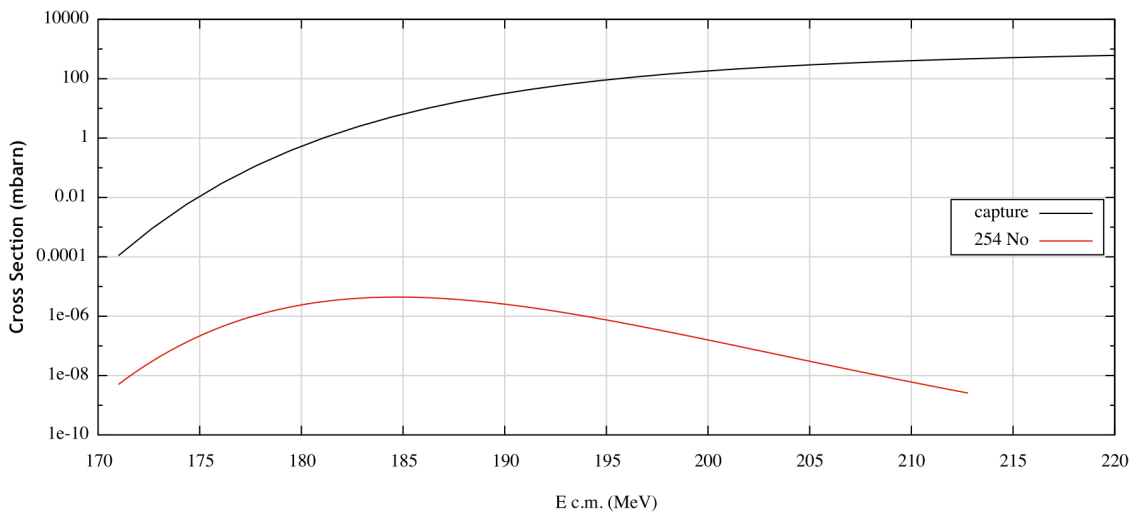


Figure 2.6: Capture (black) and ER (red) cross-section for ^{254}No in the $^{48}\text{Ca} + ^{208}\text{Pb}$ reaction. From [9].

2.3.1 The fission process

As much as the fusion-evaporation process is complex and multi-step, the same is true for fission. During fission, the nucleus goes from one continuous body to two separated fragments: $A \rightarrow F_1 + F_2$ – fission to more than two fragments is possible, but significantly

less probable. Emission of light particles (neutrons, protons, ...) and γ -rays can happen as the fragments may be formed in an excited state. The process implies a deformation of the nucleus from a null or limited value to an *infinite* one (see figure 2.4). [64–66]

A. Sierk describes the barrier in the frame of a macroscopic rotating nucleus model [67], where nuclear energy, surface energy, Coulomb energy and shape energy compete, leading to a macroscopic fission barrier value and its spin dependence. Deviation from the Sierk barrier indicates strong shell effects that stabilise the nucleus [68, 69].

2.3.2 B_f dependence on I

When the nucleus picks up angular momentum, the potential energy previously described (figure 2.4) is modified. In particular, for deformed nuclei, the rotational energy will change the position of the well (mostly its energy, but a change in β can happen). Similarly, the saddle energy E_{saddle} will change, but with a trend different from the change of the well minimum (β_{saddle} can also change) – see figure 2.7. In terms of moment of inertia, the fission barrier and its spin dependence can be expressed as :

$$B_f(I) = B_f(0) - \frac{\hbar^2 I(I+1)}{2} \left(\frac{1}{\mathcal{J}_{\text{g.s.}}} - \frac{1}{\mathcal{J}_{\text{saddle}}} \right) \quad (2.6)$$

with $\mathcal{J}_{\text{g.s.}}$ and $\mathcal{J}_{\text{saddle}}$ the moment of inertia of the ground state and the saddle point and $B_f(0) = E_{\text{saddle}} - E_{\text{g.s.}}$ the fission barrier height at spin 0.

The spin dependence of B_f is a good way to probe the spin dependence of shell effects that stabilise the ground state, since $B_f(I)$ can also be expressed as $B_f(I) = E_{\text{saddle}}(I) - E_{\text{g.s.}}(I)$, with both quantities $E_{\text{saddle}}(I)$ and $E_{\text{g.s.}}(I)$ (the energy of the ground state band) depending on shell effects.

2.3.3 Probing the fission barrier

For nuclei which can be populated by transfer reaction, probing the fission barrier is straightforward: one observes the fission as E^* increases [6, 7], which is a way to probe $P_{\text{fission}} = \Gamma_{\text{fission}}/\Gamma_{\text{total}}$. For VHE and SHE such as ^{254}No , it is not possible since there is no suitable target-projectile combination to excite the nucleus by transfer reaction [70]. However, the γ and fission decay are in competition, and one can observe this competition via $P_\gamma = \Gamma_\gamma/\Gamma_{\text{total}}$ which provides information on B_f . In cases when S_n is larger than B_f by at least ≈ 1 MeV, $P_\gamma \approx \Gamma_\gamma / (\Gamma_\gamma + \Gamma_{\text{fission}})$. The fission width rapidly dominates γ -decay

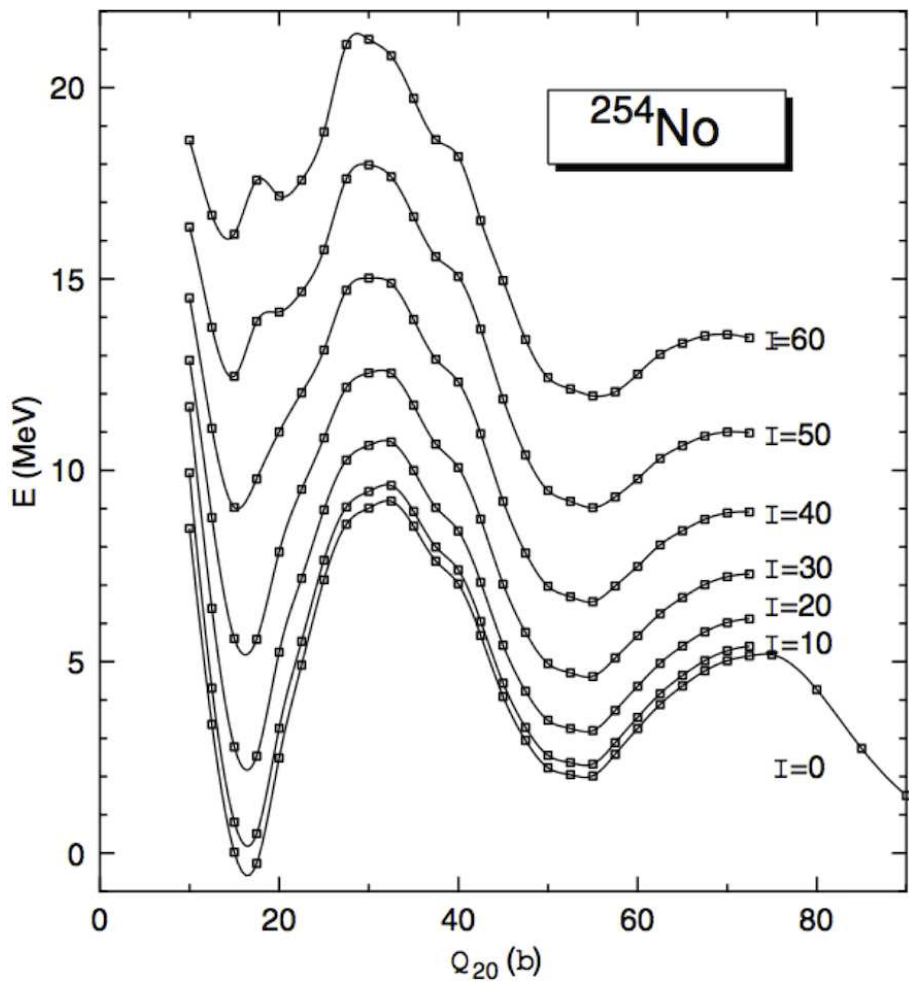


Figure 2.7: Potential energy profile of ^{254}No changing with the angular momentum (I , in units of \hbar). From [3].

as E^* increases. This causes a rapid drop of P_γ [27, 51, 71–74] which provides a sensitive probe of E_{saddle} , as will be discussed in the next chapter.

Chapter 3

Theoretical calculations

3.1 Theoretical predictions of the fission barrier height and spin dependence

As mentioned earlier in section 2.1.3, the fission barrier, or the saddle energy, is a theoretical construct, relevant because it is calculated in all models and for all processes related to fission. There are several ways to calculate the position of the saddle E_{saddle} and the spin dependence characterised by $\mathcal{J}_{\text{saddle}}$.

Liquid drop barrier

The barrier can be calculated in a purely liquid-drop framework, using the model developed by A. Sierk [67]. These calculations do not include any shell effects and the height of the fission barrier for ^{254}No is very small (less than an MeV). The model also predicts a moment of inertia for the saddle, but it is important to notice that it fails to reproduce the ground-state rotational moment of inertia, as pairing is not included.

Macroscopic-microscopic calculation

A more complete way to calculate the fission barrier is to rely on a so called *macroscopic-microscopic* calculation, which relies first on a liquid drop model in a 5-dimensions environment to account for the high-order deformations, plus shell effects introduced via

single-particle energies [1, 2]. Such calculations predict larger fission barrier thanks to the shell effects. However, they do not calculate properties at high spin and hence do not give a moment of inertia for the saddle.

Hartree-Fock-Bogoliubov calculation

In the more complex theoretical frame, self-consistent calculations can be performed, for example within the framework of the Hartree-Fock-Bogoliubov method [3–5]. This method computes energies and deformations and can predict both the height of the barrier and its spin dependence.

Table 3.1 gives a summary of all the calculated height and saddle moment of inertia for the fission barrier in ^{254}No . The *scaled SD* moment of inertia is calculated by scaling the super-deformed band moment of inertia in ^{194}Hg to the ^{254}No mass and saddle deformation $\beta_{\text{Saddle}} = 0.5$; this method takes into account the effect of pairing in the saddle, independently of any model.

Model	$B_f(I = 0)$ (MeV)	$\mathcal{J}_{\text{saddle}}$ (\hbar^2/MeV)	$\mathcal{J}_{\text{g.s.}}$ (\hbar^2/MeV)
Sierk ^(a)	0.9	152.0	135
Macro-Micro with folded Yukawa potential [1]	6.76		
Macro-Micro with Wood-Saxon potential [2]	6.76		
HFB with Gogny D1S force [3]	8.66	140	
HFB with Gogny D1S force [75]	6 – 7		
HFB with Sly4 force [5]	9.6		
HFB with SkM* force [4]	8.6		
Scaled SD		146	
Rigid Body		181	160
Experimental value			75.0

Table 3.1: Table summarising the theoretical predictions for the ^{254}No saddle energy. The g.s. band (yrast) moment of inertia is reminded. ^(a) The Sierk model does not predict a correct ground state moment of inertia.

3.2 Entry distribution calculation

We will use computer codes to simulate the entry distribution in the $^{208}\text{Pb}(^{48}\text{Ca}, 2\text{n})^{254}\text{No}$ reaction. The objective is to investigate the evolution of the entry distribution with beam energy, the effect of the fission barrier on the distribution and have a point of comparison with experimental measurements. Different codes have been tested: analytic calculations and statistical simulations.

3.2.1 Analytic width calculations

Using the simple width formulas given previously (see section 2.1.3) one can calculate $\Gamma_{\text{neutron}}, \Gamma_{\text{fission}}$ and Γ_γ and extract $P_\gamma(I, E^*)$. In particular, one can look at the E^* when P_γ falls below 50%: $E_{1/2}(I)$. These calculations can be done with $B_f(I)$ arbitrarily set to any value. One notes however that this calculations do not take the population of (I, E^*) states in ^{254}No in the reaction into account. Figure 3.1 shows the decay widths and the decay probability as function of excitation energy in ^{254}No .

3.2.2 evapOR calculation

The code evapOR [76] is an extension of the PACE2 code, which allows multi-particle evaporation in a Monte-Carlo framework. It takes as input the target and projectile information and the beam energy. It has been modified [77] to output an entry distribution and so that it is possible to vary the values of B_f . However, although evapOR manages to reproduce fairly well previous experimental measurements like the entry distribution in ^{192}Hg [78], the results calculated for ^{254}No are hard to interpret, as no evidence of fission barrier effects are seen in the calculated entry distribution and no elements were available to validate the evapOR results (for example, evapOR fails to reproduce production cross-sections for ^{254}No). Figure 3.2 shows tentative calculation with evapOR with increasing beam energy but no visible effect of fission, contrary to the expected behaviour. It was therefore decided not to trust those calculations and attempts to use evapOR were dropped.

3.2.3 KEWPIE2

The code KEWPIE2 [8, 79, 80] was written at GANIL to study the fission time in SHE synthesis. It contains a Hauser-Fesbach component, which calculates the population and

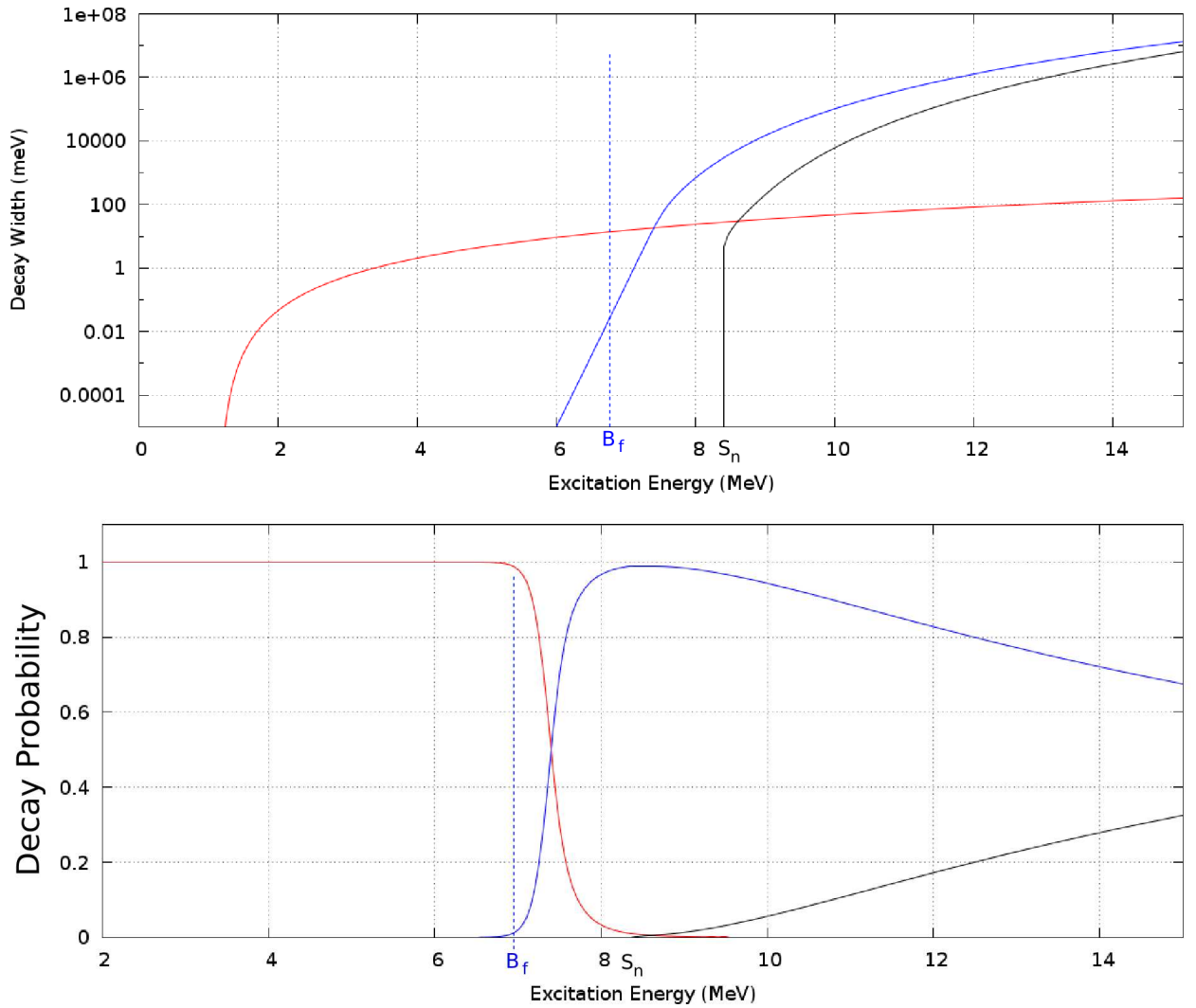


Figure 3.1: Decay widths (Top) and Decay mode probability (bottom) for $I = 0 \hbar$ calculated with analytic width formulas, the γ (red) and fission (blue) widths cross at $E_{1/2}$ which is close to the saddle energy, represented by the blue line. The neutron evaporation width is in black and kicks in at $S_n = 7.71$ MeV. The γ probability falls below 0.5 at $E_{1/2}$ which is the energy where $\Gamma_{\text{fission}} = \Gamma_\gamma$ and is slightly (≈ 1 MeV) above B_f , marked with a blue line.

decay of nuclei at given (I, E^*) . It takes as input the projectile and target nuclei and the compound nucleus excitation energy, the fusion probability is obtained with a proximity potential. Moreover, the code is available and can be modified to suit our needs. It is therefore perfect for calculating entry distribution. As the code was not primarily created to that end, modifications were made to take into account the nuclear deformation and ensure a proper spin dependence of all parameters. KEWPIE2 uses mass, deformation and fission barrier data from [1].

The population of states at (I, E^*) and the decay widths are computed by the modified KEWPIE2 code and then processed into an entry distribution. The entry distribution is populated according to which (I, E^*) states are populated by the neutron decay from $^{255,256}\text{No}$ and which of those γ decay contribute to the entry distribution.

Figure 3.3 shows a calculation of the entry distribution for ^{254}No . In particular, we look at the energy where $\Gamma_\gamma \approx \Gamma_{\text{fission}}$ and $\Gamma_\gamma \approx \Gamma_{\text{neutron}}$.

The KEWPIE calculations display an entry distribution spilling over E_{saddle} at low spin. In other words, $E_{(P_\gamma=0.5)} = 0.5$ is above E_{saddle} and $E_{(P_\gamma=0.5)} - E_{\text{saddle}}$ decreases with spin, which is the same behaviour as suggested in the simple width calculation. The calculations also indicate no effect of neutron evaporation is affecting the entry distribution since the $\Gamma_\gamma \approx \Gamma_{\text{neutron}}$ line is largely above the saddle energy. Finally, the calculations indicate that (I, E^*) states populated by neutron decay are high enough in energy to be directly affected by the fission barrier. Therefore, the truncation of the entry distribution by the fission permits E_{saddle} to be extracted.

Figure 3.4 shows examples of entry distribution at the two beam energies, calculated with KEWPIE2.

3.2.4 NRV calculation

We also used the NRV calculations [9] to simulate an entry distribution. Through the NRV website, one can compute the cross-section, partial fusion cross section and decay width for a given nucleus as a function of I and E^* . By combining all these data, one can simulate the fusion and decay in the $^{208}\text{Pb} + ^{48}\text{Ca}$ reaction down to the (I, E^*) states in ^{254}No that γ decay – hence reconstructing the entry distribution. The input is the compound nucleus (I, E^*) distribution. For consistency, we used the same distribution as the one used in KEWPIE2. This calculation method has two major drawbacks:

- It is not a fully integrated calculation but a code putting together elements from

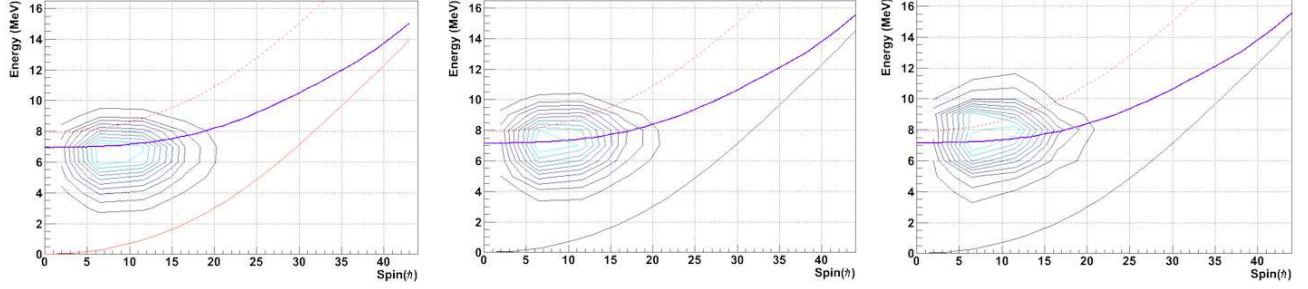


Figure 3.2: Plots of the evapOR calculation with $B_f(I = 0)$ set at 7 MeV and the CN excitation energy increasing from 219, to 221 to 223 MeV. The yrast line is represented in black, the purple line is the saddle energy and the red dotted line is the neutron separation energy. One can see that the spin distribution does not change and the energy distribution is just shifted up. There is apparently no effect of the fission barrier.

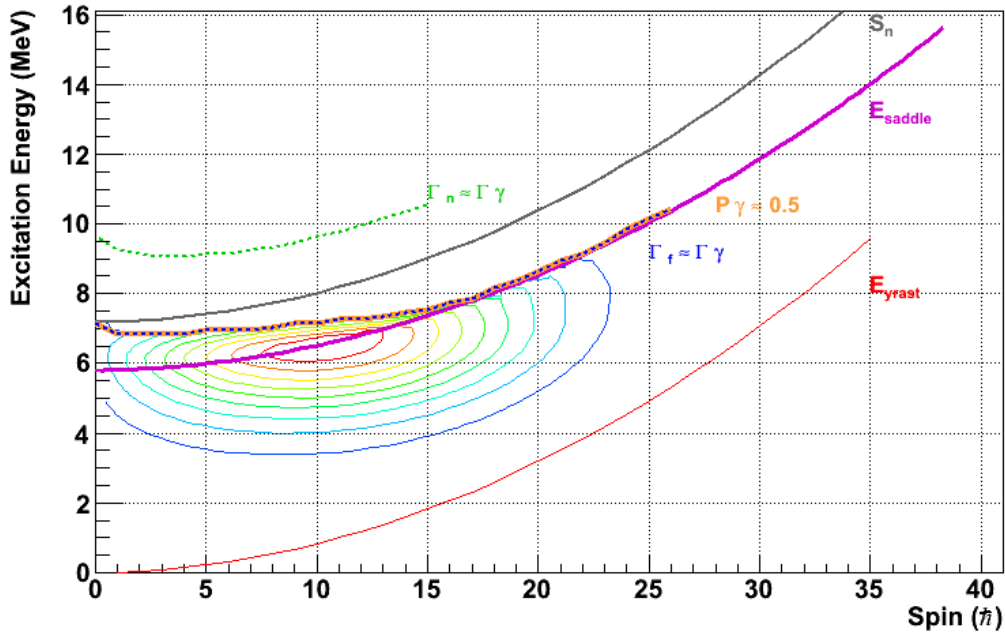


Figure 3.3: Entry distribution of ^{254}No at $E_{\text{beam}} = 219$ MeV calculated with KEWPIE2. The yrast line is in red, the saddle line used in the calculation is the purple line and the neutron separation energy is the gray line. The energy where $P_\gamma \approx 0.5$ is marked in orange and the energies where $\Gamma_\gamma \approx \Gamma_{\text{fission}}$ and $\Gamma_\gamma \approx \Gamma_{\text{neutron}}$ are marked in blue (concurrent with the orange line) and green.

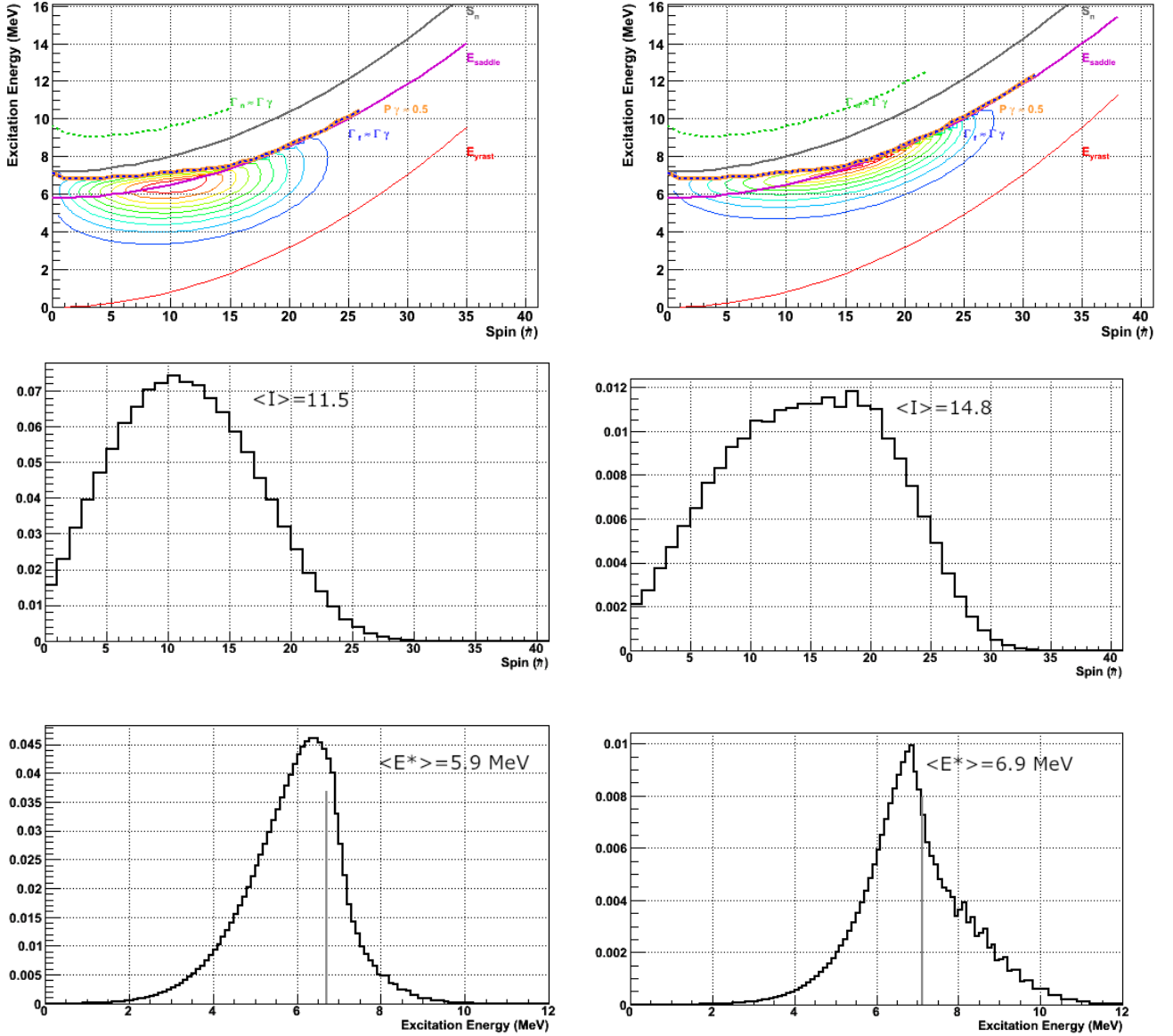


Figure 3.4: Comparison of the entry distribution (top), spin projection (middle) and energy projection (bottom) for $E_{\text{Beam}} = 219$ (left) and 223 MeV (right). In the energy projection, the position of the saddle at the average spin is marked with a gray line.

different sources.

- The decay procedure does not take into account pre-fission or pre-neutron γ emission (although this is probably a very low probability).

Figure 3.5 shows an entry distribution calculated using NRV. Like the distribution from KEWPIE2, it *spills* over the saddle at low spin and the falling point is shifted down in respect to E_{Saddle} with increasing spin.

NRV calculated entry distribution for ^{254}No

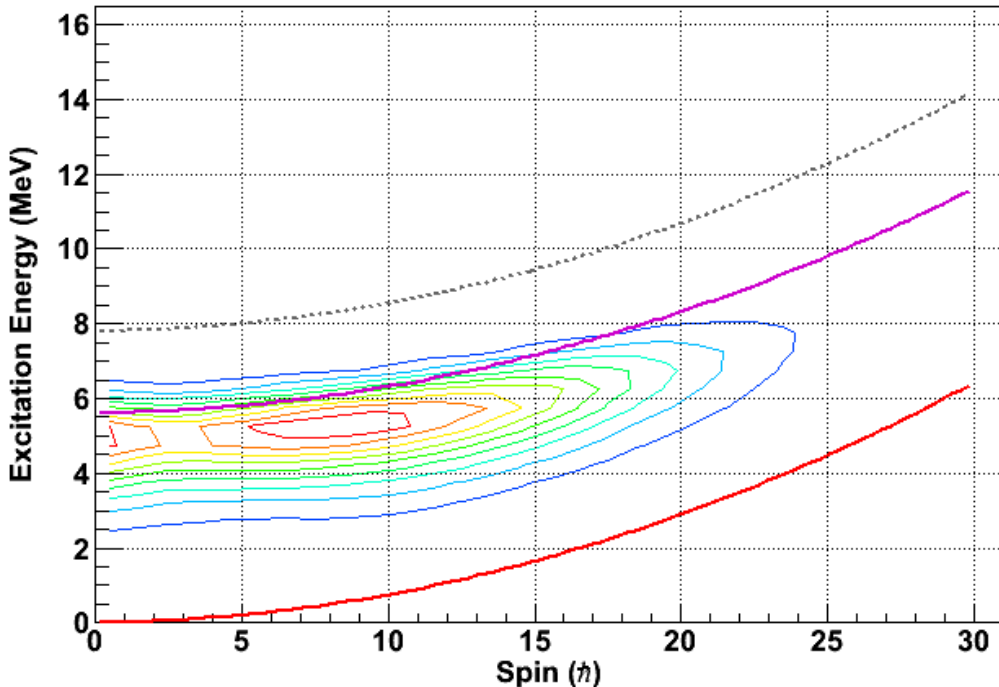


Figure 3.5: Entry distribution of ^{254}No at 223 MeV calculated using NRV. The yrast line is in red, the saddle energy used in the calculations in purple and the neutron separation threshold is the gray dotted line.

With this method, we do not have control of the position and spin dependence of the saddle – or the implementation of shell effects damping, see appendix D. But we can change the profile of the entrance channel partial fusion cross section. We can therefore verify the independence of the final ^{254}No entry distribution with the entrance channel, as shown on figure 3.6: the evaporation-residue spin distribution changes somewhat with the input spin distribution, but it is clear that partial waves higher than $\ell \approx 25 \hbar$ do not survive against fission. Therefore, the maximum spin reached by the evaporation residue is not dependent on the high spins in the entrance distribution.

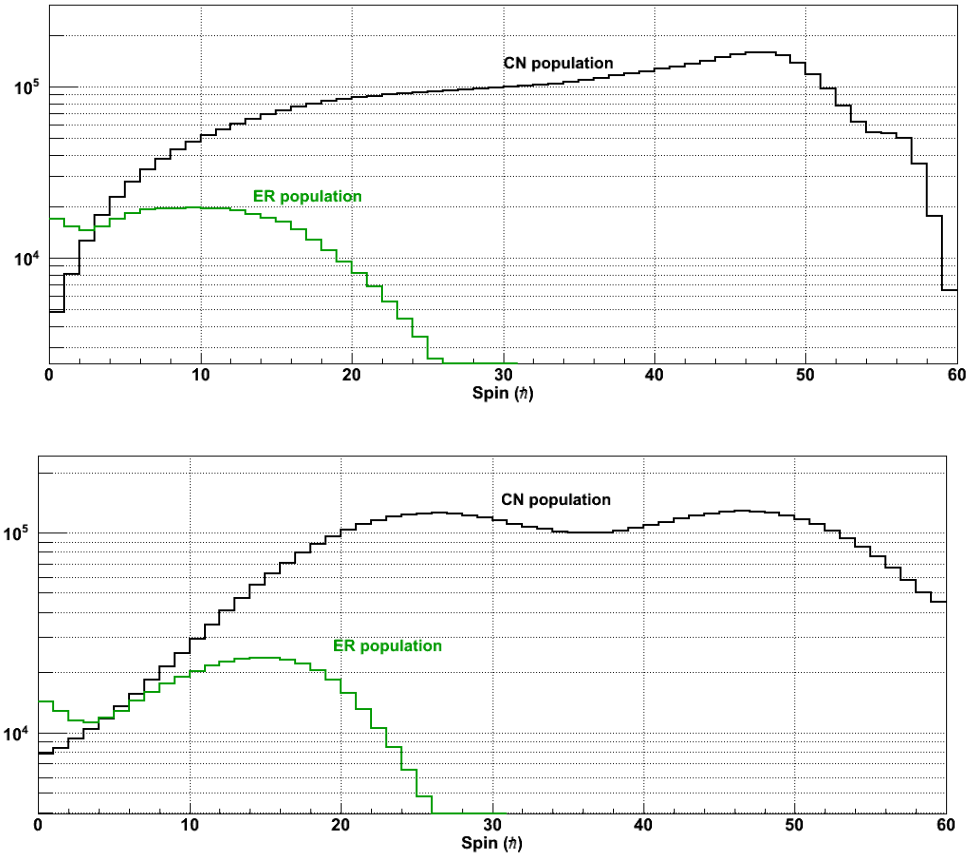


Figure 3.6: Profile of entrance (black) and final (green) spin distributions calculated in NRV for two different partial fusion cross section calculations; in particular, the bottom one follows the double peaked distribution suggested by coupled-channel calculations (see 2.1.2 and [46]). The final distribution of spin slightly changes with the entrance distribution, in particular the position of the maximum. The maximum spin in the evaporation residue distribution is not changed: $I_{max} \approx 25 \hbar$ for both entry spin distribution, because fission depletes the highest partial waves.

3.2.5 Calculations of entry distribution: results

The global characteristics of the entry distributions calculated with the two different codes, for two different *beam energies* corresponding to the experimental measurements, are given on table 3.2. We see that :

- The NRV calculations give slightly lower spin and excitation energy than KEWPIE2.
- The average spin of the entry distribution increases by $\approx 3 \hbar$ when increasing the reaction energy in both cases. The spin distribution width increases also by $1 \hbar$.
- The average excitation energy of the entry distribution increases by 0.7 to 1 MeV when increasing the reaction energy. The energy distribution width increases only slightly (by 0.1 MeV).

Code	Beam Energy (MeV)	Average Spin (\hbar)	Spin Width (\hbar)	Average Energy (MeV)	Energy Width (MeV)
NRV	219	9.8	6.1	5.2	1.2
	223	12.4	7.2	5.9	1.3
KEWPIE2	219	11.5	5.7	5.9	1.2
	223	14.8	6.7	6.9	1.3

Table 3.2: Comparison of the global characteristics of the calculations results from NRV and KEWPIE2 calculations.

As the two codes use the same entrance spin and energy distribution in the CN, the differences in results originate from the treatment of neutrons and γ -decay, in particular, the choice of parametrization of the level density will have a huge influence (damping, spin cut-off, ...). Therefore, the differences reflect the different theoretical approaches.

The two codes use the same saddle energy dependence, with a $\mathcal{J}_{\text{saddle}}$ smaller than the theoretical predictions: $\approx 80 \hbar^2/\text{MeV}$. But this can be changed in KEWPIE2 and we can investigate the effect of a higher or lower saddle, and different spin dependence, in order to determine how the parameters influence the entry distribution. Figures 3.7 and 3.8 show examples of entry distributions calculated with different parameters for the saddle. Calculations with changing $B_f(0)$, all other parameters being fixed, show that an increase in $B_f(0)$ increase the average energy of the entry distribution, as one would expect. Also, the width of the energy distribution decreases and the average spin decreases. For $E_{\text{saddle}} \approx S_n$,

the competition with neutron evaporation stops the trend of decreasing average spin – see figure 3.9. For increasing $\mathcal{J}_{\text{saddle}}$, all other parameters being fixed, we see a decrease of average spin and energy, and a small reduction of spin and energy widths, see figure 3.10.

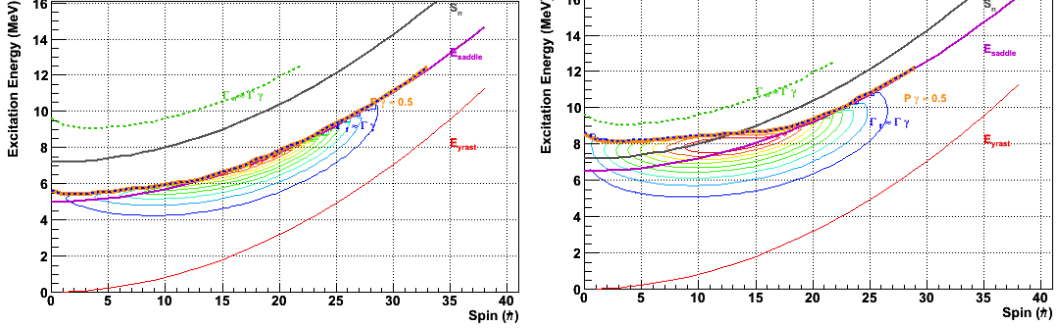


Figure 3.7: Entry distribution calculated by KEWPIE2 for $B_f(0) = 5$ (left) and 6.5 MeV (right), with $\mathcal{J}_{\text{saddle}} = 80 \hbar^2/\text{MeV}$.

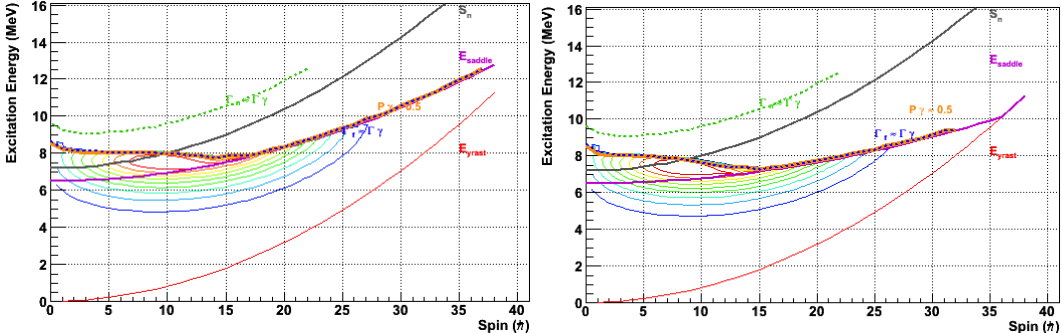


Figure 3.8: Entry distribution calculated by KEWPIE2 for $\mathcal{J}_{\text{saddle}} = 117$ (left) and $175 \hbar/\text{MeV}^2$, with $B_f(0) = 6.5$ MeV.

Relation between $E_{1/2}$ and E_{saddle}

In the calculations, we notice that at low spins, the entry distribution *spills* above the saddle energy line. To understand why the γ -decay stays strong above E_{saddle} , we will consider the quantity $E_{1/2}$, defined as the energy where $P_\gamma(E^*) = 0.5$, with $P_\gamma = \Gamma_\gamma / (\Gamma_\gamma + \Gamma_{\text{neutron}} + \Gamma_{\text{fission}})$ (see section 2.1.3). We will define an equivalent quantity in the experimental entry distribution.

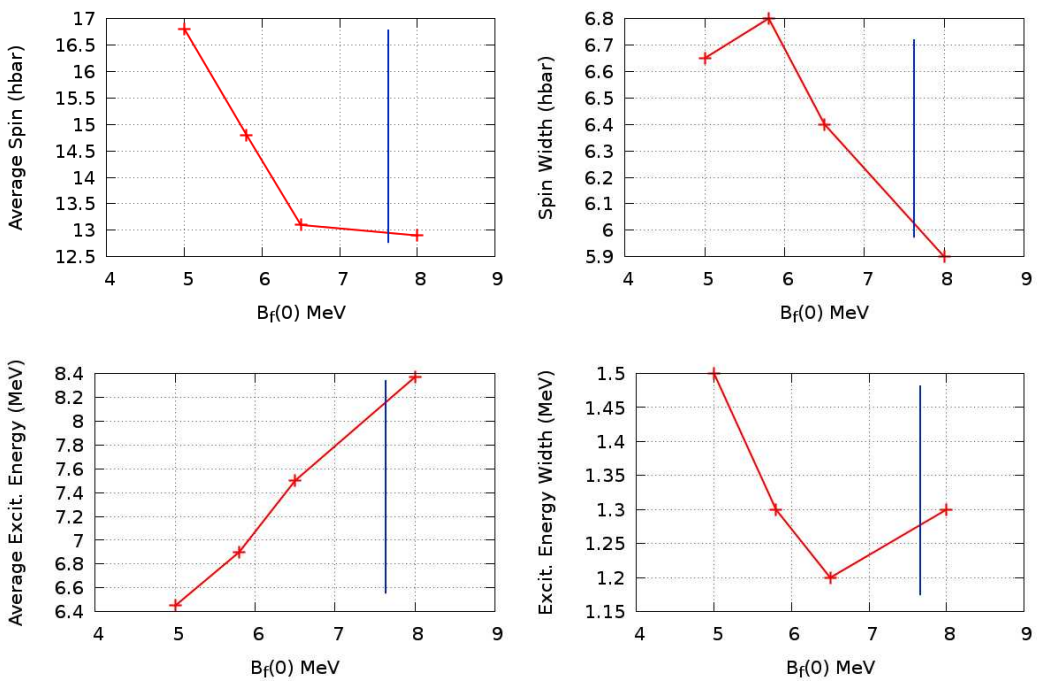


Figure 3.9: Evolution of the global characteristics of the entry distribution simulated with KEWPIE2 for different values of $B_f(0)$. The neutron separation energy ($S_n = 7.71$ MeV) is marked with a blue line. Average (left) and width (right) of the spin (top) and energy (bottom) distributions.

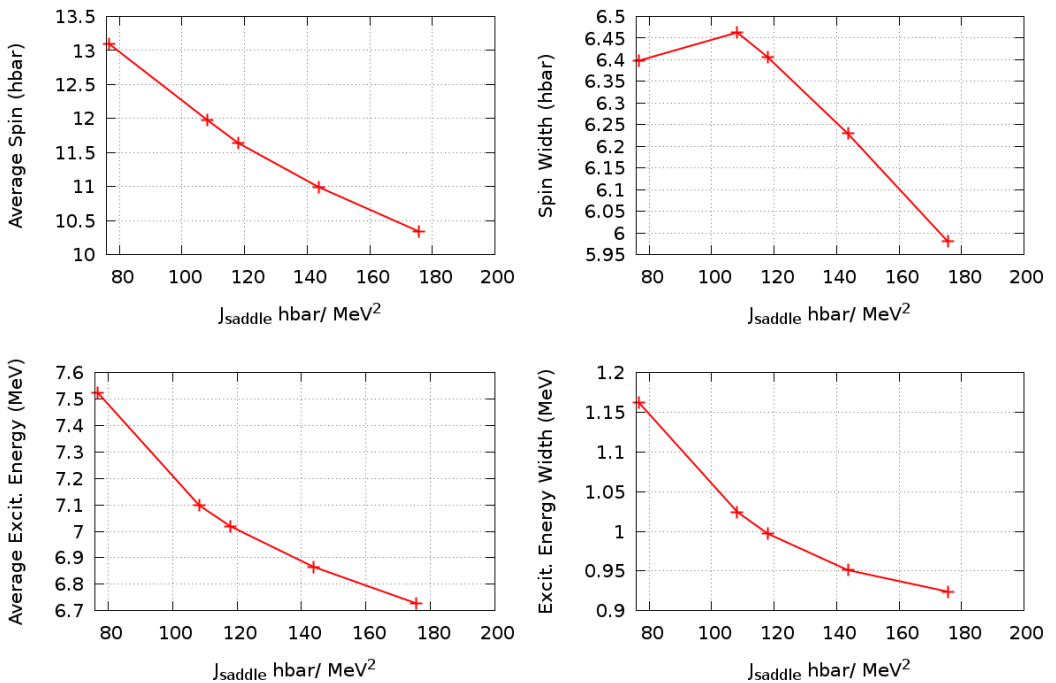


Figure 3.10: Evolution of the global characteristics of the entry distribution simulated with KEWPIE2 for different values of $\mathcal{J}_{\text{saddle}}$. Average (left) and width (right) of the spin (top) and energy (bottom) distributions.

The $E_{1/2}$ energy is linked to the saddle energy and the relation between the two as a function of spin $\Delta(I) = E_{1/2}(I) - E_{\text{saddle}}(I)$ can be extracted from calculations. In the limit of $E_{\text{saddle}} < S_n$, $E_{1/2}$ is found by solving $\Gamma_{\text{fission}} = \Gamma_\gamma$. One can consider that Γ_γ grows exponentially with excitation energy, while Γ_{fission} grows with $E^* - B_f$, therefore, for spins where B_f is large (at low spins) Γ_γ is large when the excitation energy is around B_f while the fission width is still small, and $E_{1/2}$ will be higher than E_{saddle} . At higher spins, where B_f is smaller, Γ_γ is not as large at B_f and the fission and γ widths are equal at an excitation energy closer to B_f .

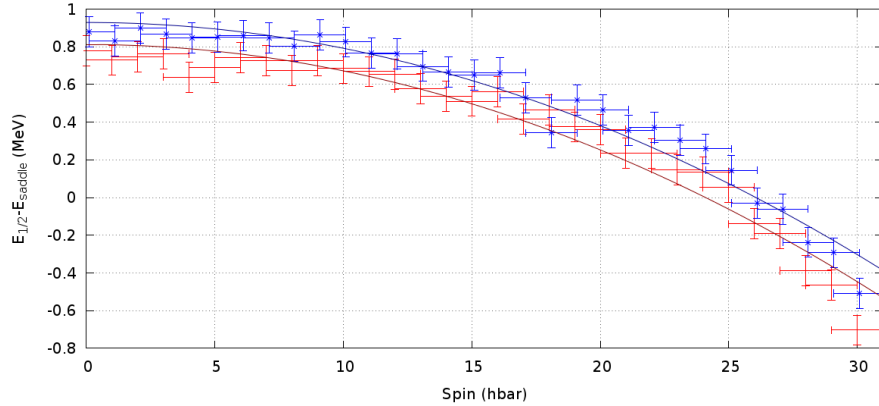


Figure 3.11: Profile of $\Delta(I) = E_{1/2}(I) - E_{\text{saddle}}(I)$ obtained from analytic width calculations. The points are the calculated values, uncertainties come from integration steps, lines represent quadratic fits. The red and blue series correspond to two different parametrization of the saddle: $B_f(0) = 6$ MeV and $\mathcal{J}_{\text{saddle}} = 150 \hbar^2/\text{MeV}$ in red and $B_f(0) = 6.5$ MeV and $\mathcal{J}_{\text{saddle}} = 170 \hbar^2/\text{MeV}$ in blue.

Figure 3.11 shows the profile of $\Delta(I)$: One can see that the $E_{1/2}$ points are above E_{saddle} at low spin and this difference decreases at higher angular momentum. Those calculations lead to $\Delta(I = 0) \approx 1$ MeV and falling to $\Delta(I \approx 30 \hbar) = 0$.

It is very important to notice that $\Delta(I)$ is a calculated quantity that depends on the $B_f(I)$ used in the calculation, and also on the calculation model. In figure 3.11 we see that small changes in the saddle energy parametrization affects Δ only slightly. Also, as shown in figure 3.12, each code gives a different behaviour for $\Delta(I)$. One will have to be careful of the self-dependence of B_f extracted from experimental data using a calculated Δ .

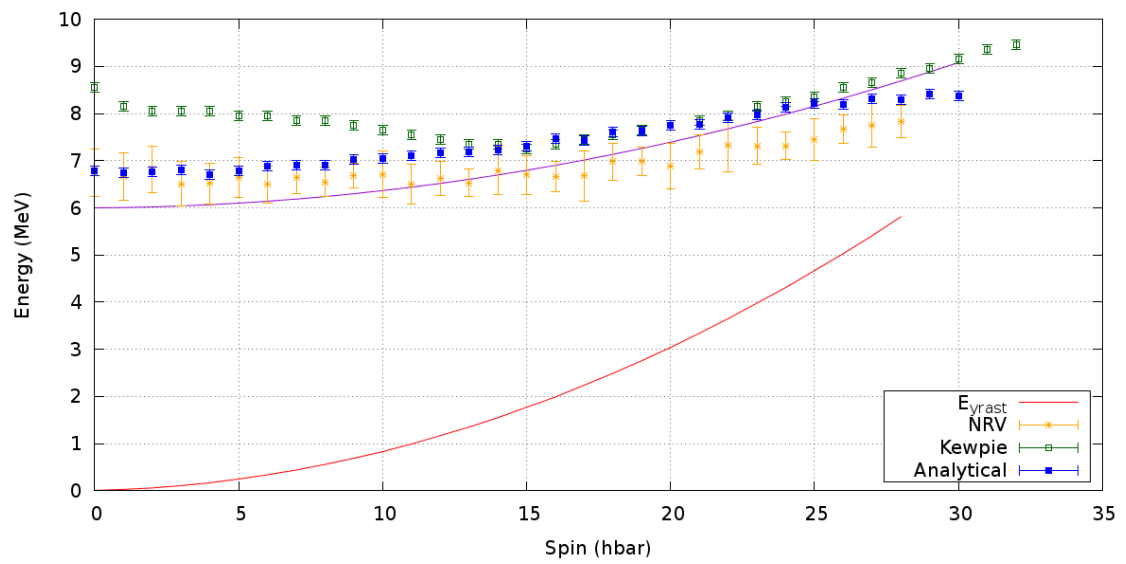


Figure 3.12: Values of $E_{1/2}$ from different calculations: NRV (orange), KEWPIE2 (green) and analytic calculation (blue) compared to the E_{saddle} parametrization (purple line). The yrast line is the red line. The $E_{1/2}$ points are above E_{saddle} by as much as 2 MeV at low spin and decrease with respect to E_{saddle} with increasing spin.

3.3 Conclusion on calculations

From the calculations, we learned:

- The average spin of the entry distribution is expected around $10 - 15 \hbar$ and the distribution extends up to spin $25 \hbar$.
- The average energy in the entry distribution is expected around 5 to 7 MeV with the distribution extending up to 8 MeV.
- Increasing the beam energy from 219 to 223 MeV increases the average spin by up to $3 \hbar$ and the excitation energy by 1 MeV.
- With larger $B_f(0)$, higher excitation energies in the entry distribution are obtained. With larger moment of inertia $\mathcal{J}_{\text{saddle}}$, the maximum spin is reduced.
- The entry distribution is clearly truncated at $E_{1/2}$ which is above E_{saddle} at low spin and decrease with higher spins.

These calculations clearly show that the entry distribution is largely dependent on the position of the saddle (it also slightly depends on the entrance spin distribution), and that confirm the possible extraction of the fission barrier from an entry distribution measurement.

Chapter 4

Experimental measurement of Fission Barrier

4.1 Experimental setup

4.1.1 Reaction

The reaction used to produce ^{254}No is $^{208}\text{Pb}(^{48}\text{Ca},2\text{n})^{254}\text{No}$. This reaction is well documented and has been used since 1979 to produce ^{254}No with a reasonable cross section. References [62, 81, 82] gives the excitation function for the reaction, reproduced in figure 4.1. One can see the ^{254}No can be produced with cross-section up to about $3 \mu\text{barn}$. The beam energies used in the experiment are 219 and 223 MeV – respectively 178 and 181 MeV in the Center of Mass frame. These energies are above the peak of the cross section. However, the energy loss in the target will bring the beam energy down to a corresponding higher cross section, and more importantly, as we intend to populate ^{254}No at the highest spin possible the higher beam energy will bring more angular momentum to the system. Due to energy spread in the target, the incoming ^{48}Ca energy varies between 218.2 and 214.5 MeV (222.3 and 218.5 MeV respectively) in the laboratory frame. The corresponding maximum excitation energy depends on the centre of mass energy and the Q value of the reaction $E_{\max}^* = E_{cm} + Q$. Table 4.1 gives the relevant energies. The maximum excitation energy for the ^{254}No is between 8 and 11.0 MeV (between 11 and 13.5 for 223 MeV beam). At those energies, the cross-section are of the order of $2 \mu\text{barn}$ for the 219 MeV beam and $1 \mu\text{barn}$ for the 223 MeV beam (cross sections at mid-target energies)– see figure 4.1.

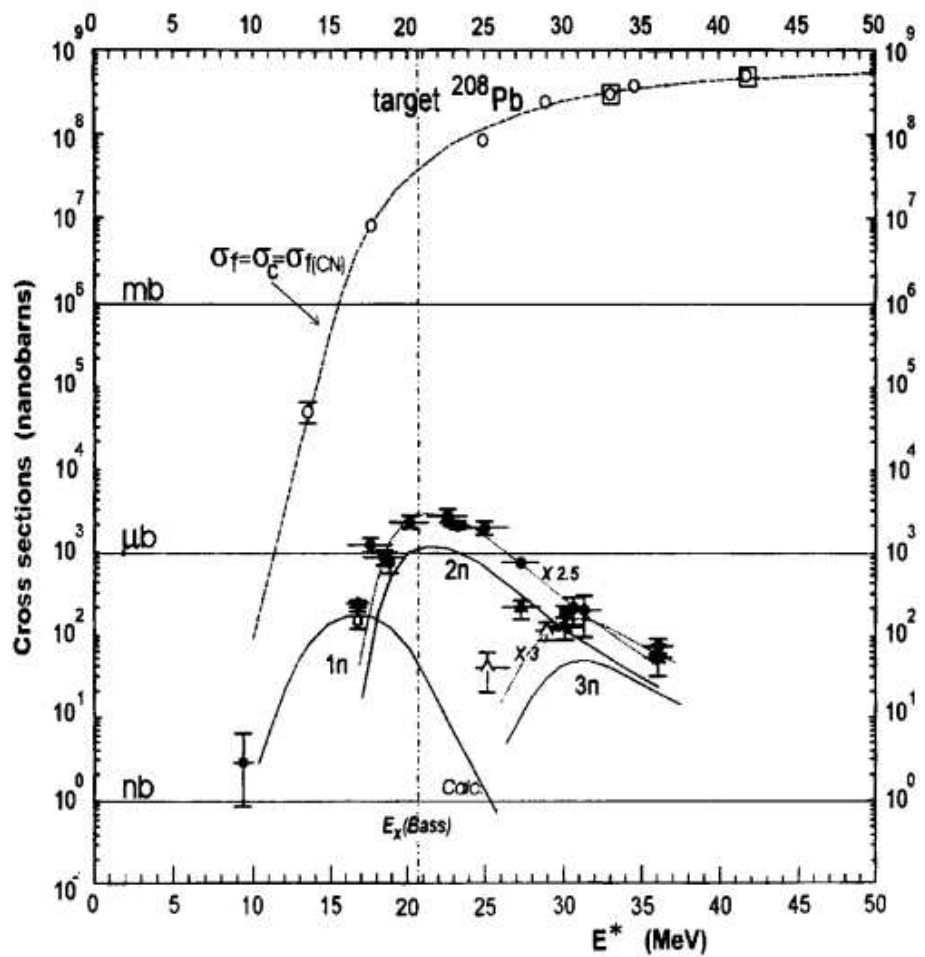


Figure 4.1: Excitation function for the $^{208}\text{Pb}(^{48}\text{Ca}, 2\text{n})^{254}\text{No}$ reaction. The position of the Bass barrier is marked by E_x [81, 82].

$^{208}\text{Pb} + ^{48}\text{Ca} \rightarrow ^{256}\text{No}$	Q -value	-153.8 MeV
^{256}No 2 neutrons separation		13.04 MeV
^{256}No neutron separation		7.05 MeV
^{255}No neutron separation		5.99 MeV
$^{208}\text{Pb} + ^{48}\text{Ca} \rightarrow 2\text{n} + ^{254}\text{No}$	Q -value	-166.6 MeV
^{254}No neutron separation		7.71 MeV

Table 4.1: Q -values for the formation of the compound nucleus and the ^{254}No residue. The neutron separation energies are also given. The Q -value of the full reaction is equal to $Q_{CN} - S_{2n}^{256\text{No}}$. By definition, $S_{2n}^{256\text{No}} = S_n^{256\text{No}} + S_n^{255\text{No}}$.

Reaction kinematics

The reaction kinematic characteristics are given in table 4.2. The kinematics of the reaction are of importance for the separation of the recoils after the target (in the FMA see section 4.1.7) and the Doppler correction of the γ -ray energies. In addition to purely kinematic considerations, the beam and recoils loose energy in the target. That influences the reaction energy and recoil speed. For ^{254}No recoils, the stopping power in matter is not known and has to be extrapolated from the heaviest known nuclei to the appropriate mass with the same kinematic energy per nucleon. The recoiling ^{254}No have an angular dispersion (half angle) of the order of 3.8 ° in the laboratory frame (this has to be compared with the separator solid angle acceptance : 8 msr or 5.6 ° aperture – see section 4.1.7) – taking into account the kinematic dispersion from the neutron evaporation and the straggling in the target material.

4.1.2 Beam structure

The beam of ^{48}Ca was delivered by the ATLAS accelerator with a charge state $Q = 11^+$ as a 12.1 MHz (82.48 ns period) pulsed beam. The average intensity was 100 enA, varying between 90 and 120 enA – giving a current of 8.2 to 10.9 pA. Figure 4.2 shows the beam structure visualised as time of γ -ray events. The current was held down to avoid saturating Gammasphere with fission gammas and neutrons.

Beam energy (MeV)	219	223
Projectile speed (c)	0.0989	0.0998
Min.– Max. Reaction Energy ^a (MeV)	215 – 219	218.5 – 222
Mid-target Reaction Energy (MeV)	217	220.5
Mid-target Recoil speed (c)	0.0179	0.0181
Mid-target Recoil energy (MeV)	38.0	38.7
Min.– Max. Recoil Energy ^b (MeV)	37.5–38.3	38.2–39.0

Table 4.2: Reaction kinematics characteristics, for the two beam energies. The energies and recoil speed take into account the energy loss in the target and in the backing material.

^a takes the loss of kinematic energy of the projectile in the target material and the front target backing into account. ^b takes the projectile and recoil energy loss in the target, the backing material and the reset foil into account; the recoil energy governs the time of flight through the FMA and implant energy at the focal plane. See section 4.1.8.

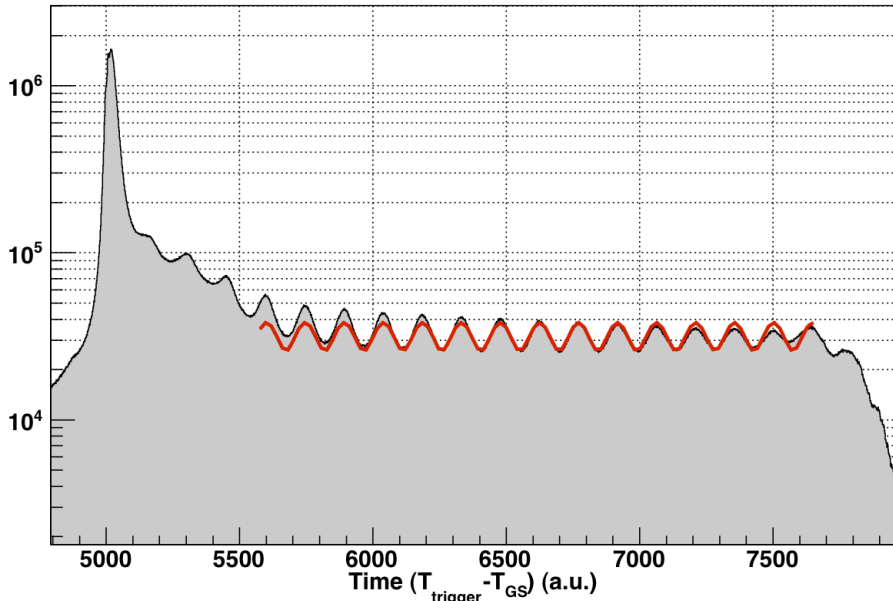


Figure 4.2: Beam structure, seen in the spectrum of time difference between the events in individual Gammasphere modules and the trigger signal when a certain multiplicity of γ rays is reached. The red line shows a sinusoidal fit on the oscillations. The period is 82.48 ns, corresponding to the expected time between beam bursts.

4.1.3 Beam spot

To avoid putting too much energy on the target at the risk of melting it, the beam was slightly defocused in the horizontal direction (about 2 mm wide) and the beam was *wobbled* in the vertical direction with a 2-3 mm range.

4.1.4 Target

The enriched ^{208}Pb target used was $\approx 0.5 \text{ mg/cm}^2$ thick with a ^{12}C front (0.04 mg/cm^2 thick) and back (0.1 mg/cm^2 thick) backing.

The carbon backing of the target is used primarily as support: in the preparation process the ^{208}Pb is deposited by evaporation on the carbon foil. The second backing is added on top of the target material to protect it from oxidation in the open air. During the experiment, the backing also prevents the ^{208}Pb from sputtering out from the target.

We used four quarter-of-a-circle targets mounted on a rotating wheel, as one can see on the picture in figure 4.3. The wheel was rotating at 500-600 rpm. The beam was swept using an electrostatic sweeper to avoid irradiating the wheel spokes. The beam was swept-off about 27% of the time.

4.1.5 Reset foil

At the exit of the target, the recoiling nuclei have a broad distribution of charge states between 16^+ and 24^+ , centred on 19^+ [83]. After the target, the electron cloud may be perturbed by internal conversion and other atomic processes following the decay of long-lived excited states. Those processes can increase the charge state by several units.

A 0.007 mg/cm^2 thick carbon foil was placed about 5 cm after the target for charge resetting. It brings the charge states back to an average $Q \approx 19 - 20^+$. The presence of the reset foil does not influence the recoil kinematic energy by more than 0.52 %. The reset foil was changed several times during the 10 days of experiment.

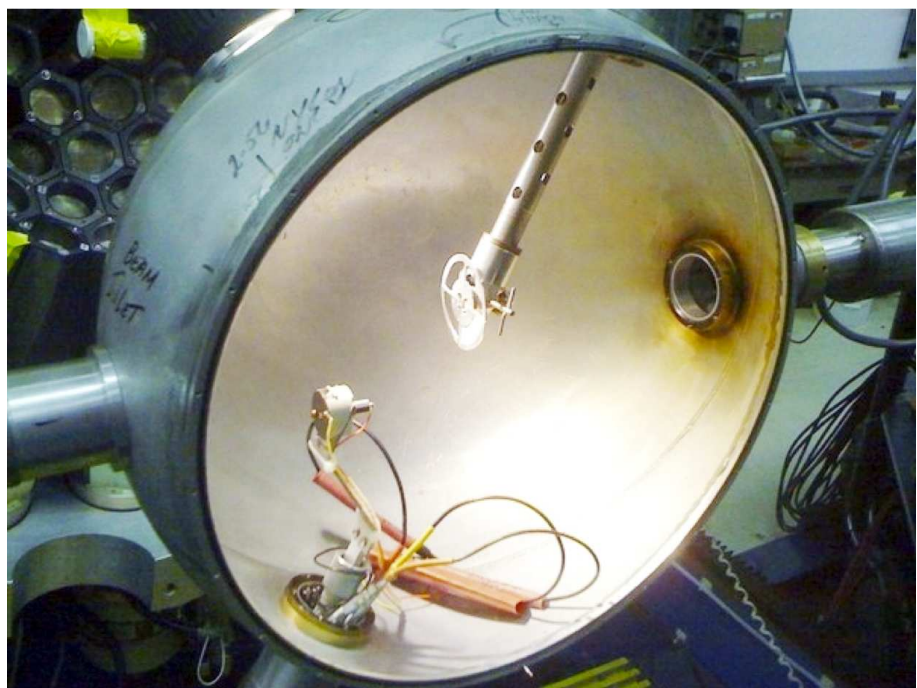


Figure 4.3: Target chamber with the target wheel inside.

4.1.6 Gammasphere

Gammasphere is the world's most powerful gamma ray spectrometer for nuclear structure research today¹. It consists of up to 110 high-purity germanium detectors, arranged in a sphere covering about 50 % of the solid angle and with an average detection efficiency of 14% (up to 22% at 300 keV, 9% at 1.3 MeV). A photography of a Gammasphere hemisphere is visible on figure 4.4.

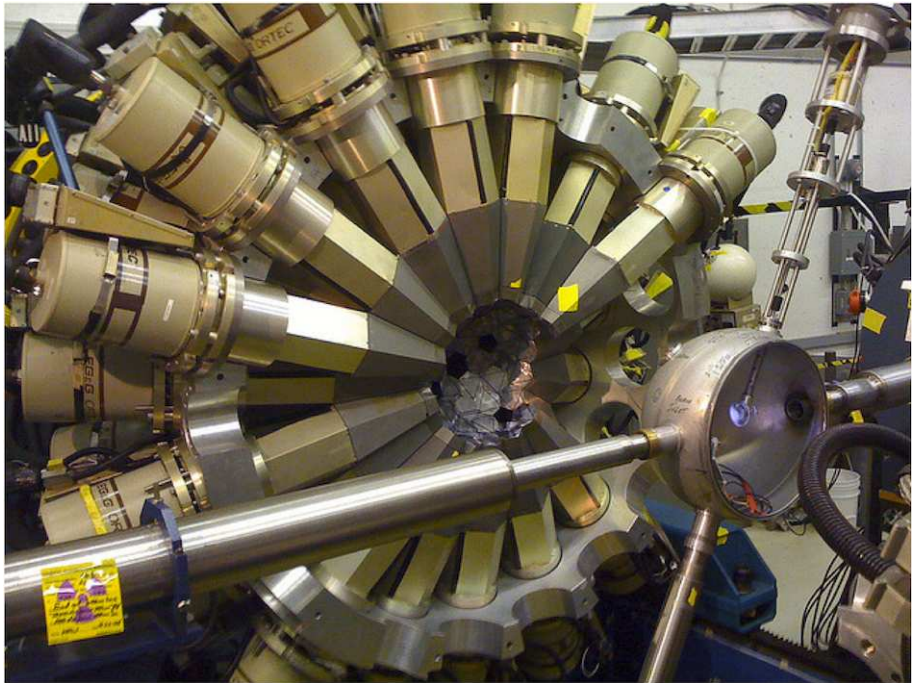


Figure 4.4: Target Chamber with an hemisphere of Gammasphere (the sphere is open).

The Ge crystals are enclosed in a Bismuth-Germanium-Oxide (BGO) shields divided into six sectors, each served by a pair of photo-multipliers, plus one additional *back plug* sector located behind the Ge crystal, that serves as a Compton suppressor. The Peak-To-Total of the gamma ray detection is about 60% (up from $\approx 25\%$ for unsuppressed detection). The large number of detectors allow the study of high multiplicity reactions [84,85]. A Ge crystal and the enclosing BGO shield make a *module*. A schematic view of a module is given on figure 4.5.

The BGO signal consists of the sum signal of all BGO sectors plus the *hit pattern* of each indicating which BGO sectors fired. It is coded as a byte with each of the first 7

¹Gammasphere was used as model in the 2003 movie *The Hulk* in which B. Banner is irradiated by a device called Gammasphere looking exactly like the original. Unlike in the movie, the real Gammasphere does not shoot γ -rays but detect them.



Figure 4.5: Schematic view of a Gammasphere module. The Ge crystal (Ge) (in green) is surrounded by a BGO shield (in purple) around and at the back (*back plug*) to catch scattered γ rays escaping from the rear of the Ge crystal. An absorber foil is set at the front of the module (not represented). A hevimet shield (orange) can be placed in front of the BGO, but has been removed in our experiment. The Ge crystal is kept cold with liquid nitrogen.

bits standing for one sector (6 surrounding plus the back plug). Events in Gammasphere modules come with a time for Ge and BGO signals; these are the intervals between the detection of a γ in the Ge (or BGO) and the global trigger signal – see section 4.1.9. In the following, we will mention these times as t_{Ge} and t_{BGO} .

To attenuate for the intense ^{208}Pb X-rays in the experiment – from passage of the beam through the target material and to a smaller extent Coulomb excitation of the target nuclei – absorbers of Cu (0.23 mm thick), Ta (0.05 mm thick) and Cd (0.51 mm thick) were placed in front of the modules to decrease the low energy detection efficiency – see figure 4.6. The X-rays are produced after atomic excitation or electronic conversion.

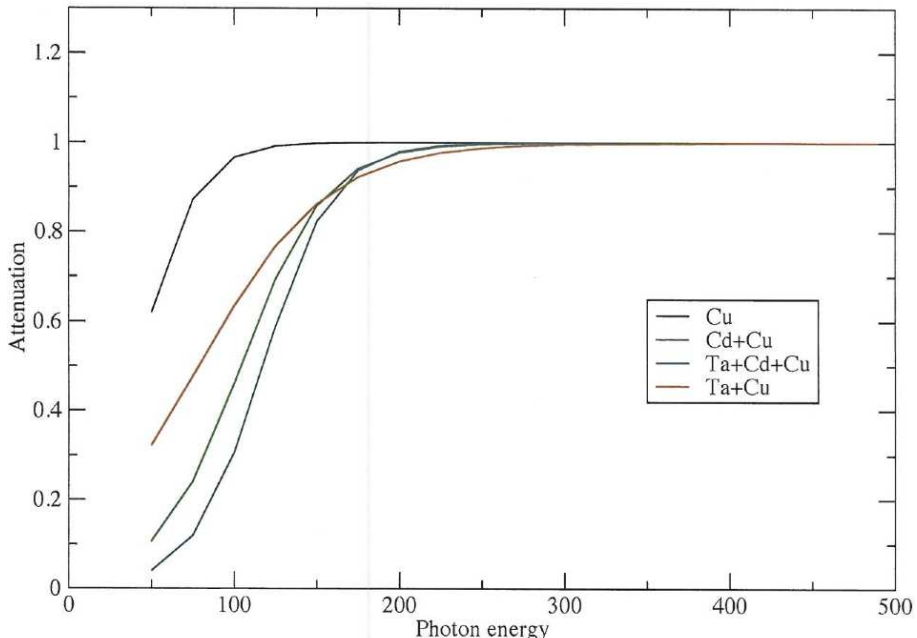


Figure 4.6: Transmission curve with different absorbers placed in front of the Gammasphere modules. During the experiment, Cu, Ta and Cd where used to cut the X-rays of Pb.

During the experiment, Gammasphere comprised 108 BGOs (with at least one sector working) and 101 Ge crystals.

Calorimetric mode

We used Gammasphere in a special mode, to get calorimetric measurements. In this mode, we measure for a single event the total energy deposited within all the active material of Gammasphere and the number of detected hits. For this purpose the BGO shields are not used as Compton suppressors, but as part of the detection system. The calorimetric

measurement is described in detail in section 4.3.

The modules are usually fitted with *hevimet* shields in front of the BGO (composed of 80 % Tantalum, 13 % Nickel and 7 % Copper, with a density of 19 g/cm^3 .), so that only the Ge crystal have a direct view of the target and the BGO are hit only by γ -rays scattered from the Ge. But for the calorimetric measurement the shields were removed from Gammasphere in order to allow all γ -rays to be directly detected.

4.1.7 Fragment Mass Analyzer

The Fragment Mass Analyzer (FMA) was used to sort the scattered beam and transfer products from the evaporation residues. The FMA is installed at ATLAS and placed after Gammasphere. It separates the primary beam from nuclear reaction products and disperses those according to their mass-to-charge ratio (m/q) in the horizontal direction (thereafter noted X). The separation of ions is obtained by a symmetric combination of two electric dipoles and one magnetic dipole, plus two quadrupole doublets at the entrance and exit of the separator for focusing. Moreover, the FMA is *isochronous*, i.e. the time of flight of ions through the separator does not depend on the trajectory they follow, but only on their velocity. The FMA acceptance is $\approx 8 \text{ msr}$ and the overall transmission efficiency is estimated to be $\approx 7\%$ for this reaction. For other reactions, the FMA transmission can be as high as 85 % [86,87]. The transmission of V&SHE in fusion-evaporation reaction by the FMA is poor, due to the acceptance of only two charge states, compared to other facilities: RITU at Jyvaskyla has a $\approx 40\%$ transmission, the Berkeley Gas Separator's transmission is around 70 %, – see appendix B. Figure 4.7 shows a schematic of the FMA layout.

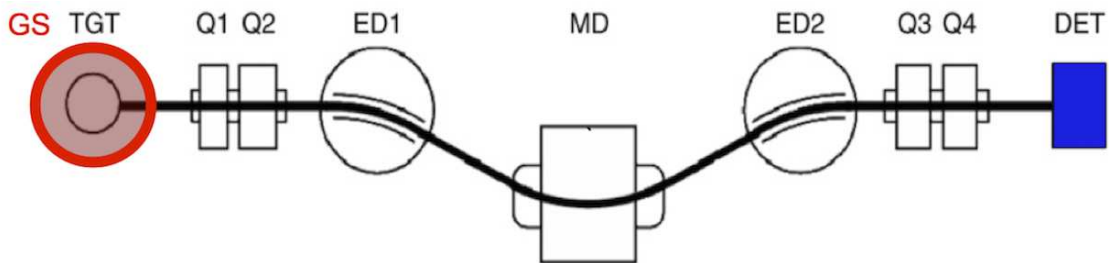


Figure 4.7: Schematic view of the FMA. Gammasphere (GS, in red) surrounds the target position (TGT) 4.1.4. The FMA is made of four quadrupoles (Q), two electric dipoles (ED) and one magnetic dipole (MD). Detectors (DET, in blue) are located at the focal plane for recoil identification and delayed spectroscopy. See 4.1.8 for focal plane detectors.

The FMA magnets system has been calibrated [88] so that it can be automatically set to transmit a given nucleus with a given charge state to the focal plane. The dispersion is

done in the horizontal direction. Therefore, the vertical wobbling of the beam does not affect the recoil separation.

4.1.8 Focal plane detectors

At the focal plane of the FMA were placed detectors for recoil identification and delayed spectroscopy. Figure 4.8 shows a schematic of the focal plane detectors.

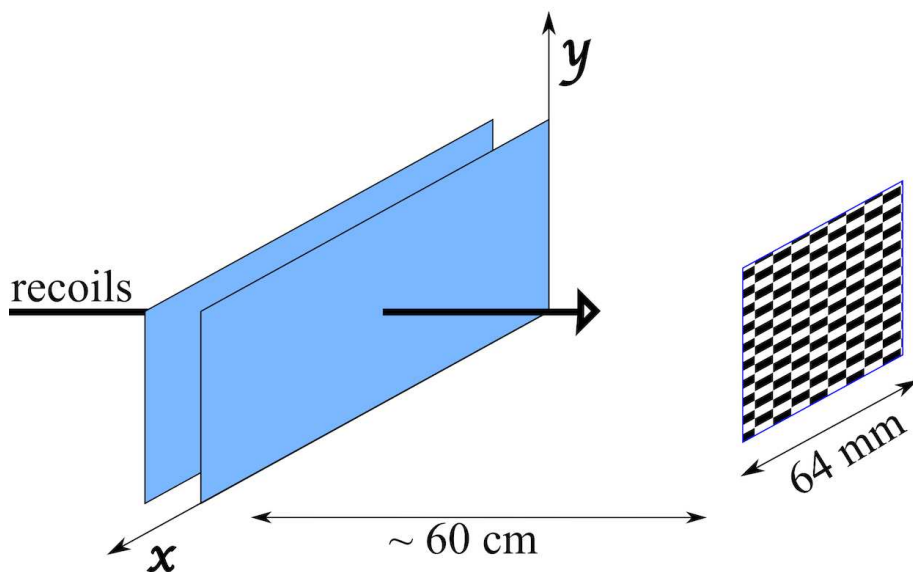


Figure 4.8: Schematic drawing of focal plane detectors. The recoils first go through the PPAC (in blue) where ΔE , x and y information are measured. The recoils implant in the DSSD (chessboard square), where E_{implant} and pixel information are measured. The time of flight is measured between the DSSD and the PPAC.

PPAC

A multiwired proportional counter (called *PPAC* for Parallel Plate Avalanche Counter), is placed at the focal plane and provides energy loss (ΔE) and position (X, Y, in the horizontal and vertical direction) information. It can be used to identify the recoil. The PPAC consists in two Mylar windows surrounding the cathode-X-anode-Y electrode wires, and is filled with isobutane (C_4H_{10}) at 3 Torr. The energy loss in the PPAC is of the order of 9 MeV for a ^{254}No recoil with a kinetic energy of 38 MeV.

DSSD

The FMA focal plane implantation detector is a Double Sided Stripped Silicon detector, with 160 strips on each side. Figure 4.9 shows a picture of the DSSD. The detector active area is a $6.4 \times 6.4 \text{ cm}^2$ and the strips are $400 \mu\text{m}$ wide. The Si detector is $100 \mu\text{m}$ thick, with a front dead-layer of $0.8 \mu\text{m}$.

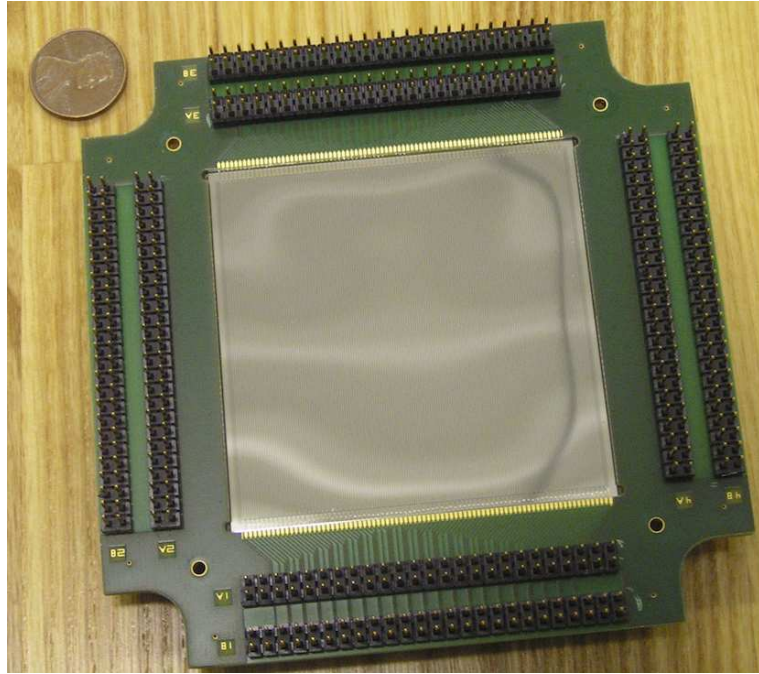


Figure 4.9: Picture of the 160×160 strips DSSD. The detector measures 6.4 cm for each sides.

Recoils are implanted in the silicon and the front and back strips where the observed signal is the highest are assigned to the event, defining an implantation pixel. The pixel position will be used to follow the decay of the implanted nuclei over time inside the Silicon. The time of flight (ToF) between the PPAC and the DSSD is measured for the recoil identification. The recoil and decay events are processed by different electronic chains.

4.1.9 Trigger

The data acquisition triggers on any event detected at the focal plane of the FMA. The Gammasphere data is kept on the data bus for up to $2 \mu\text{s}$ waiting for the validation from the PPAC as an external trigger.

Thee are two types of event:

Decay event: A decay event is triggered by the overlap of a front and back signal in the DSSD decay channel. The event is built from the DSSD decay signals and comprises the pixel ID, the timestamp of the event and the energy in the DSSD. The Gammasphere signals have no trigger conditions (whether in time, energy or multiplicity), moreover, because of the calorimetric mode, there is no Compton suppression (but the modules can be tagged as *dirty* offline).

Recoil Event A recoil event is triggered by a signal in the PPAC; it vetoes the trigger of a decay event. Recoil events contains the PPAC information ($X, Y, \Delta E$), the DSSD information (pixel coordinates, energy), the time of flight and the Gammasphere information, if any.

Figure 4.10 describes the trigger logic. During the experiment, the average global trigger rate was 170 to 180 Hz, with a DSSD event rate around 1 – 2 Hz.

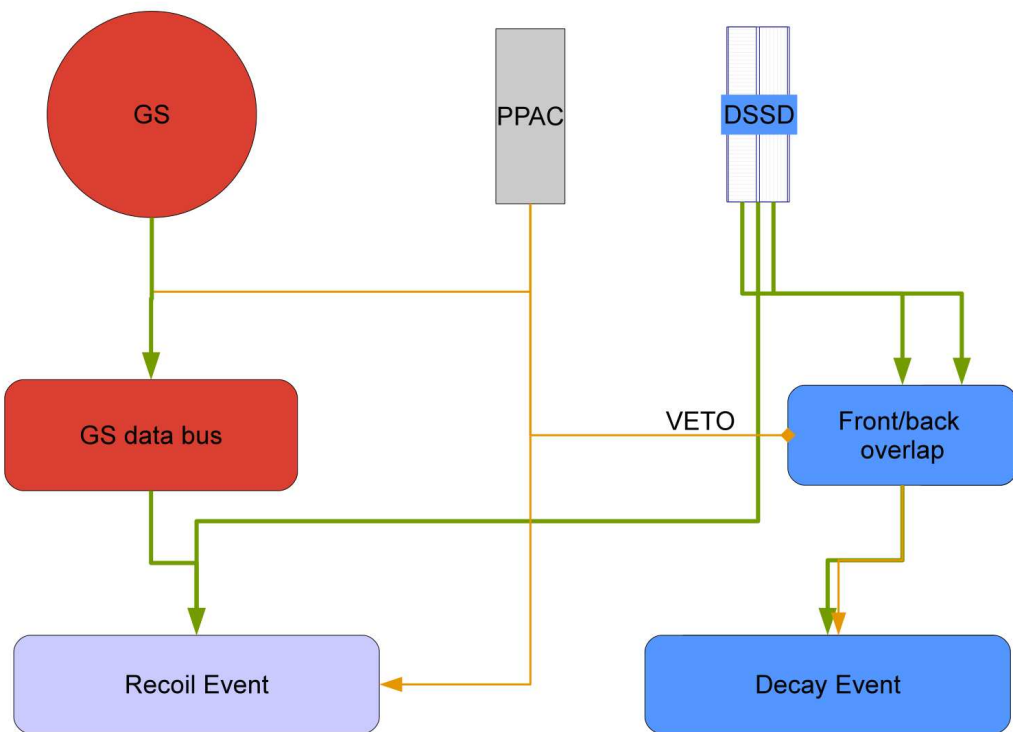


Figure 4.10: Trigger logic schematic representation. The green lines represent the signals read by the acquisition, the orange lines are the logical trigger signals. The two types of event are associated with different trigger signals. The PPAC signal triggers the reading of the Gammasphere information and the PPAC and DSSD recoil signals, while vetoing the decay overlap trigger. The decay trigger initiates readout of the DSSD decay signals.

4.2 Recoil and recoil decay tagging

The very small cross section of the reaction makes it hard to observe ^{254}No γ -rays at the target position, which we need for the calorimetric measurement. The information from the PPAC is not quite enough to unambiguously identify the nuclei of interest and to select the corresponding target-position events. The best signature of ^{254}No is the α decay energy and half life. The correlation between recoils and subsequent decays over time allows the unambiguous identification of nuclei.

4.2.1 Target-position – focal plane correlation

Target-position – focal plane correlation: Every implant event is associated with the target-position events: γ energies detected by the Ge or BGO and time between the detection in Gammasphere and the event trigger (PPAC signal). Implant events contain the relevant *prompt* Gammasphere data. The only additional selection needed is the time between the detection of the recoil at the focal plane and the detection of the γ -ray which has to be the time of flight of the recoil.

4.2.2 Pixel correlation in the DSSD

Pixel correlation in the DSSD: The high pixelization of the silicon detector leads to a low rate of implant and decay in each pixel. With an average 200 Hz experimental rate of DSSD implant, there was a rate of the order of 8 mHz implants per DSSD pixel; with an average decay rate around 2 Hz the average decay rate in a pixel is 80 μHz . With an average 2.5 minutes between two pixel events and about 200 minutes between decays, there is enough time to observe two subsequent decays of ^{254}No or its daughter nuclei (respectively 51 and 1800 seconds half lives).

The decays in the DSSD are correlated to a previous implant in the same pixel using the pixel coordinates. A time condition is put on $\Delta T_{1\text{st decay}} = T_{\text{decay}} - T_{\text{implant}}$ restricting the implant-to-decay correlation time to a few half lives of ^{254}No ($T_{1/2}(^{254}\text{No}) = 51 \text{ s}$) to avoid correlating with random events. One limit of the method is that the detection efficiency of the α is about 55 % because the emitted α might escape from the silicon and leave only a tiny fraction of its energy.

4.3 Calorimetric measurement

4.3.1 Principle of measurement

The calorimetric measurement with Gammasphere is done by using the BGO shields as part of the detection system. We measure the total energy detected at the target position and the number of Gammasphere modules that fired – the *fold*. We will need to calibrate the BGO energy reading precisely to find the original total energy and the number of γ -rays emitted by the nucleus. The calibration has been performed sector by sector with ^{88}Y , ^{203}Hg , ^{207}Bi and ^{137}Cs sources, with energies at 898, 1836, 279, 569, 1063, 1770 and 662 keV. See later section 5.1.1 for calibration.

Gammasphere module: hit

For calorimetric measurements, the number of hits is either one or zero for one module. We consider that a module has a hit if any of its BGO sectors or its Ge triggers are within the appropriate time gate. Two γ -rays interacting in the same module will therefore register as one hit only. For the energy deposited in the module, the Ge and BGO energies are read and multiple gamma hits will naturally lead to the measure of the sum energy. For the purpose of calorimetric measurement, it has been shown it is not useful to separate Ge crystal, BGO shield and BGO sectors to increase the number of *modules* [85].

Selection of hits in time and energy

The γ -rays hits, whether in the Ge detectors or in the BGO, are selected according to the time of the event, relative to the implantation of the recoil, in order to select precisely the γ rays associated with a recoil and not any γ from background or another reaction (see previously, section 4.2). It is also important to take the time *walk* of the time, coming from the charge collection dynamics or the leading-edge discriminator, into account. Figure 4.11 shows the selection of events. The γ time peak is larger than for a source measurement because of the energy dispersion in the target, implying a dispersion in ToF.

Building the k and H quantities

The number of hits detected – the fold, noted k – and the detected energy – noted H – are built *off-line* from the events selected as previously described. In one individual module i ,

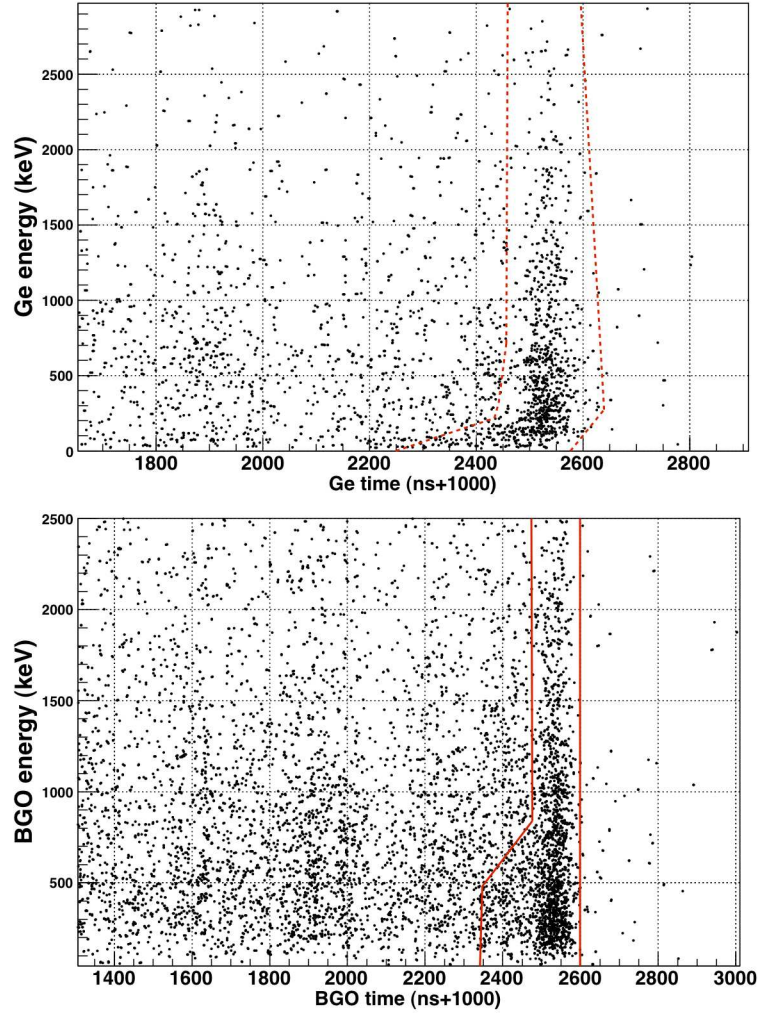


Figure 4.11: Selection of Ge (Top) and BGO (bottom) hits for the (k, H) distribution: the red lines are the *banana gates*. The low energy events are shifted to later times (smaller differences between global trigger and module trigger) due to the charge collection dynamics or the *leading-edge* discriminator of the detector. The comparison with source data in figure 4.12 shows that the gates are wide enough to account for the time walk.

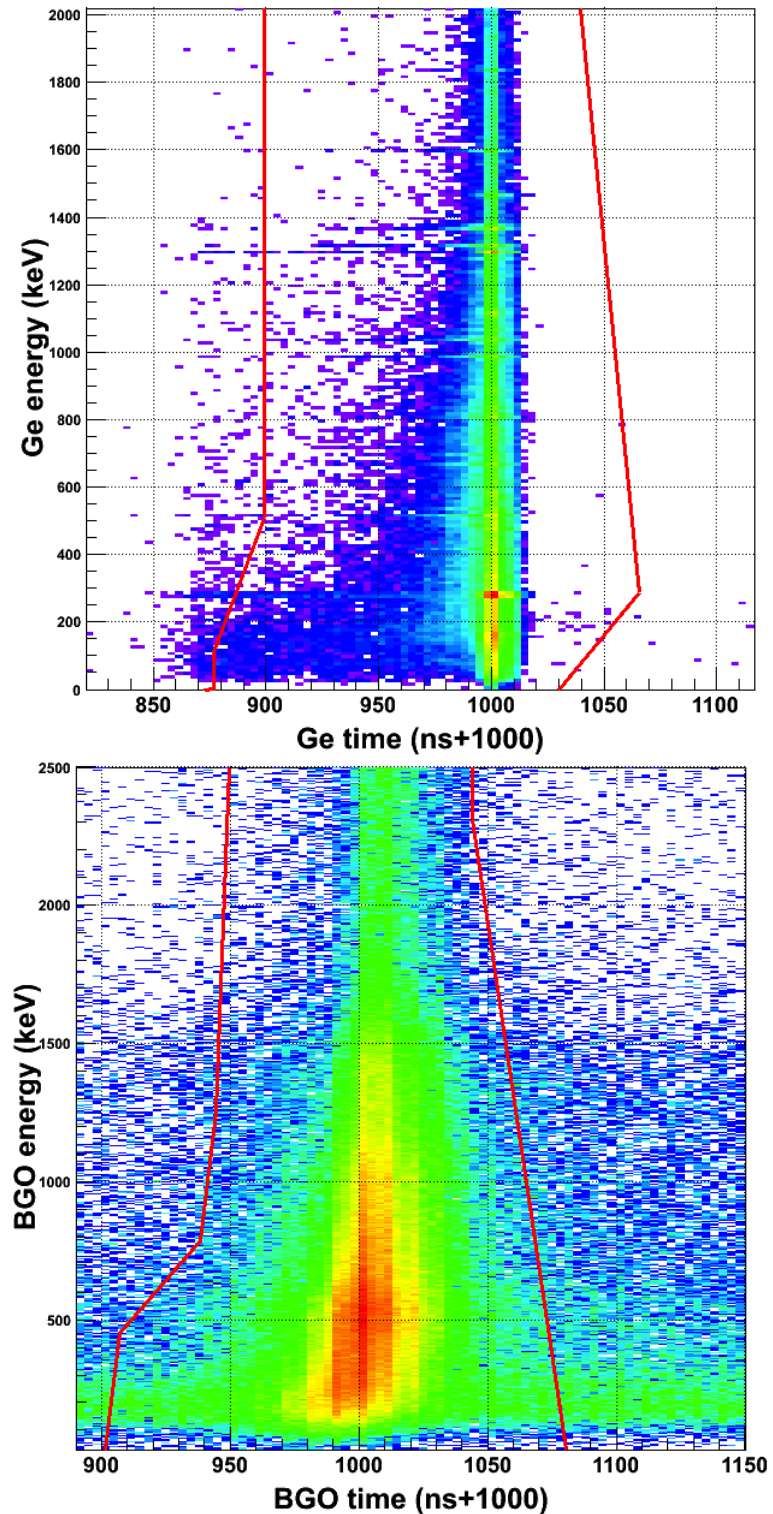


Figure 4.12: Selection of Ge (Top) and BGO (bottom) on a ^{203}Hg source: the red lines are the *banana* gates. The source emits a 279 keV γ ray that is perfect to check the time walk. The red lines are the graphic selections applied to the experimental data, shifted to the centre of the time peak.

the individual fold and energy, k^i and H^i , are built following three possible scenarios :

- **Ge time in Cut AND BGO time in Cut:** $H^i = E_{Ge}^i + E_{BGO}^i$, $k^i = 1$.
- **Ge time in Cut AND BGO time not in Cut:** $H^i = E_{Ge}^i$, $k^i = 1$.
- **Ge time not in Cut AND BGO time in Cut:** $H^i = E_{BGO}^i$, $k^i = 1$.

Afterwards, the global fold and sum energy are simply $k = \sum_i k^i$ and $H = \sum_i H^i$.

4.3.2 Partial loss of BGO and Ge signals

Electronic bus

The electronics has to hold the signal information (amplitude, time, ...) long enough to wait for the delayed trigger signal coming from the PPAC at the FMA focal plane. The FMA is 8.2 meters long, the recoil mass around 254 u and the average kinetic energy of the recoils is approximately 38 MeV; therefore it takes about $1.54\text{ }\mu\text{s}$ for recoils to fly from out of the target chamber to the PPAC. The electronics bus is designed to keep the BGO signal for $2\text{ }\mu\text{s}$ – but in reality, it is observed that some channels have a bus width as short as $1\text{ }\mu\text{s}$. For Ge & BGO modules with an *early* bus end (t_{end}), signals coming after t_{end} are lost. For those modules, both the Ge and BGO information are lost, except in a few cases where the Ge signal is still present. The loss of those information is linked to short cables between the Gammasphere modules and the acquisition, leading to an early arrival of the module signal and a bus signal not long enough to hold the electronics information until the arrival of the focal plane trigger signal.

The spectra on figure 4.13 explains the issue: some modules are completely missing the recoil gated time peak. One can compute the fraction of the recoil time peak being lost by a module. Let P_{recoil} be a normalised Gaussian distribution reproducing the recoil peak (see figure 4.14), the fraction of events seen by the BGO i is therefore $f_i = \int_0^{t_{\text{end}}^i} P(t)dt$ (where t_{end}^i is the bus end time for modules i) – this way, we compare the data loss with a reference time distribution for ^{254}No recoils tagged γ -rays.

One can calculate that 80 % of the modules keep more than 90 % of the signal, and the global fraction of events kept ($\frac{1}{N_{\text{modules}}} \sum_{i=1}^{N_{\text{modules}}} f_i$) is 80.5 %. This fraction of data lost is in agreement with the observed calorimetric efficiency of 63 %, compared to 78 % for similar measurement without the problem of module loss [89].

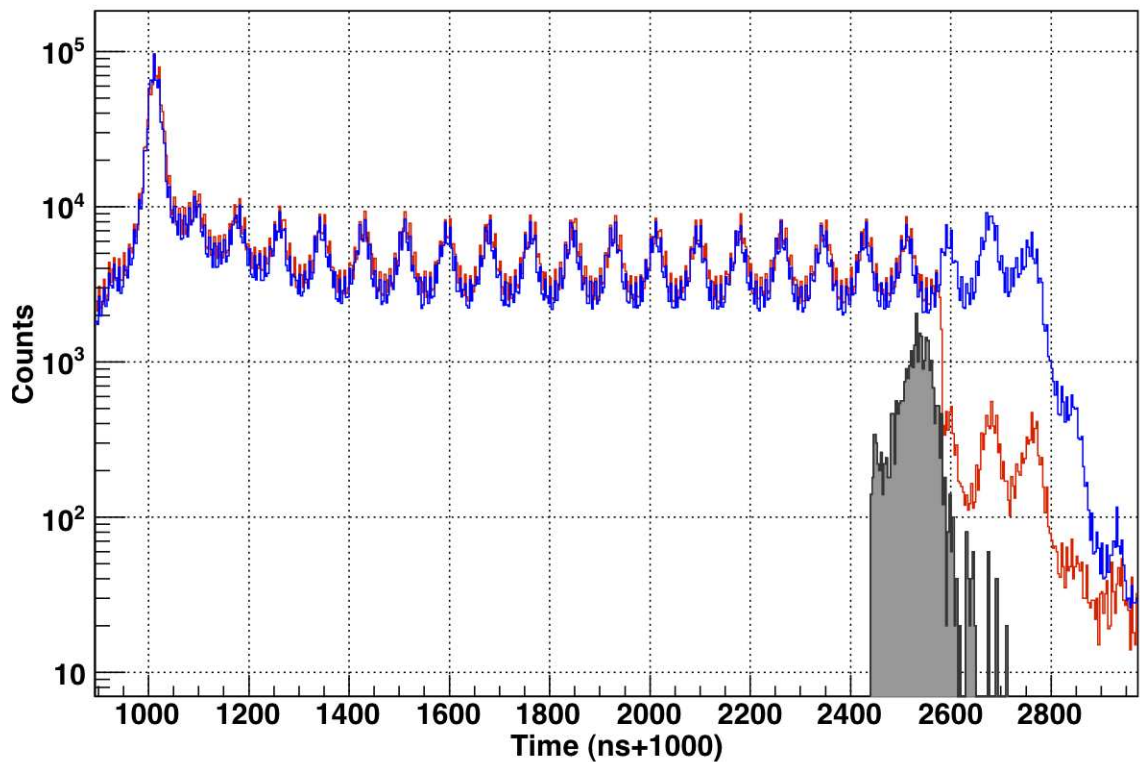


Figure 4.13: Visualisation of the early end of BGO bus. The **blue** spectrum of time event shows a normal bus with time signal being detected up to more than 1800 ns. The **red** spectrum shows a bus with an early end with a significant loss of data after 1580 ns. The **gray** area is the time peak of recoil gated events, corresponding to the gamma in the ²⁵⁴No reaction

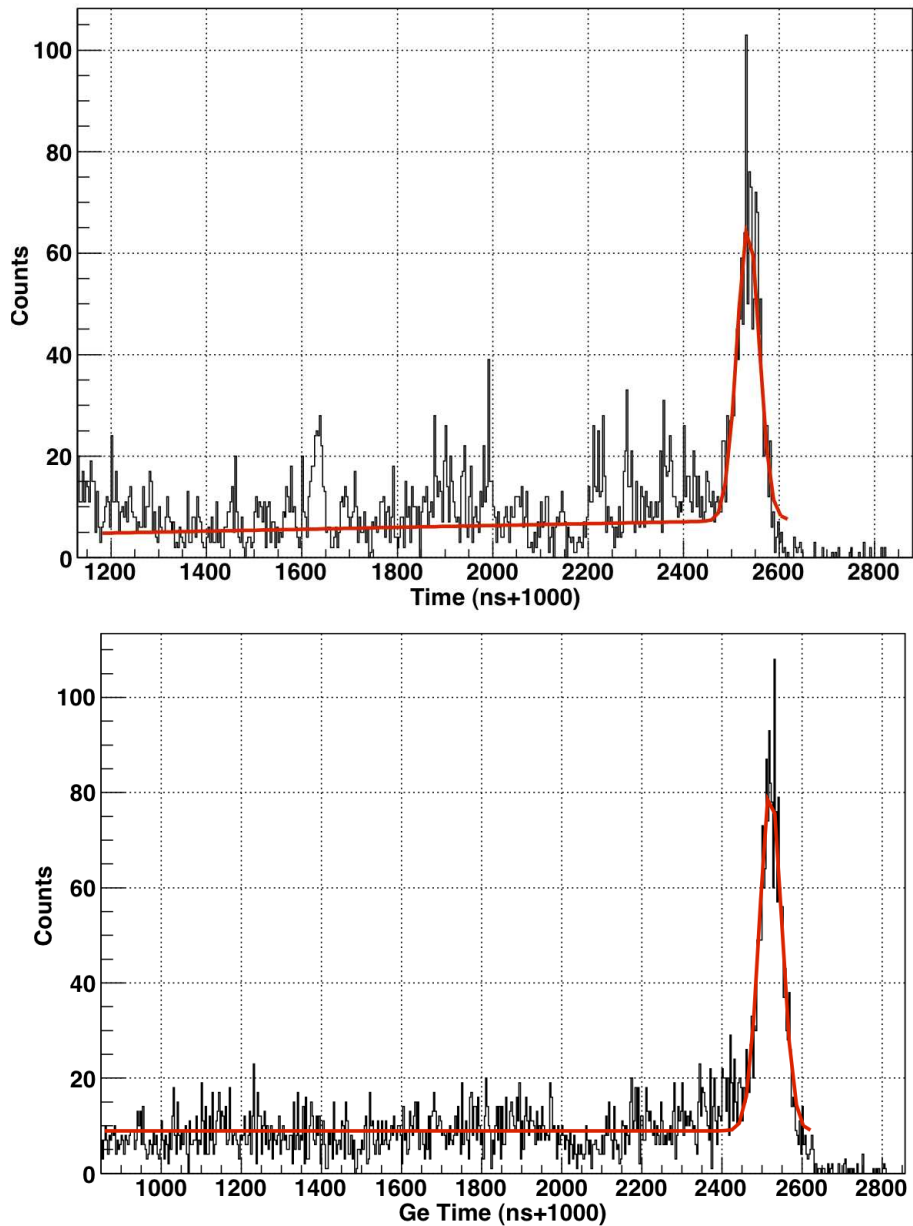


Figure 4.14: BGO (Top) and Ge (bottom) time spectra gated by recoils. One can see the recoil peak around $1.54 \mu s$ at the end. The red line is a fit of the distribution with a Gaussian and a linear background. The Gaussian parameters are used to calculate the fraction lost for modules with a short bus signal.

Problem for response calibration

The information loss in the modules implies that part of the experimental data for k and H will be lost, while they will be present in the calibration data since these data are taken from a source and without the issue of waiting $1.54 \mu s$ before a trigger. Indeed, the calibration data has a peak centred of $t = 0 ns$. We devised two ways to take into account this problem.

Use of self-triggering Gammasphere To reproduce the condition of the experiment as closely as possible in the response calibration, we took the source data with Gammasphere triggering on an external signal, this signal was a delay of the *OR* of the modules. With that, we could set the delay up to $1.54 \mu s$ like it is in the experimental data and observed the same loss of data in module buses. However, this method could not be used entirely due to the poor statistics of the source data taken with a delay self-trigger, as we were not aware of the magnitude of the problem at the time.

Correction of source data To account for the partial loss of experimental data, we have to remove the equivalent amount of data from the calibration data used to build the Gammasphere response. As each detector sees a fraction of the signals in the experiment, we have to remove the appropriate quantity of data from the source.

In the collection of fold and energy data from the source, we will randomly suppress each detector according to the fraction f_i defined earlier: a signal in the module i will be masked (i.e. not read) with a probability $1 - f_i$. This decision is taken using a random number generator, which provide a random *float* r between 0 and 1. If $r \leq f_i$ the event is kept, if $r > f_i$ the event is suppressed.

Chapter 5

Data analysis

5.1 Calibration of detectors

5.1.1 Gammasphere

Calibration of Ge detectors

Energy The energy reading from the Ge detectors of Gammasphere is processed by ADCs and calibrated using ^{88}Y , ^{207}Bi , ^{60}Co , ^{152}Eu , ^{137}Cs , ^{203}Hg and ^{56}Co source; example of background subtracted spectra are shown on figure 5.1. Each Ge crystal is calibrated by a linear function. This leads to a 2.6 keV resolution at 1.3 MeV. The average threshold in the Ge detector is 40 ± 10 keV.

The background spectra are collected in between source runs. The background lines come from activation of the chamber and beam line during irradiation and also fission-product activities. Some of the activities have quite short lifetimes and the corresponding background lines are not properly subtracted out. However, this will have little effect on our construction of the calorimetric response (see section 5.8) as coincidences between γ rays are used.

Efficiency The detection efficiency of the Germaniums is measured with ^{152}Eu , ^{60}Co , ^{207}Bi and ^{88}Y sources.

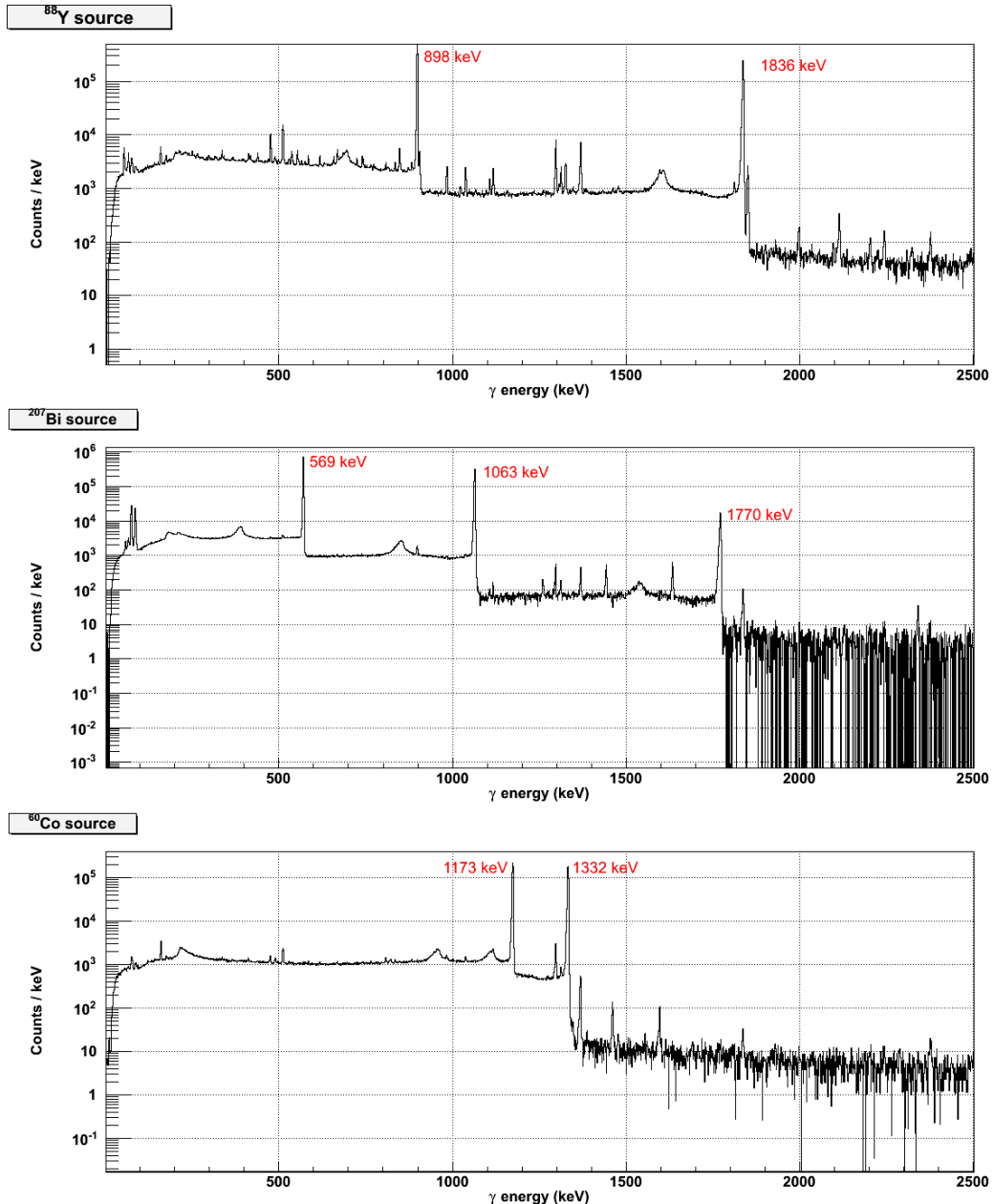


Figure 5.1: Background subtracted spectra of the sources used for energy calibration of Gammasphere. ^{88}Y (top), ^{207}Bi (middle) and ^{60}Co (bottom). The energy of the main peaks are noted in red.

Relative efficiency The relative efficiency profile is obtained by combining the γ peaks areas information from sources, using the RADWARE *gf3* and *effit* utilities [90]. The profile shows a maximum efficiency around 270 keV and falling to half its maximum above 1 MeV.

Absolute efficiency The absolute detection efficiency has been obtained at different energies using sources with coincident γ -rays, like for the Gammasphere response calibration. In a source where two γ -rays γ_1 and γ_2 are emitted in coincidence, the number of coincidence detected is given by $N_{\gamma_1 \& \gamma_2} = A\lambda(\theta)\varepsilon_1\varepsilon_2$ with A the source activity, $\lambda(\theta)$ the angular correlation function characterising the geometry of the γ emission. $\lambda(\theta)$ depends on the angle between the two γ -rays (averaging to 1 over all the Gammasphere detectors combinations). ε_i , the detection efficiency at the energy E_{γ_i} , verifies $N_{\gamma_i} = A\varepsilon_i$, with N_{γ_i} the number of full-energy E_{γ_i} detected. Therefore, the ratio $N_{\gamma_1 \& \gamma_2}/N_{\gamma_1} = \varepsilon_2$ – after correction for angular correlation and possible non-100% correlation between *gamma*-rays (for example, converted transition in the ^{207}Bi). Table 5.1 give the values obtained with this method. This method works best for two γ -rays of close energies.

Source	Energy E_2 (keV)	Coincidence $N_{\gamma_1 \& \gamma_2}$	Number γ_1 N_{γ_1}	Efficiency ε_2 (%)
^{152}Eu	121	3256 ± 57	19151 ± 44	17.0 ± 0.3
^{152}Eu	344.8	27800 ± 260	142050 ± 380	19.7 ± 0.2
^{207}Bi	570.1	142050 ± 1625	918800 ± 960	15.4 ± 0.2
^{88}Y	898.4	101940 ± 1190	903710 ± 950	11.3 ± 0.15
^{60}Co	1332.8	57415 ± 1085	602555 ± 365	9.5 ± 0.2
^{88}Y	1836.4	122280 ± 1155	1436900 ± 1200	8.5 ± 0.1

Table 5.1: Absolute efficiency extracted from coincident γ s data.

One can also get an absolute efficiency values by examining the *sum* peak for sources emitting 2 coincident γ -rays, when they are detected in the same detector. The probability of detecting both γ_1 and γ_2 in the same detector is given by $\lambda_0\varepsilon_1\varepsilon_2$ where $\lambda_0 = \lambda(\theta = 0)$. The ratio of sum peak intensity and single γ intensity, corrected for λ_0 is therefore a simple way to measure the efficiency [91]. In ^{60}Co , the λ_0 coefficient is 1.074 [92].

Figure 5.2 shows the absolute efficiency profile with the experimental data points.

Energy in the BGOs

For our calorimetric measurement, we need to get the BGO sectors calibrated in energy.

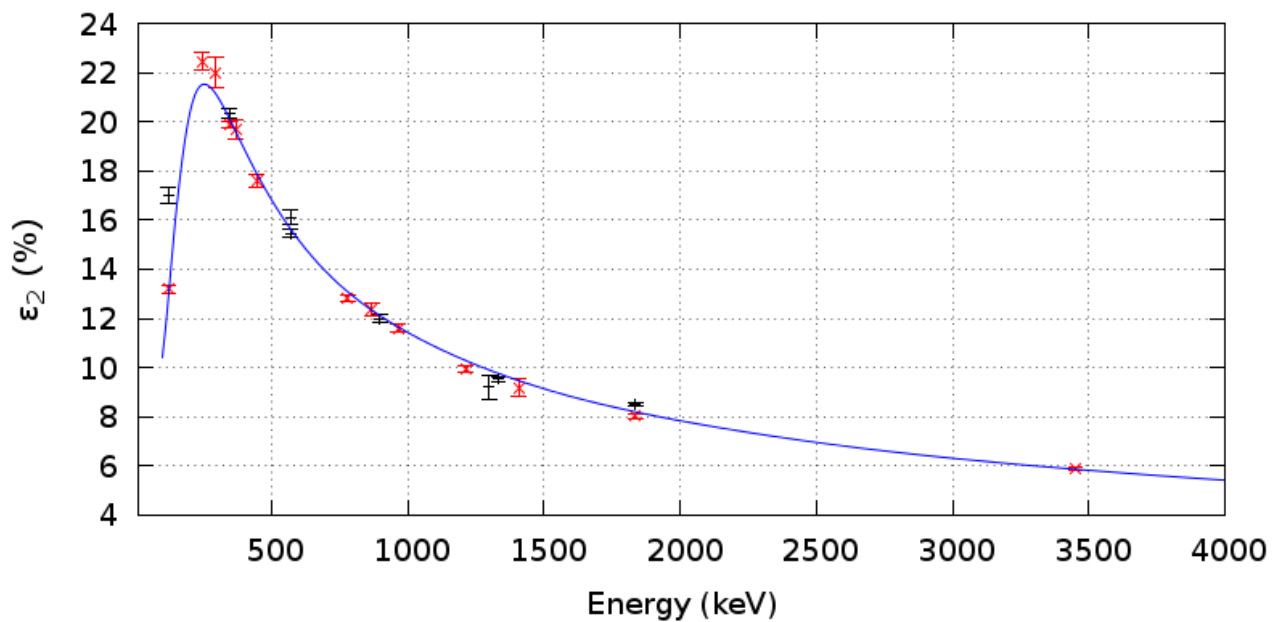


Figure 5.2: Absolute efficiency profile for Gammasphere. The black points are the absolute efficiency measurement from correlated γ rays. The red points are the points used for relative efficiency calibration, scaled down to match the absolute efficiency measurement. The blue line is the relative efficiency profile scaled down to the absolute values.

The energy read in each sector is not directly available from Gammasphere. Only the sum of all sectors is given, and the hit pattern indicates which sectors fired. By selecting specific hit patterns, sectors were calibrated one by one with the same sources as Ge crystals, see figure 5.3 and 5.4.

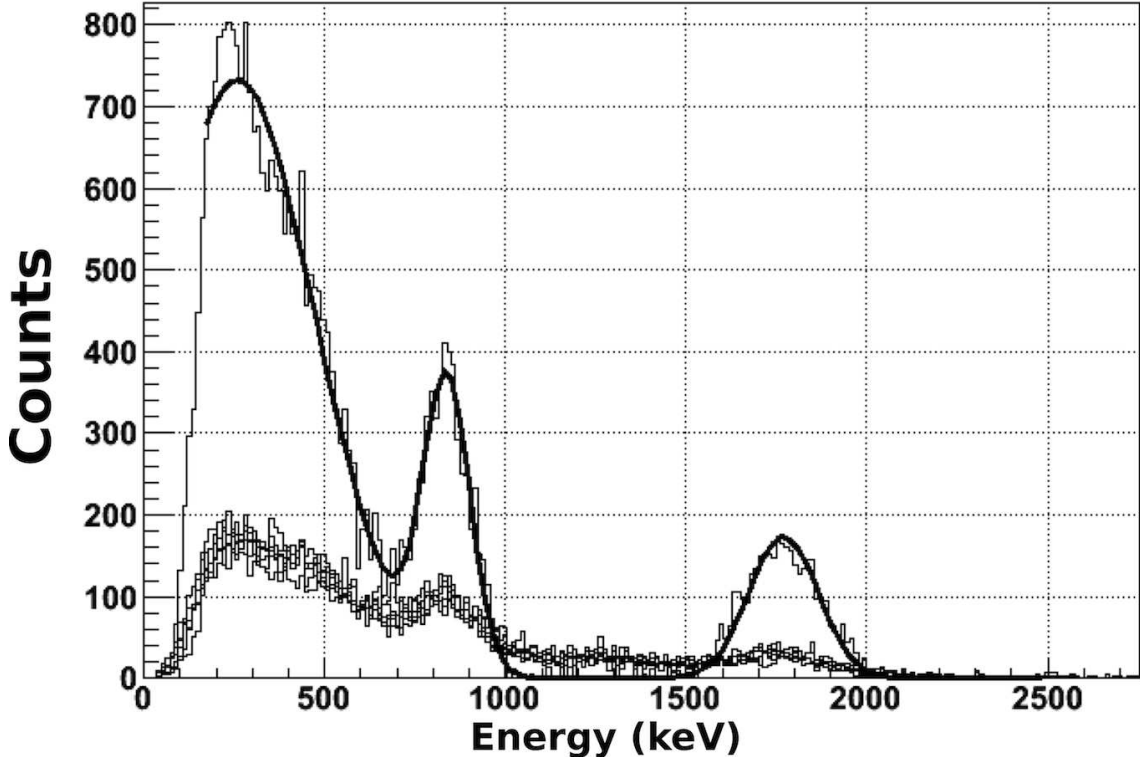


Figure 5.3: Fit of the BGO energy, on a ^{88}Y source. The seven sectors spectra are aligned and overlaid at the bottom. The module energy is fitted.

In cases where more than one BGO sector fires, we divide the sum signal equally between each sector and used the calibration on each sector. The final energy resolution of the BGO is around 120 keV at 570 keV and 200 keV at 1.3 MeV. The relative resolution is about 20 % FWHM. The average threshold in the BGOs is 120 ± 30 keV.

Time

To analyse the γ -rays, one has to select the hits corresponding to a specific beam burst. Each Ge and BGO channel has its own TAC that gives t_{Ge} and t_{BGO} – see section 4.1.6 for description. The TAC channels have to be aligned and calibrated. The time alignment is performed using Gammasphere self-triggering on the delayed *OR* of all modules. With that, it is easy to get a set of values of times between γ detection and trigger. Using

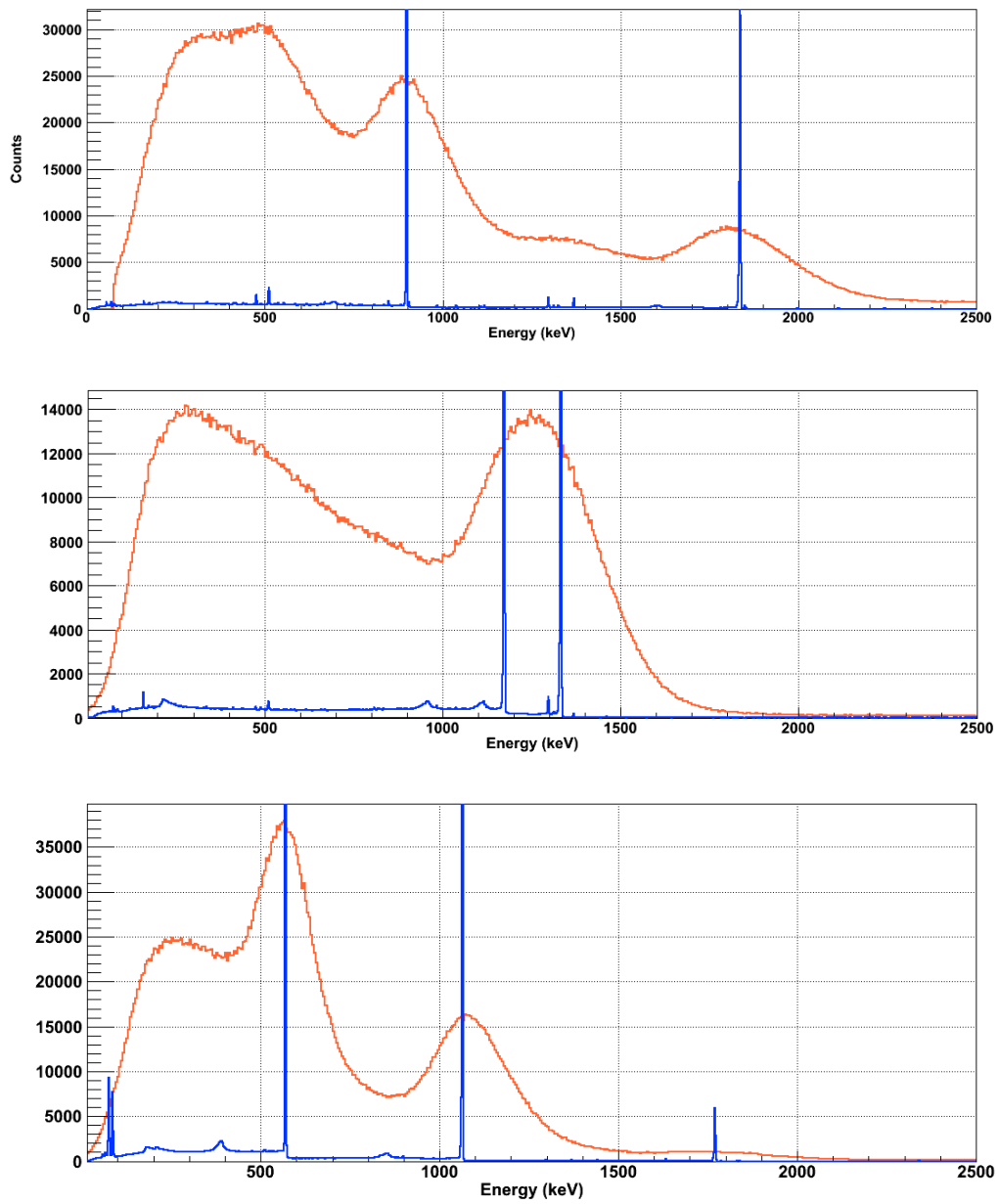


Figure 5.4: From top to bottom: ^{88}Y , ^{60}Co and ^{207}Bi sources. Overlay of calibrated BGO (orange line) and Germanium (blue line) energy spectra.

different values of delay, the linearity of the time signal in the modules is calibrated. To account for the width of the peak, we choose to offset the time $t = 0$ by 1000 ns. Figure 5.5 shows the alignment of Ge time signals. The similar process has been made for BGOs.

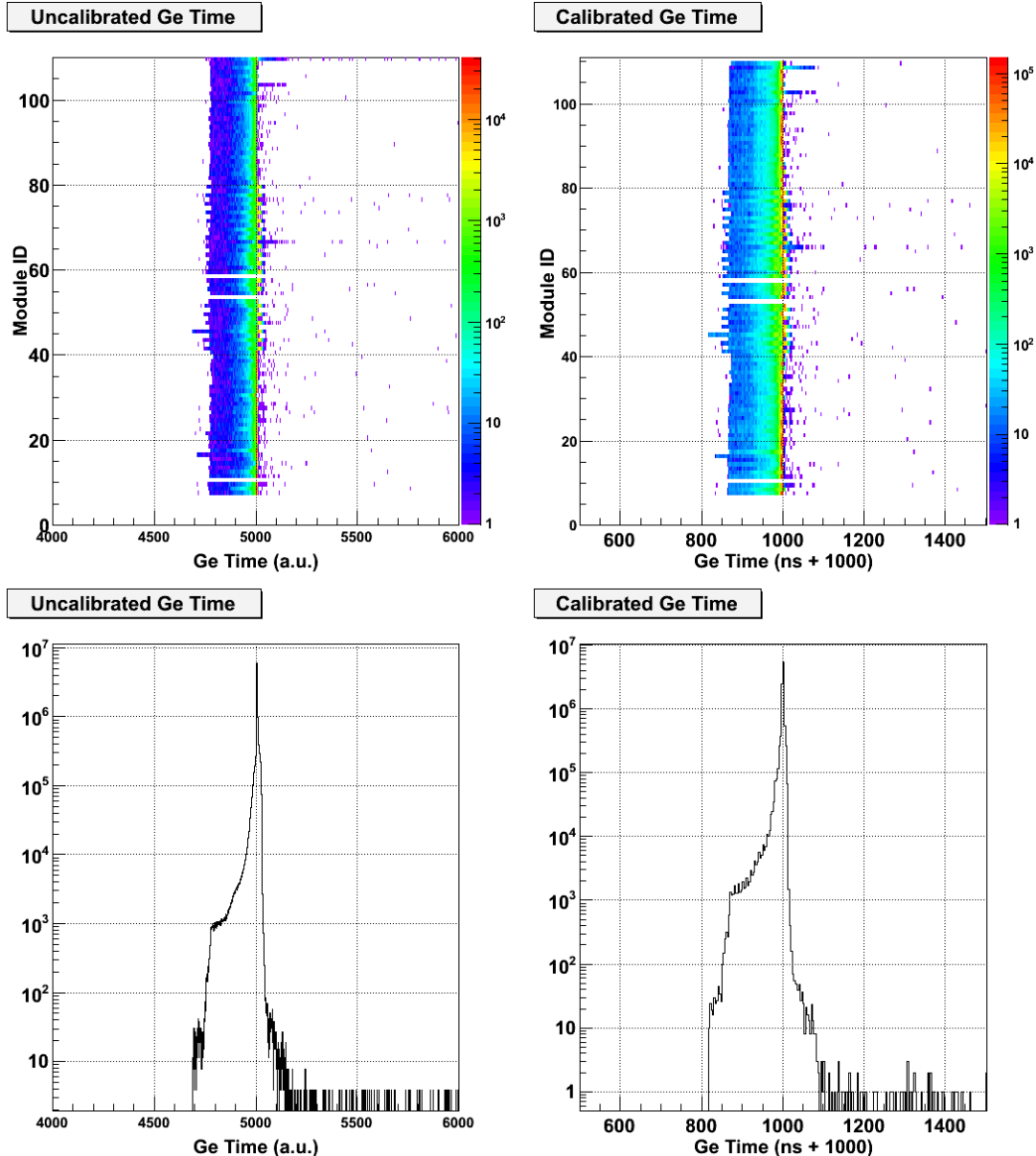


Figure 5.5: Time distribution of events for a ^{88}Y source. The uncalibrated time is on the left, the aligned time on the right. (Top) distribution of events for each Ge detector. (Bottom) projection of the total time distribution. The data compression (bin width) differs between calibrated and uncalibrated spectrum.

5.1.2 DSSD calibration

Decay channels

The DSSD decay channels have been calibrated using an external α -source and the α -decays of reaction products implanted in the silicon during the experiment – in particular during the test reaction, see section 5.3.

The channel alignment is done with a classical 3- α source, whose energies are well tabulated – see table 5.2. Because the α from the source have to go through the detector dead-layer, the energy loss in it is taken into account. The source is located about 20 cm in front of the DSSD, therefore the effective dead-layer is at most 2 % thicker for the pixels on the edge of the silicon; no correction for the pixel location is made since the difference in energy is significantly smaller than the resolution.

Radio nuclide	α Energy (MeV)	α energy after the DSSD dead-layer
^{240}Pu	5.105	5.00
	5.156	5.05
^{241}Am	5.485	5.39
^{244}Cm	5.763	5.66
	5.805	5.70

Table 5.2: α energies in the PuAmCm 3- α source. We give the energies of the α and the energy deposited in the active volume of the DSSD after an energy loss in the dead-layer.

After aligning the channels, the experimental decay of implanted nuclei is used to set the energy scale. The final energy resolution is about 35 keV FWHM. Figure 5.6 shows the calibration of the front and back side of the DSSD with the α source.

The DSSD events are triggered by an overlap between the front and back strip within a 250 ns time window. Even if the two sides of the DSSD are calibrated, we will use the measurement from the front side which is more precise because the recoil nuclei are implanted in the *front* side (The average implantation depth is below 5 μm). Hence, the decays happen mainly close to the front strip and the charge carriers have to drift to the back side through a larger thickness of matter and are spread between strips at the back. Figure 5.7 shows the calibrated front and back energy for the experimental decay of ^{254}No . The better charge collection on the front side is clearly illustrated by the tails on the left side of the diagonal.

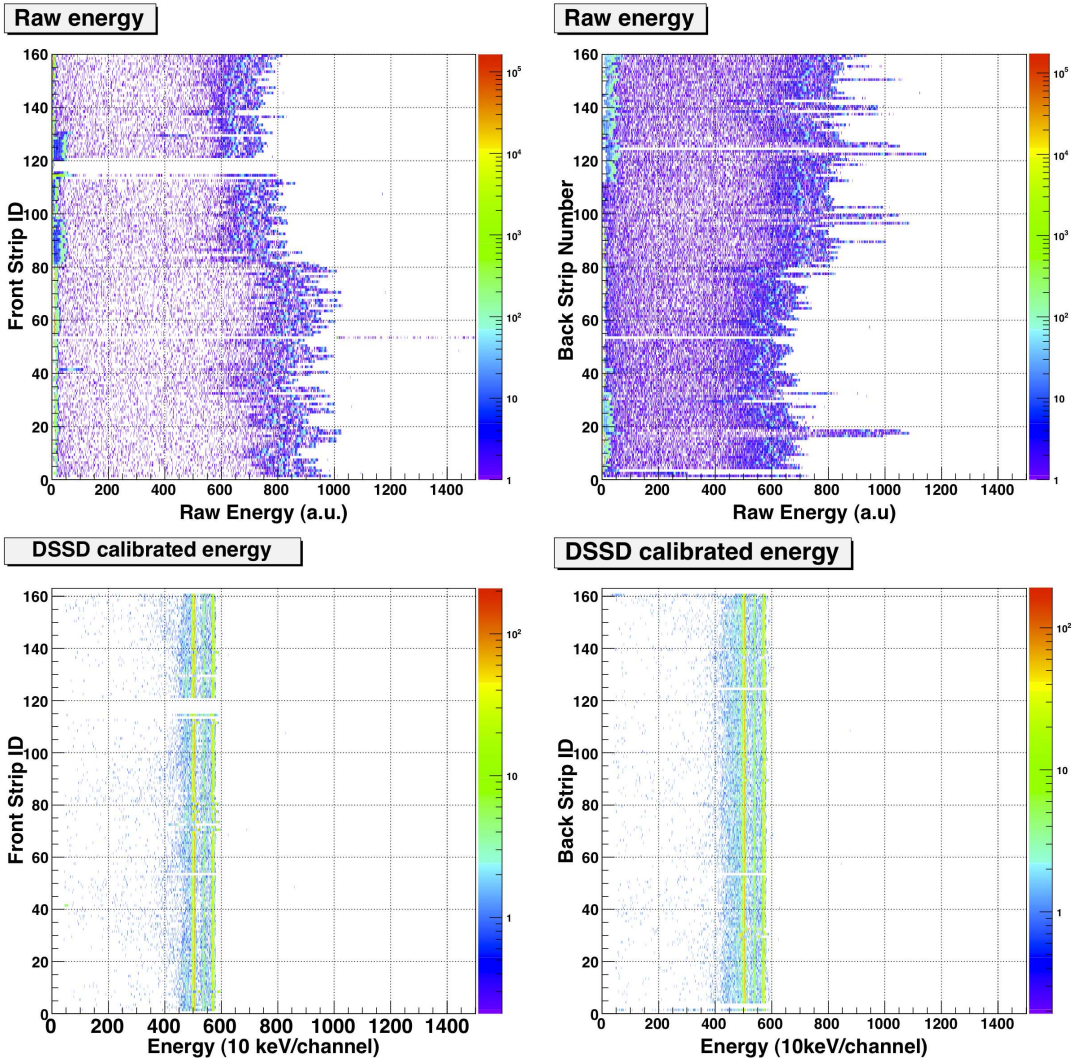


Figure 5.6: DSSD channels front (right) and back (left), before (top) and after (bottom) channel alignment with $3-\alpha$ source. The uncalibrated spectra show important number of counts at low energy, implying the need of significant thresholds: the average energy threshold is 160 ± 15 keV.

Recoil channels

As for the decay, the recoil energies have been calibrated too. The implantation energy in the DSSD is around 30 MeV, but the dynamic of charge creation in the silicon reduces the measured energy: around the implanting ion, a plasma is created and the holes-electron pairs recombine before being collected. This effect called Pulse Height Deficit reduced the measured energy by about 50 % [93].

For the recoil calibration, the gains has been aligned with a pulser and the $3\text{-}\alpha$ source has been used to set roughly the energy scale.

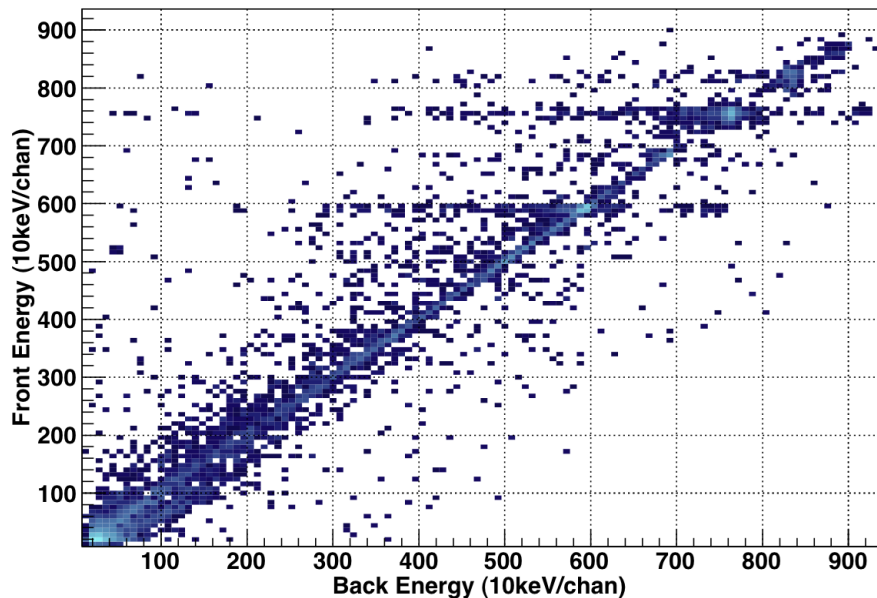


Figure 5.7: Plot of the front vs. back energy in the DSSD for experimental ^{254}No α decays with no conditions on the signals. The front side sees more energy than the back side.

5.2 Recoil selection at the focal plane

The FMA transports to the focal plane all recoils of a given m/Q . The recoil velocity can also be used for extra selection via the time of flight. At the target position, ^{254}No is produced and enters the FMA. We set up the FMA to transmit the charge state 20.5^+ at the centre of the focal plane, charge states $Q = 20^+$ and $Q = 21^+$ will be collected. Along with ^{254}No , all particle with m/Q around the set up value ($\frac{254}{20.5} \approx 12.4$) will be transmitted, although with a different mass, kinetic energy, time of flight, ... Therefore, separation is possible using the following measurements :

- X dispersion in the horizontal direction at the focal plane, corresponding to the m/Q ratio, measured by the PPAC.
- Time of Flight (ToF), between the PPAC and the focal plane DSSD.
- Energy Loss in the PPAC (ΔE_{PPAC}).
- Implantation Energy in the DSSD (E_{implant}).

5.2.1 Contaminants

Given the low production cross section of ^{254}No , the nucleus of interest is a small fraction of all the recoils getting to the focal plane. It is therefore very important to sort through all the events at the focal plane. Three types of elements gets to the focal plane:

- The nuclei of interest: ^{254}No .
- Target like products: scattered target and transfer products (Pb, Po, Bi, ...).
- Scattered beam and beam like products from transfer reactions.

Beam like products

The scattered beam and beam like products undergo multiple scattering in the target and on the walls of the FMA. Therefore their charge state and energy are not well defined. However, we know they are light (A around 48) and very energetic, therefore fast. The scattered beam will be characterised by a high and broad recoil energy, a low ToF and a low energy loss in the PPAC (because of the Bethe-Bloch formula : $\Delta E_{\text{PPAC}} \propto \frac{AZ^2}{E_{\text{implant}}}$).

Furthermore, the scattered beam will be the dominant contaminant, by many orders of magnitude.

Target like products

In the target, the ^{208}Pb atoms may undergo elastic scattering giving them a kinetic energy of about 40 MeV. Also, inelastic reactions between the beam and target may lead to transfer products with $A \approx 208$ scattering to the focal plane. The heavy mass of the target element will lead to a ToF lower but of the same order of magnitude than the ToF of the recoils of interest; the energy loss in the PPAC will be less than for ^{254}No .

5.2.2 ^{254}No recoils

The kinetic energy of the ^{254}No recoils is around 38.7 MeV for $E_{\text{beam}} = 223$ MeV (38 for $E_{\text{beam}} = 219$ MeV). The recoils are heavy (the heaviest of everything that gets to the end of the FMA) and with a large Z (102, charge state around 20^+). The time of flight of ^{254}No recoils will be about the same as forward scattered target atoms (since $v = \sqrt{\frac{2 \cdot K}{M}}$ – with K the kinematic energy of the recoil and M its mass, the ratio of scattered target speed over recoil speed is $\approx \sqrt{\frac{K_{\text{Pb}}}{208} \frac{254}{K_{\text{No}}}} \approx 1.13$). However, the energy loss in the PPAC will be larger for the Nobelium recoils due to the higher Z.

5.2.3 Cuts and Selections

The selection is made by combining several cuts on the quantities. To be more selective without cutting the events of interest, the 2D plots and *banana gates* are preferred. To visualise where to put the gates, it is helpful to plot decay tagged events (see section 4.2).

Primary selection: data completion

The first selection on all the events is to make sure all the needed quantities are available. Due to thresholds in the detectors and electronics, some events are *incomplete*: quantities such as X or E_{implant} are 0. A proper selection is impossible for these events. Table 5.3 gives the selection budget with the count of valid events. A large fraction of events have ΔE_{PPAC} information missing, therefore, this quantity has been removed from the completion selection, and these events were kept.

Condition	Number of recoils	%
No Selection	100116	100
Invalid ToF	4482	4.5
Invalid Implant Energy	2288	2.3
Invalid X,Y	0	0
Any Invalid parameter	30261	8.2
Valid Events	91106	91
In E_{implant} -ToF	3105	3.4
In $X-\Delta E_{\text{PPAC}}$	3644	4
In E_{implant} -ToF and $X-\Delta E_{\text{PPAC}}$	915	0.91

Table 5.3: Selection budget for the data set at $E_{\text{Beam}} = 219$ MeV. The number of event of interest is just a fraction of the total.

Time of flight and implant energy

The time of flight and energy of the implanting recoil are two very selective parameters, since they are tied in the kinematic relations by the mass of the recoil: $\text{ToF} = L \sqrt{\frac{m}{2E_{\text{implant}}}}$, with L the distance of flight.

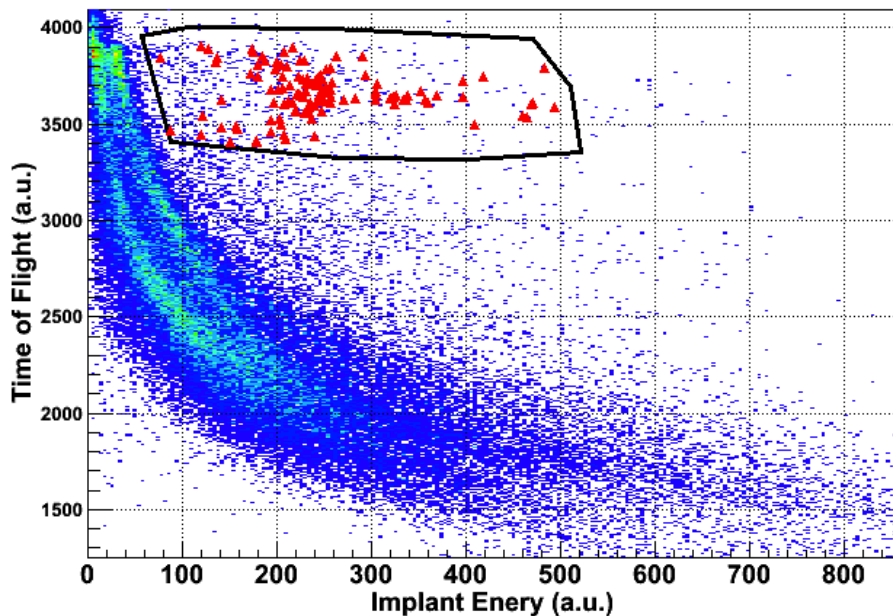


Figure 5.8: Selection of recoils on the Energy, Time of Flight map. The black line is the graphic cut applied to select recoils. The red points are the α -decay gated events.

The distribution of events on a (ToF, E_{implant}) plot gives a large group of events with a broad recoil energy distribution and a long time of flight. We associate this with the scattered beam and light transfer products. Above the scattered beam, events with higher ToF are associated with heavier recoils (longer flight for the same energy). Figure 5.8 shows the selection of events on the Energy, Time of Flight map.

Energy loss in the PPAC and X position

The energy loss in the PPAC and the X position at the FMA focal plane provide additional selectivity according to charge state and mass. The FMA is set on a precise value of m/Q . The distribution of ($X, \Delta E_{\text{PPAC}}$) shows the recoil of interest with peaks in the X direction and ΔE_{PPAC} somewhat larger than the beam and target-like recoils. Combining the PPAC energy loss with the ToF measurement (which is also related to the recoil energy and mass) gives a way of identifying the recoils – figure 5.8. The ^{254}No recoils are expected to have larger ΔE_{PPAC} than scattered beam and target. Figure 5.9 gives the selection of events on the $X, \Delta E_{\text{PPAC}}$ map and figure 5.10 gives the selection of events on the $X, \text{Time of Flight}$ map.

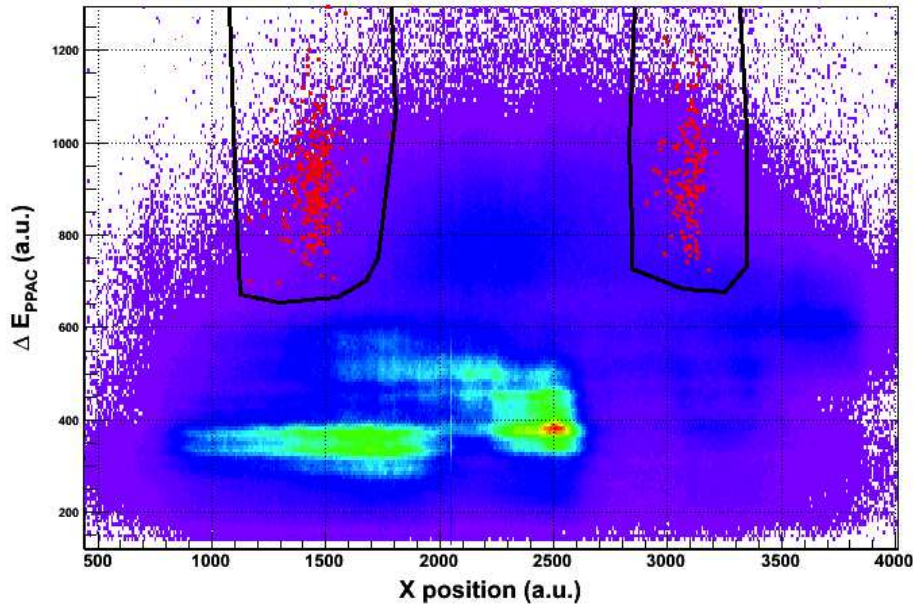


Figure 5.9: Selection of recoils on the X and Energy loss map. The black lines are the graphic cuts applied to select recoils. The red points are the α -decay tagged events.

Figure 5.11 shows the final X distribution of the selected events. It shows the two charge states peaks for $Q = 20^+$ and 21^+ . The peak at higher X is smaller because of a poorer

transmission of those charge states in the FMA and smaller population of the $Q = 21^+$ charge state.

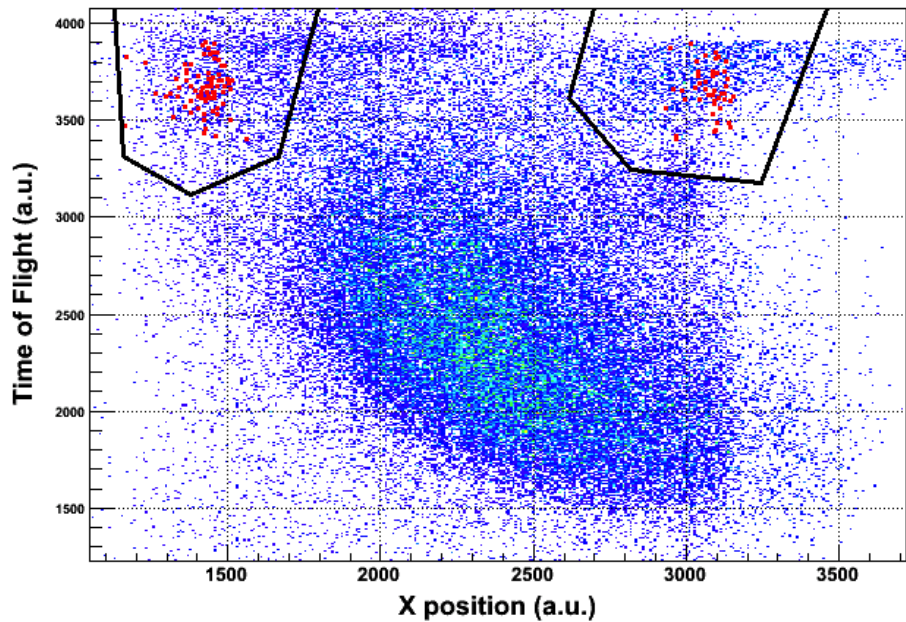


Figure 5.10: Selection of recoils on the X and Time of Flight map. The red points are the decay gated events. The black lines represent the selection.

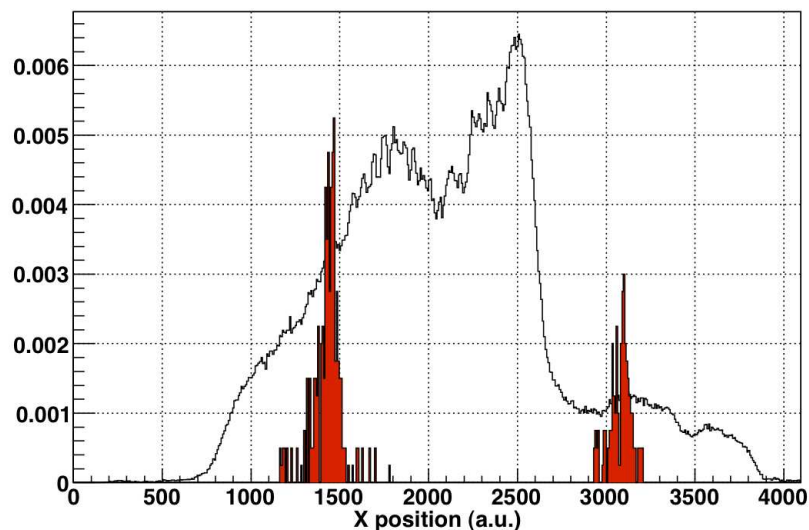


Figure 5.11: Selection of recoils in X. The black histogram is the distribution of X for all the PPAC events, normalised to 1. The red filled histogram is for decay tagged events, it is scaled up by a factor 10 (unscaled integral is 0.0097).

5.3 Test reaction: $^{176}\text{Yb} (^{48}\text{Ca}, 4 - 5n)^{220,219}\text{Th}$

We tested the setup using a reaction with a larger cross section. We chose to produce ^{220}Th because in addition to presents prompt γ -rays and α -decay its entry distribution has been measured previously with the same setup and presents a good comparison point to validate the calorimetric measurement – see appendix C.

5.3.1 Reaction and production cross section

The $^{48}\text{Ca} + ^{176}\text{Yb}$ reaction is not the preferred way to produce ^{220}Th but it has a large cross-section (compared with the production of ^{254}No) and has the advantages of using the same beam and same energy as for the $^{208}\text{Pb}(^{48}\text{Ca}, 2n)$ reaction. However, at this energy, both ^{220}Th and ^{219}Th are produced at the same time with cross sections of the order of 10 to 100 μbarns .

During a little less than one day ($\approx 17 \pm 2$ hours) of test run with a beam intensity averaging 30 pnA, we accumulated about 3950 $^{219,220}\text{Th}$ events, which, assuming a 7 % transmission efficiency through the FMA gives $20 \pm 10 \mu\text{barn}$ in agreement with the production cross section values.

5.3.2 γ and decay spectroscopy of ^{220}Th

The two isotopes ^{220}Th and ^{219}Th can be separated on the X distribution (see figure 5.12) and we can check the γ spectra associated with each. In particular, the ^{220}Th X-gated spectrum is in agreement with references [94]. See figure 5.13 for the spectrum.

The Thorium isotopes produced are implanted in the DSSD at the FMA focal plane and undergo α decay inside the DSSD. One can follow the decay and identify the decaying nuclei by the combination of decay energy and half life – see section 4.2 and figure 5.14. However, the short lifetimes of the species ($\approx 1 - 10 \mu\text{sec}$) make it difficult to observe all the decays. It is possible to identify clearly the decays of ^{215}Ra and ^{212}Rn by their α energies and half-lives, as shown on figure 5.15.

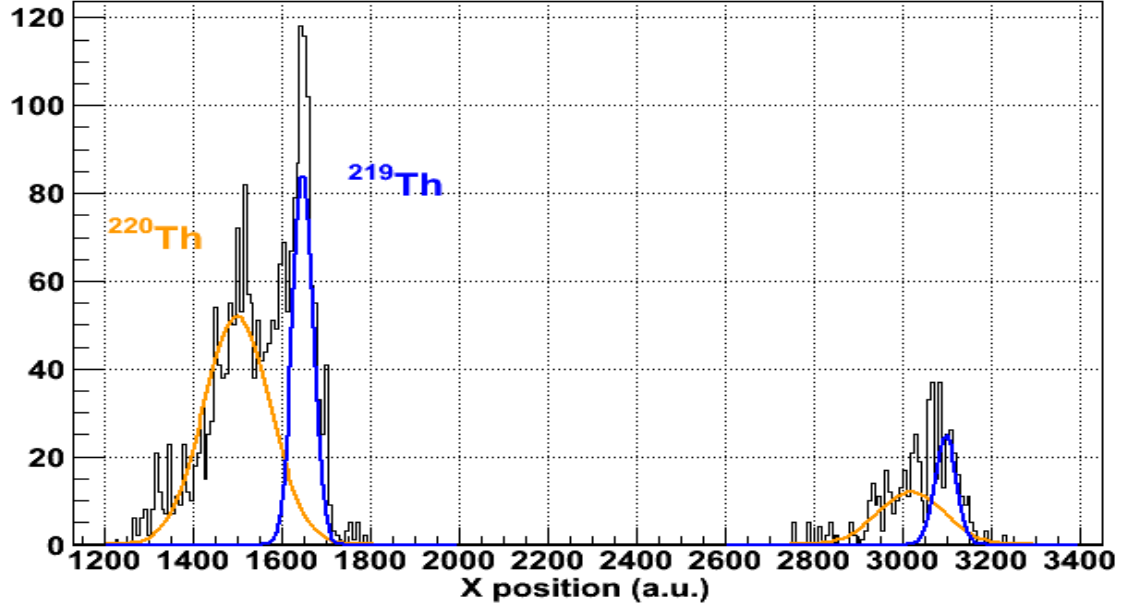


Figure 5.12: Distribution of X positions for $^{219,220}\text{Th}$ recoils. The two isotopes can be separated in mass, in particular at low Xs where there is more population. The line in blue show the distribution for ^{219}Th and the one in orange for ^{220}Th .

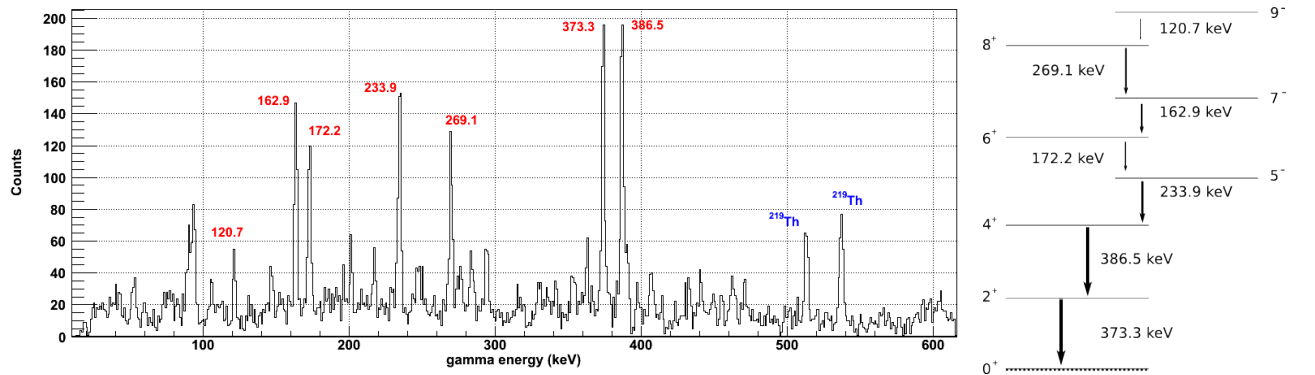


Figure 5.13: Prompt γ rays spectrum for ^{220}Th . The known transition energies are marked in red, following [94]. The corresponding level scheme is on the right. Two higher energy lines come from ^{219}Th , marked in blue.

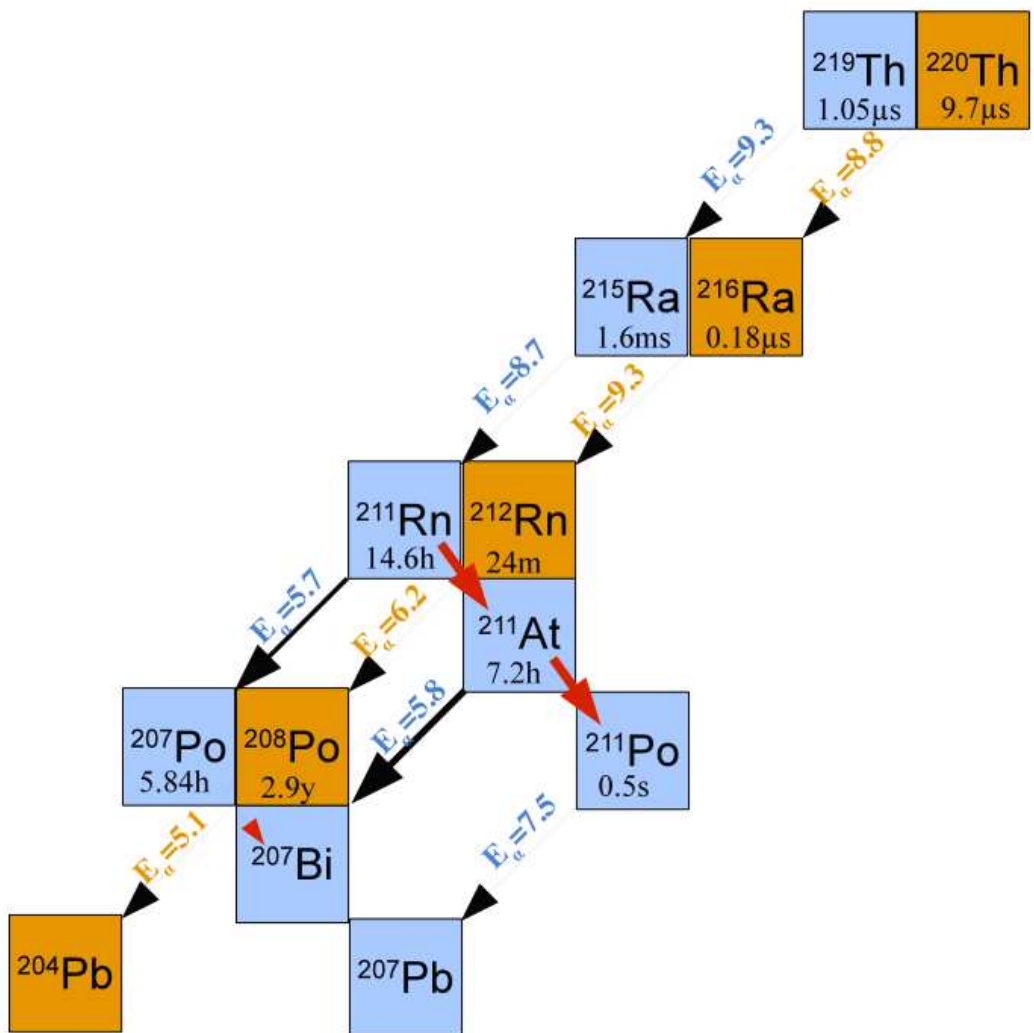


Figure 5.14: Decay path of ^{220}Th (orange) and ^{219}Th (blue). The half-life of nuclei are written in the squares. The red arrows represent electron capture decay. The black arrows stand for the α decay, with the tabulated α energy in MeV indicated over the arrow. For ^{211}Rn and ^{211}At , the size of the arrow indicates the branching ratio between the two decay modes.

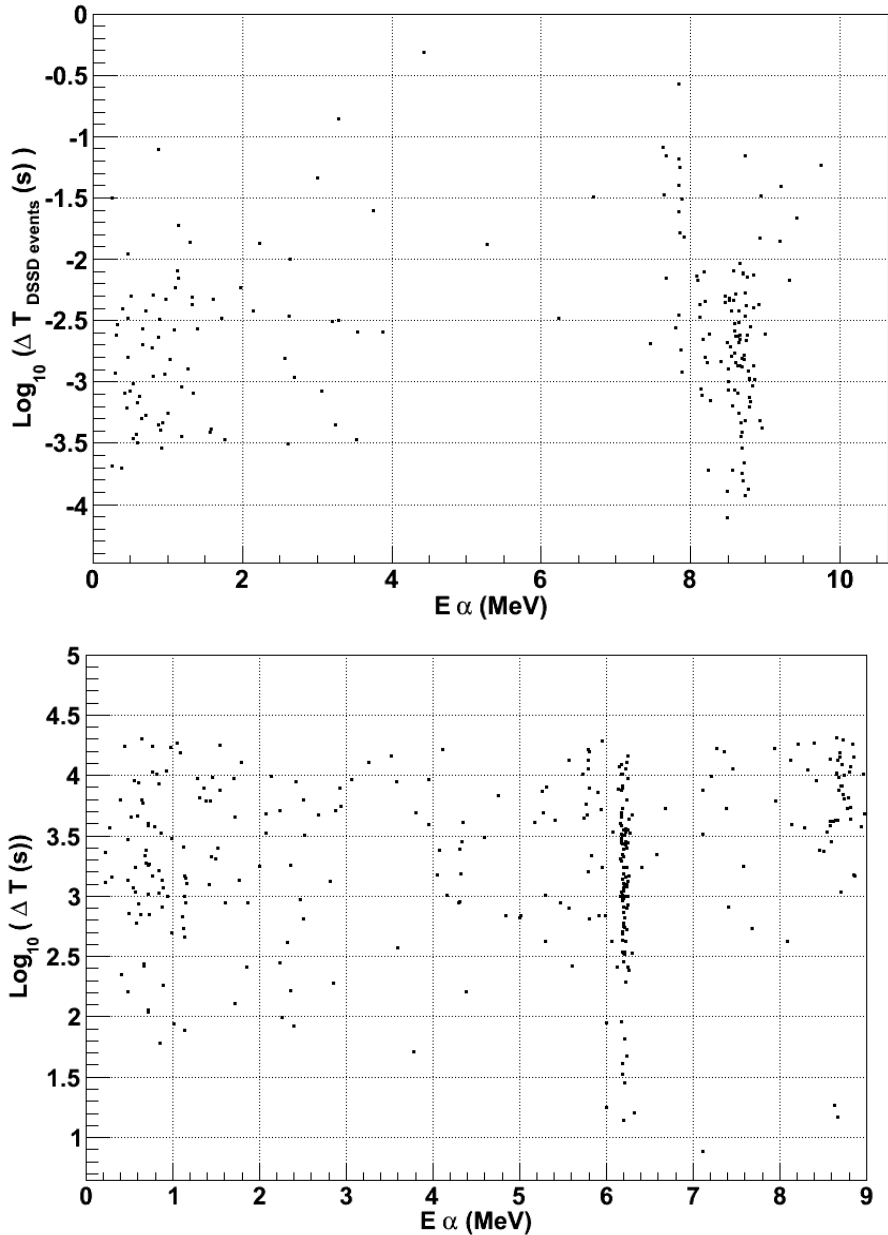


Figure 5.15: Energy and time of the decay of ^{215}Ra (top) and ^{212}Rn (bottom) inside the DSSD. The selection on the two decays have been done by correlation time condition. The α energy and lifetime correspond to the expected values of 8.7 MeV and 1.6 ms for ^{215}Ra , and 6.2 MeV, 24 minutes for the Rn isotope.

5.4 Cross section

The first quantity we check in the data collected for ^{254}No during the experiment is the production cross section at the two energies.

We collected respectively 915 ± 40 and 1475 ± 60 events for the experiment at 219 and 223 MeV (uncertainty comes from the data selection); assuming a transmission cross section from the target position to the FMA focal plane of 7%, with a beam exposure of 43 hours at $E_{\text{Beam}} = 219$ MeV and 118 hours at $E_{\text{Beam}} = 223$ MeV, with an average beam intensity of 10 pA, and a duty cycle of 73% (due to the target wheel spokes), plus a 60 % efficiency of recoil tagging at the focal plane – due to geometrical consideration, the focal plane chamber being not setup in the most ideal configuration during the experiment – we can estimate the production cross section of ^{254}No . Table 5.4 gives the results and compare them to references. See also figure 5.16.

Beam Energy (MeV)	Counts	Observed σ (μbarn)	Expected σ (μbarn)
219	915	2.1 ± 0.6	1.85
223	1475	1.2 ± 0.4	1.15

Table 5.4: Summary of observed ^{254}No production cross section compared to the references. Expected cross section are taken at the mid-target energy.

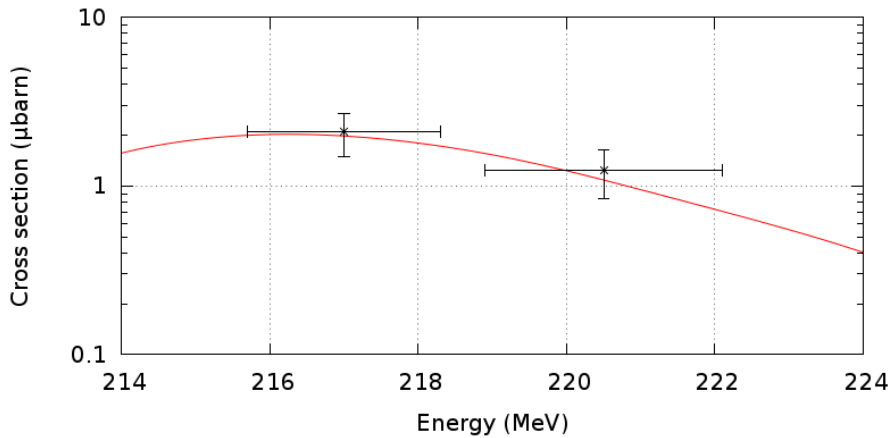


Figure 5.16: Plot of the ^{254}No production cross section — red line is the reference calculated by the NRV code [9]. Black points are our experimental value, with energy taken at mid-target.

5.5 Prompt γ spectroscopy

The prompt γ information collected during the experiment allows us to check the production of ^{254}No and also to directly observe the spin population via the yrast decays associated with known angular momentum [25, 26, 95–97]. Figure 5.17 shows the recoil-gated γ spectrum for all data. Figure 5.18 shows the spectra at both beam energies.

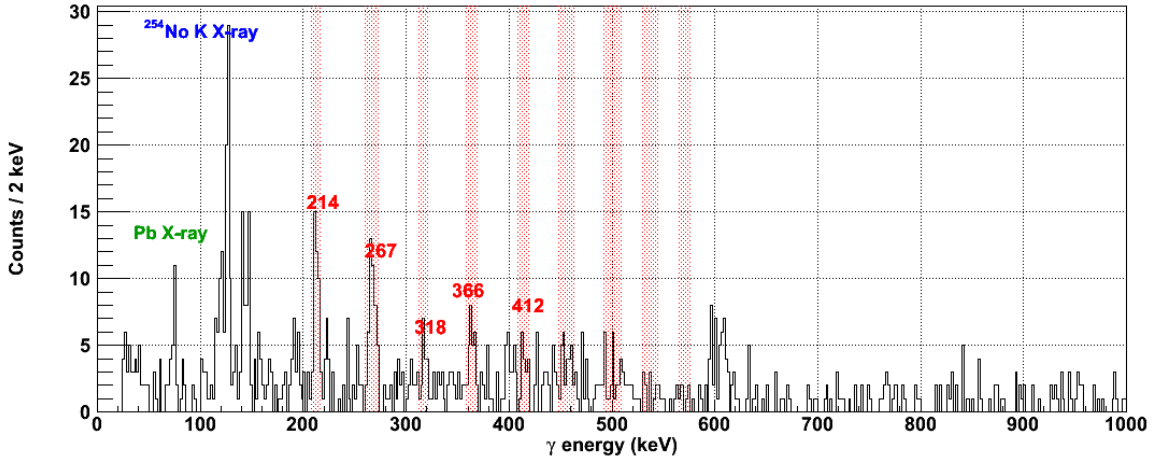


Figure 5.17: Recoil-gated γ ray energy spectrum for all data ($E_{\text{Beam}} = 219$ MeV and $E_{\text{Beam}} = 223$ MeV). The known *yrast* transitions γ energies are marked in red; ^{254}No X-rays are marked in blue. We observed the *yrast* transitions up to 14^+ . The ratio of ^{254}No X-rays to the peak at 600 keV in the spectrum is 4.3 ± 1.2 , consistent with the spectrum collected during the previous experiment where it was 5.3 ± 1 [98].

Decay-gated spectra In order to remove background and close in on the ^{254}No data, we can use additional conditions in the γ ray spectrum. In particular, recoil- α and recoil- α - α correlation. The additional condition removes background, but it also reduces the statistic by the efficiency of α or $\alpha - \alpha$ detection, for example. Figure 5.19 shows the γ spectra for recoil-gated, recoil- α gated and recoil- α - α gated events.

Spin population

Since we are interested in the spin distribution of formed ^{254}No , we can get a first estimate of the profile by looking at the yrast transitions and their intensities. Once corrected for efficiency and electron conversion, it is a good measure of how much of the nuclei were

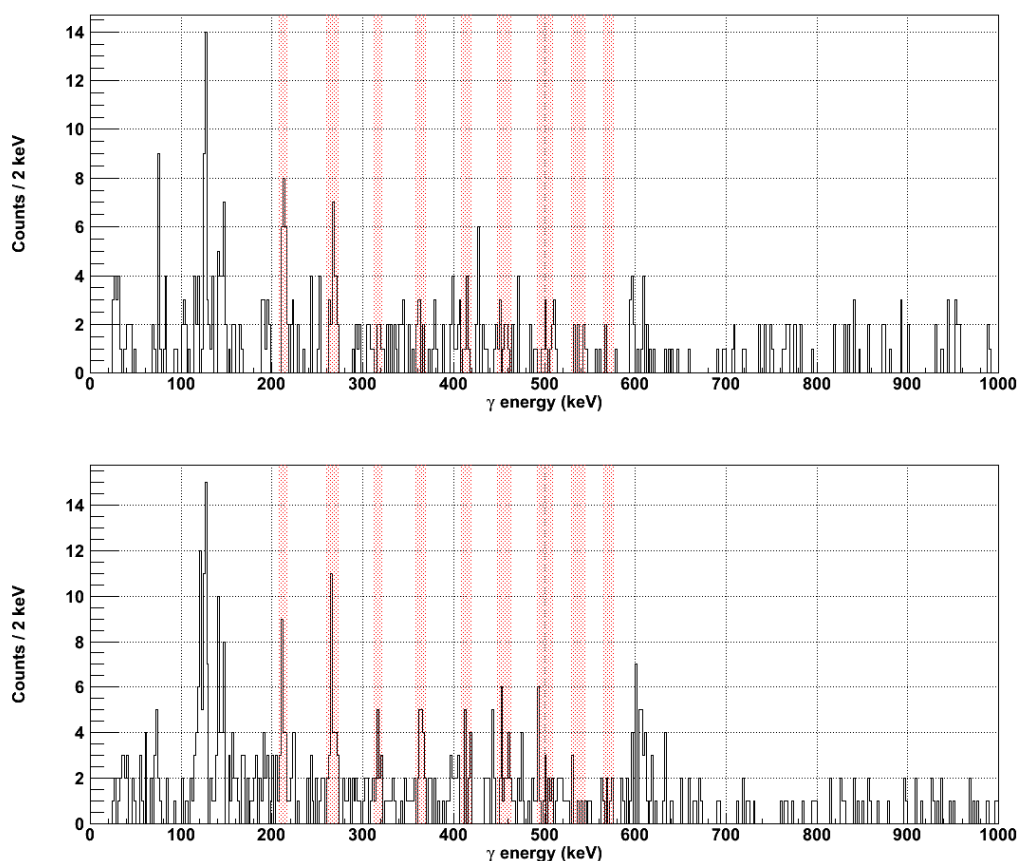


Figure 5.18: γ energy spectra for the two beam energies: $E_{\text{Beam}} = 219$ MeV (top) and 223 MeV (bottom).

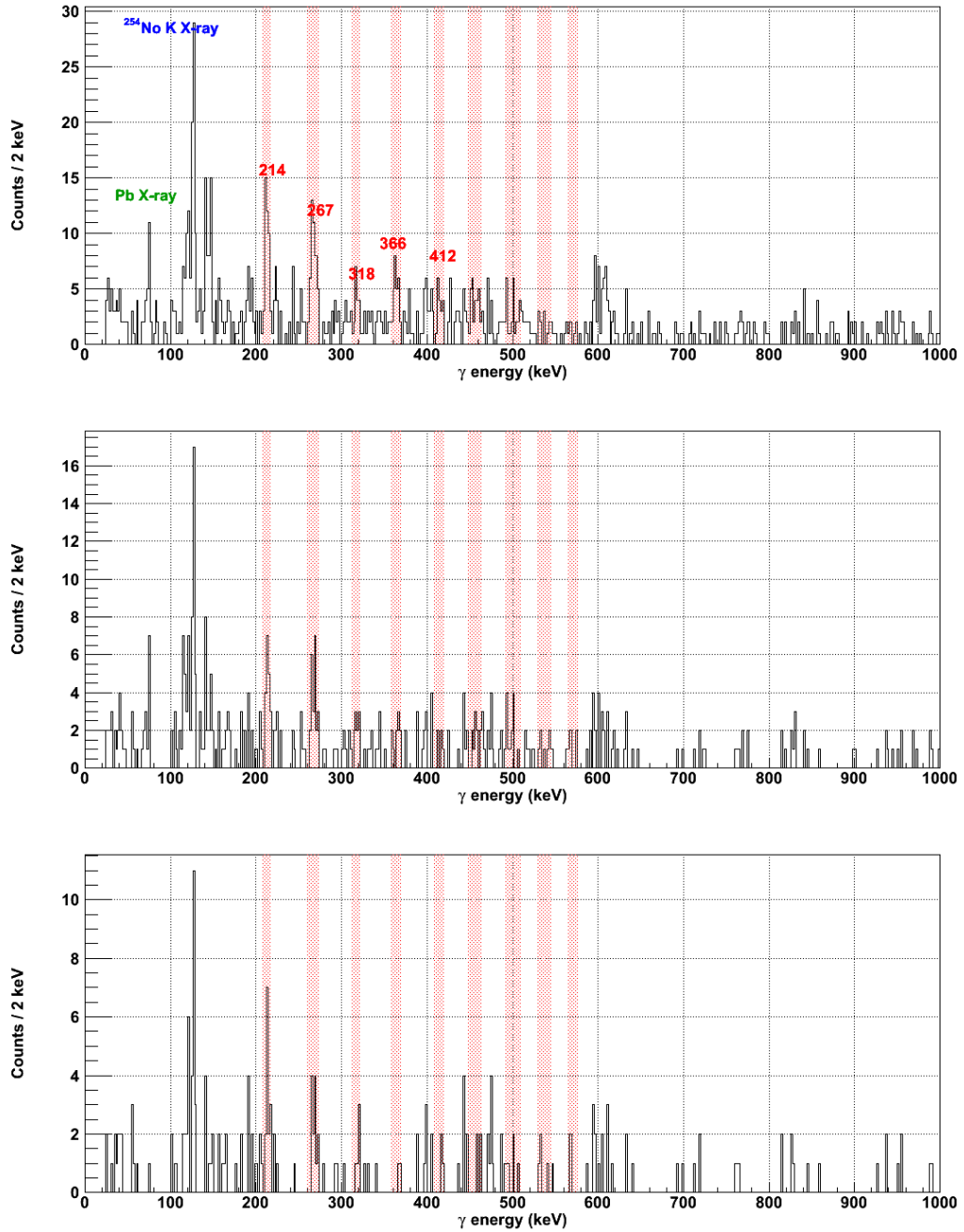


Figure 5.19: γ energy spectra for different conditions. From top to bottom: Recoil-gated, Recoil- α gated, Recoil- α - α gated.

formed at a given spin. Figure 5.20 gives the intensity profile for the two beam energies of the experiment; it shows the population stays above 20 % up to spin $\approx 18 \hbar$. No sizeable increase at high spin is seen between the two beam energies.

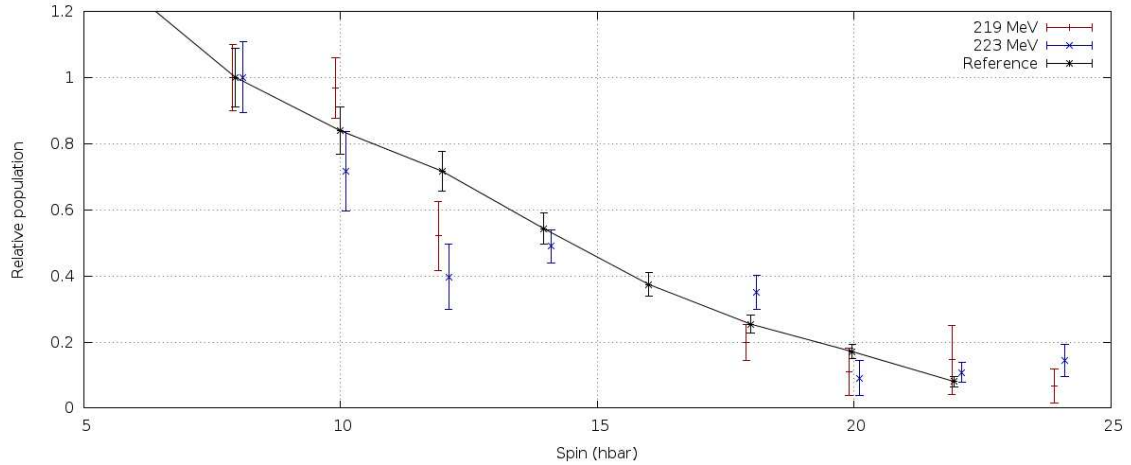


Figure 5.20: Intensity in each *yrast* transition, corrected for detection efficiency and conversion. The black points correspond to data taken from a high-statistics spectrum measured with Jurogam [31]; red for the data set at $E_{\text{Beam}} = 219$ MeV and blue for $E_{\text{Beam}} = 223$ MeV. The values are normalised to the $8^+ \rightarrow 6^+$ transition ($E_\gamma = 214$ keV). The data combine our experiment and a previous measurement at the same energy.

5.6 Alpha spectroscopy

5.6.1 Decay chain

The implantation of ^{254}No recoils in the DSSD pixels allows to follow the decay path over time. Figure 5.21 shows the decay path of ^{254}No ; due to the low statistic of the events, only the α branch is visible, the small electron capture branch is too weak.

Contaminants from test-reaction: Decay products from the test reaction ($^{219,220}\text{Th}$) have a long combined half life (several hours and more). Their decays are visible in the alpha spectrum. When looking at the spectrum run-by-run, one sees that the intensity of these contaminant-peaks decreases.

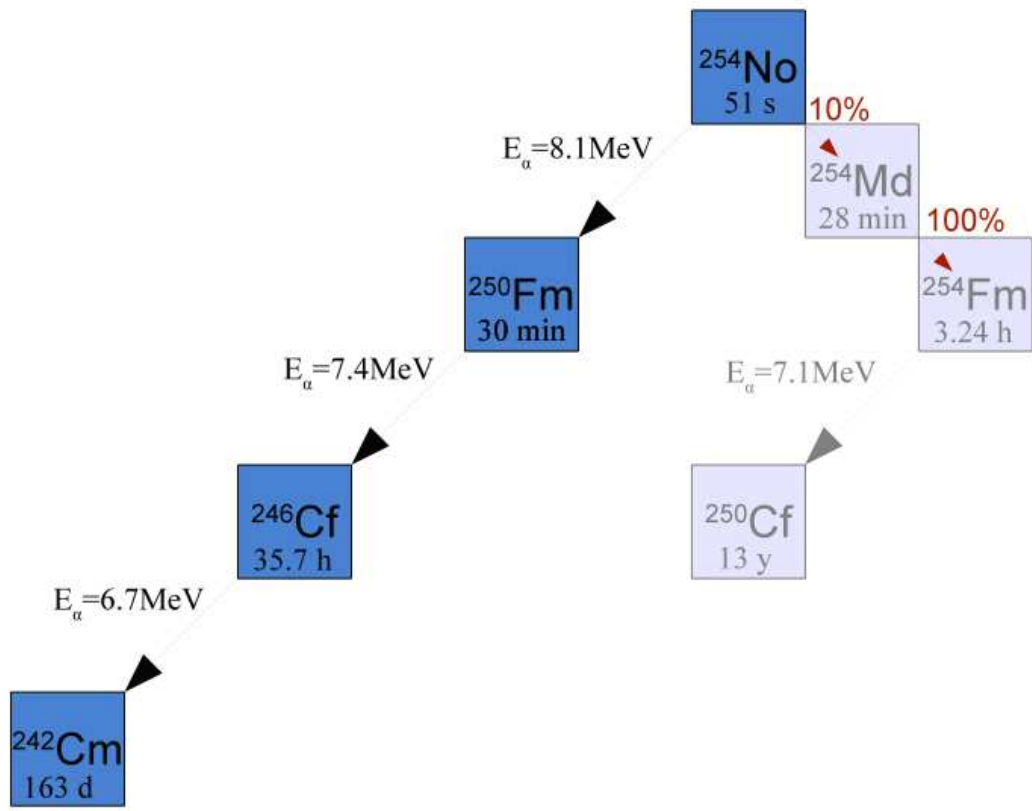


Figure 5.21: Decay path of ^{254}No , with the α energies and nuclei half-lives marked. ^{254}No presents a small branch ($\approx 10\%$) of electron capture leading to the α decay of ^{254}Fm , however, the small probability should not lead to any significant peak. The decay chain is stopped by nuclei of very long half lives.

End of the decay chain: ^{246}Cf decays with a half-life of about 1.49 days into ^{242}Cm – that explains the lower population of the peaks – and ^{242}Cm with a half-life of 162 days, hence, the Cm decay at $E_\alpha = 6.1$ MeV is not visible. That reduces the observation of such decays and the ability to correlate them over time. Over an 8 hours window (the average length of an acquisition run), only about 14% of ^{246}Cf events can be correlated. However, on a course of 7 days (total duration of the experiment) we will see about 90% of the ^{246}Cf decays, therefore, the uncorrelated decay spectrum should show the corresponding events.

Figure 5.22 shows the energy spectrum in the DSSD.

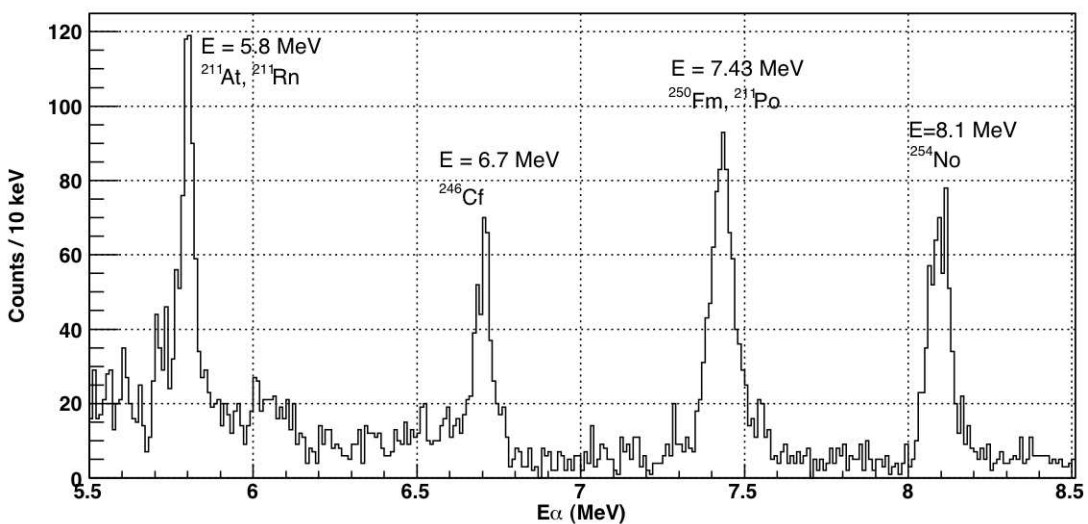


Figure 5.22: α energy spectrum for all decays in the DSSD, with no conditions. The three decays associated with ^{254}No are visible, in addition to long lived products of the test reaction.

5.6.2 Decay energy and time

The α -decay is characterised by an energy and a half-life, both being tied together (see section 1.2.3). One can plot the map of decay energy and $\log(\Delta T)$ which is a very nice way to identify the groups of specific decays. The maximum of the events $\log(\Delta T)$ distribution relates to the half-life of the decay as described in [99, 100].

Figure 5.23 shows such map for the alpha decays for ^{254}No , and figure 5.24 shows the same for the decay of ^{250}Fm .

The half-life of each nucleus can be measured from the implant-decay and decay-decay correlations. Table 5.5 gives the measured half lives compared to the references.

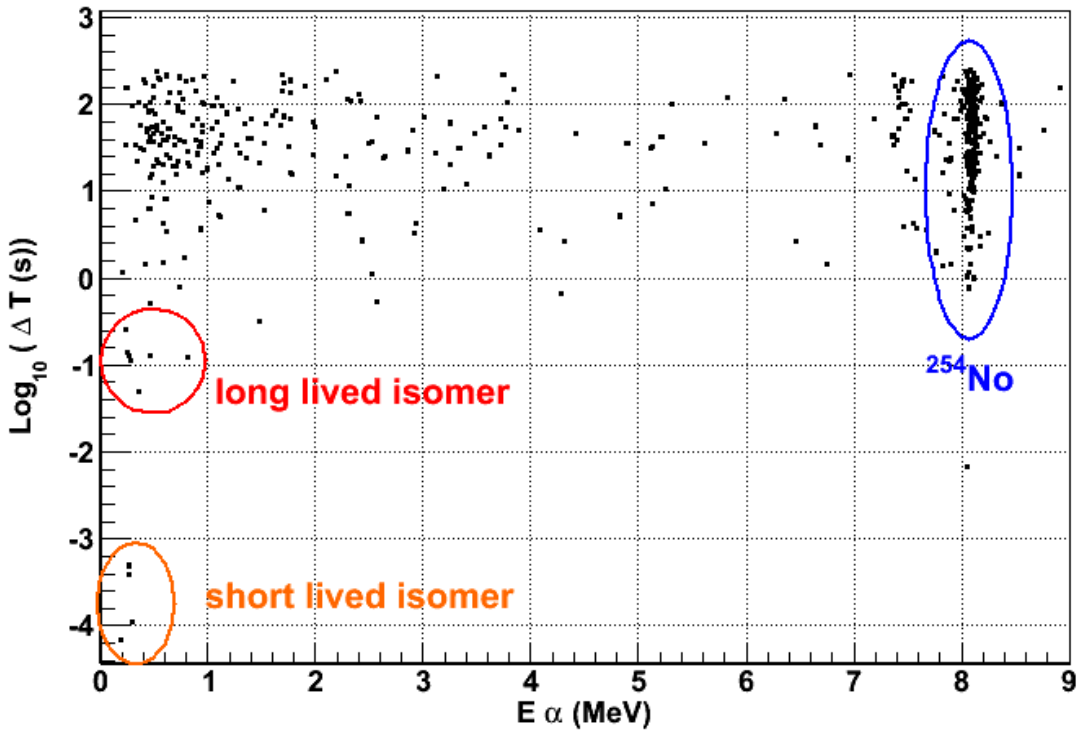


Figure 5.23: α energy and log of the time difference between recoil implantation and the first decay in the DSSD. ^{254}No is clearly identified, as are the isomer events. At lower energy than the ^{254}No α s, events with life-time in agreement with ^{250}Fm are seen: they correspond to correlation for which the decay of ^{254}No was missed.

Nucleus	Measured Half-life	Reference
^{254}No	$52 \pm 3 \text{ s}$	51 s
^{250}Fm	$29 \pm 7 \text{ min}$	30 min
^{246}Cf		35.7 h

Table 5.5: Summary of the measured half-lives for the ^{254}No α , and the decay of daughter nuclei. Uncertainty on ^{250}Fm come from ^{211}Po contamination.

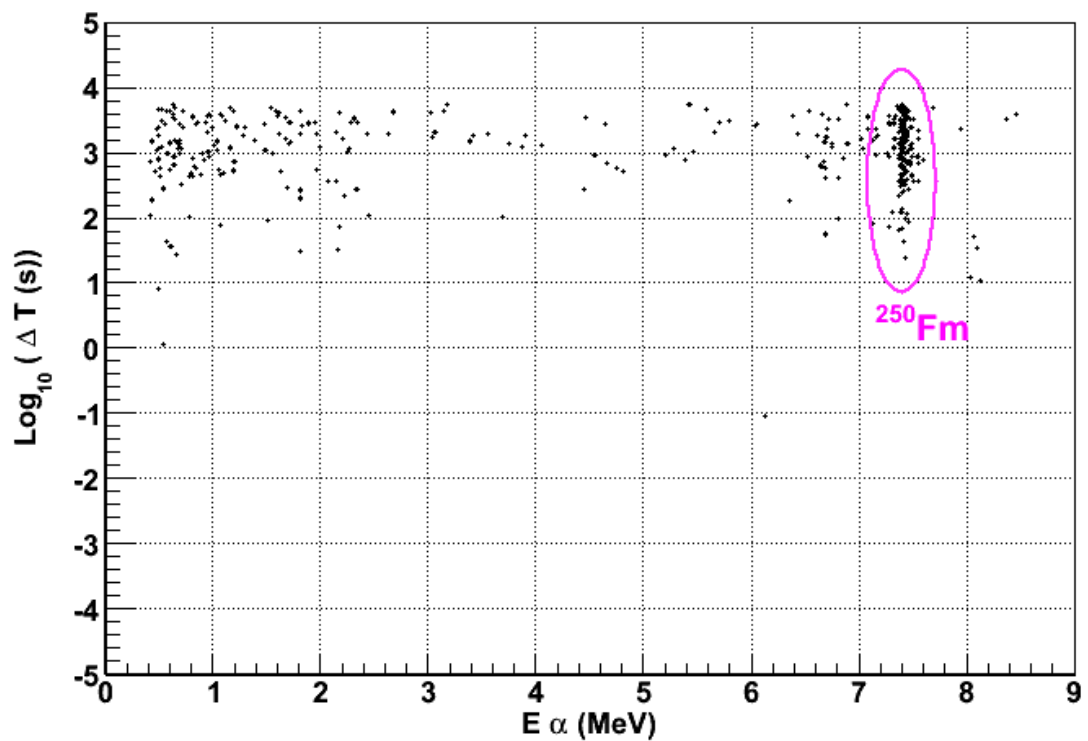


Figure 5.24: α energy and log of the time difference between first decay and second decay in the DSSD. ^{250}Fm is clearly identified.

Correlation deficit from implant to decay In the DSSD events, we observe that only 40 % of the ^{254}No decays – identified by the full α energy (8.1 MeV) – are correlated to an implant event. In the same way, 26 % of the ^{254}No decays are correlated to a ^{250}Fm (full energy), while 55 % are expected. There is a $\approx 50\%$ correlation deficit between recoil-decay and decay-decay events.

We tried to understand the origin of the issue, in particular, we investigated the possibility of a recoil-decay electronic mapping mismatch (since recoils and decays have different electronics); but nothing supports this hypothesis. It is not a threshold effect since the deficit is seen at high energy. We also tried to locate subsequent decays in neighbouring pixels, but this did not solve the problem.

It is possible that a bad front-back signal overlap, required for decay and recoil events in order to locate the pixel, is at the origin of the problem.

5.7 Isomer decays

There are two known isomeric states in ^{254}No :

- One 2 quasi-particle $K=8$ long lived isomer identified at Argonne and Jyväskylä [40, 101] and confirmed by Berkeley and GSI [95, 97]. This isomeric state is highly populated (about 30 %).
- A short lived isomer at higher energy, less populated. It is likely a 4 quasi-particle excitation with $K > 14$.

It is also possible to observe isomer decays in the DSSD. If ^{254}No is implanted in the DSSD in an isomeric excited states, the subsequent decay to the ground state will produce conversion electrons, Auger electrons and X-rays. Those will contribute to a low energy sum signal (a few hundred keV) [102] that can be detected in the DSSD. Unfortunately, our high thresholds made the detection of isomer decay events difficult and only a few of those events were seen.

In figure 5.23, we see the two event groups corresponding to isomer decay; it will be possible to select specifically isomeric events by putting a gate around these points on the plot. Table 5.6 gives the half-lives found for the isomer.

Isomer	Measured Half-life	Reference
Long lived isomer	298 ± 75 ms	266 ± 10 ms
Short lived isomer	113 ± 63 μ s	171 ± 9 μ s

Table 5.6: Summary of the measured half lives for the ^{254}No isomer decays (reference from [40, 95, 97, 101]).

5.8 Principle of calorimetric measurement and calibration

The calorimetric measurement gives the number of emitted γ transitions in the nucleus (multiplicity) and the associated total energy: m and $E_{\gamma}^{\text{total}}$. Although Gammasphere is a great detector is not perfect and the measured quantities: k (the fold) and H (the measured energy) are correlated to m and $E_{\gamma}^{\text{total}}$ but not in a simple way. In fact, the relation is neither direct nor reciprocal: to a given m correspond several k and a given k can be detected associated with different values of m – same for the energy. Therefore, it is impossible to simply associate each ^{254}No event to a $(m, E_{\gamma}^{\text{total}})$. We have to work with a global distribution and averages. We will use a statistical method that will reconstruct the most likely $(m, E_{\gamma}^{\text{total}})$ distribution that leads to a given (k, H) distribution.

5.8.1 Measured quantities

Energy

The quantity H is the total energy measured by Gammasphere for a ^{254}No event. Due to the limited detection efficiency of the HPGe crystal (maximum $\approx 22\%$ at 300 keV and 10 % at 1.3 MeV), we rely also on the BGOs to measure this energy. In our experiment, the total detection efficiency was 63%.

Fold

k is the number of measured *hits* in Gammasphere, defined as one module firing within a given time window and with an energy over the thresholds (see section 4.1.6). One notes that a hit will correspond to a wide range of BGO sector and Ge firing combinations. It is important that the time window and hit definition stays the same for calibration and measurement.

5.8.2 Fold and Energy calibration

The fold and energy response of Gammasphere to events of given multiplicity and energy (m, E) is calibrated using sources with coincident γ -decays. In practices, one uses a source emitting two γ -rays γ_1 (E_1) and γ_2 (E_2) with an (ideally) 100% correlation and gates on

the full energy detection of γ_1 in any one Ge detector. Whatever is detected in GS in coincidence is the response of Gammasphere to one γ -ray of energy E_2 . The coincidence requirement removes practically all the background from the relevant source spectra.

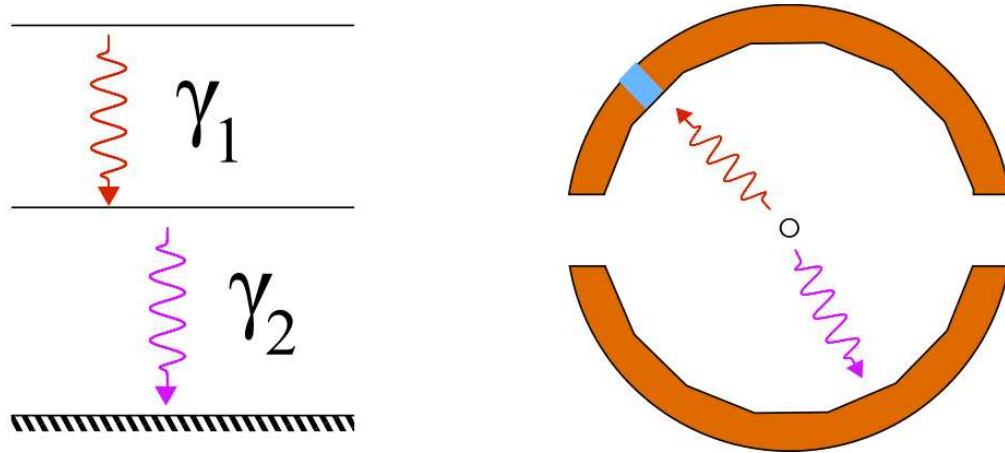


Figure 5.25: (Left) Coincident γ decays, schematic level and decay scheme showing the ideal case of fully correlated decays. We use sources with decay pattern close to this to calibrate the fold and energy response of Gammasphere. (Right) Response calibration in Gammasphere: γ_1 is gated on with Ge detector (in blue) and γ_2 is detected (or not) by the rest of Gammasphere (the separation of BGO and Ge is not represented).

We calibrated the response in fold and energy, with ^{88}Y , ^{60}Co , ^{207}Bi and ^{152}Eu . Table 5.7 gives the sources used for calibration and the energies of the γ -rays involved in the calibration and figure 5.26 shows the decay pattern of the sources.

One has to correct the number of γ -rays observed for the branching of decay to the levels involved in the cascade used for the response calibration and also for possible electron conversion of the transition. Table 5.7 shows the correlation and conversion factor for the used sources. The correction factor ($= N_{\gamma_2}/N_{\gamma_1}$) accounts for the difference between the number of gated γ_1 and the expected number of emitted γ_2 . Those have to be taken into account in building the response.

An additional correction has to be applied for the fact that one module is *blind* because it is gating on the γ_1 transition (a *clean* Ge is required, i.e. no hit in the surrounding BGO). Therefore, the probability of missing one γ is increased by a factor $1/N_{\text{detectors}}$.

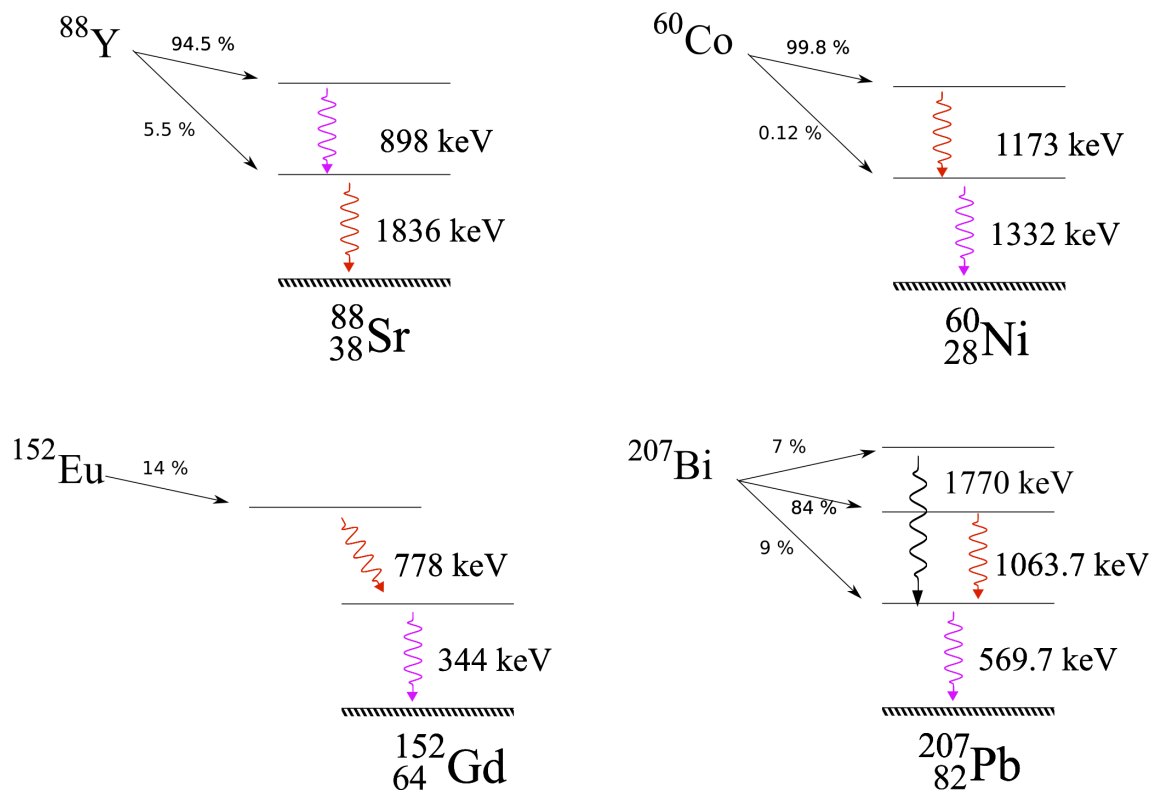


Figure 5.26: Level and decay scheme of the sources used for response calibration. Only the levels and γ -rays of interest for the response calibration are shown. The γ transition marked in red are the ones on which we gate to build the response.

Source	E_1 (keV)	E_2 (keV)	Correlation factor (%)	γ_2 Conversion coefficient	Global correction factor (%)
^{88}Y	1836	898	94	< 0.0005	94
^{60}Co	1173	1332	100	< 0.0005	100
^{207}Bi	1063	569	100	0.0217	97.9
^{152}Eu	778	344	100	0.0398	96.2

Table 5.7: Correlation and conversion coefficients for the source used for response calibration. The global correction factor $N_{\gamma_2}/N_{\gamma_1}$ gives the ratio of expected calibration γ_2 in respect to the number of gated γ_1 .

Event Mixing method

To build the response matrices to multiplicities higher than 1 and energies larger than E_{γ_2} , an event mixing technique is used. With this method a *pseudo event* of multiplicity M is built by grouping M one- γ events into a one M - γ s event. In other words, for an event of multiplicity M and energy $M \cdot E_{\gamma_2}$, we consider a set of M events of multiplicity and energy $(1, E_{\gamma_2})$ and sum the measured energy : $H_{(M,M \cdot E_{\gamma_2})} = \sum_1^M H_{(1,E_{\gamma_2})}$. For the fold of the $(M, M \cdot E_{\gamma_2})$ event, the k of the pseudo-event is not the sum of individual k s but it is built from the list of IDs of the modules contributing to the fold to account for the fact that $k = 0$ or 1 . In this method, the correction coefficient from table 5.7 and the correction for the blind module are a scaling of the axes, done after the response building.

Random Generation

One can reduce the dependence on a limited number of events and implement the correlation and conversion corrections in a different manner by reproducing the characteristics of individual events from the one- γ fold and energy spectra. In practice, the individual fold (k) and energy (H) of a pseudo event is not read from the data but randomly selected from the distributions of those quantities. In this method, the correction of the spectrum for the missing γ -rays from non-100% correlation and conversion electron is done by down-scaling the counts in the $k = 0$ and $H = 0$ bins of the spectra. This method offers an unlimited number of events by sampling the distributions. The IDs of the module triggering are also simulated using such statistical method, in order to correctly reproduce the experiment and account for the *blind* module.

Comparison of the two methods

Figure 5.27 shows the responses from the two methods. Although they are very similar the randomly generated response is slightly under the event-mixing one.

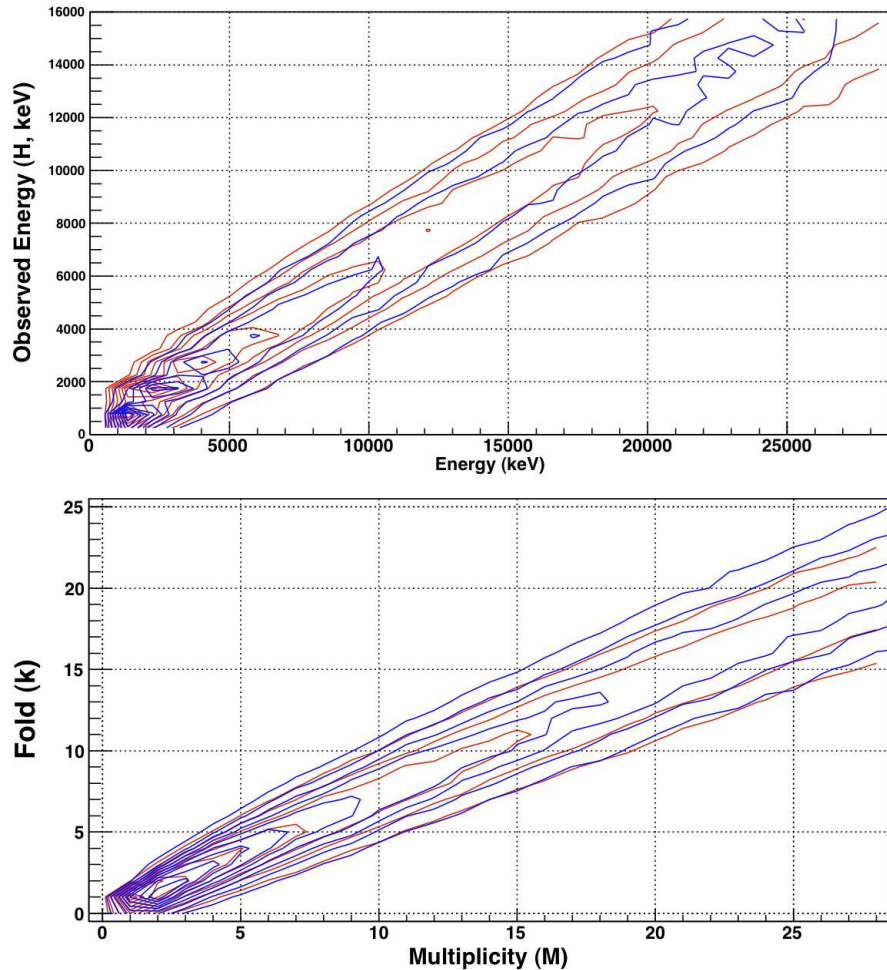


Figure 5.27: Comparison of the responses – energy (top) and fold (bottom) – built by event mixing (blue) and random generation (red). The responses are very similar, however, small differences are visible : the randomly generated response is slightly below the event mixing one, it is particularly visible at high energy and multiplicity.

The single γ events used to make the response, are the same, except for corrections for the background and correlation correction. For the event mixing, correlation corrections are an axis scaling while the statistical method allows a better correction by applying them from the source. Furthermore, the background, particularly visible at high energy, can be removed in the statistical method, which cannot be done in event mixing – see figure 5.28

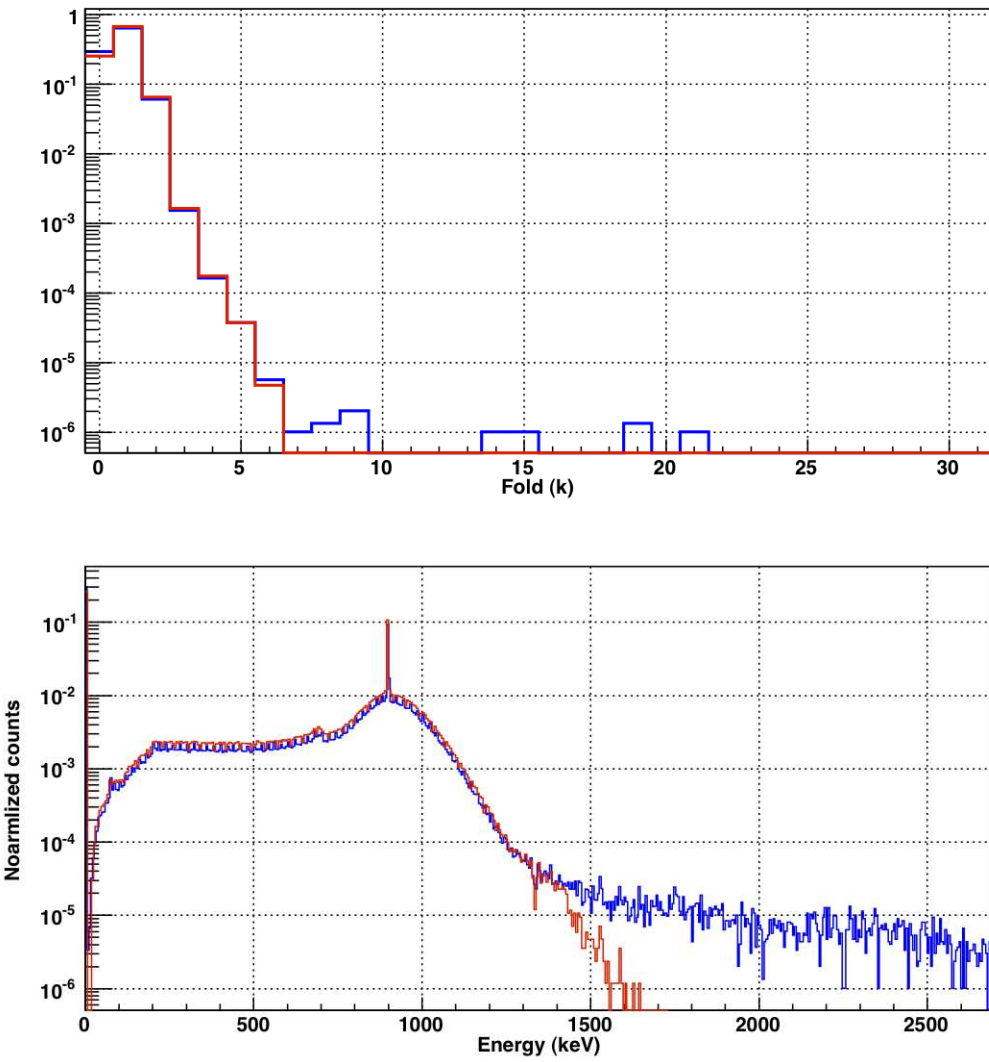


Figure 5.28: Distribution of fold (top) and energy (bottom) of one γ events used to build the response by event mixing (blue) and random generation (red). The background subtraction at high energy and fold is clearly visible. One should note the high number of counts at 0 in the H spectrum.

Random γ contribution We want to determine the importance of the contribution of γ -rays from background radiation, multiple reactions in the same beam burst (the probability of a fission reactions at the same time as the formation of a ^{254}No is about 2 %), ... to the (k, H) distribution.

The average rate of γ events in the Ge detectors of Gammasphere being $R_{\gamma\text{Ge}} \approx 12$ kHz, accounting for the average multiplicity of events ($M = 6$), the module detection efficiency $\varepsilon_{\text{mod}} \approx 80$ % and a 140 ns time window, we expect an average $R_{\gamma\text{Ge}} \times M \times \frac{\varepsilon_{\text{mod}}}{\varepsilon_{\text{Ge}}} \approx 0.07$ random γ /recoil. This number is consistent with what is seen in the data. In plots like in figure 4.14, we extract from the background at low times a rate of randoms of $\approx 0.5 10^{-3} /ns$, or ≈ 0.04 random γ /recoil. The contribution of randoms to the measurement is weak, of the order of a few per cent, but can not be neglected. Moreover, the energy contribution of random γ -rays is unknown and hard to quantify.

Mathematical parametrization

The *shape* of the responses is rather simple and can be parametrized assuming a Gaussian distribution with the centroid and width functions of the energy or multiplicity :

$$(\langle H \rangle, \sigma_H) = \left(H_0 + b \cdot E, \sqrt{\sigma_0^2 + (\sigma_1 \cdot E^{1/3})^2} \right) \quad (5.1)$$

$$(\langle k \rangle, \sigma_k) = \left(N \left(1 - \left(\frac{1 - \varepsilon}{N} \right)^M \right), \sqrt{\sigma_0^2 + (\sigma_1 \cdot M^{1/3})^2} \right) \quad (5.2)$$

In equation 5.1 the average energy H is proportional to the total energy emitted E . In equation 5.2 the average fold is determined by the number of modules N , the multiplicity of events M and the multiplicity efficiency ε and can be seen as a probability of not missing k out of M events in N detectors. The width parametrization is arbitrary. The modelling is a simplification and can not be used as a proper method to build a response. However, the mathematical formulae, in particular for efficiency, is a good way to characterise a response.

5.8.3 Response characteristics

For different energy

The simplest way to characterise the response is to look at *snapshot* quantities, for given values of the multiplicity and energy, the distribution of relative fold (k) and observed

energy (H) is a good value to look at. These quantities follow the same pattern: the relative fold (k/M) and energy (H/E) increases from low values ($\approx 35\%$) for low γ energies, peaks at $\approx 60 - 75\%$ around 800-1000 keV and decrease for higher energies. Figures 5.29 show this evolution. The rise of efficiency with energy at low energies is due to the detection thresholds and the low probability of scattering. We see that the fold response saturates at high energy while the energy efficiency does not. The decrease in energy efficiency is possibly linked to the missing modules since γ -ray scattering becomes more important at higher energy.

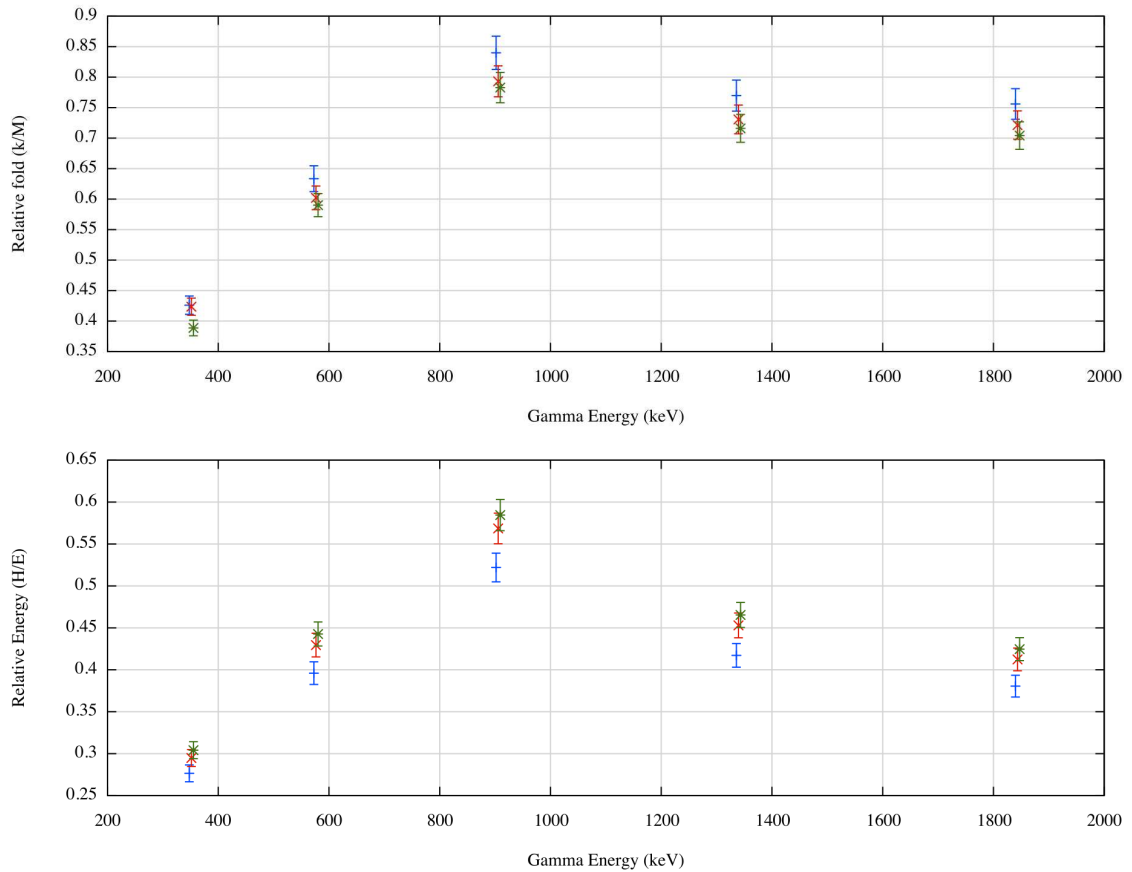


Figure 5.29: Relative fold (k/M) [Top] and energy (H/E) [Bottom] for different sources used for the response, at multiplicities 5 (blue), 10 (red) and 15 (green), plotted as a function of the energy of the γ -ray detected in the one- γ events (the points are slightly shifted proportionally to the corresponding multiplicity to distinguish them).

There is small dependence of the relative fold and energy measurements with increasing multiplicity (see figure 5.29). This evolution is much less significant than the energy dependence, and the decrease in detection efficiency with increasing multiplicity can be explained by the fragmenting of the total energy into several γ -rays. This shows that there is a clear dependence of the response on the energy of the γ -rays, while the multiplicity does not

change the response in any significant extent. This is expected since detector thresholds and scattering depend very much on the energy of the γ -rays.

Decoupling of fold and energy response

As we saw previously, the energy of the γ ray used for the response calibration changes the response in multiplicity and energy. So far, however, we have considered these two quantities to be independent. This goes against the natural idea that the response to one γ -ray of very high energy will differ from the one for many γ -rays of small energies.

In a very complex γ environment, with a broad distribution of multiplicities and γ energies, it becomes virtually impossible to calibrate the response to match perfectly the experimental conditions and we have to rely on our best estimate of the fold and γ energies to pick the adequate source to build the response – nothing is against using the multiplicity response from one source and the energy response from another – to match as best as possible the experimental conditions. We choose to use the response from ^{88}Y because the average γ energy detected in the Ge and BGO detectors is of the order of 900 keV. For this response, the energy efficiency is 63 % and the multiplicity efficiency, obtained from a fit of the average k as a function of M as in equation 5.2, is 71 %.

The best way would be to calibrate in a 4-dimensions space (E, M, H, k) and not two 2-dimensions spaces as we do $(E, H), (M, k)$. But the unfolding in 4D would be very hard to perform since no source allow us to control independently E and M ; moreover, the unfolding would become extremely long due to the bi-quadratic size of the space needed to solve the unfolding system.

5.9 The unfolding procedure

To go from the (k, H) distribution to (M, E) , one has determine the original distribution which gave the measured (k, H) . The relation $k \rightarrow m$ and $H \rightarrow E$ is not straightforward, therefore, a stochastic trial and error method is used. This method will allow the reconstruction of the most likely distribution of multiplicity and energy (M, E) that would lead to the observed (k, H) distribution.

5.9.1 Principle of the unfolding

The response matrices only allow the transformation from multiplicity to fold or energy to observed energy (H). The *unfolding* process will therefore rely only on the $M \rightarrow k$ and $E \rightarrow H$ direction. This method has been described in [103, 104]. The iterative process finds the relevant (M,E) points that, once folded, give a (k,H) combination that is in the measured distribution. Repeating the operation until all the (k,H) points have been matched by a (M,E) point, the whole distribution is *unfolded*. The final (M,E) distribution contains the points that reproduce the measured (k,H) distribution.

5.9.2 Formal description of the unfolding

In mathematical terms, the unfolding involves the following quantities:

- $N_{folded}(k, H)$: the number of counts in the folded distribution at fold k and observed energy H ; this is the experimental measurement.
- $P_M(k)$ the probability distribution of k values associated with the multiplicity M .
- $P_E(H)$ the probability distribution of H values associated with the energy E .
- $N^{(i)}(M, E)$ the number of counts in the *unfolded* distribution at multiplicity M and energy E for the unfolding iteration i .

The goal is to get the unfolded distribution $N_{unfolded}(M, E)$ so that $N_{folded}(k, H) = \sum_{M,E} N_{unfolded}(M, E) \times P_M(k) \times P_E(H)$. The unfolding iteration represented in figure 5.30, follows these steps:

- Starting from a test distribution $N^{(i)}(M, E)$, we prepare an empty next-iteration $N^{(i+1)}(M, E)$.
- As long as $\sum_{M,E} N^{(i+1)}(M, E) < \sum_{M,E} N^{(i)}(M, E)$, the following loop is performed:
 - Test multiplicity and energy M_{test} and E_{test} are random obtained from the distribution of $N^{(i)}(M, E)$ ((a) in figure 5.30).
 - If $N^{(i)}(M_{\text{test}}, E_{\text{test}}) > 0$:
 - * The associated k_{test} and H_{test} are randomly obtained from the distributions $P_{M_{\text{test}}}(k)$ and $P_{E_{\text{test}}}(H)$ (step (b) in figure 5.30).

- * If $N_{folded}(k_{test}, H_{test}) > 0$:
 - Counts of $N_{folded}(k_{test}, H_{test})$ is decremented by one ((c) in figure 5.30).
 - Counts of $N^{(i+1)}(M_{test}, E_{test})$ is incremented by one ((d) in figure 5.30).

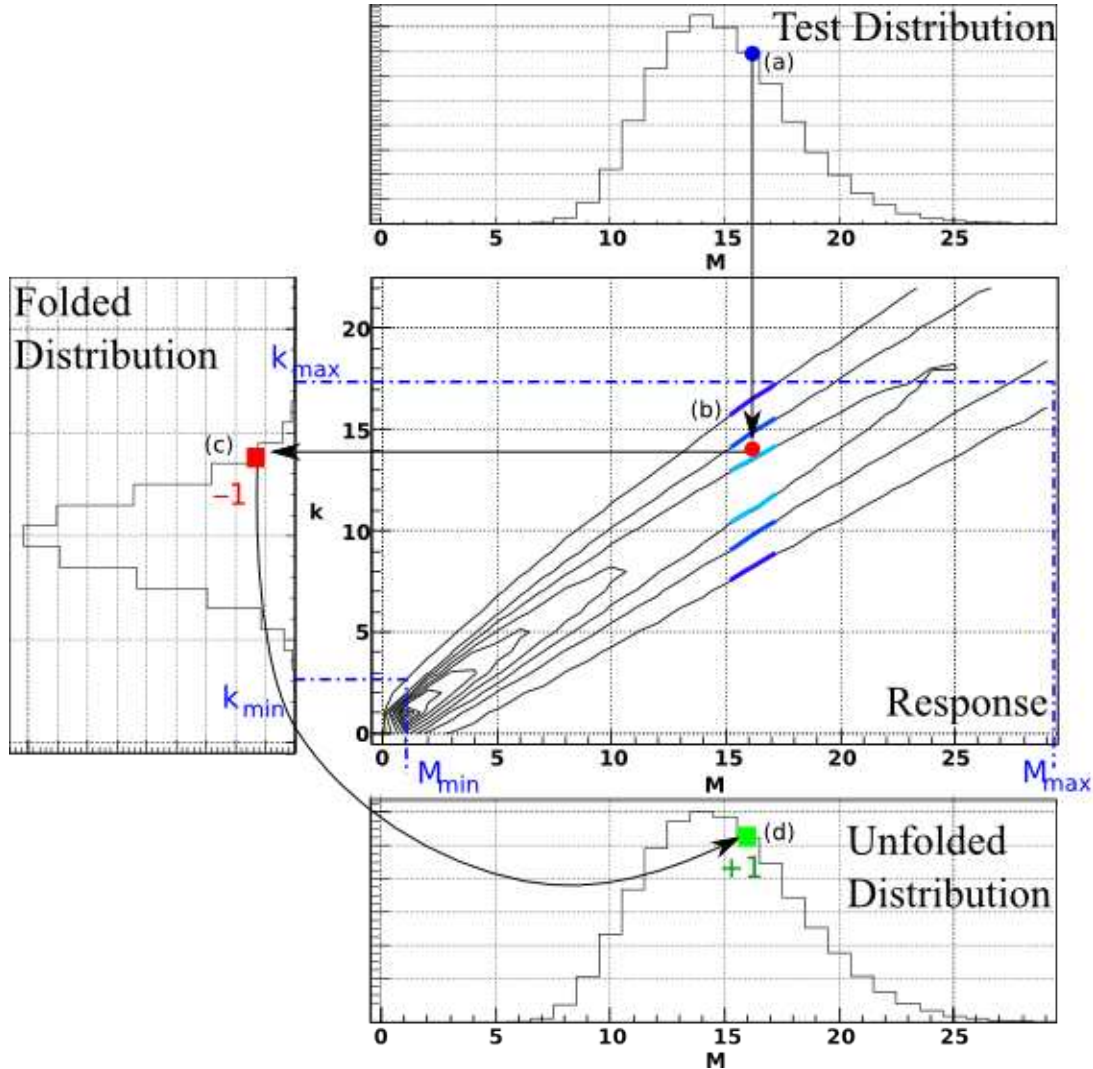


Figure 5.30: Schematic view of one unfolding step: A test multiplicity M_{test} is randomly selected (a), and a test fold k_{test} is obtained from the response at M_{test} (b). If The folded (experimental) distribution has a count at k_{test} , the experimental distribution is decremented at this fold (c) and the unfolded distribution is incremented at M_{test} (d). The limits in the experimental distribution (k_{min} and k_{max}) determine the limits on multiplicity to consider M_{min} and M_{max}

The starting distribution $N^{(0)}(M, E)$ is arbitrarily set to a uniform distribution; it has been observed that unfolding procedure converges after only a few iterations. A uniform

distribution is therefore good enough and has the merit of introducing no bias in the unfolding by letting all the (M, E) space open for the final distribution. The range of M and E to consider in the unfolding can be limited in order to reduce the time and memory necessary to perform the operation – see figure 5.30.

5.9.3 Validation of the unfolding

To validate the unfolding process, one simply has to generate a test distribution (M, E) , fold it using the response to obtain a (k, H) distribution, and unfold it back for comparison with the original. The differences that may arise between the original test distribution and the corresponding unfolded distribution will be an indication of how good the unfolding process can be. Figures 5.31 and 5.32 show such distributions and compare their projections. The unfolded distribution matches the source test distribution position and width but the unfolded result is *smoother*: the sharp edges of the source distribution are not well reproduced. This is a very important aspect of the unfolding: due to the spread in the response, it is impossible to get sharp edges in the unfolded distribution.

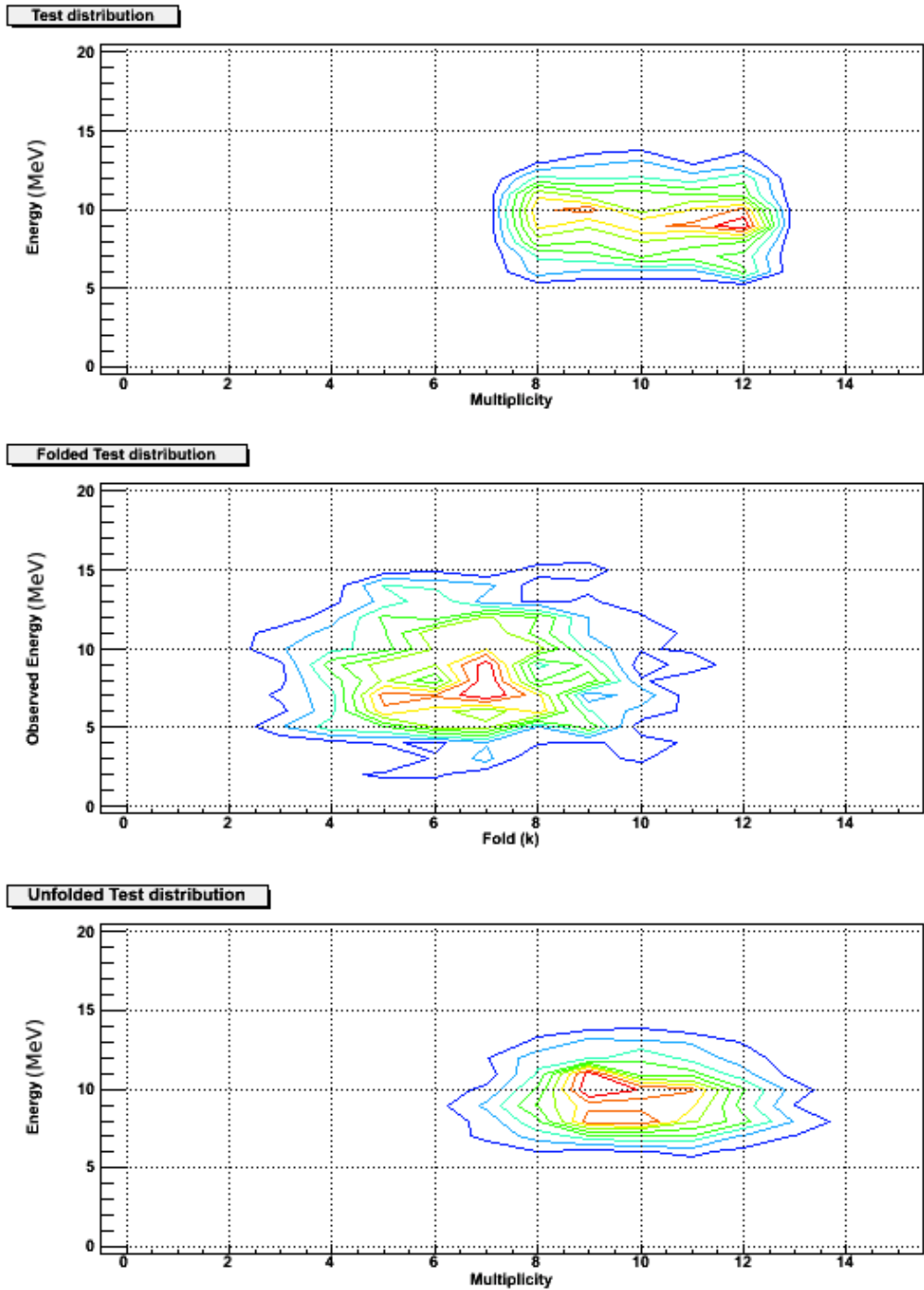


Figure 5.31: Validation of the unfolding: A test distribution (top) is folded (middle) then unfolded (bottom). The unfolded distribution (with 18 iterations) reproduces the global properties of the original test distribution (average quantities, widths) but not the sharp edges.

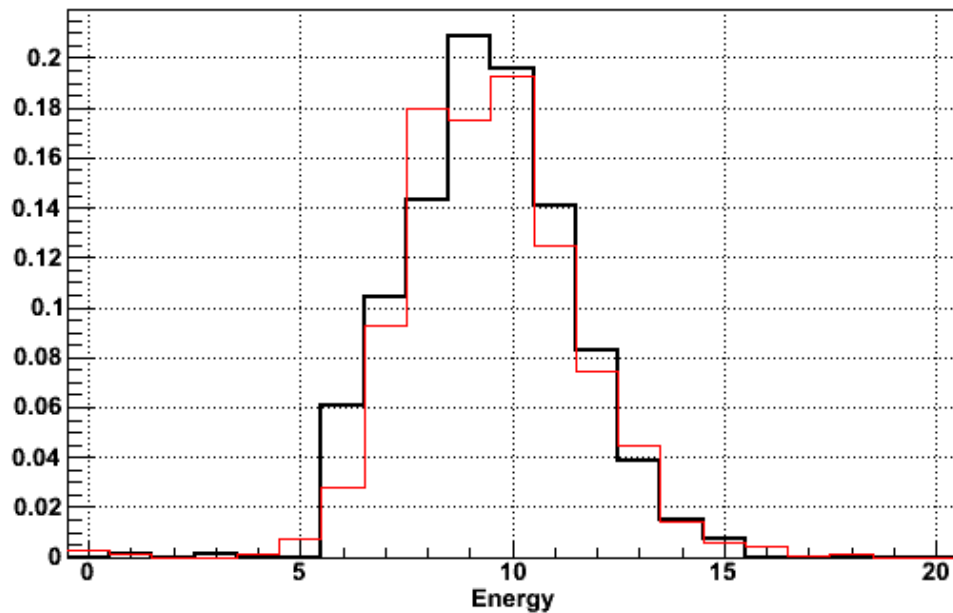
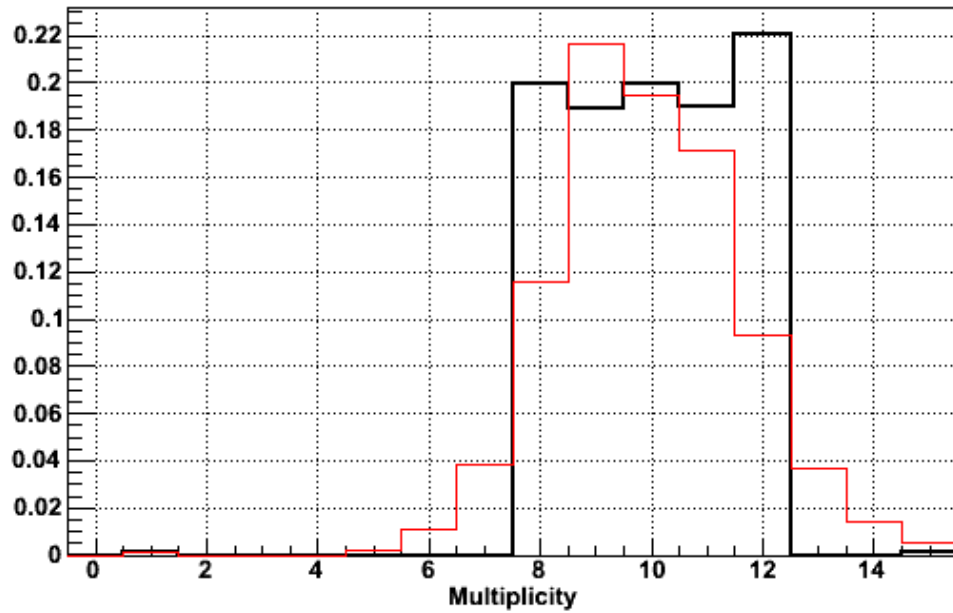


Figure 5.32: Overlay of the multiplicity and energy projections of the original test distribution (black) and unfolded distribution (red), as described in 5.31.

Effect of the number of iteration

A key parameter of the unfolding is the number of iterations. An insufficient number of iterations will lead to a broad and undefined distribution. Figures 5.33 and 5.34 show the result of unfolding with only 3 iterations. And too much iteration will lead to a deformed distribution – see figure 5.35 for the distribution unfolded with 100 iterations and figure 5.36 for the projections: the average values, like the distribution centroid and width are in agreement with the original distribution, but some sub structure appear that should not be there. This is because the unfolding tends to gather the points around local maxima and therefore will aggregate the data around statistical fluctuations.

In general, we get good results with a number of iteration around 20. In fact, we can look at the widths and average of the distribution as a function of the iteration number. Figure 5.37 shows the evolution of projection centroid and width of the distribution evolution over 50 iterations. Both quantities drop quickly over the few first iterations, then stabilise. An exponential decay fit gives a decay constant of ≈ 5 iterations, indicating that the procedure converges quickly.

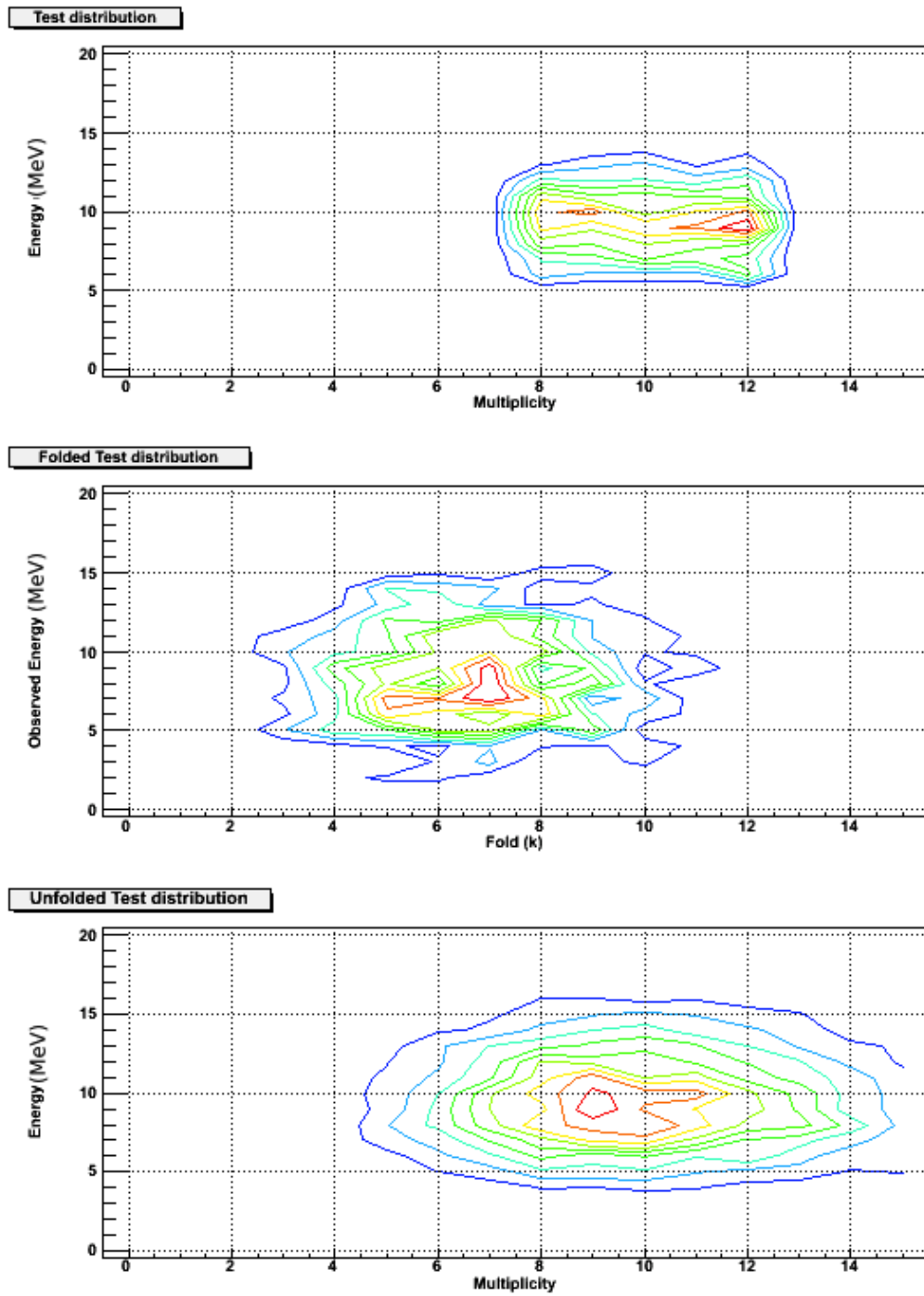


Figure 5.33: Same test distribution as in figure 5.31 (top), folded (middle) and unfolded (bottom) after 3 iterations.

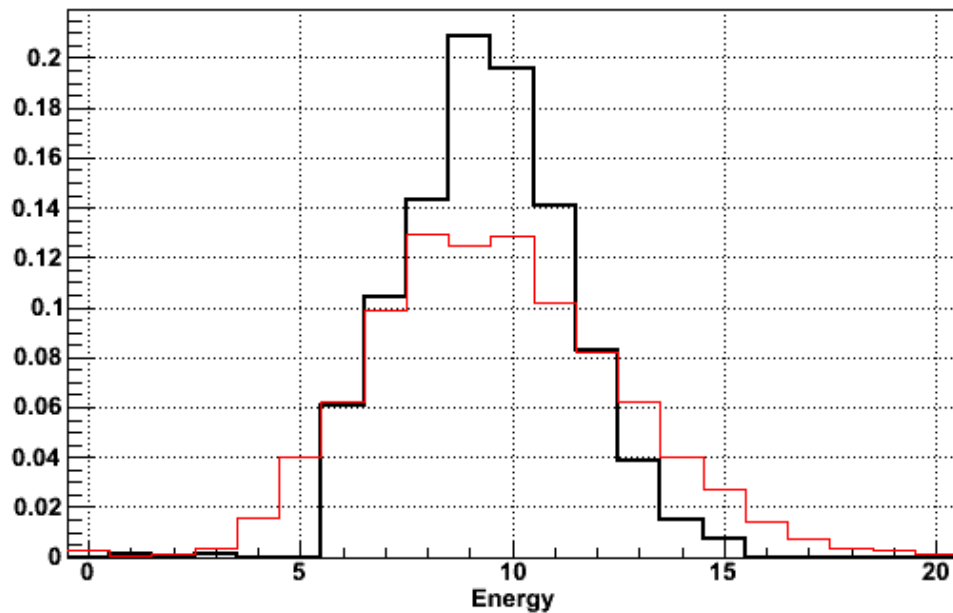
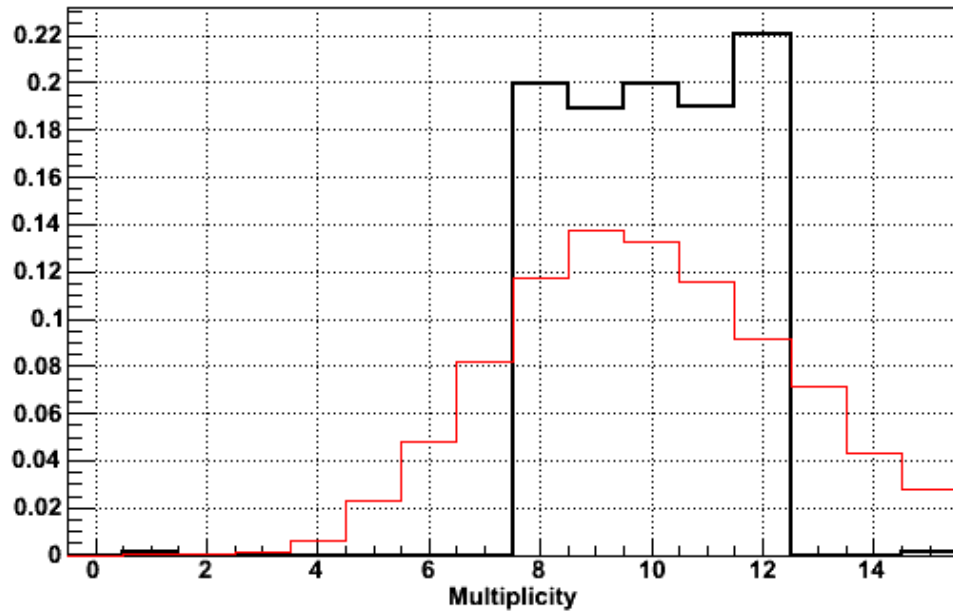


Figure 5.34: multiplicity and energy projections of the original test distribution (black) and unfolded distribution after 3 iterations (red), as described in figure 5.33.

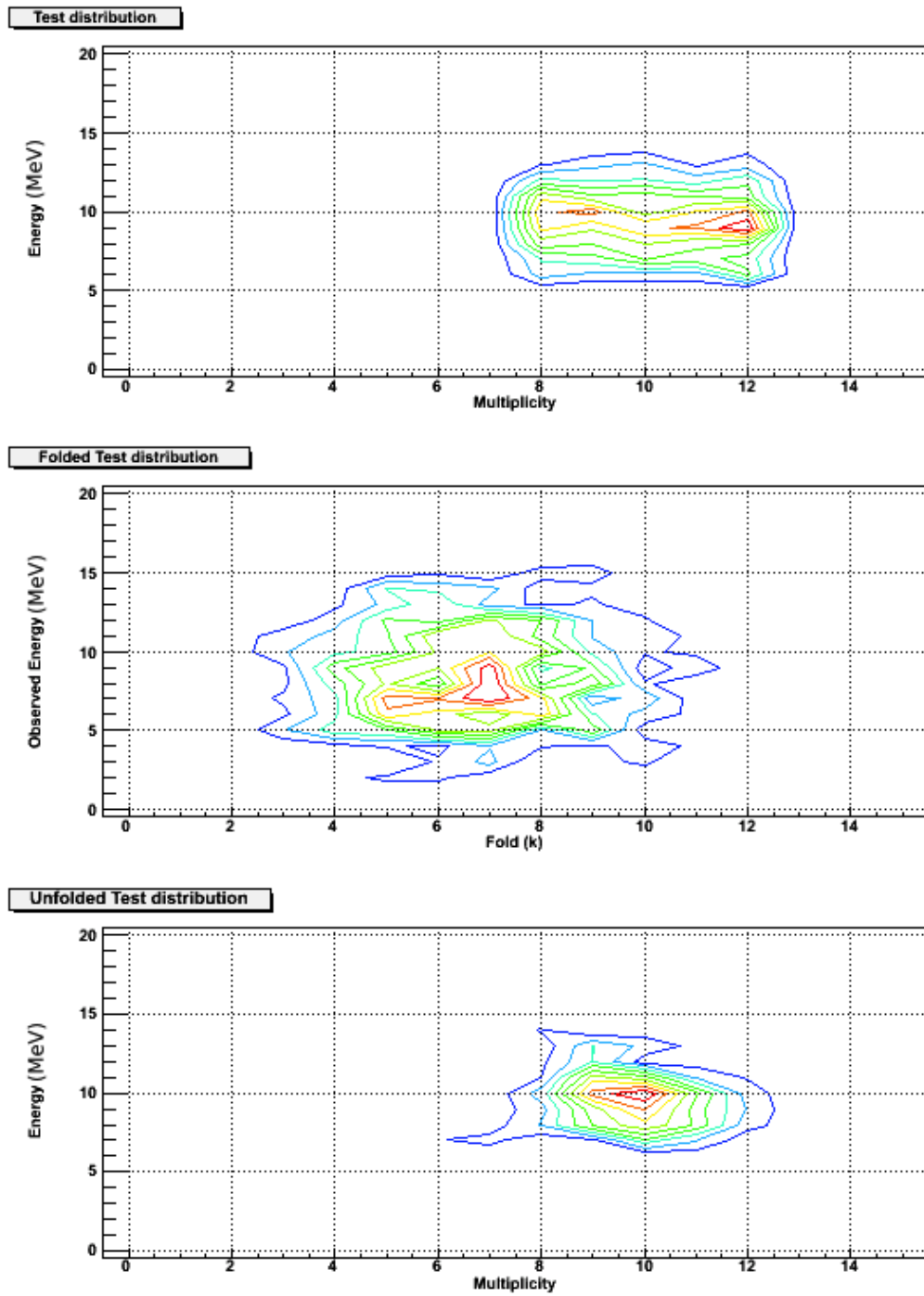


Figure 5.35: Same test distribution as in figure 5.31 (top), folded (middle) and unfolded (bottom) after 100 iterations.

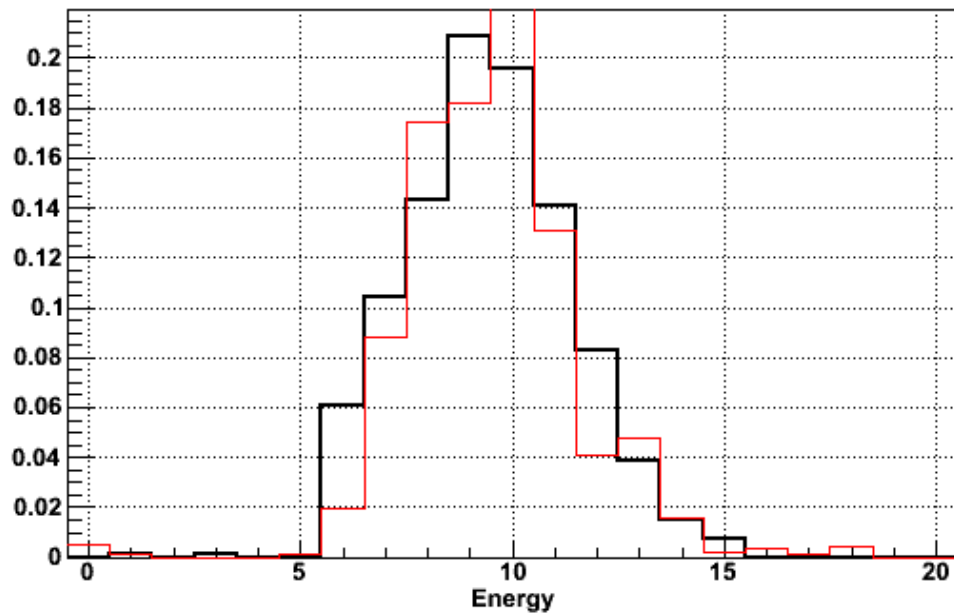
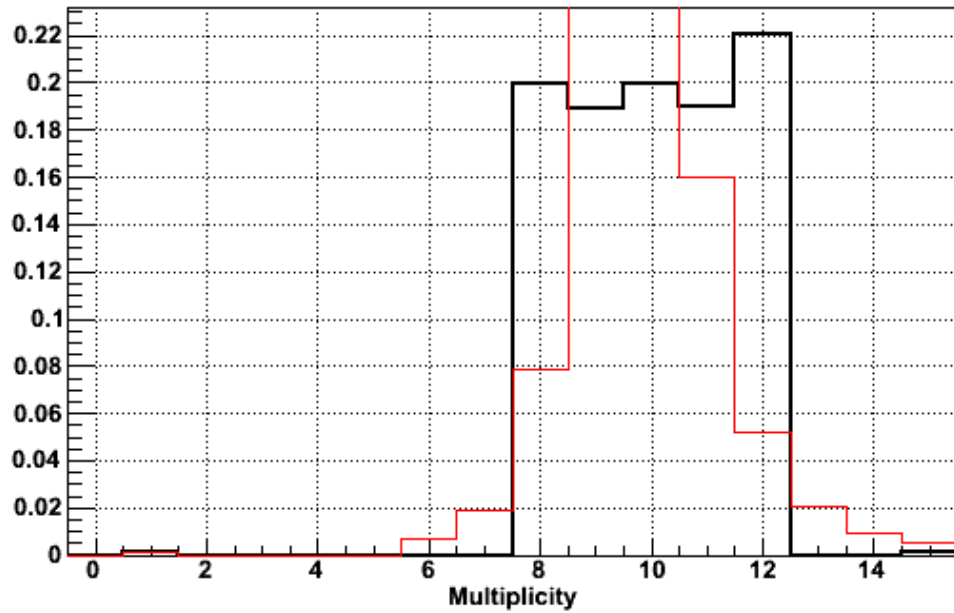


Figure 5.36: multiplicity and energy projections of the original test distribution (black) and unfolded distribution after 100 iterations (red), as described in figure 5.35.

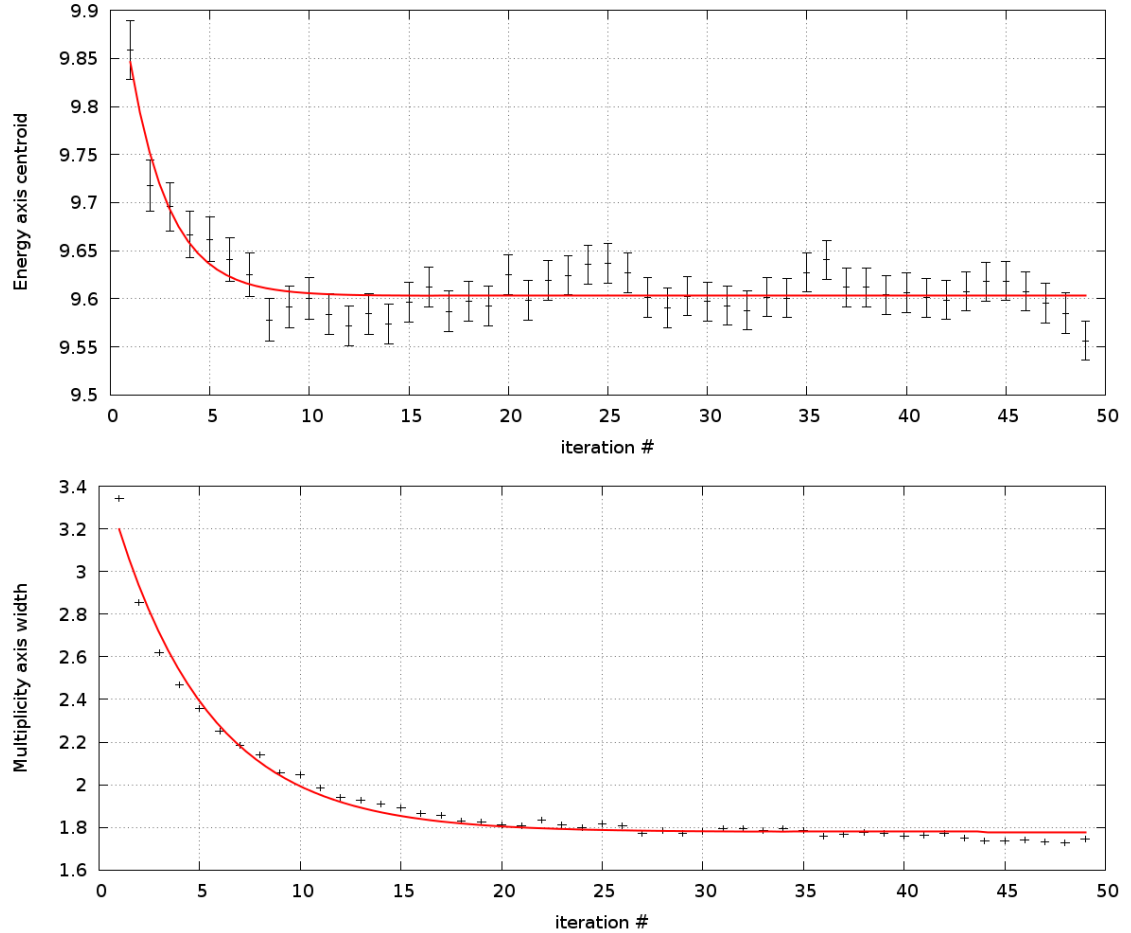


Figure 5.37: Evolution of the average energy (top) and the width of the multiplicity distribution (bottom) as a function of the unfolding iteration number (black points). The red curves are fits of double exponential decays plus a constant.

Effect of the prescaling

The initial data distribution can be scaled up (or down) before unfolding. This means in practice that each point will be unfolded several times. It is a good way to make up for a low statistic and try all the possible unfolded configuration associated with the measured (k, H) distribution.

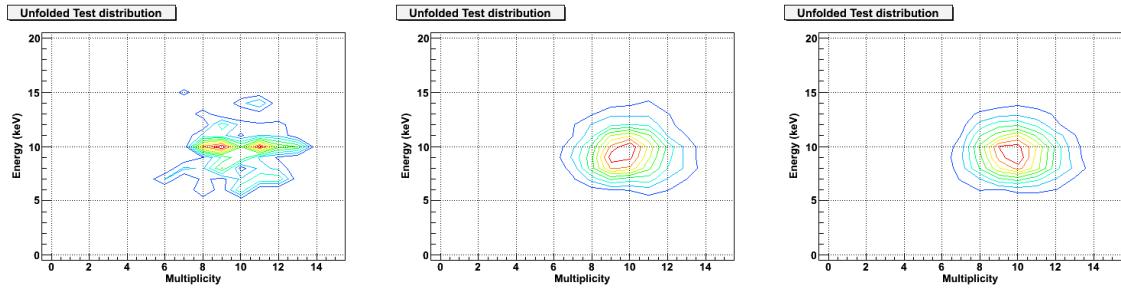


Figure 5.38: Unfolded distribution with a pre-scaling factor of 1 (left), 50 (center) and 150 (right).

Figure 5.38 shows an unfolded distribution for a pre-scaling factor of 1, 50 and 150. One notice that the larger the pre-scaling the smoother the final distribution is. It is therefore important not to scale too much up, for that may smooth out sub-structures in the distribution. On the opposite side, not enough scaling will lead to important statistical fluctuations.

There is no rule to choose the pre-scaling factor. The *good* factor would depend on many parameters such as the number of iterations, the number of counts in the original distribution, the size of the matrix, the dispersion of points in the distribution, even the response matrices will influence the need for a pre-scaling. It is generally recommended to get a number of point in the starting (k, H) distribution of the order of a few thousands. As an arbitrary rule of thumb, we choose to scale up the input distribution by the size of the matrix (i.e. 32 for a 32-by-32 matrix).

Separation of peaks

We also want to check if and with what precision the unfolding can separate two distinct peaks, as the distributions we study may have structures.

In practice, neighbouring peaks in a distribution may be *fused* together in the folded distribution because of the loss of resolution and that will lead to the two peaks being unresolved or connected in the unfolded distribution. More iterations will be needed to

get a separation, and the shape of the peaks will be incorrectly reproduced. Figure 5.39 and 5.40 show different examples for two peaks distributions.

In general, we conclude that the unfolding procedure fails to reproduce sub-structures for not clearly separated peaks. Peaks that are too close together are distorted and their relative intensity is not conserved in the unfolding. Therefore, we should regard all visible sub-structure as possible artefact and be careful in the interpretation of the shape of the distribution: only the average quantities (centroid, widths, possible *tilts*, ...) can be considered certain.

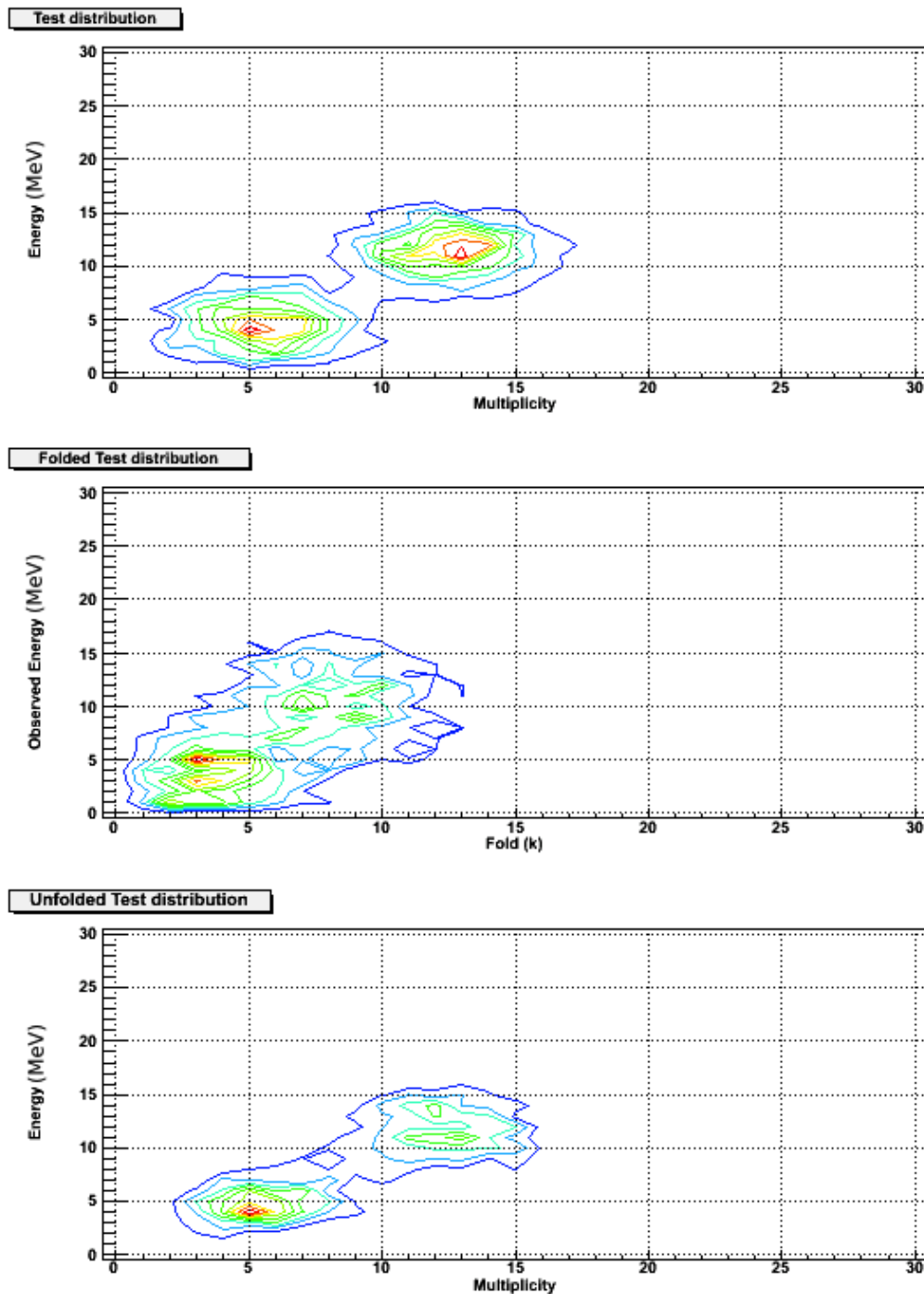


Figure 5.39: Source (top), folded (middle) and unfolded (bottom) distributions for two peaks, with the peak at lower multiplicity having less counts. The separation between the peaks is still visible in the unfolded distribution, but they are distorted and their relative intensity has changed.

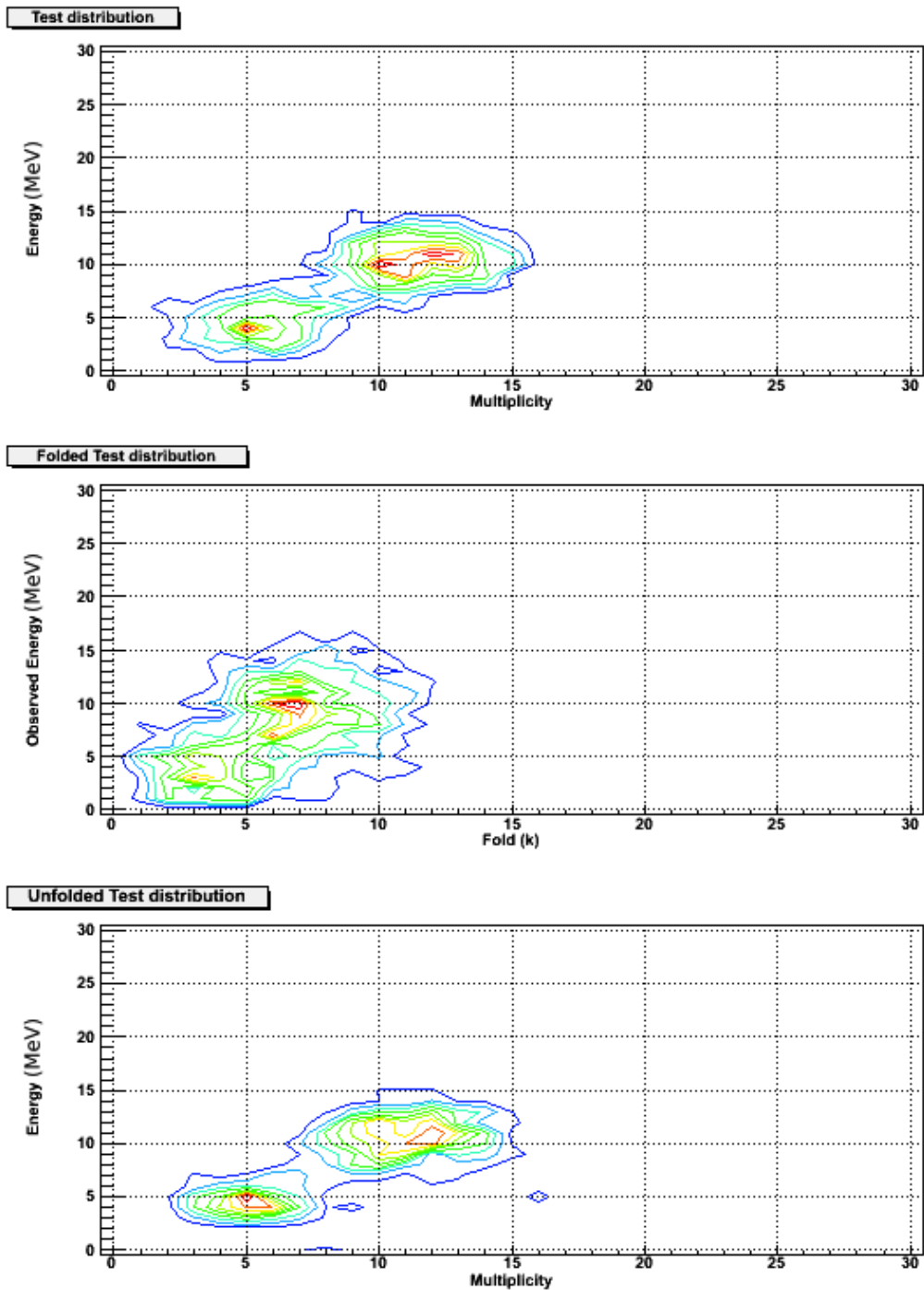


Figure 5.40: Source (top), folded (middle) and unfolded (bottom) distributions for two peaks. The separation is good in the source distribution, but are deformed in the unfolded distribution.

Macroscopic quantities

It is possible to determine the goodness of the unfolding by inspection of global parameters of the distribution: mean value, widths, position of the maximum, shape, ... In particular, we can verify the agreement between the original (k, H) distribution and the refolded matrix from the unfolded result. Figure 5.41 shows the evolution of the average multiplicity of the refolded distribution as a function of the iteration number and how it compares to the source (k, H) .

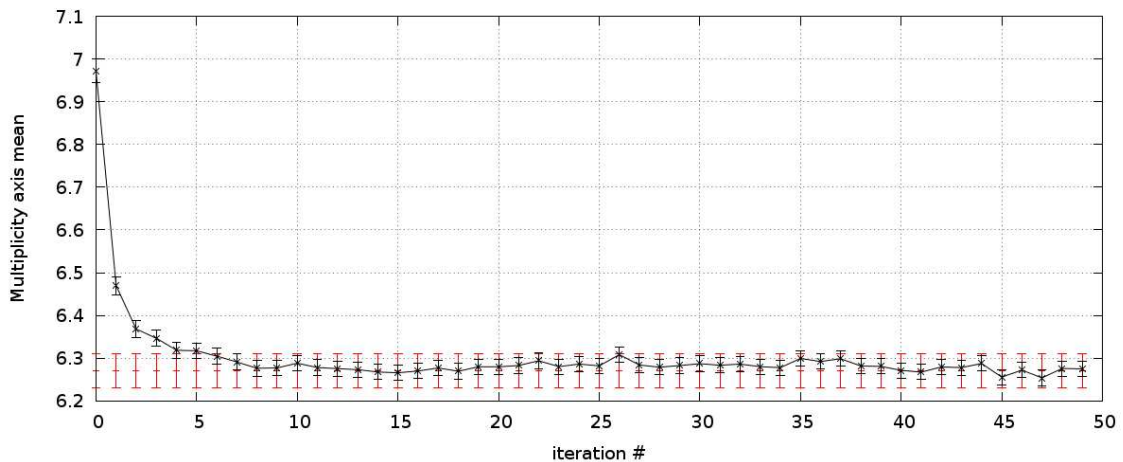


Figure 5.41: Average multiplicity of the refolded distribution (black points) compared to the original (k, H) distribution (red points) as a function of the iteration number. The two quantities agree for iteration above ≈ 8 .

χ^2 between distribution

We can compare two distributions precisely using a measurement of the difference between the two. For two distributions $N^{(1)}(M, E)$ and $N^{(2)}(M, E)$, we calculate $\chi^2 = \sum_{M,E} (N^{(2)}(M, E) - N^{(1)}(M, E))^2$; χ^2 is zero for equal distributions and positive for different distributions.

First, the difference between a test (M, E) distribution (as in 5.31) and the unfold of the folded source has been measured as a function of the iteration number on figure 5.42: the χ^2 drops for the first ≈ 10 iterations, is minimal for $\approx 12 - 15$ iterations and grows again. This suggest that the best unfolding result is obtained for a number of iteration between 10 and 15.

For the experimental distribution, we don't have a distribution to compare the unfolded

response to, but it is possible to compare the source (k , H) distribution to a refold of the unfolded distribution, and compare the two distribution. Figure 5.43 shows the evolution of χ^2 with iteration number. The differences between the distributions decrease exponentially over the ≈ 10 first iterations. Contrary to the test distribution, the χ^2 does not grow at high iteration number but is rather stable. This confirms that at least ≈ 10 iterations are necessary to get a proper unfolding and that additional iteration above ≈ 20 are at best not useful (figure 5.43), and possibly harmful (figure 5.42).

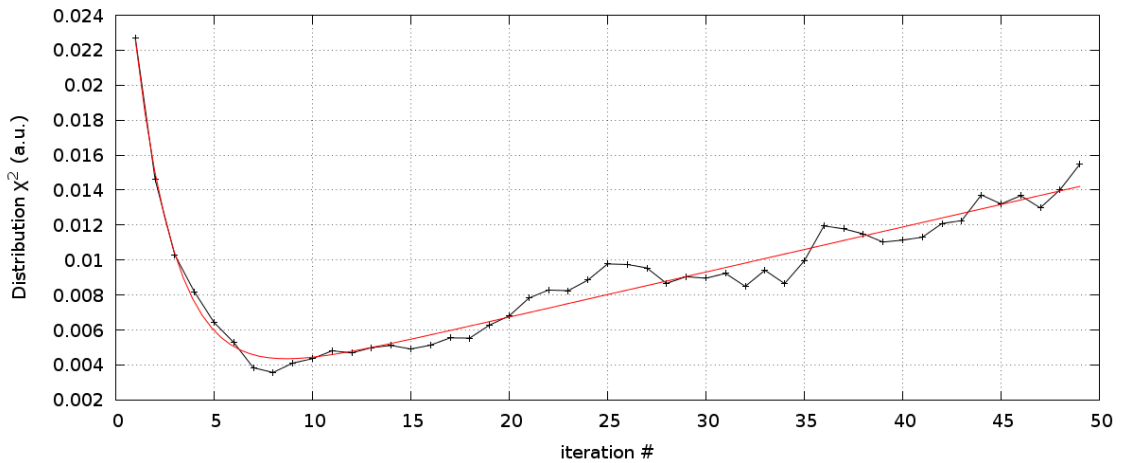


Figure 5.42: χ^2 of the source (test) and unfolded distribution as a function of the iteration number. The red line is an exponential decay plus a linear function fitted on the data (black points).

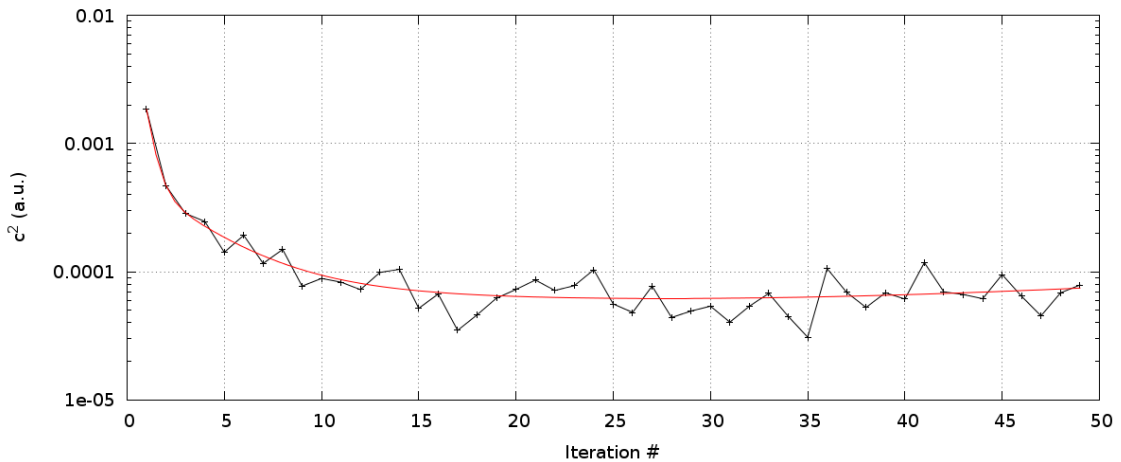


Figure 5.43: χ^2 : difference between the experimental (k,H) distribution and the refolded unfolded distribution, as a function of iteration number. The χ^2 stabilises above $n_{\text{iteration}} \approx 15$. The red line is a double exponential decay fitted on the data. Note the log scale in χ^2 .

Choice of parameters

As we showed, the choice of unfolding parameters is of importance: too much smoothing (via a large pre-scaling) will hide possible sub-structures, while not enough statistics or too many iterations may create artefacts from statistical fluctuations. The *good* set of parameters depends on the entrance distribution, the size of the matrices, the precision of the response, ... it is therefore hard to fix one good set of parameters to perform the unfolding.

Based on the test of the unfolding procedure, we find that the optimum parameters are: about 20 iterations and a pre-scaling factor of the order of 30. But to account for the possible artefacts and consider only the persistent features in the unfolded distribution, we will *scan* over several set of parameters and consider only the characteristics of the unfolded distribution that are independent of the unfolding parameters.

5.10 Experimental Calorimetric measurements

5.10.1 (k, H) distribution

For ^{254}No , we obtained the calorimetric distributions of fold and observed energy : (k, H) , at the two beam energies. We isolated in particular the recoil-gated (k, H) distribution and the recoil- α -gated (k, H) distribution. Figure 5.44 shows the (k, H) distributions for $E_{\text{Beam}} = 219$ and 223 MeV, the recoil- α -gated distributions are shown on figure 5.45. The isomer-gated distributions are on figure 5.46. To obtain these distributions, the selection is done on $\Delta T_{\text{implant - decay}}$ and E_{Decay} in the DSSD, see figure 5.23. They have only about 30 counts in total, while up to 300 were expected. The high thresholds in the DSSD and the issue with correlation explains the poor statistic for isomer events. The unfolding of those events will likely not be relevant, due to the low number of counts.

In figure 5.44 we see that some events have a significant contribution at $(0, 0)$, which correspond to a recoil being detected at the focal plane of the FMA but no γ -ray is detected in Gammasphere; those events account for about 6 % of the population. In both figures 5.44 and 5.45, we also observe events with larger high (k, H) which correspond to event contaminated by random γ -rays, those events, correspond to about 3 % of the total distribution, in agreement with the rate of random γ -rays.

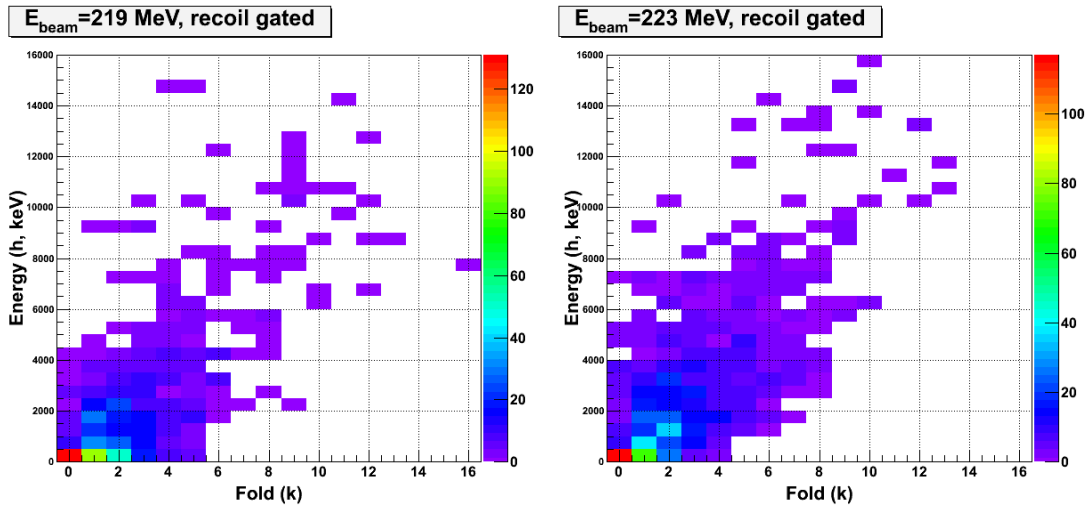


Figure 5.44: Recoil gated (k, H) distributions for $E_{\text{Beam}} = 219$ (left) and 223 MeV (right).

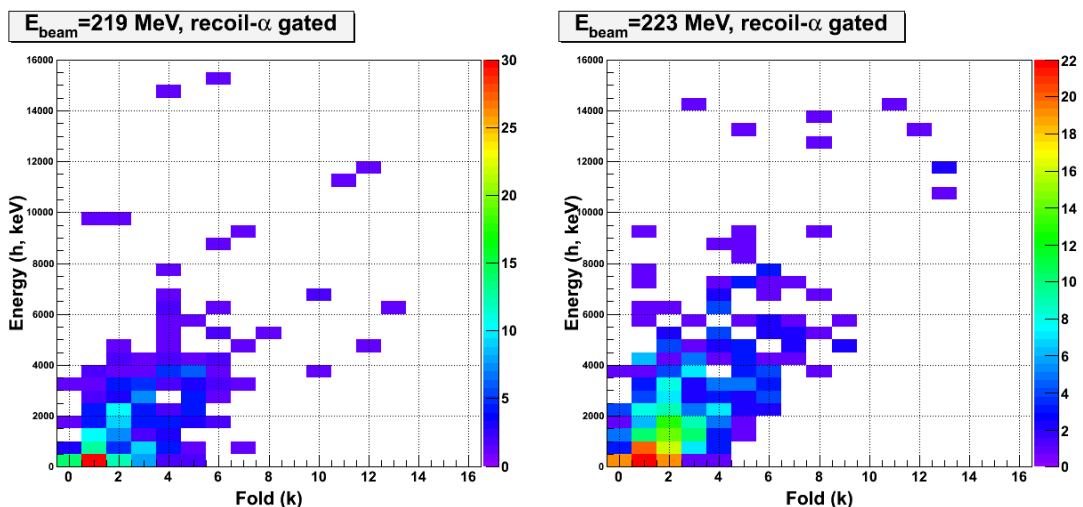


Figure 5.45: Recoil- α gated (k, H) distributions for $E_{\text{Beam}} = 219$ (left) and 223 MeV (right).

5.10.2 Unfolding

The (k, H) distributions are afterward unfolded using the responses as described earlier (see section 5.9). Figure 5.47 shows an example of an unfolded distribution (M, E) , compared to the original (k, H) distribution; plus the refold of the result, in order to check at the folding of the obtained (M, E) distribution reproduces the experimental (k, H) . The unfolding gives the multiplicity and sum energy distribution (M, E) : the number of γ -rays emitted by the nucleus and the total energy carried by those γ -rays.

5.10.3 Multiplicity to Spin and E_{Sum} to E^* conversion

The conversion from Multiplicity and E_{sum} to spin and excitation energy is based on general hypotheses on the formation and γ decay process in the excited nucleus. Figure 5.48 shows the general picture of the γ decay process. The nucleus is supposed to be formed at an excitation energy above the yrast line. It decays first by emitting *statistical* γ that carry an important energy (of the order of 1 MeV) and a small angular momentum ($\approx 0.5 \hbar$); afterward, the γ decay connects with the yrast line or close to yrast bands, and follow it by emitting yrast γ s with smaller energy ($\approx 200 - 600$ keV and larger angular momentum ($2 \hbar$ per γ).

From this model of γ decay, we can separate the multiplicity in two : the statistical and yrast multiplicities; such as $M = n_{\text{stat}} + n_{\text{yrast}}$. From what we described of the angular momentum for each type of γ decay, we can assert the spin of the original state as $I = n_{\text{yrast}} \times \Delta I_{\text{yrast}} + n_{\text{stat}} \times \Delta I_{\text{stat}}$. In practice, we cannot differentiate between yrast and statistical decays, that is why we will use an average value for n_{stat} . This lead to $I = \Delta I_{\text{yrast}} \times (M - n_{\text{stat}}) + \Delta I_{\text{stat}} \times n_{\text{stat}}$. The yrast γ -rays are identified as E2 transition, therefore $\Delta I_{\text{yrast}} = 2 \hbar$.

Statistical γ -rays

The number of statistical γ -rays n_{stat} is extracted from the γ -ray spectrum. The high energy part of the spectrum is consider the range where only statistical *gamma*-rays are detected. Therefore a function describing such γ -rays can be fitted and extrapolated. Comparing the integral of the statistical spectrum to the area of a known transition,, one can extract the ratio number of statistical γ -rays per de-excitation cascade in the nuclei [104, 105]. We did the calculations on a high statistic spectrum from Jurogam [31, 106]. The spectrum was unfolded to remove the Compton contribution and efficiency corrected. We determined

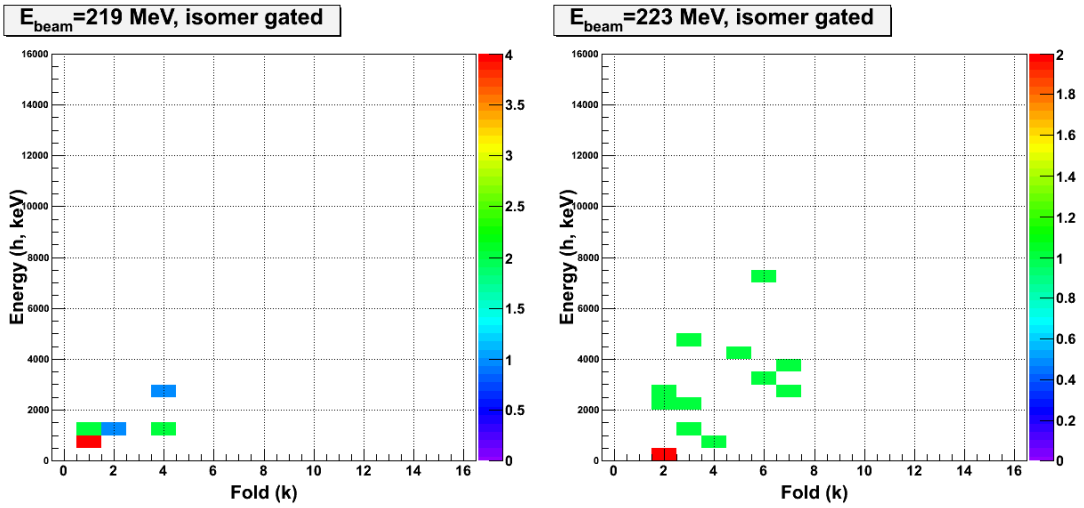


Figure 5.46: Isomer gated (k, H) distributions for $E_{\text{Beam}} = 219$ (left) and 223 MeV (right).

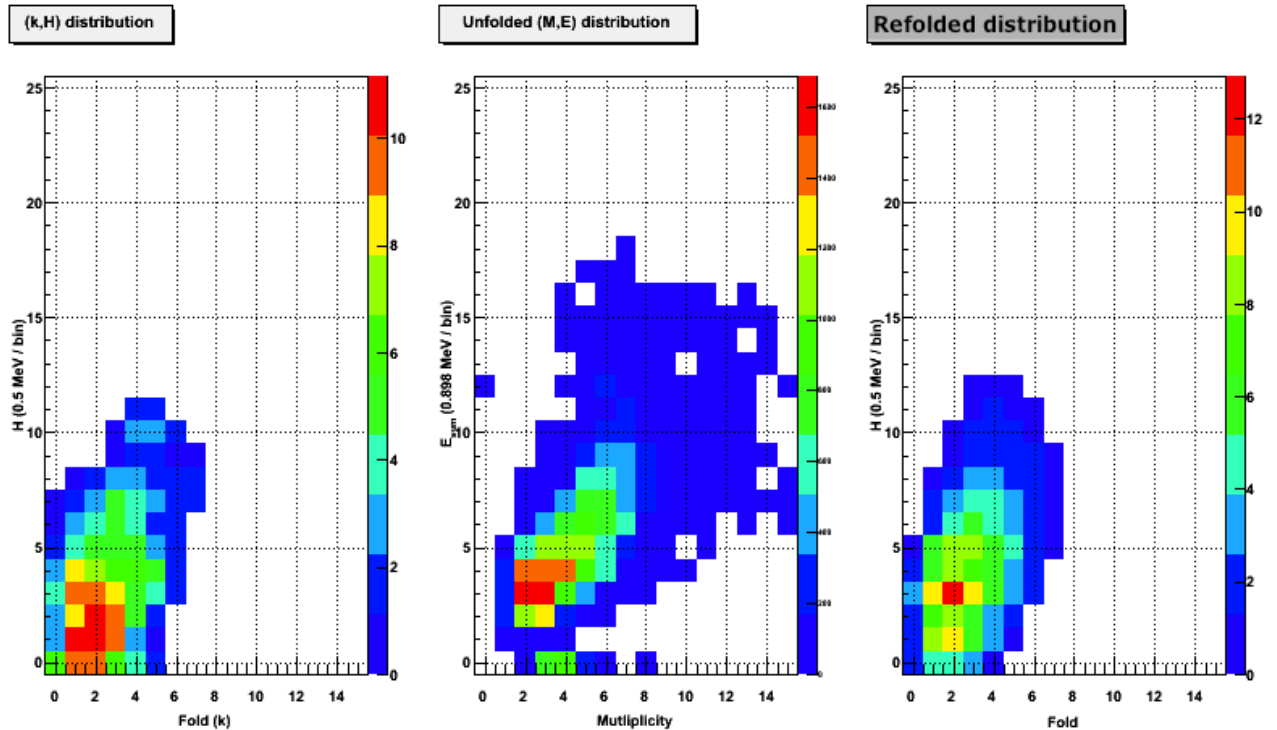


Figure 5.47: Example of unfolded experimental distribution. The original (k, H) distribution is on the left, the unfolded (M, E) distribution is in the centre, a refold of (M, E) is on the right and clearly similar in shape to the original (k, H). The distribution unfolded was the recoil gated (k, H) for $E_{\text{Beam}} = 219$ MeV, unfolded with the response from ^{88}Y .

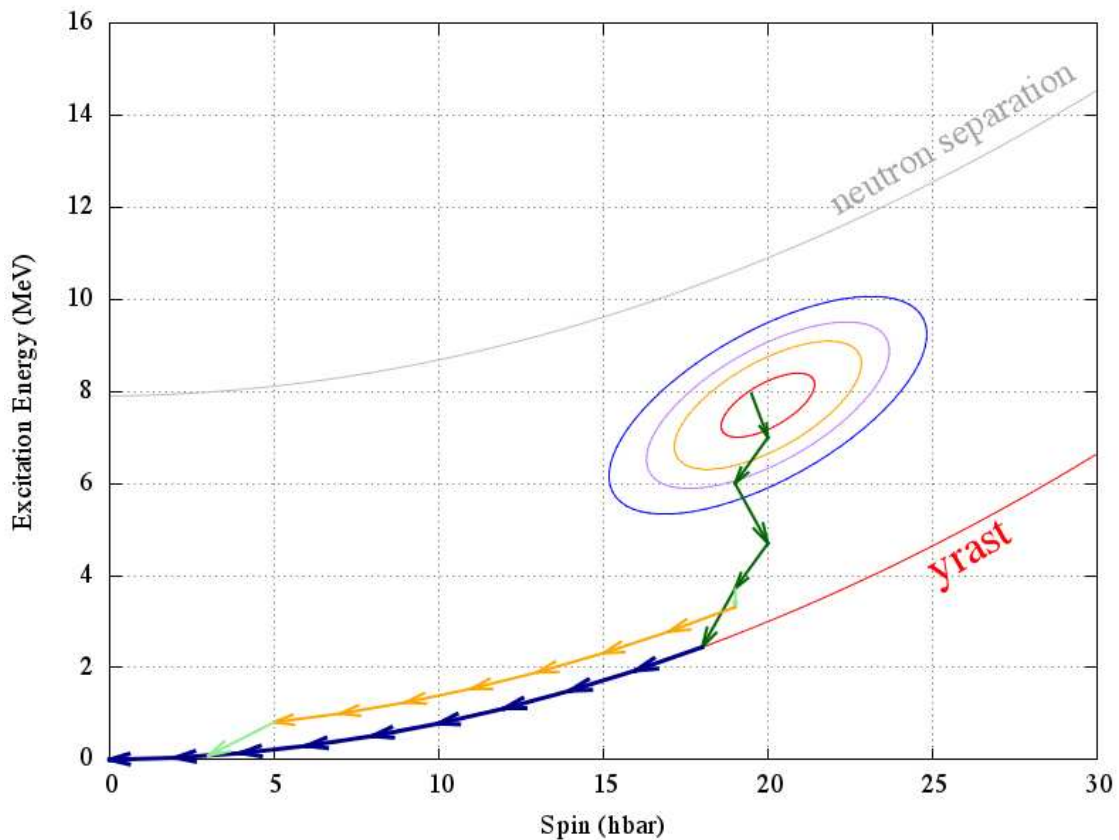


Figure 5.48: Schematic illustration of the γ decay process. The distribution of entry (I, E^*) points is represented by the colour ellipses and a typical yrast γ decay chain is represented: statistical γ -rays in **green** and the rotational band transitions in **blue**. The light **green** and **orange** arrows represent the decay path through an off-yrast band.

that $2.4 \leq n_{\text{stat}} \leq 5.9$ depending on the shape of the statistical spectrum. The higher bound contains non-statistical events and so the actual number of statistical gamma-rays is expected to be much lower than 5.9. Previous experimental measurement suggests $n_{\text{stat}} = 3$ [107]. A simple statistical model can be used to check the compatibility of n_{stat} with the resulting entry distribution.

For our experiment, we obtained $n_{\text{stat}} = 3.0 \pm 0.4$. We also assume $\Delta I_{\text{stat}} = 0.25 \pm 0.50 \hbar$.

Effect of conversion electron

The electron conversion of some transitions, for example at the bottom of the yrast band, means that some γ -rays will not contribute to the observed multiplicity and E_{sum} . To correct for that, we introduce the averages spin and energy carried out by the converted electrons: I_{CE} and E_{CE} . The excitation energy and spin are corrected for the conversion electrons by adding these quantities:

$$I = \Delta I_{\text{yrast}} \times (M - M_{\text{stat}}) + \Delta I_{\text{stat}} \times M_{\text{stat}} + I_{CE} \quad (5.3)$$

$$E^* = E_{\text{sum}} + E_{CE} \quad (5.4)$$

The contribution of electrons is calculated according to the known structure of ^{254}No [25, 26, 95–97, 108]. The three bands listed are not actually the only bands in ^{254}No , but they capture most of the γ flux and it is a good approximation to evaluate the contribution of electrons. The table 5.8 gives the contribution of the conversion electron in three bands of ^{254}No .

Band	Population (%)	I_{CE}	E_{CE} MeV
g.s.	44	7.9	0.594
8^-	30	6	0.896
3^+	26	13.6	1.256
Total	100	8.8	0.857

Table 5.8: Table of coefficients for the electron contribution to the energy and spin.

The parameters chosen for the multiplicity to spin transformation are $\Delta I_{\text{yrast}} = 2 \hbar$, $\Delta I_{\text{stat}} = 0.25 \hbar$, $n_{\text{stat}} = 3.0$, $I_{CE} = 8.8 \hbar$ and $E_{CE} = 857$ keV.

Effect of isomers

For isomer events, the γ decay as described previously is changed: the decay-path is *stuck* in a level at a finite spin and energy. Figure 5.49 shows the decay for an isomer.

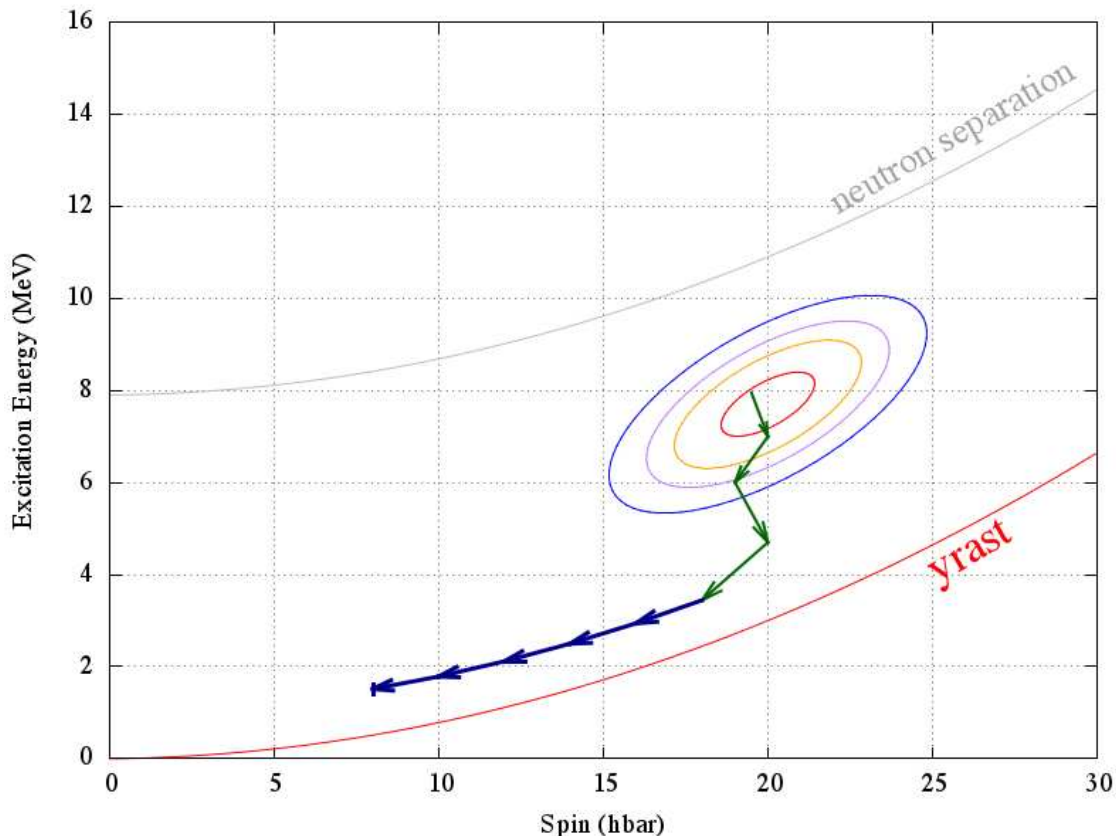


Figure 5.49: Schematic illustration of the γ decay process. The distribution of entry (I, E^*) points is represented by the colour ellipses and a typical γ decay chain leading to an isomer is represented: statistical γ -rays in green and the rotational band transitions in blue. The γ decay stops at a finite excitation energy and spin.

In that case, the prompt detection of γ -rays will miss all the transitions below the long lived state in which the decay is *stuck*. An additional correction is needed for those events: the previous formulae are modified into: $I = \Delta I_{\text{yrast}} \times (M - n_{\text{stat}}) + \Delta I_{\text{stat}} \times n_{\text{stat}} + I_{CE} + I_{\text{isomer}}$ and $E^* = E_{\text{sum}} + E_{CE} + E_{\text{isomer}}$. One notes that, if not properly corrected with I_{isomer} and E_{isomer} , isomer events will be assigned to a lower spin and excitation energy in the entry distribution. This placement will be incorrect, for up to 30 % of events in the case of ^{254}No . However they do not affect the region of interest for the determination of the fission barrier.

5.11 Entry distribution

Following the procedure described above, the (k, H) distributions are unfolded and transformed into a (I, E^*) distribution. Figure 5.50 shows an example of the unfolded (M, E) distribution and the corresponding entry distribution. The points in the entry distribution will be compared to E_{yrast} , S_n and E_{max}^* (see section 4.1.1), and the evolution of the distribution with spin will be investigated to determine the position of the saddle energy in the next chapter.

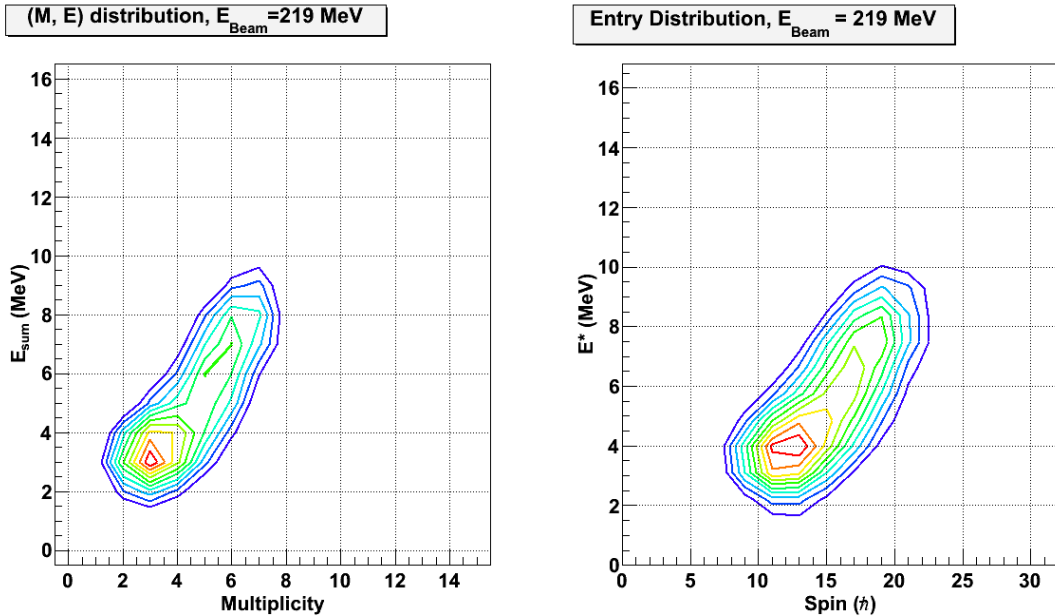


Figure 5.50: (Left) Multiplicity and sum energy distribution (right) and the corresponding entry distribution (spin, excitation energy).

5.11.1 Comparison with previous measurement

The previous measurement by P. Reiter *et al.* [98] established a lower limit on the fission barrier height, via the entry distributions at beam energies of 215 and 219 MeV.

Experimental setup

The previous measurement of ^{254}No was also performed with Gammasphere and the FMA, but some details of the experimental setup were significantly different than for the present experiment : The number of detector modules was different (101 modules, against 101 full modules – Ge and BGO shield – plus 7 modules with only the BGO shield in the present work). Moreover, a different set of absorbers were placed before the detectors: Cu and Ta (against Cu, Ta and Cd for our work), which increases the detection efficiency at low energy ($\lesssim 200$ keV) – in particular, the X-rays will be more efficiently detected. Finally, the trigger mode was different – this prevented the loss due to data falling off the bus – with a Gammasphere trigger requiring $n_{\text{clean Ge}} \geq 2$. This is a very strong requirement in the trigger and that will impact the shape of the distribution largely by favouring higher multiplicity and energy.

The response in multiplicity and energy of the previous measurement show clearly a higher detection efficiency in the original measurement, with a calorimetric efficiency of 70.2 % (63 % for our work). See figure 5.51. The change in efficiency comes not only from the change in absorbers and trigger mode, but the *ageing* of the detectors, in particular the photo-multiplier tubes of the BGOs, is a source of decrease in efficiency. Our responses have lower resolutions than the previous one, which will affect the unfolded distribution, in particular this will lead to unresolved sub-structures and larger width of the distributions.

Analysis

At the time of the previous experiment, only the *yrast* rotational band was known for ^{254}No and the electron conversion was considered only for this band in the multiplicity to spin conversion. For those reasons, the published entry distribution in [98] will be overall in agreement with our measurement but not necessarily exactly like it. It is possible to compare the unfolded (M, E) distributions and check if the data are compatible.

Figure 5.52 compares the (M, E) distribution for $E_{\text{Beam}} = 219$ MeV from [98] and the equivalent distribution from our experiment with a software requirement of 2 clean Ge. No multiplicity to spin conversion has been done. The two distributions have strong similarities:

- The energy range is about the same for the two distribution: from $\approx 1.5 - 2$ to ≈ 10 MeV.

- The distribution in multiplicity are very similar: in the 2 to 11 range, with a maximum at ≈ 6.5 .
- The average energy of the two distribution are about the same: 5.2 MeV for P. Reiter, 5.3 MeV for our work, and the maximum of the distributions are 5.7 MeV and 6.0 MeV respectively.
- In the original measurement, the average multiplicity is 7 against 6.5 in our work.

In short, for two distributions taken in the same conditions ($n_{\text{clean Ge}} \geq 2$), the unfolded (M, E) distribution are very similar, indicating the agreement between the two data set and validating the unfolding procedure.

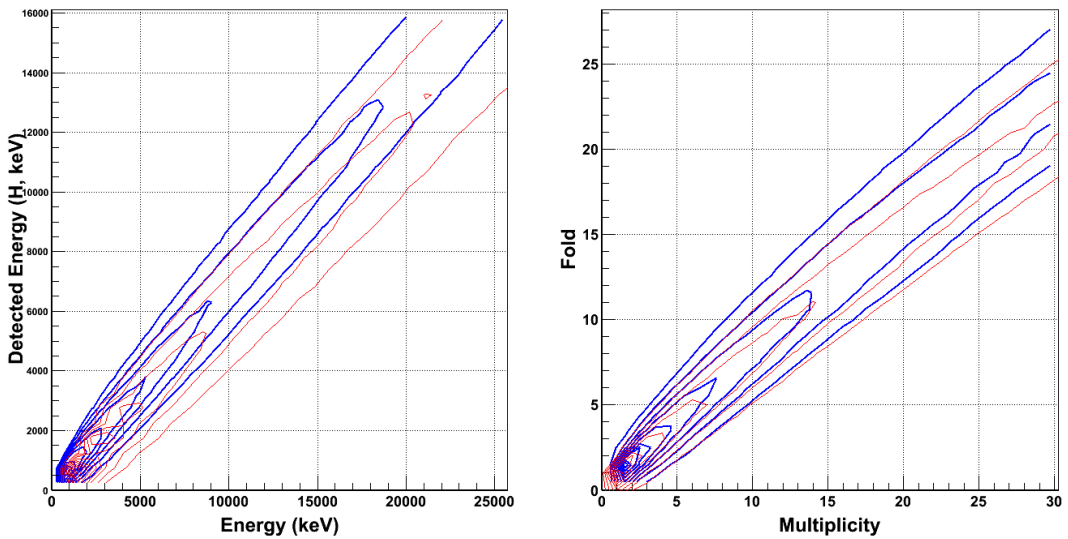


Figure 5.51: Comparison of the energy (left) and multiplicity (right) responses for the entry distribution measurement by P. Reiter (blue) and our work (red). The previous measurement clearly had a better calorimetric efficiency.

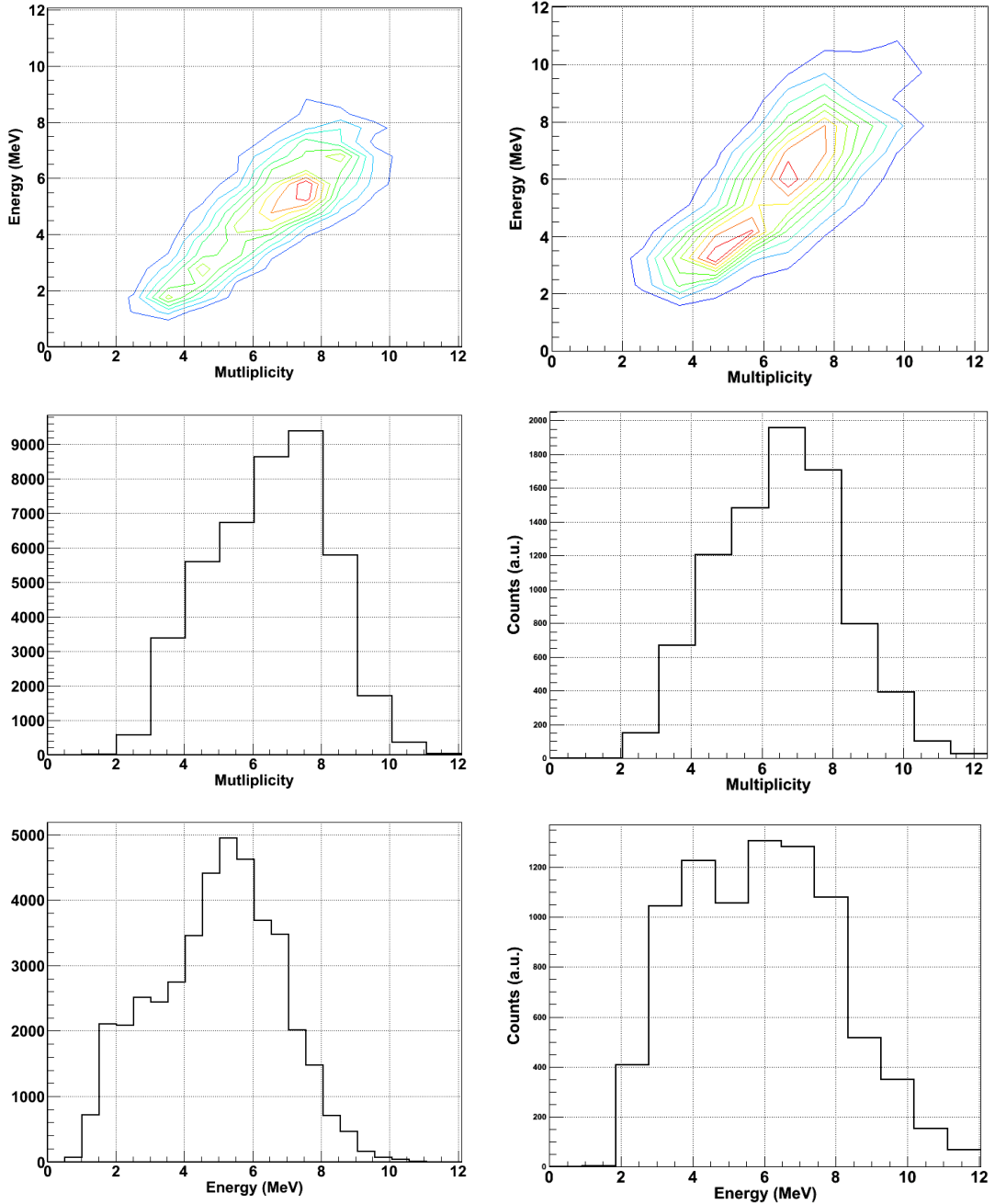


Figure 5.52: Comparison of the (M, E) distribution measured in P. Reiter's experiment (left) and our work (right) : distribution (top), multiplicity projection (middle) and energy projection (bottom).

Chapter 6

Entry distribution and fission barrier of ^{254}No

In this chapter, we will examine the entry distribution produced following the procedures described in sections 5.8, 5.9 and 5.10 and determine the height and spin dependence of the fission barrier.

6.1 Entry distribution: measurement and analysis

6.1.1 Measured unfolded distributions

The (k, H) distributions are unfolded and converted to entry distribution according to the transformation explained earlier – see sections 5.8, 5.9 and 5.10. Figures 6.1 and 6.2 show the entry distributions for recoils, α and isomer-gated events. As mentioned in section 5.9.3, we will analyse the results of several unfoldings for each (k, H) distribution, with iteration numbers between 10 and 20 and different scalings; this to avoid any artefact that a particular set of unfolding parameter could create.

Contribution of the isomers to the entry distribution

In the recoil-gated distribution, the isomeric events are unfolded using the same parameters as for the general distribution. This is technically incorrect: γ cascades feeding isomeric states will yield a lower value of spin and excitation energy, since the isomer decays outside

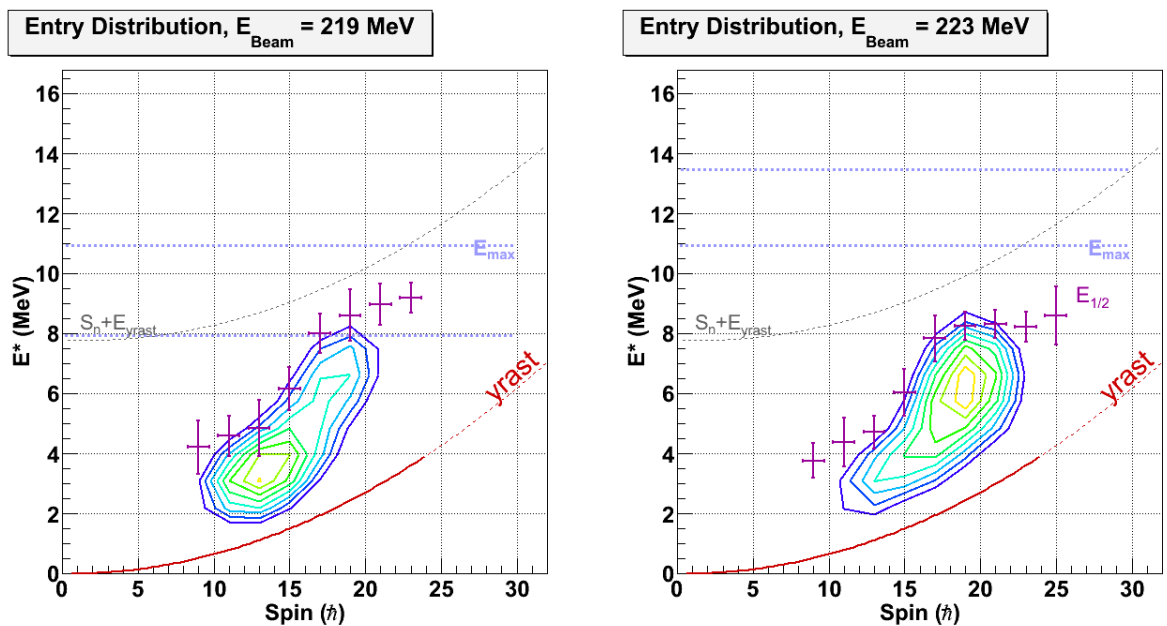


Figure 6.1: Entry distributions for $E_{\text{Beam}} = 219 \text{ MeV}$ (left) and 223 MeV (right) for recoil-gated events, unfolded with ^{88}Y statistically built response. The $yrast$ line is drawn in red, the neutron separation is the dotted line in gray and the range of maximum excitation energy is marked with two dotted blue lines. For each spin bin, the point of half maximum $E_{1/2}$ is marked.

of Gammasphere (at the FMA focal plane). The isomer-gated entry distributions allow us to determine where on the (I, E^*) distribution the isomer events lie – figure 6.3. The isomer-gated distributions show that the associated events sit at low energy ($\approx 2 - 4$ MeV) and spin ($\approx 5 - 17 \hbar$). Below the average of the recoil or α -gated distribution. Therefore, γ cascades populating the isomers contribute to the entry distribution at artificially low spin and excitation energy, and will not modify its profile at high (I, E^*) , which is where we expect to see effects of the fission barrier. However, the average and maximum of the distribution could be shifted down by those events. But we will see that the isomer effect is small in the spin range of interest for our measurement.

6.1.2 Analysis of the Entry Distribution

To analyse and qualitatively compare the entry distributions, we need to choose specific observables to look at and be able to quantitatively compare different distribution. We choose values that give information on the shape of the distribution and how it extends.

Global quantities

We first consider quantities that are *global*:

Position of the maximum: The first quantities of interest is the point with maximum population: $(I, E^*)_{\max}$.

Average Spin and Energy: The projections on the I and E^* axes lead to an average spin and excitation energy that is, *a priori*, different from the position of the maximum.

Width and asymmetry of the distribution: Finally, the distribution extends in the spin and excitation energy in a certain way, characterised by the width of the projected distribution and the asymmetry (measured with the *skewness*, which is the ratio of the third moment of the distribution over the cube of the standard deviation).

These global quantities are *basic* and simple to extract but give us very valuable information on the distribution. Table 6.1 gives these values for the recoil-gated distributions. We see that increasing the beam energy increases the average spin by $2.5 \hbar$ and changes the position of the maximum spin from $13 \hbar$ to $19 \hbar$. The average energy is increased by 1 MeV, the

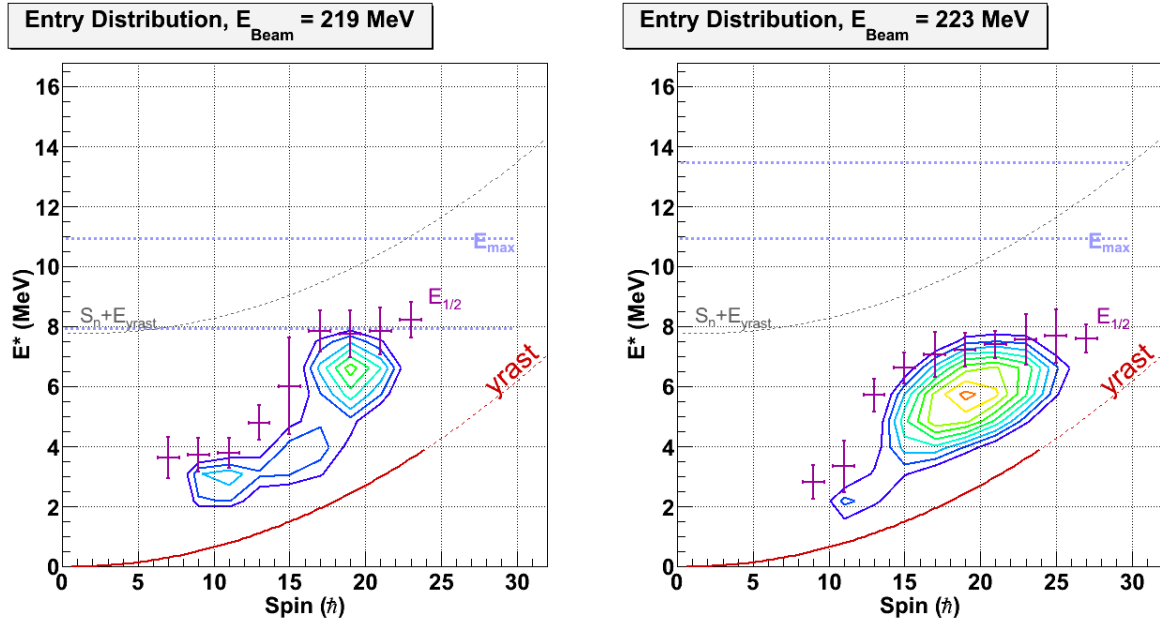


Figure 6.2: Entry distributions for $E_{\text{Beam}} = 219 \text{ MeV}$ (left) and 223 MeV (right) for α -gated events, unfolded with ^{88}Y statistically built response. The distribution at $E_{\text{Beam}} = 219 \text{ MeV}$ has only 51 % of the statistics at $E_{\text{Beam}} = 223 \text{ MeV}$.

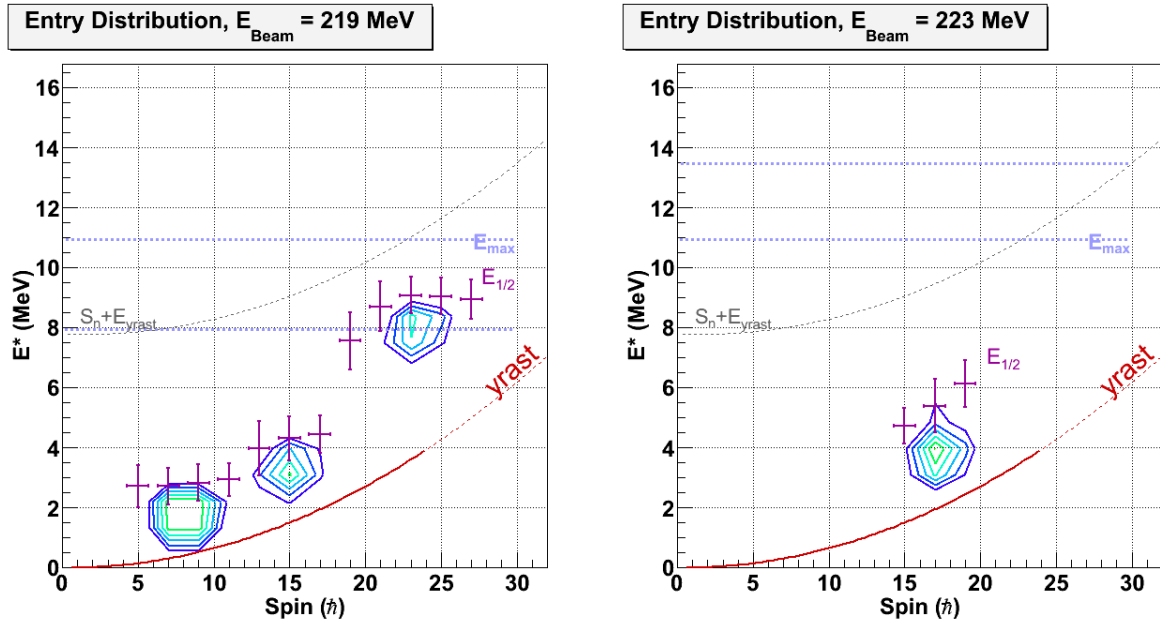


Figure 6.3: “Entry distributions” for $E_{\text{Beam}} = 219 \text{ MeV}$ (left) and 223 MeV (right) for isomer-gated events, unfolded with ^{88}Y statistically built response. The very low statistic of isomer events makes it difficult to interpret the entry distribution, but demonstrates that they are artificially shifted in spin and energy.

E_{Beam} (MeV)	219	223
$(I, E^*)_{\text{max}}$	$(13 \pm 0.31, 3.1 \pm 0.2)$	$(19.3 \pm 0.7, 6.3 \pm 0.5)$
Average spin (\hbar)	15.9 ± 0.6	18.3 ± 0.7
Spin width (\hbar)	4.0 ± 0.2	4.17 ± 0.1
Spin Skewness	0.25 ± 0.1	0.0 ± 0.1
Average energy (MeV)	5.2 ± 0.1	6.2 ± 0.2
Energy width (MeV)	2.7 ± 0.1	3.1 ± 0.1
Energy Skewness (MeV)	1.2 ± 0.3	0.8 ± 0.1

Table 6.1: Global characteristics of the recoil-gated entry distribution. The values are average over several unfold with ^{88}Y response and different number of unfolding iterations and pre-scaling factor. The error bars reflects the dispersion of values for different unfolds.

maximum energy is up by 3 MeV. Furthermore, the distribution gets more *symmetric* at higher beam energy.

α -gated events show the same behaviour for the average values, but the maximum point does not change and the shape of the distribution is very different. The change in shape can be explained in part by the better selectivity of the α -tagging (rejection of possible contamination) and mostly low statistics (The α -gated distribution have 60 % less statistics than the recoil-gated ones, see section 5.6.2). Table 6.2 give the values for α -gated entry distributions.

E_{Beam} (MeV)	219	223
$(I, E^*)_{\text{max}}$	$(18.7 \pm 0.9, 6.2 \pm 0.8)$	$(19 \pm 1, 5.9 \pm 0.3)$
Average spin (\hbar)	16.4 ± 0.1	19.2 ± 0.1
Spin width (\hbar)	4.3 ± 0.2	4.9 ± 0.1
Spin Skewness	-0.1 ± 0.2	-0.1 ± 0.1
Average energy (MeV)	5 ± 0.1	6.5 ± 0.1
Energy width (MeV)	2.2 ± 0.1	3.5 ± 0.1
Energy Skewness (MeV)	0.7 ± 0.3	0.9 ± 0.1

Table 6.2: Global characteristics of the α -gated entry distribution.

Spin dependent quantities

In addition to the global characteristics of the distribution, we are particularly interested in the spin dependence of the energy distribution. For this purpose, we will look at the

projection on the excitation energy axis for each spin *slice* (the spin slices are $2 \hbar$ wide because of the multiplicity to spin transformation that multiplies M by 2). For each spin slices, we will look at similar quantities: average excitation energy, distribution width, ...

Evolution of spin population As hinted from the average and width of the spin distribution, the spin increases with beam energy: the average spin is higher at higher beam energy. However, the comparison of the spin population on figure 6.4 shows that the two spin population both fall to 1/10 of the maximum above spin $26 \hbar$. This behaviour is

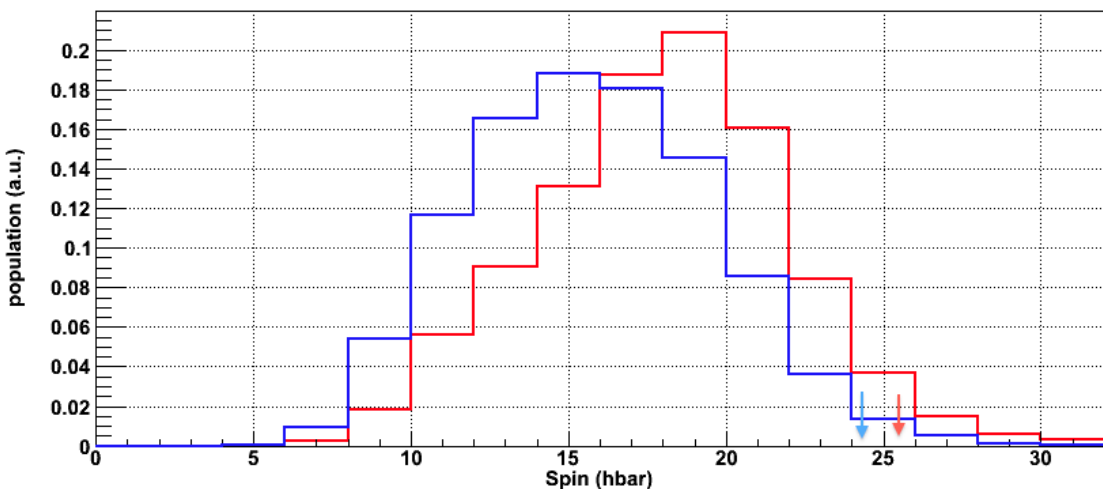


Figure 6.4: Spin distribution profile for $E_{\text{Beam}} = 219$ MeV recoil gated (blue) and $E_{\text{Beam}} = 223$ MeV recoil gated (red). The blue and red arrows mark the spins for which the distribution at $E_{\text{Beam}} = 219$ and 223 MeV falls to 10 % of the maximum.

an indication that a limit is reached in ^{254}No since adding more energy in the reaction increases the average spin, but does not increase the maximum spin by much.

Half maximum points A key quantity we are examining is the half maximum energy $E_{1/2}$, i.e. the energy at which the distribution falls below half of its maximum. In particular, we are looking above the maximum of the distribution – the way to determine this energy is described in appendix F. In previous measurements, the $E_{1/2}$ points have been used as estimates of the fission barrier height [71, 98] – or at least a lower limit.

We will also consider E_{max} , the energy with the maximum population at each spin. Figure 6.5 shows the energy distributions at spin $20 \hbar$ for the recoil-gated entry distributions at $E_{\text{Beam}} = 219$ and 223 MeV.

Saturation of energy with spin In the plots of $E_{1/2}$ and E_{\max} as a function of spin, we observe a saturation of these quantities at high spins – see figures 6.6 and 6.7. For spins 17 to 23 \hbar there is a clear saturation of $E_{1/2} \approx 8$ MeV and $E_{\max} \approx 6$ MeV, which is visible in the recoil and α -gated distributions.

This is a clear indication that although the increased beam energy makes possible a larger excitation energy in the nucleus, the excitation energy is limited. This saturation is attributed to **fission**: with E^* getting closer to E_{Saddle} , the fission width becomes important and reduces the γ -decay probability $P_\gamma = \Gamma_\gamma / (\Gamma_\gamma + \Gamma_{\text{fission}})$.

Below spin $\approx 15 \hbar$, the $E_{1/2}$ points do not have a trend following the saddle energy. This can be explained by several factors: The entry distribution could be artificially shifted down to lower excitation energy by isomer events, as suggested by figure 6.3. The lowest spin distribution could be depleted by the 3 neutron evaporation channel. Finally, in the excited nucleus, at low spin, the $E^* - E_{\text{rot}}(I)$ is larger which translates into a larger temperature T , therefore the neutrons emitted by the $^{255}\text{No}^*$ at low spins to form ^{254}No will remove more kinematic energy following $\langle K_{\text{neutron}} \rangle \propto T$ [109].

For spins $\gtrsim 25 \hbar$, we do not consider the $E_{1/2}$ or E_{\max} points relevant as less than 5 % of the total population is above spin $25 \hbar$, the width of the energy distribution increases up to 4 MeV, larger than the response width (≈ 2 MeV) and the values are not independent on the unfolding (in particular in figure 6.7). Moreover, these points originate from the events suffering from random summing in the (k, H) distributions. The behaviour of those points is likely a pure effect of low statistics in the tail of the distribution and random effects in the unfolding.

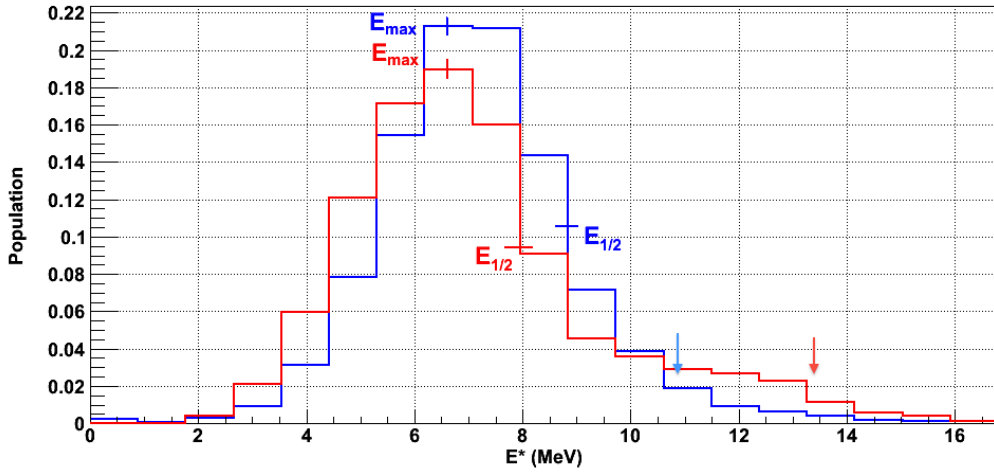


Figure 6.5: Energy distribution at spin $20 \hbar$ for the recoil-gated entry distributions at $E_{Beam} = 219$ (blue) and 223 MeV (red). The $E_{1/2}$ and E_{max} points of the distributions are marked. The E_{max} values are the same for the two beam energies (7 MeV), the $E_{1/2}$ values differ (8 and 9 MeV). The blue and red arrows mark the energies for which the distribution at $E_{Beam} = 219$ and 223 MeV falls to 10 % of the maximum.

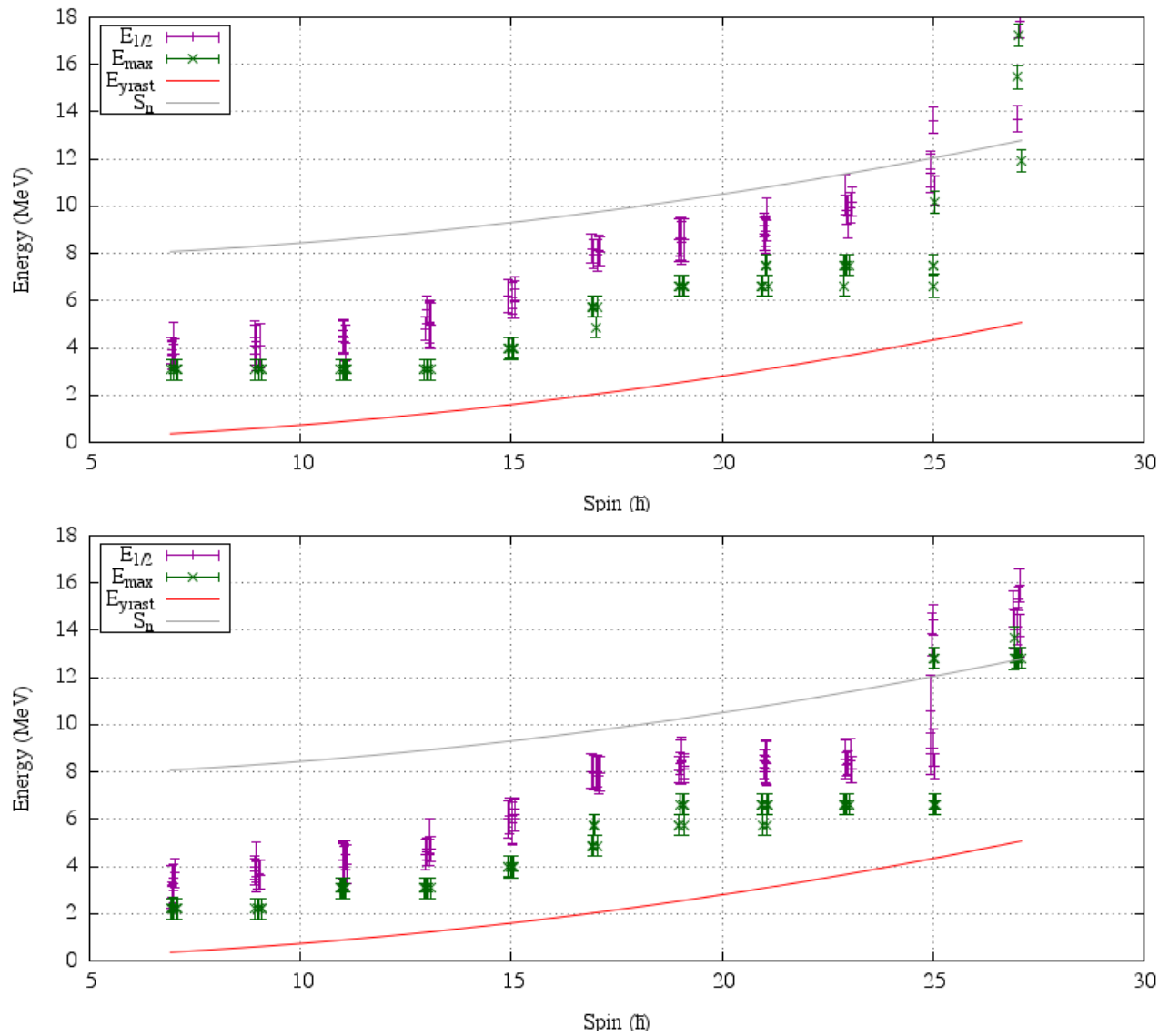


Figure 6.6: Saturation of the $E_{1/2}$ (purple) and E_{max} (green) with spin for E_{Beam} (Top) 219 MeV (Bottom) 223 MeV in recoil-gated distributions. The yrast line is shown in red and the neutron separation energy in gray. Points are gathered from different unfolds and dispersed around the corresponding spin for better visibility.

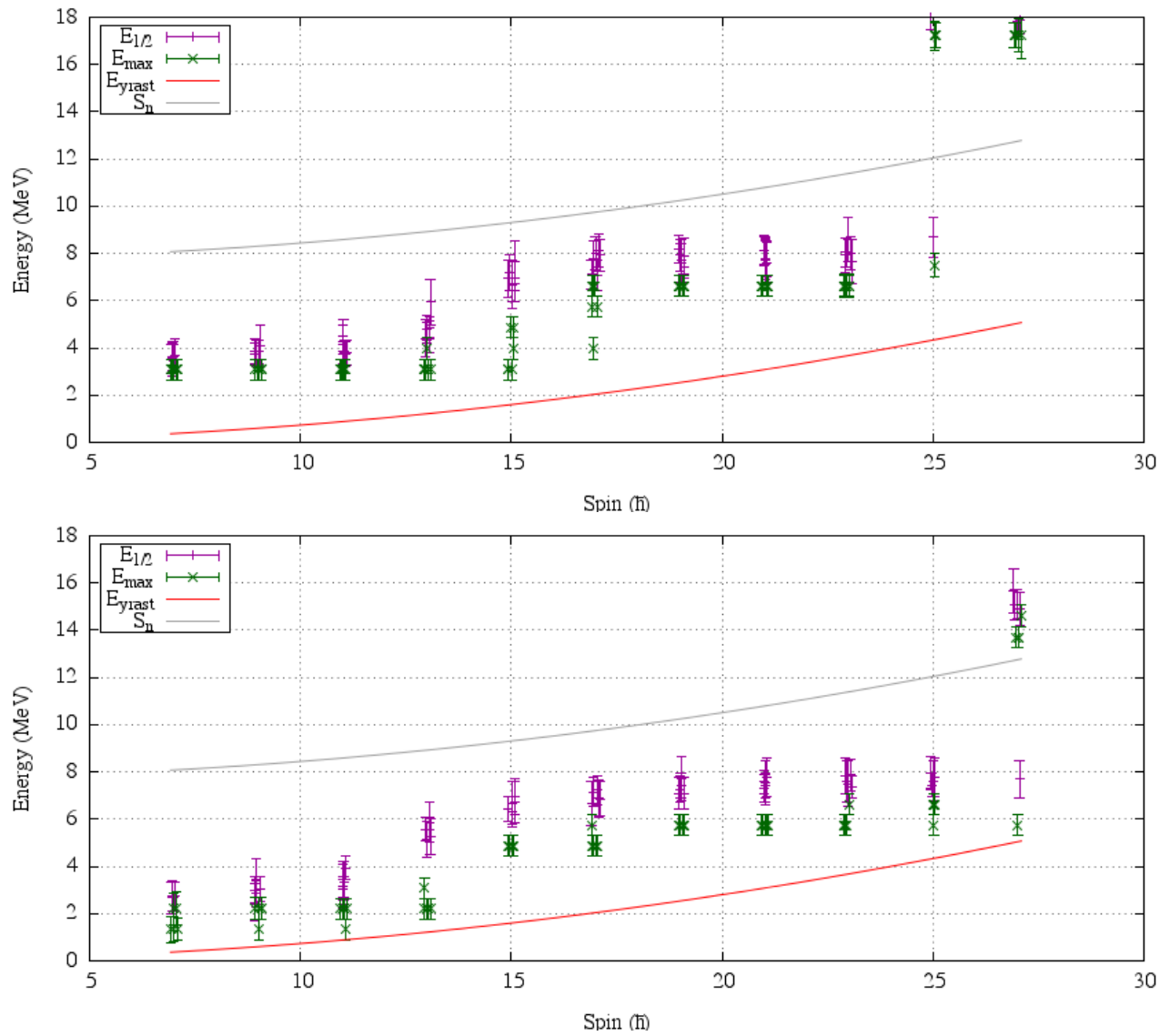


Figure 6.7: Saturation of the $E_{1/2}$ (purple) and E_{max} (green) with spin for α -gated distribution at E_{Beam} (Top) 219 MeV (Bottom) 223 MeV. The yrast line is shown in red and the neutron separation energy in gray. Like in figure 6.6, the energies saturates at respectively 8 and 6 MeV from spin 14 to $\approx 24 \hbar$.

6.2 Extraction of the saddle energy

From the experimental data, it is possible to extract the value of E_{saddle} , which can indirectly give the height of the fission barrier $B_f = E_{\text{saddle}} - E_{\text{yrast}}$; in particular, at spin 0, $B_f(0) = E_{\text{saddle}}(0)$.

6.2.1 Fit on $E_{1/2}$

We assume that the experimental $E_{1/2}$ points in the distribution correspond to the theoretical $E_{1/2}$ points (see section 3.2.5) for which $P_\gamma(E_{1/2}) = 0.5$. Therefore, using the calculated relation $\Delta(I) = E_{1/2}(I) - E_{\text{saddle}}(I)$, we can deduce the height of the saddle energy and its spin dependence.

We will fit the saddle parametrization $E_{\text{saddle}} = B_f(0) + \frac{I(I+1)}{2\mathcal{J}_{\text{saddle}}}$ (see also equation 2.6) on the experimental $E_{1/2} - \Delta(I)$ points, with $\Delta(I)$ chosen from the ones calculated in chapter 3. We restrict the fit to the points where a saturation of $E_{1/2}(I)$ is observed because it is the only range where we expected a direct relation between $E_{1/2}$ and E_{Saddle} . This means the behaviour of E_{Saddle} at lower spins and in particular the value of $B_f(0)$ will be extrapolation. Figure 6.8 shows the fit on recoil-gated data.

We found $B_f(0) = 6.2 \pm 0.8$ MeV, in good agreement with macroscopic-microscopic model calculation (6.76 MeV [1, 2]) and $\mathcal{J}_{\text{Saddle}} = 145 \pm 60 \hbar^2/\text{MeV}$ for the saddle moment of inertia, just between the rigid body value ($180.7 \hbar^2/\text{MeV}$) and the value calculated in the HFB framework ($140 \hbar^2/\text{MeV}$) or the scaled SD band moment of inertia ($142 \hbar^2/\text{MeV}$, see section 3.1). We note that the value of $\mathcal{J}_{\text{Saddle}}$ is the same for all spins. Table 6.3 gives the results of the fit on different data set (beam energies and α -gated) as well as the average value.

6.2.2 Mapping the best parameters

We propose to visualise what parameters for the saddle energy $B_f(I = 0)$ and $\mathcal{J}_{\text{saddle}}$ are compatible with our experimental data. We establish a measure of the compatibility with the experimental data and $E_{\text{saddle}}^{B_f(0), \mathcal{J}_{\text{saddle}}}$: χ^2 is defined in 6.1 as the squared difference between our experimental $E_{\text{saddle}} = E_{1/2} - \Delta(I)$ and a calculated $E_{\text{saddle}}^{B_f(0), \mathcal{J}_{\text{saddle}}}$.

$$\chi^2 = \sum_0^n \left((E_{1/2}^{(n)} - \Delta(I^{(n)})) - E_{\text{saddle}}^{B_f(0), \mathcal{J}_{\text{saddle}}}(I^{(n)}) \right)^2 \quad (6.1)$$

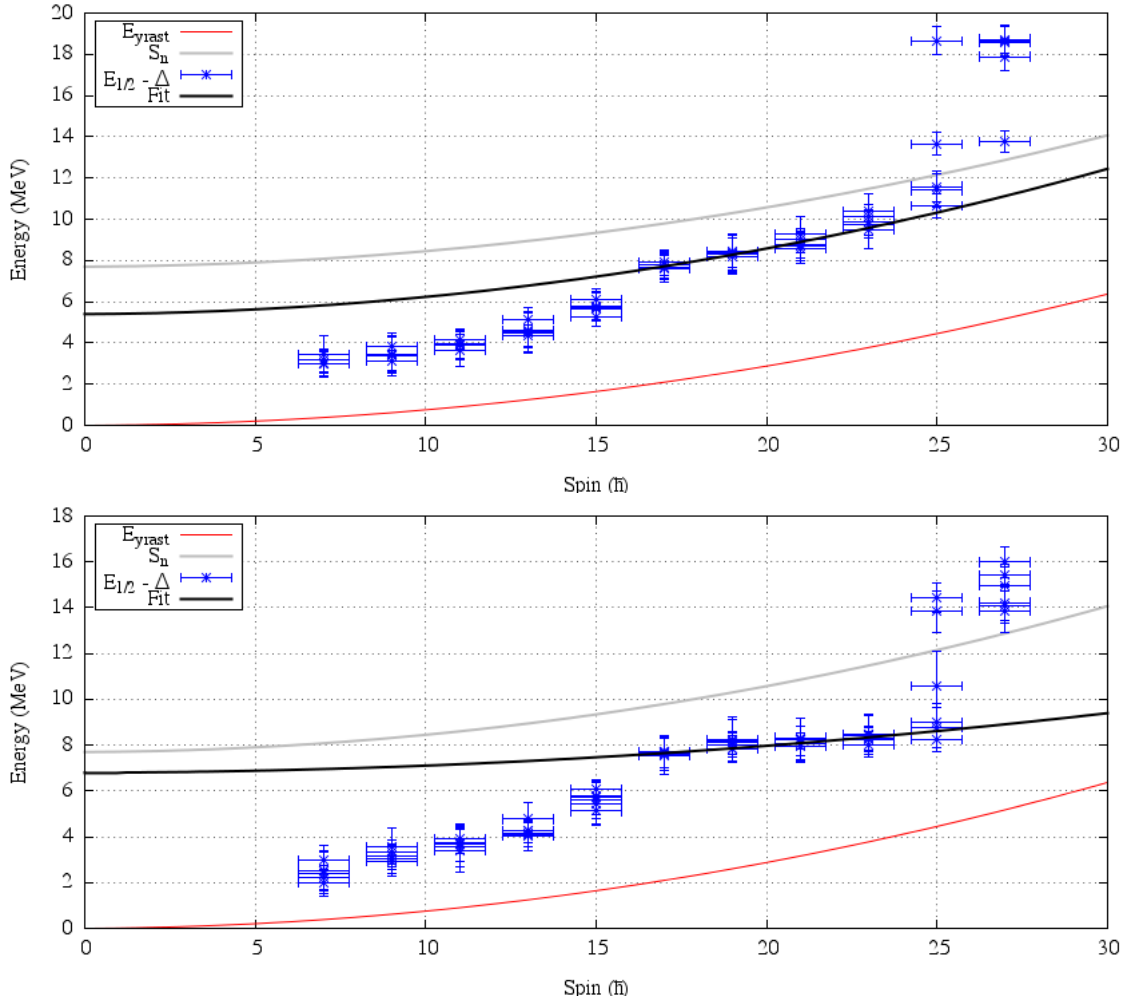


Figure 6.8: Fit of the $E_{1/2} - \Delta \approx E_{\text{saddle}}$ experimental data point for recoil gated events at $E_{\text{Beam}} = 219$ MeV (top) and 223 MeV (bottom). The yrast line is represented in red and the neutron separation threshold in gray. The data points (from several unfolding results) are in blue, the thick black line is the fitted E_{saddle} , for which the parameters are given in table 6.3.

Data set	$B_f(0)$ (MeV)	MoI (\hbar^2/MeV)
$E_{\text{beam}} = 219$ MeV	5.41 ± 0.5	66 ± 25
$E_{\text{beam}} = 219$ MeV, α gated	5.7 ± 0.6	113 ± 35
$E_{\text{beam}} = 223$ MeV	6.8 ± 0.5	179 ± 25
$E_{\text{beam}} = 223$ MeV, α gated	5.7 ± 0.5	147 ± 40
All data combined	6.6 ± 0.6	183 ± 35
Average	6.2 ± 0.8	145 ± 60

Table 6.3: Results of the fit on $E_{1/2} - \Delta(I)$ data, to extract the saddle height and moment of inertia. *All data combined* is a fit done on all the data. The average values are average on the fit results, weight by the uncertainties and the number of events for each data set.

When *scanning* over all the possible $B_f(I = 0)$ and $\mathcal{J}_{\text{saddle}}$, the regions of lowest χ^2 are the most likely parameters for the saddle. Figure 6.9 shows the map of χ^2 values and compares it with predictions and our experimental measurement.

One notes that this method is just a visualisation of the fit procedure and does not bring new information. But it clearly shows why the uncertainty on $B_f(0)$ is rather small while the uncertainty on the moment of inertia is important: this is linked to the *topology* of the χ^2 surface.

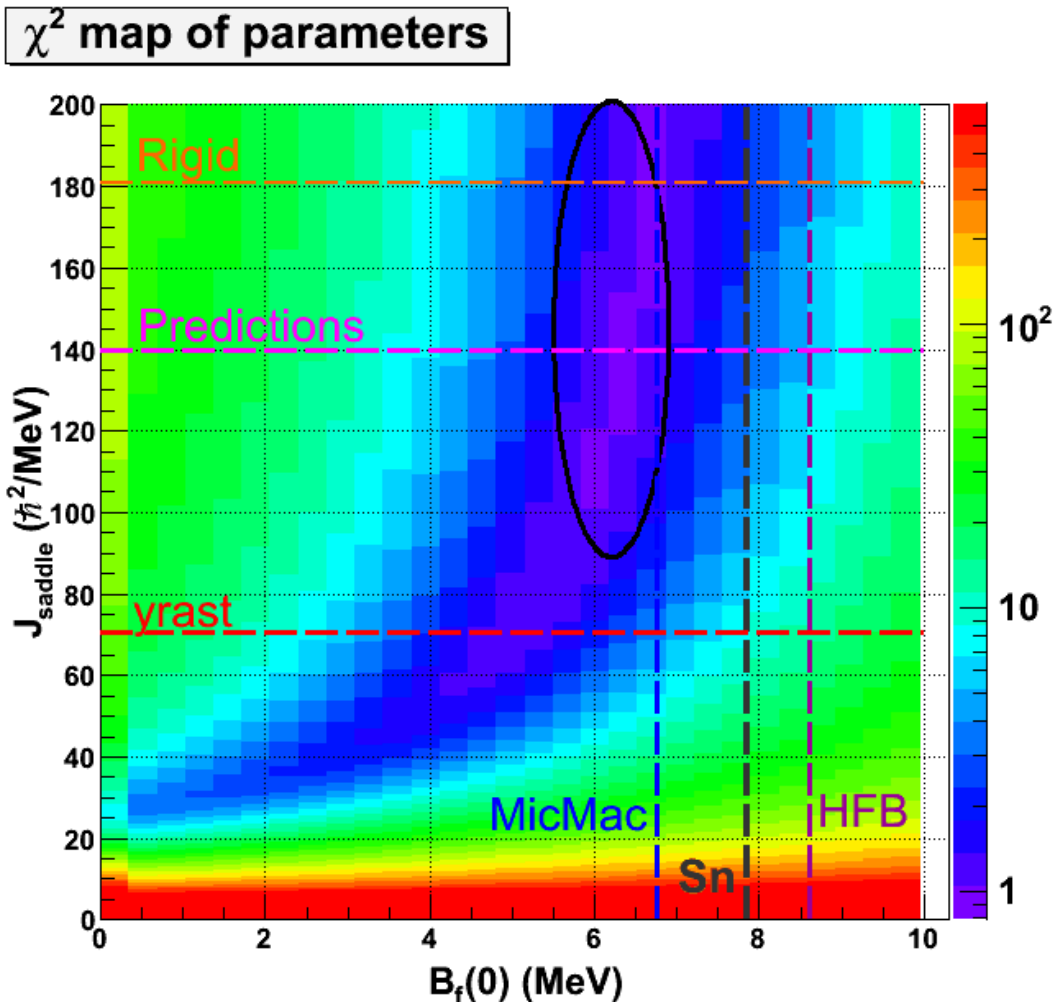


Figure 6.9: Map of χ^2 value calculated for all the data points in our experiment. The moment of inertia of the yrast line is marked in red, the predictions for moment of inertia (by HFB or scaled SD, see 3.1) is in purple, the rigid body moment if inertia is in orange. The neutron separation energy is in black, the predicted $B_f(0)$ by Macroscopic-Microscopic calculations is in blue, and the value from HFB calculations in purple (see 3.1). The values from the fit and the uncertainties are represented with the black ellipse.

6.3 Conclusions on the Fission barrier

The fit on $E_{1/2}$ give a saddle parametrization with $B_f(0) = 6.2 \pm 0.8$ MeV and $\mathcal{J}_{\text{saddle}} = 145 \pm 60 \hbar^2/\text{MeV}$, in agreement with predictions. Our result favours the fission barrier height calculated by microscopic-macroscopic model and the measured moment of inertia is between the HFB result and the rigid body values – see section 3.1. Figure 6.10 shows

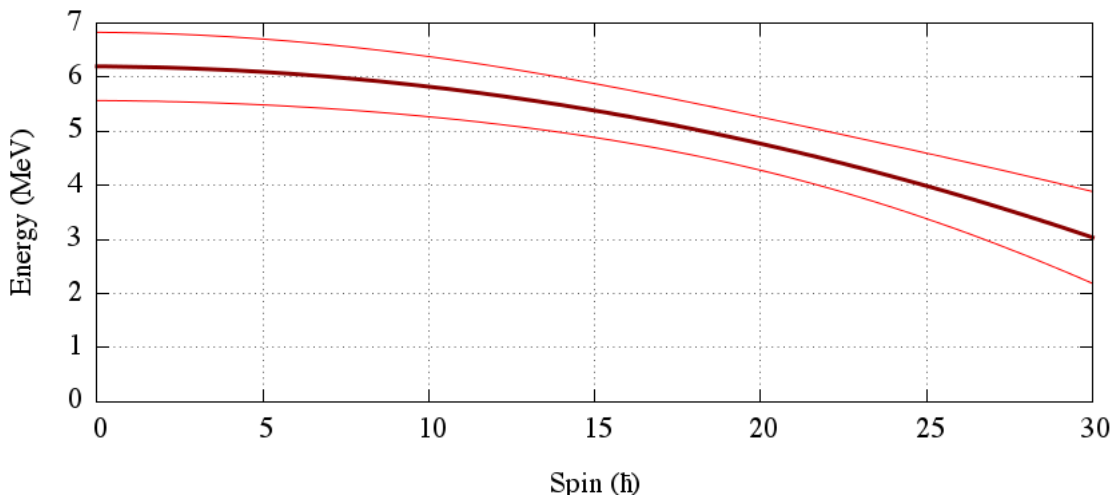


Figure 6.10: Plot of the fission barrier spin dependence. The two external thin lines correspond to the limits and the thick line is the average. $B_f(I)$ stays sizeable up to spin $30 \hbar$, but could drop below 2 MeV above $30 \hbar$. The uncertainty on B_f is lower between $I = 15$ and $20 \hbar$ since the fit was performed on this region.

the height of the fission barrier as a function of spin. It is in agreement with previous measurement [98] with $B_f(20) = 4.8 \pm 0.5$ MeV and stays sizeable up to spin $30 \hbar$.

6.3.1 Agreement with $\Delta(I)$

As mentioned in chapter 3, the $\Delta(I)$ is a calculated quantity dependent both on the saddle energy and the model used for the calculation. However, the effect will be less dramatic since we are considering points around spin 15 to $20 \hbar$ where $\Delta(I)$ is smaller and the different models agree better – see figure 3.2.5. We tried different height and spin dependence of $\Delta(I)$ and extracted the saddle energy each time and found that the variation of $B_f(0)$ is less than 0.1 MeV and the variation of $\mathcal{J}_{\text{saddle}}$ is less than $5 \hbar^2/\text{MeV}$. This weak dependence on Δ is explained by the uncertainties on $E_{1/2}$ and the dispersion of the points on which the fit is done. In the end, the dependence on Δ is shadowed by other

uncertainties.

6.3.2 Agreement with calculation

There is a general agreement with the calculations for the global quantities. Although the average spins do not agree in absolute values but the $\approx 2.5 \hbar$ increase between $E_{\text{Beam}} = 219$ and 223 MeV is consistent with what was seen in calculation. For the energies, the 5 and 6 MeV average and ≈ 1 MeV increase between the two beam energies is consistent with the calculations. Although the details of the shape of the calculated distributions were somewhat different from the experimental measurement, as visible on figure 6.11, there is a general agreement within our experimental uncertainty. This allows us to validate our conclusion and affirm that the saddle energy in ^{254}No is determined by $B_f(0) = 6.2 \pm 0.8$ MeV and a moment of inertia $\mathcal{J}_{\text{saddle}} = 145 \pm 60 \hbar^2/\text{MeV}$.

We successfully performed the first experimental measurement of a fission barrier in the Transfermium region.

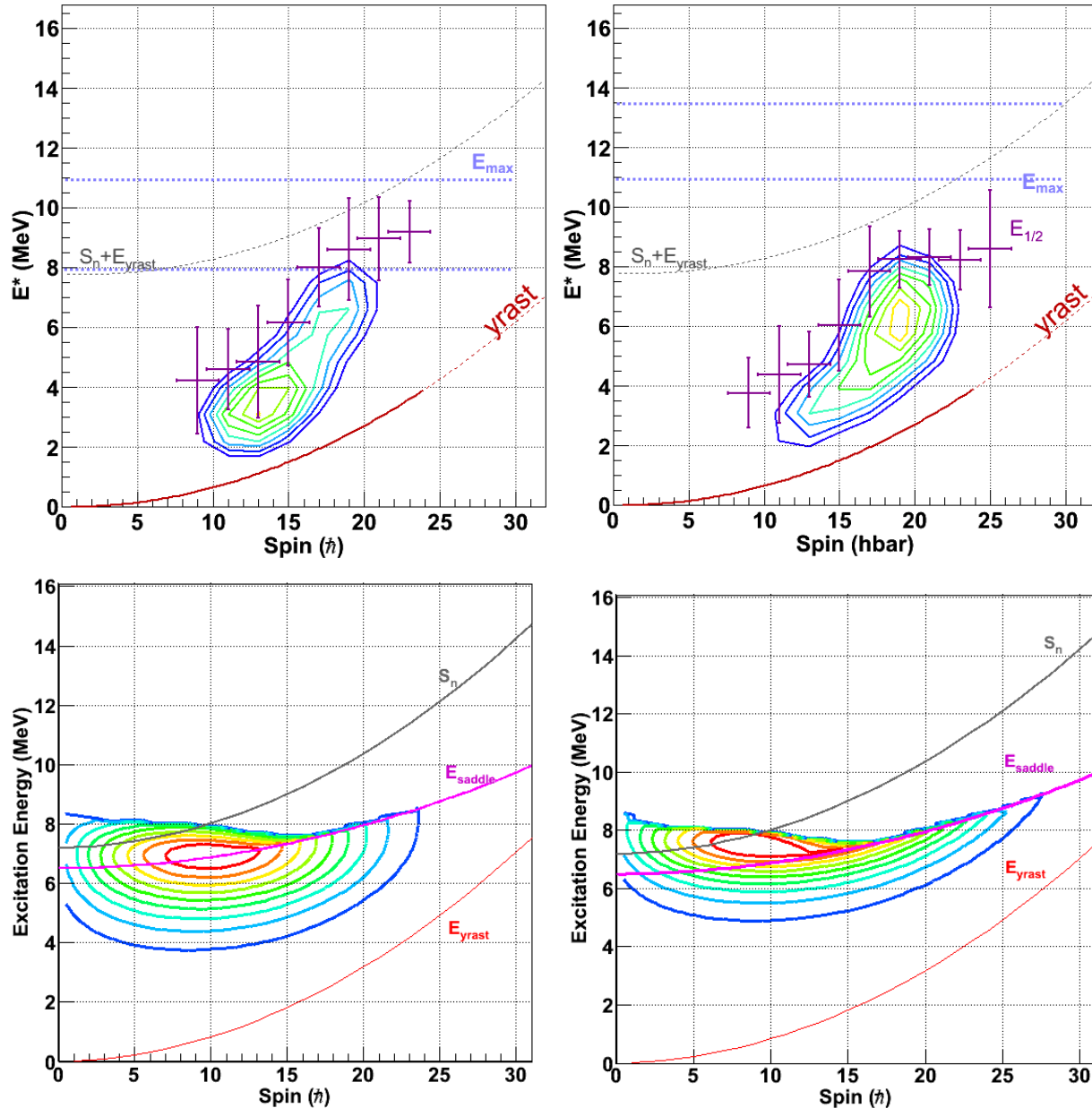


Figure 6.11: Comparison of the experimental (top) and calculated with KEWPIE2 (bottom) entry distribution for ^{254}No at $E_{\text{beam}} = 219$ (left) and 223 MeV (right).

Chapter 7

Perspectives

7.1 Measurement improvement: digital electronics

The main limitation in our experiment is the limited amount of statistics. This is due in part to the beam intensity kept down to keep the count rate in Gammasphere at ≈ 10 kHz, below the acceptable limit. It is also due to the FMA poor transmission.

The move from analog to digital electronic for detectors will reduce the dead time in data acquisition and allow the use of higher intensities on target (Jurogam in Jyväskylä accepts a rate up to 40 khz). For small cross-section, this will easily bring a 2 to 4 gain in production rate. This offer to the experimentalist options to perform experiment faster or collect more statistics or explore regions of the nuclear landscape where production cross sections are smaller. See appendix B.1.

The Argonne Gas Filled Analyzer (AGFA) project at Argonne National Laboratory will be a high transmission separator for such studies.

7.2 Neutron effect

In this analysis, we did not take into account the effect of neutrons in the (k, H) distribution. Indeed, two neutrons are emitted in coincidence with the ^{254}No γ -rays and interact with the environment and the Gammasphere detectors: we see γ -rays energy from neutron scattering on Ge in the prompt spectra, proving that neutrons contribute to the fold and measured energy. The question is: how much is the (k, H) distribution affected by neutrons?

We have started running GEANT4 simulation of neutron in Gammasphere, including detectors thresholds, data loss, ... The simulated γ efficiency is in agreement with experimental measurements. Simulation of the response to neutrons is underway, but one needs to be careful especially since GEANT4 has some trouble with neutron scattering at low energy [110].

The effect of neutron is believed to be small enough so that the bulk of the distribution is not changed significantly and the changes are expected to be smaller than the differences in (k, H) distribution observed at the two beam energies. See appendix A for more details.

7.3 Complementary measurements

7.3.1 Prompt electron spectroscopy

The prompt spectroscopy of conversion electrons in ^{254}No performed with the SACRED array confirmed the ground state rotational band low spin levels. This experiment also highlighted the conversion of electrons from high- K bands [111].

A proposal for “Study of high- K states in ^{254}No using the SAGE spectrometer” has been accepted at JYFL and will yield extra information on the electrons from high- K bands. As we saw in the data analysis, a good understanding of the electron conversion is necessary to correctly reconstruct the entry distribution. The configuration of identified and expected bands lead to large $M1$ admixtures in $\Delta I = 1$ intraband transitions, which are highly converted (section 5.10.3).

7.3.2 Formation of ^{254}No by other reactions

A measurement of the entry distribution of ^{254}No produced in a different reaction would be a good way to test our results. In addition, ^{254}No formed in, for example, the hot fusion reaction $^{238}\text{U}(^{22}\text{Ne}, 6\text{n})$ will likely be populated in a different region of spin (and maybe excitation energy). Exploration of a different spin range would be a good way to confirm the extrapolated values of $B_f(0)$.

7.3.3 Measure of partial fusion cross section

As mentioned in chapter 2, the sub-processes in fusion-evaporation reactions are still mostly unknown and could influence the final spin (and energy) distribution of the evaporation residues.

The current experimental measurements of such fusion cross section are scarce and focus mostly on energies above the fusion barrier [112, 113]. More measurement around the barrier would give valuable information on the barrier distribution, validate coupled-channel calculations and lead to better simulation of the compound nucleus spin and energy distribution.

7.3.4 Improvement of cascade code and simulations

Following the previous point, there is no code today that can calculate from the compound nucleus to the evaporation residue and provide an entry distribution. We started creating such codes with our modifications of KEWPIE2 and the cascade code using NRV data. A fully integrated code that would compute cross sections and entry distributions, with the possibility of changing the saddle energy or entrance spin distribution according to different models, would be very helpful to interpret entry distribution data. Moreover, coupling such code to a γ -decay cascade calculation and the GEANT4 simulation of Gammasphere that has been developed for this work would give a full simulation framework for such studies.

7.3.5 Systematic spin measurement in other facilities

In order to build a systematic of measurements over a wide range of excitation energies and nuclei, it might be possible to collect fold information and reconstruct the entry spin distribution.

For any detector array registering γ -rays in Ge and anti-Compton shields, it is possible to get a fold measurement and a proper fold response calibration. Realistic simulations for the Jurogam array suggest a multiplicity response as in figure 7.1. The detection efficiency is clearly much smaller than for Gammasphere (of the order of 25 %), but for γ multiplicity above 5, it will be possible to extract a correct average entry spin. Moreover, the high transmission of a separator like RITU would bring high statistics data. This has to be confirmed by more developed calculations (for example within GEANT4) and source measurement to build an actual response.

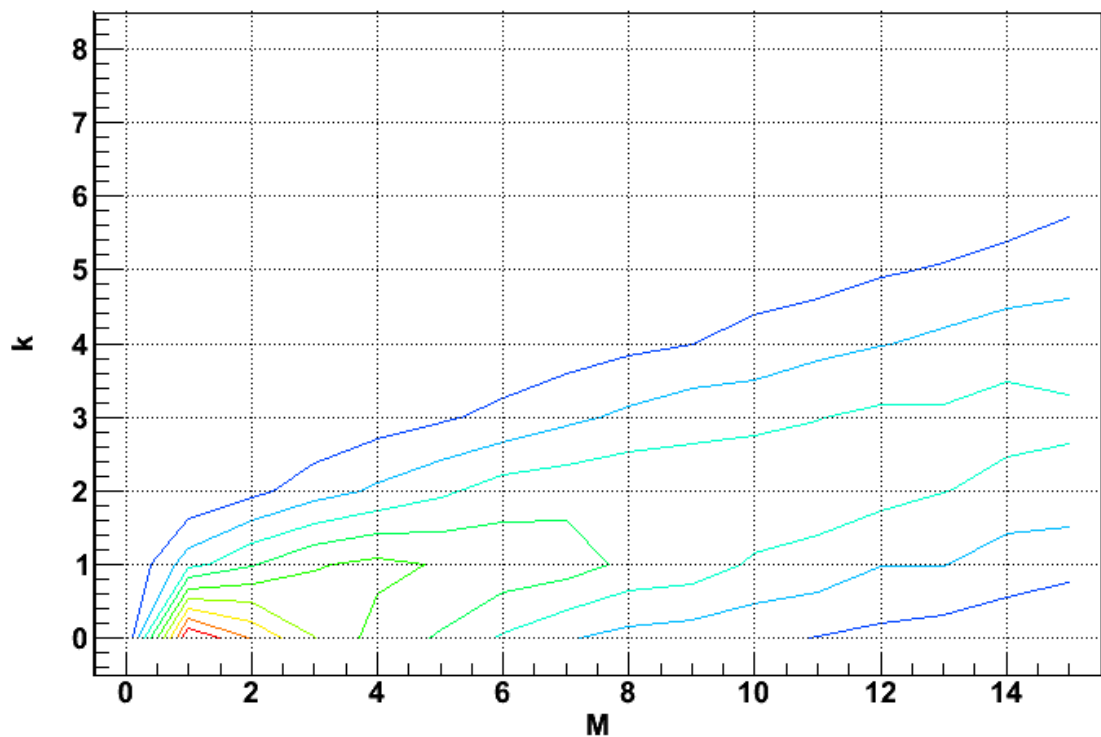


Figure 7.1: Simulation of the multiplicity response in a multi-Ge detector like Jurogam. The detection efficiency is poor but still enough for multiplicities above 5.

7.3.6 Measurement of ^{255}Lr entry distribution

Following our measurement of ^{255}No fission barrier, we proposed to measure the same quantity for ^{255}Lr . This measurement in an odd- A nucleus will provide information on the role of the odd nucleon, on the K quantum number and the reduced pairing. In addition, investigating the evolution of the fission barrier for increasing Z , is a natural next step. The proposal has been approved by the ATLAS PAC.

For ^{255}Lr , Möller et al. [1] predicts a barrier height of 6.6 MeV. This is close to the ^{255}No value and that makes it a good case for comparison. Moreover, it is expected that the odd nucleon will increase the stability of the nucleus and an experimental measurement of this effect is of great interest [114].

We already ran theoretical calculations for the proposed reaction in order to assess the possible observations – see figure 7.2. We expect the same competition between γ and fission decay than for ^{254}No and it is very likely that it will be possible to extract a fission barrier value from the experiment. Moreover, the upgrade of Gammasphere to digital electronic will help us by allowing a more intense beam on target and greater statistics by a factor 3 to 5.

7.3.7 Insight on the reaction mechanism from the entry distribution

The entry distribution is primarily sensitive to the position of the saddle, but it can also give some insights on the whole reaction mechanism. It is possible to extract the average energy removed by the neutrons emitted by the compound nucleus following $E^* = E_{CN} - S_{2n} - K_{n_1} - K_{n_2}$. The low population of low spins may be a consequence of depletion of those partial waves in the reaction mechanism. More work on the entry distribution and theoretical interpretation is needed to decelerate between reaction mechanism and experimental effects.

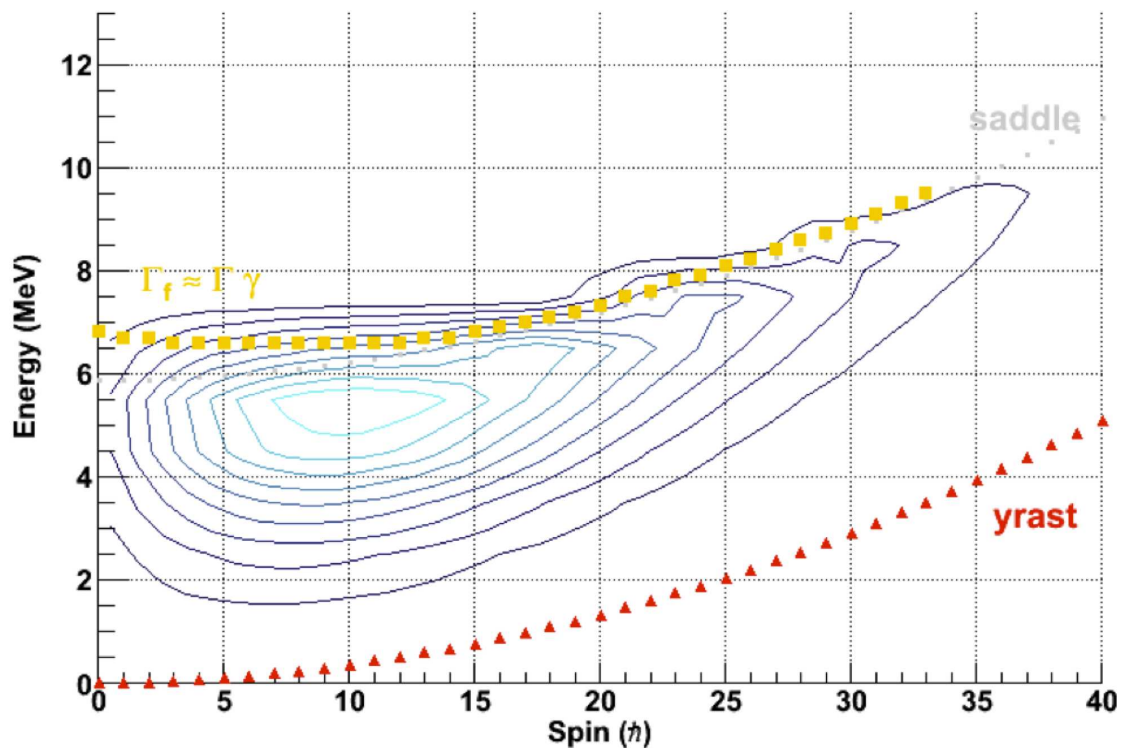


Figure 7.2: Theoretical calculations of an entry distribution for ^{255}Lr in the reaction $^{209}\text{Bi}(^{48}\text{Ca}, 2n)$ using KEWPIE2 [8, 80]. The yellow represent the excitation energy where the widths for γ and fission decay are approximately equal.

Appendix A

Effect of neutrons

In the fusion-evaporation reaction used to populate ^{254}No , two neutrons are ejected from the compound nucleus and carry energy. Those neutrons may interact with the Gammasphere detectors, deposit energy and register hits. This cannot be removed in the data analysis since the neutron hits are obviously coincident with the ^{254}No γ -rays. Therefore, a correction of the neutron contribution has to be applied in the (k, H) distribution before unfolding.

A.1 GEANT4 Simulation of the neutron contribution

The response of Gammasphere to neutrons with a Maxwellian distribution of kinetic energies with $< E > = 2$ MeV has been simulated with GEANT4 [115]. The neutron induced signals are qualitatively well reproduced by the simulation, as shown on figure A.1. But we still have to verify the absolute intensity of the neutron contribution.

The average energy deposited in Gammasphere by one neutron of energy 2 MeV is $H_{\text{neutron}} \approx 560$ keV and the average fold is $k_{\text{neutron}} \approx 1.0$. Figure A.2 shows the energy and fold response for one-2 MeV neutron.

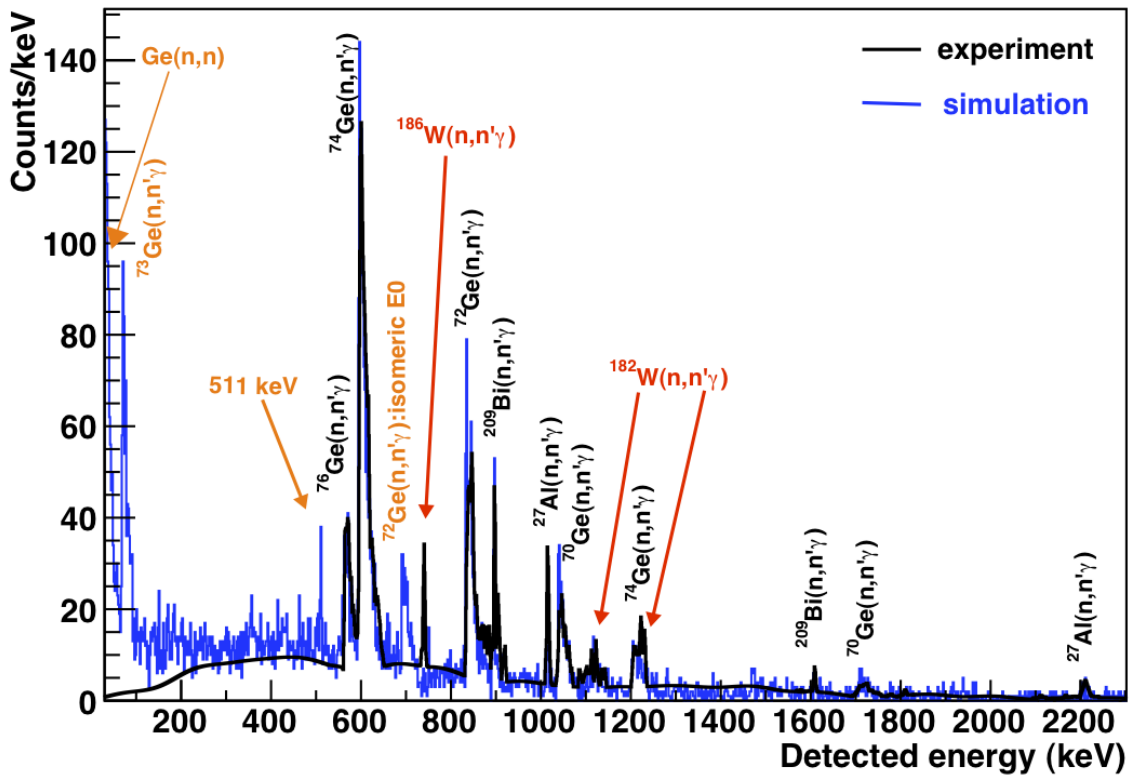


Figure A.1: Overlay of an experimental and simulated neutron induced spectra. In black, the experimental spectrum (from [116]), in blue the simulated spectrum. The γ -ray energies marked in orange are the ones not seen in experiment because of the time cut and detection thresholds. The energies marked in red correspond to the materials not included in the GEANT4 simulation because our experiment did not use hevimet shields (see section 4.1.6).

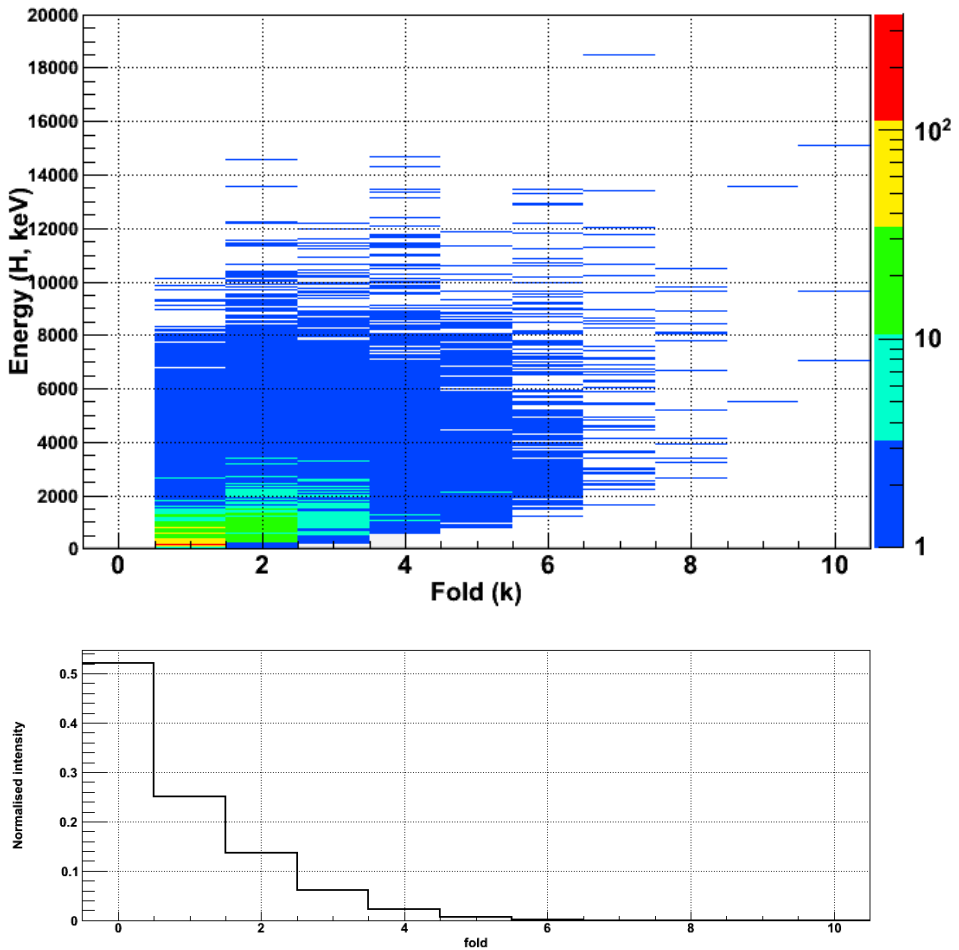


Figure A.2: (Top) Gammasphere response in energy and fold to neutrons with a Maxwellian distribution of energy and $\langle E_{\text{neutron}} \rangle = 2$ MeV. The distribution does not show the (0, 0) point with 37 % of the population. (Bottom) Distribution of fold from neutrons with a Maxwellian distribution of energy and $\langle E_{\text{neutron}} \rangle = 2$ MeV.

A.2 Correction of the neutron contribution

The neutron contribution is statistically removed from the measured (k,H) distribution, taking into account that k and H need to stay positive. The correction for 2 MeV neutrons reduces the average fold by 28 % and the average energy measured by 16 %. Figure A.3 shows the (k,H) distribution before and after correction for the neutrons. The average neutron correction applied is 1.1 for the fold (up to 5) and 550 keV (up to 4 MeV). Using a Maxwellian distribution for the neutron energies reduces the neutron fold contribution by 15 %.

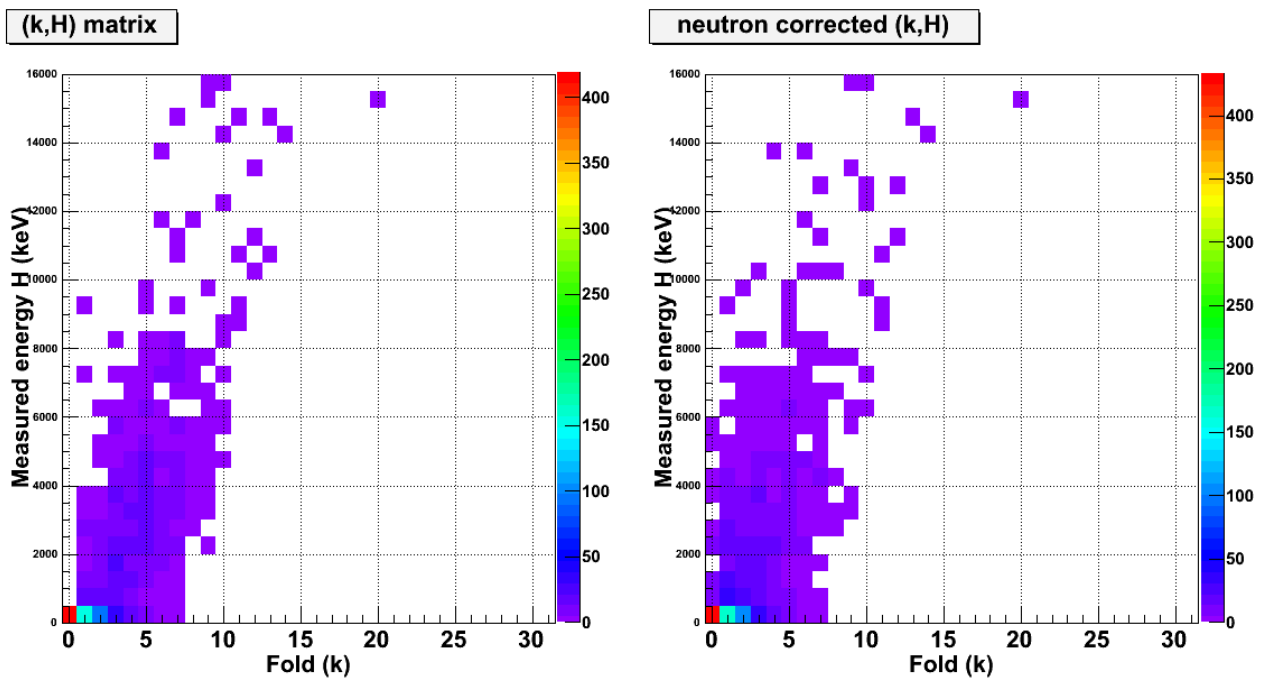


Figure A.3: (k,H) distribution without (left) and after (right) neutron contribution removal. Although the bulk of the distribution is not changed, the slope is slightly shifted up and the distribution is denser at lower folds.

A.3 Caveat

The GEANT4 simulation is doing a good job at reproducing the gamma-ray efficiency (simulation finds a calorimetric efficiency of 63 %) - but further work is required to test the neutron response. There is a known issue in GEANT4 that low-energy neutron inelastic

scattering is not correctly reproduced (cross sections, angular distributions and energy of recoils and neutrons, gamma lines...) [110]. Until all the issues are resolved, it is not judicious to attempt a correction of the neutron effects.

Another issue is that we do not know what the kinetic energy distribution of the neutrons, the kinetic energies of the neutron evaporated by ^{256}No and ^{255}No being probably different. The measured entry distribution can give indication on the sum energy spectrum of the two emitted neutrons.

Appendix B

New and upgraded facilities for the study of SHN

B.1 Digital Gammasphere and FMA

Gammasphere suffers from some technical limitations: The Germanium signal shaping time is $\approx 10\mu\text{sec}$, which leads quickly to pile-up as the count rate increases (40% pile-up at 50kHz). Moreover, the acquisition dead-time is of the order of $25\mu\text{sec}$ per event, hence a one- or two-fold γ trigger saturates the DAQ capabilities.

To allow higher beam intensity on target, increased rates and a more flexible trigger, Gammasphere is being upgraded with digital electronic¹. This will reduce the shaping time down to $2\mu\text{sec}$ and enable the observation of γ -rays with rates as high as 40 kHz (compared to 10kHz now). In addition, the FMA electronic is also being upgraded with digital electronic.

B.2 Gretina

GRETINA is the first phase of an American project of γ -ray tracking detector called GRETA (Gamma Ray Energy Tracking Array) [117]. This detectors use pulse shape analysis in a large highly-segmented Germanium crystal to determine the interaction point

¹The digital electronic used in Digital Gammasphere is the same as the one designed for Gretina. See B.2

of the γ -ray in the crystal. Moreover, this type of detector does not use BGO shield to suppress Compton scattering, but uses a full array of Germanium crystals and *tracking* is performed to reconstruct scattering events.

The Gretina array is under commissioning at the Berkeley Gas Separator at Berkeley and has been tested mainly on the $^{208}\text{Pb} (^{48}\text{Ca}, 2\text{n})^{254}\text{No}$ reaction.

A similar tracking array is under development in Europe under the name AGATA (Advanced GAMMA Tracking Array) [118]. AGATA has not been used in V&SHN reactions yet, but a V&SHE study program is schedule with the Exogam and the VAMOS separator when AGATA will be installed at GANIL.

B.3 Jurogam, Ritu, GREAT

The University of Jyväskylä hosts a very efficient setup for the study of V&SHN.

Jurogam is a γ -ray multi-detector array composed of 39 Germanium detectors – 24 *clovers* and 15 mono-crystals – Compton suppressed with BGO shields. The detection efficiency is 6% at 1.33 MeV.

Digital electronics have recently been installed on Jurogam, allowing an energy resolution around 2.6% at 1.33 MeV even at count rates as high as 70 kHz in one clover detector.

RITU The Recoil Ion Transport Unit (RITU) is a gas-filled magnetic separator. It is composed of a quadrupole, a magnetic dipole for separation and a horizontal-vertical quadrupole doublet for focusing. In a gas filled separator, the recoil charge state is the result of an electron exchange equilibrium in the gas and depends only on the atomic charge and the recoil velocity ; hence the recoils are separated according to an average charge state.

RITU's transmission is between 2 and 35% depending on the recoil. The overall length of the separator is only 4.8m, and that favours the study of short lived isomers with the reduced flight time.

GREAT The focal plane detection system GREAT (Gamma Recoil Electron Alpha Tagging) is used to identify the recoils and perform decay spectroscopy. It is composed of one

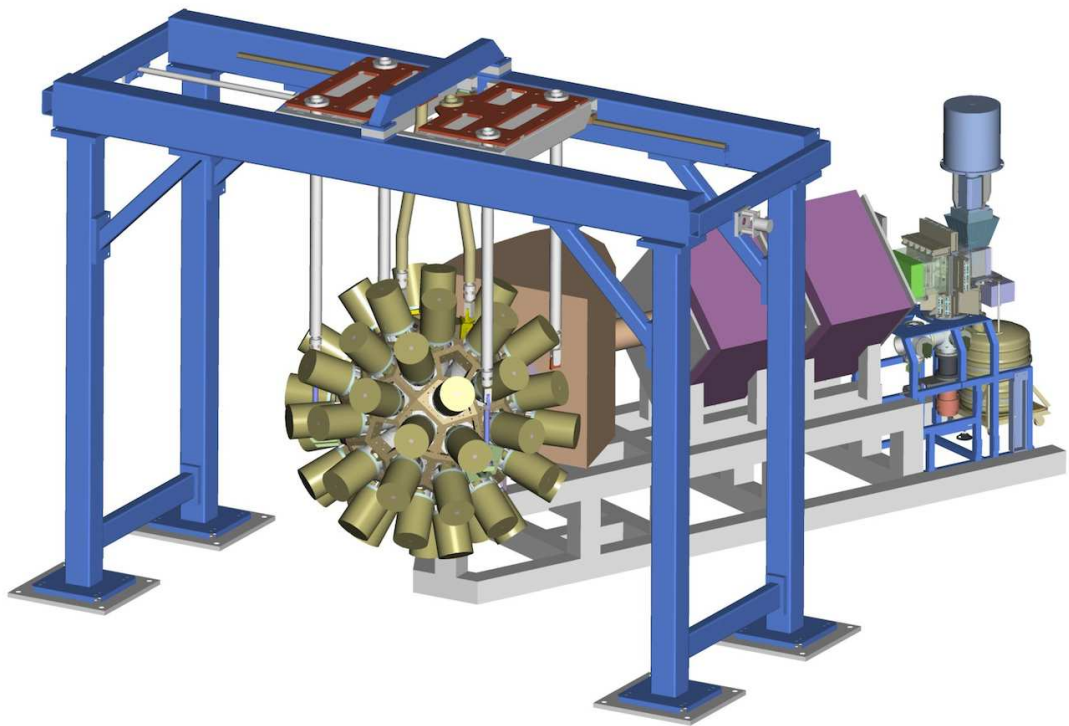


Figure B.1: Jurogam, RITU, GREAT facility at the University of Jyväskylä.

Multi-wire proportional counter for energy loss, time of flight and focal plane position measurements, one DSSD to implant the recoils and observe subsequent electrons and α decays, one Silicon tunnel to measure escape electrons and α s, one segmented planar Ge detector for detection of low energy γ -rays and X-rays correlated with the DSSD pixels, and BGO suppressed clover Ge detectors to detect γ rays.

SAGE The Silicon And GERmanium (SAGE) spectrometer combines the Jurogam γ detectors and an electron detection system. This spectrometer aims to measure converted electrons at the target position, for the spectroscopy of highly converted transition in V&SHN.

B.4 JINR

The Flerov Laboratory for Nuclear Reaction, at the Joint Institute for Nuclear Research in Dubna, Russia, hosts the GABRIELA spectrometer, placed after the VASSILISSA separator. The spectrometer is designed for delayed spectroscopy and provides Time-of-Flight measurement, implant and decay detection in a DSSD, escape detection with a Silicon tunnel and γ -ray spectroscopy with Compton suppressed Germanium mono-crystals.

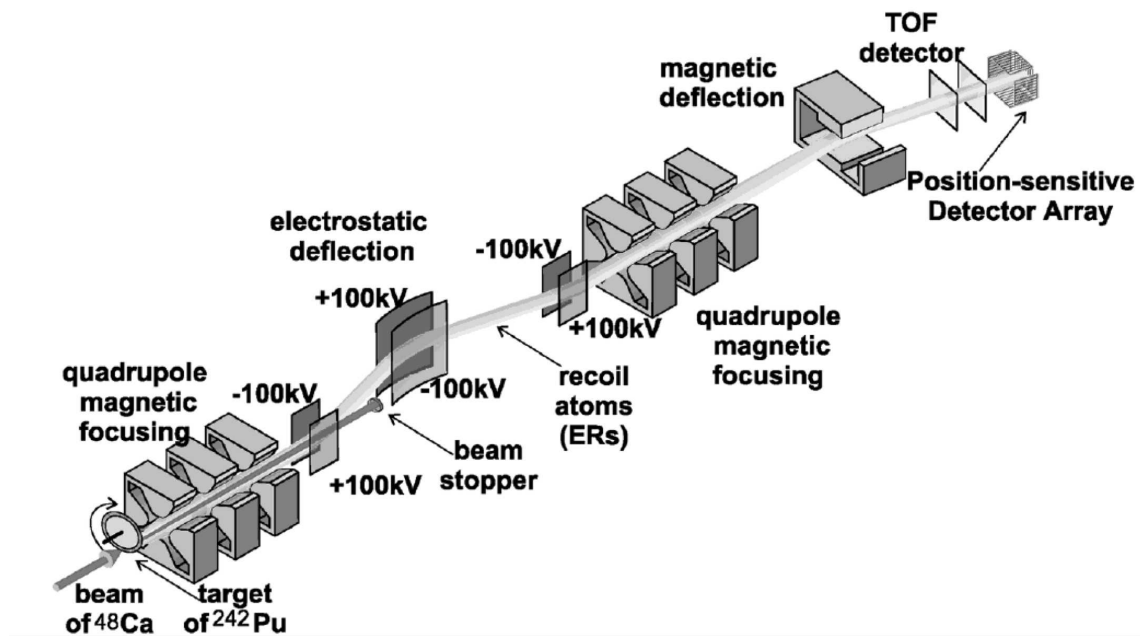


Figure B.2: Schematic view of the VASSILISSA separator.

The VASSILISSA separator is being upgraded in order to increase its transmission and the GABRIELA focal plane detectors will be improved with a bigger DSSD and more strips.

B.5 S³

The GANIL laboratory facilities in France are being upgraded to SPIRAL2. Part of the project is the new separator S³ (Super Separator Spectrometer), for studying the synthesis and spectroscopy of V&SHN, with a focal plane detection system specifically designed that will feature a 10 cm by 10 cm DSSD, with a silicon detector tunnel for the escaped electrons and α and clover Germanium detectors. S³ is expected to start running in 2015.

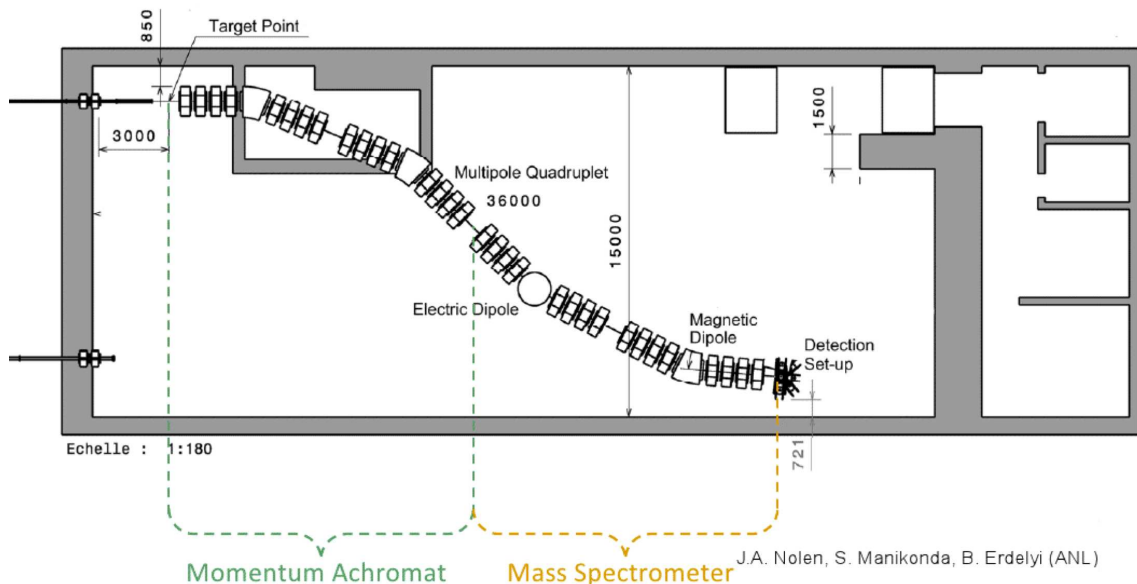


Figure B.3: Blue print of the S³ installation in an experimental hall at GANIL.

Appendix C

^{220}Th entry distribution

The entry distribution of ^{220}Th has been previously measured using the same technique as described in this thesis. The test reaction $^{176}\text{Yb}(^{48}\text{Ca},4\text{n})^{220}\text{Th}$ was therefore a great opportunity to check the setup.

C.1 Data

For the data collected in the test reaction, we used the same selection on the recoils as for the γ -ray spectrum presented in section 5.3. This led to a (k, H) distribution with a statistics similar to the one observed for ^{254}No . Figure C.1 shows the fold and measured energy distribution. One notes that it extends to larger k and H than for ^{254}No .

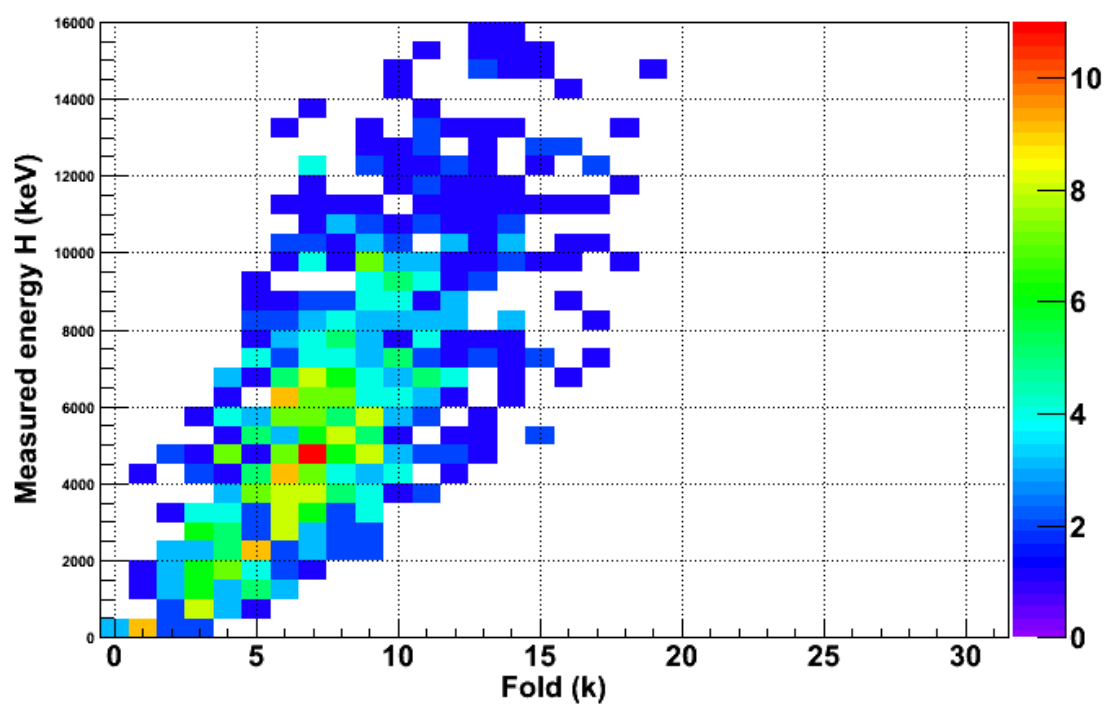


Figure C.1: Distribution of (k, H) for recoil-gated ^{220}Th events.

C.2 Multiplicity to spin transformation

The multiplicity to spin parameters are different for ^{220}Th than for ^{254}No . Following the example of [71], the $M \rightarrow I$ transformation was :

$$I = \Delta I(M - n_{\text{stat}}) + \Delta I_{\text{stat}} \times n_{\text{stat}} + I_{\text{elec}}$$

With $\Delta I = 1.75$, $n_{\text{stat}} = 4.0$, $\Delta I_{\text{stat}} = 0.5$ and $I_{\text{elec}} = 0$. The coefficients are different than from ^{254}No because the bands in ^{220}Th have a different structure.

C.3 Results

After unfolding and transformation in an entry distribution, we obtain the distribution showed in figure C.2. The entry distribution extends up to spin $\approx 20 \hbar$ and the energy extends up to ≈ 30 MeV but the half maximum point is at about 9-10 MeV.

Figures C.3 and C.4 compare the entry distribution measured in [71] and our test reaction. The two data set agree very well. The spin distribution peaks around $8 \hbar$ and falls to 1/10 of the maximum above $20 \hbar$; the energy distribution has a maximum around 6 MeV and falls below 1/10 of the maximum above 14 - 16 MeV.

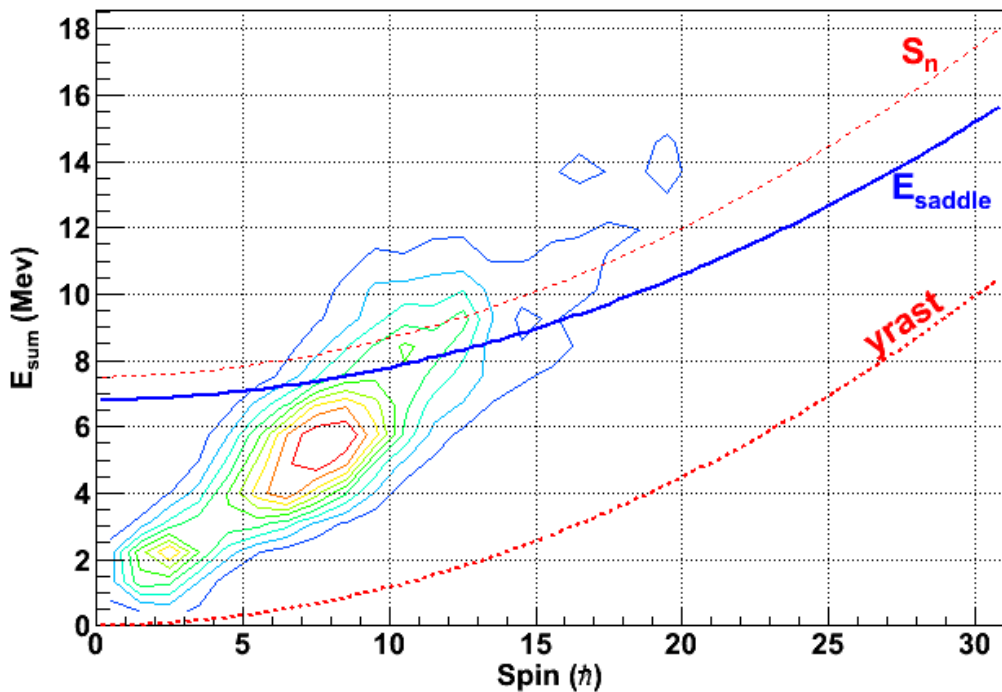


Figure C.2: Entry distribution for recoil-gated ^{220}Th unfolded with ^{88}Y randomly generated response. The yrast energy is shown in red, the adopted saddle energy is in blue and the neutron separation energy in thin red line.

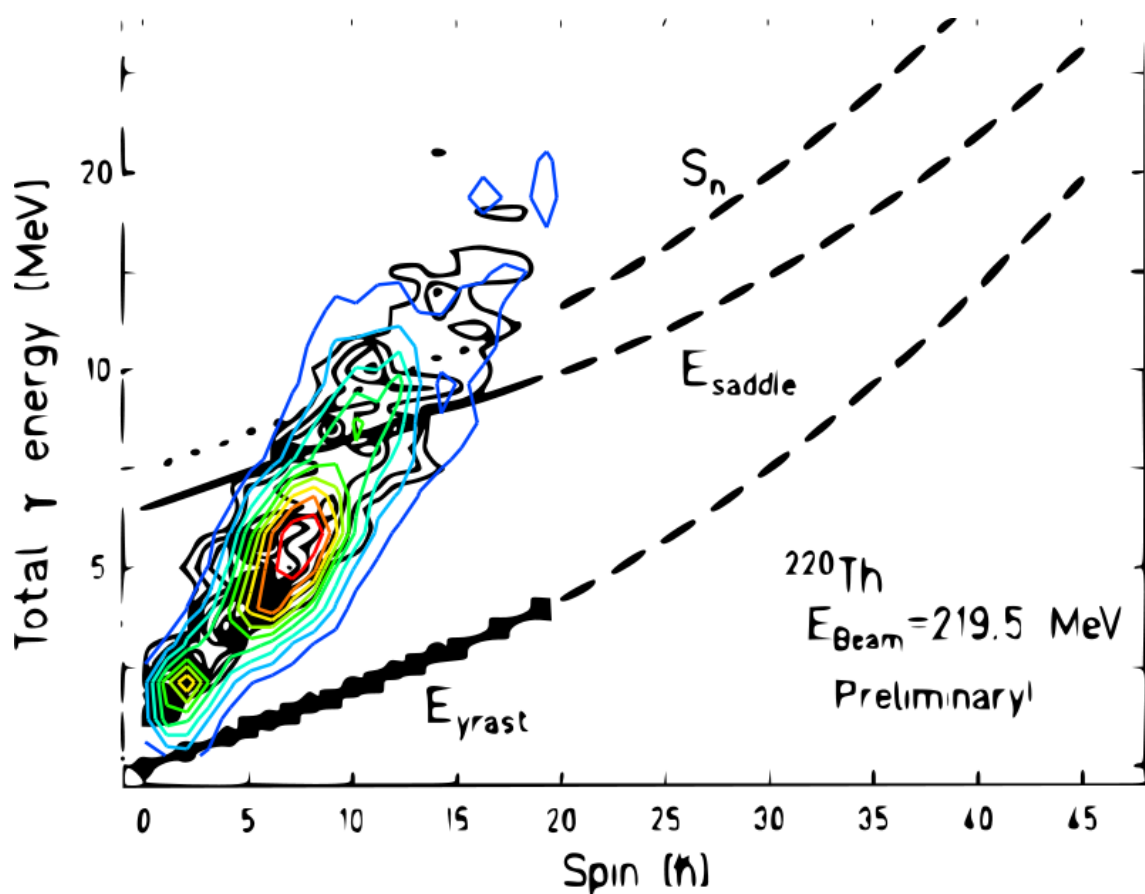


Figure C.3: Overlay of the entry distribution measured in [71] and our measurement in the test reaction. Our data set agrees very well with the previous measurement.

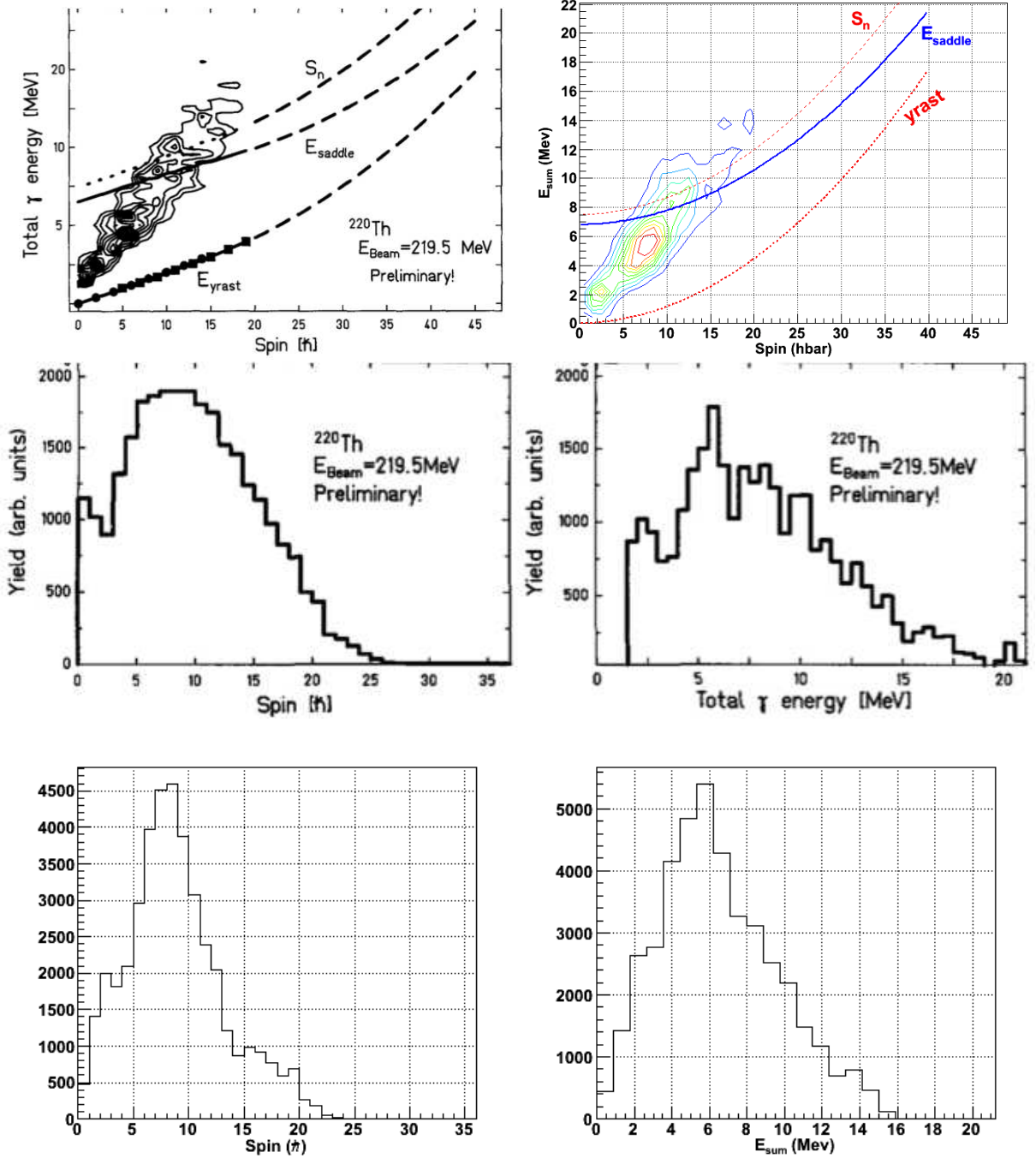


Figure C.4: Comparison of the entry distributions and projections from the previous measurement [71] and our test reaction. The contour of the entry distribution agree (see figure C.3), the projections are not exactly the same but share similar characteristics.

C.4 Conclusions

The two entry distribution agree well. There are some limitations to the measurement: There could be a small contamination from ^{219}Th , even if the cut in X is quite clear (as showed in the γ -ray spectrum of ^{220}Th , figure 5.13). On an absolute scale, both analyses would benefit from an analysis of the discrete structures in ^{220}Th as well as the statistical spectrum. This would improve the multiplicity-to-spin conversion parametrization. Finally, as 4 neutrons are emitted in the reaction, the effect of the neutron correction should be investigated.

As a test reaction, this result shows that our calorimetric measurements are good and compatible with previous ones.

Appendix D

Damping of shell effects

At high excitation energy, the strength of shell effects decreases. This is incorporated in calculation by using A. V. Ignatyuk's prescription [48], the level density parameter a depends on the excitation energy E :

$$a = a_0 \left(1 - \delta W \frac{1 - e^{-E/E_d}}{E} \right)$$

with a_0 the asymptotic value, δW the shell correction energy and E_d the damping parameter.

The level density parameter is used in the calculation of the level density, which, in its simplest form, is $\rho(E) \propto \exp\left(2\sqrt{aE}\right)$, subsequently used in widths calculations.

D.1 Expected consequences for fission width

In the case of fission, the fission barrier is expressed in terms of liquid drop and shell correction energy:

$$B_f = B_{LD} - \delta W$$

In the calculation of fission width, one expects that :

- At low excitation energy, shell effects are strong and the fission width is close to the undamped one: $\Gamma_f^{\text{damped}} \approx \Gamma_f^{\text{undamped}}$.
- At high excitation energy, shell effects disappear and the fission width is equivalent to the one with no shell effect: $\Gamma_f^{\text{damped}} \approx \Gamma_f^{\text{LD}}$.

In fact, the fission width calculation can be approximated at high excitation energy with an effective barrier [8]: $B_{eff} = B_{LD} - \delta W e^{-E/E_d}$. However, this is only an approximation and a consequence of the damping in the level density.

To obtain this effective barrier expression, one can do a simple calculation. By keeping only the exponential part of the level density in the width calculation, the fission width is:

$$\Gamma_f \approx \frac{\exp\left(2\sqrt{a_0 E(1 - B_f/E)}\right)}{\exp\left(2\sqrt{a_0 E(1 - \delta W \frac{1-e^{-E/E_d}}{E})}\right)}$$

The numerator part is not damped because it corresponds to the saddle point where there are no shell effects. The denominator is the starting point, i.e. in the potential well, affected by the shell effects.

If we consider this width at high excitation energy so that $E \gg \delta W$ and $E \gg B_f$, then we can approximate in the square-roots:

$$\Gamma_f \approx \frac{\exp\left(2\sqrt{a_0 E[1 - \frac{B_f}{2E}]}\right)}{\exp\left(2\sqrt{a_0 E[1 - \delta W \frac{1-e^{-E/E_d}}{2E}]}\right)}$$

Then, the ratio can be expressed:

$$\Gamma_f \approx \exp\left(-\sqrt{\frac{a_0}{E}} (B_{LD} - \delta W e^{-E/E_d})\right)$$

This expression is similar to the Bohr and Wheeler formula : $\Gamma_f \propto \exp(-\frac{B_F}{T})$ with $T = \sqrt{\frac{E}{a_0}}$. Therefore, we have an effective barrier depending on the excitation energy :

$$B_{eff} = B_{LD} - \delta W e^{-E/E_d}$$

D.2 Simple proof of principle calculation

To illustrate the differences between level density and fission barrier damping, one can compute fission widths using simple expressions and reasonable values. Following the formulae in [50], we use :

The level density: $\rho(E) = \exp(2\sqrt{aE})$

The fission width: $\Gamma_f = \frac{1}{\rho(E)} \int_0^E T(\varepsilon) \rho_{saddle}(E - \varepsilon) d\varepsilon$

in the integral the transmission is : $T(E) = 1 / \left(1 + \exp\left(-\frac{E-B_f}{\hbar\omega}\right)\right)$

Furthermore, there is no damping of the level density in the integral, as we neglect the shell effects at the saddle.

We used $B_{LD} = 6$ MeV, $\delta W = -2$ MeV, $a_0 \approx 20$ MeV $^{-1}$ and $E_d = 18$ MeV.

Making the calculation of fission width with (1) no damping, (2) **damping in the level density (via the parameter a)**, (3) **damping in the fission barrier**, (4) **damping in the level density and the fission barrier** and (5) no damping and a liquid drop barrier without shell effects, we can see the effect of the damping.

In figure D.1 showing the different calculations value as a function of excitation energy. One can clearly notice the following features :

- The undamped width (black) and the level density damped width (**red**) are similar at low excitation energy, as expected.
- The width with a damped fission barrier (**blue**) and the damped level density (**red**) widths are similar at high excitation energy.
- The width with damped fission barrier (**blue**) and damped level density (**red**) widths are similar to the fission width (gray) without shell effects at high energy, as expected.
- The width with damping of both fission barrier and level density (**green**) are similar only to the fission barrier damped width (**blue**) at low excitation energy and do not match the expected trend (no shell effects, in gray) at high energy.

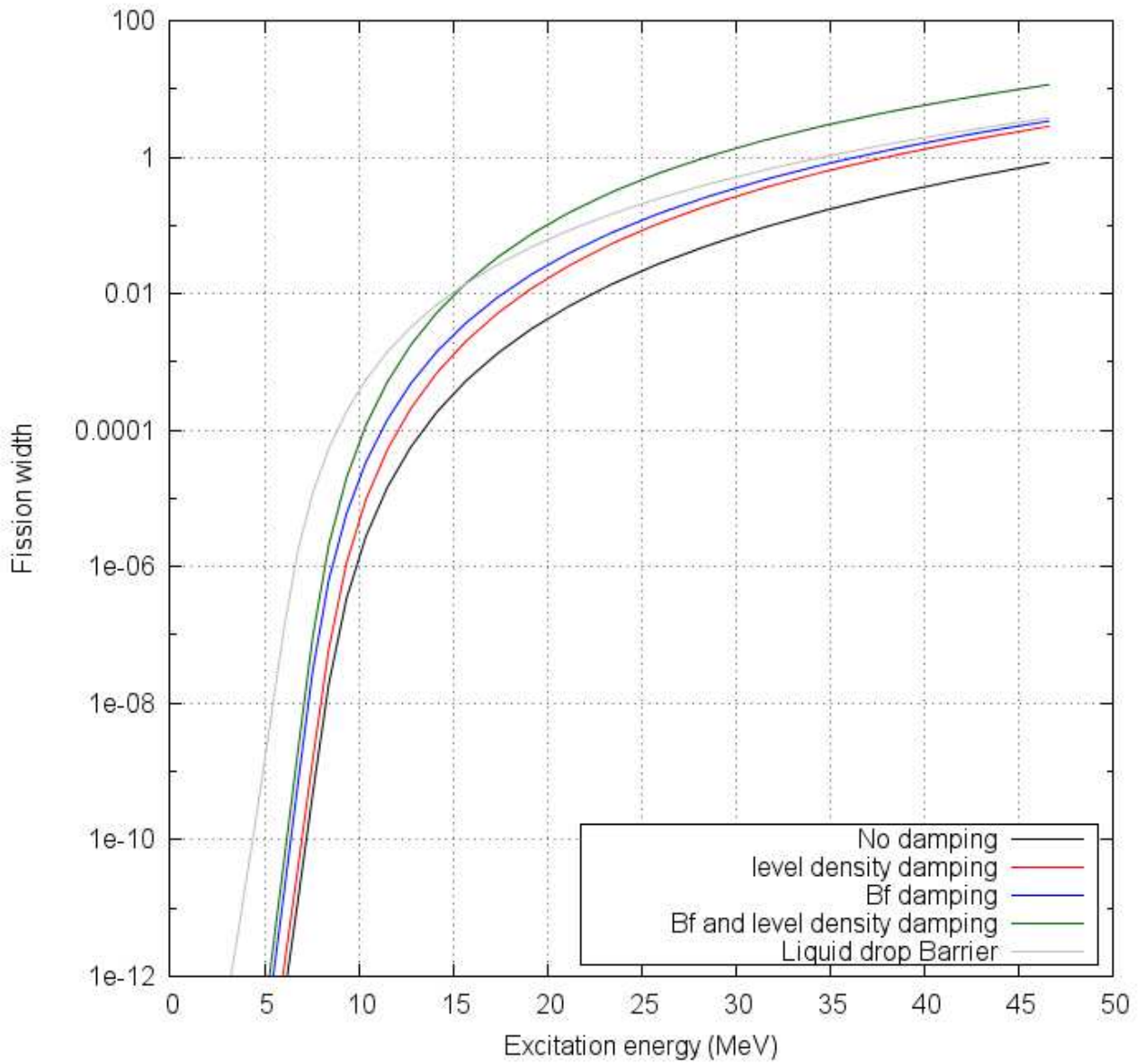


Figure D.1: Comparison of calculated fission widths for different damping parametrization. In black, the width with no damping, expected to reproduce the behaviour of Γ_{fission} at low excitation energy. In gray, the width with no shell effects, expected to have the good behaviour at high excitation energy. The red line is the width with damping of the level density, the blue one is the width with a damped fission barrier and the green line the width with damping both in the level density and B_f .

D.3 Conclusions:

The calculation clearly indicate the equivalence of level-density damping (via the parameter a) and fission barrier damping at high excitation energy.

But only the level density damping can reproduce the expected transition from full to no shell effects.

The use of damping in both level density and fission barrier, which is adopted in some approaches, seems incorrect and lead to an overestimate of the value of the fission width at all the excitation energies.

Appendix E

Random selection of value from a probability distribution

In many situations, in particular in the unfolding procedure (5.9), we have to randomly select a number from a probability distribution. We will describe here the procedure.

E.1 Probability and cumulative probability distribution

Starting from a distribution of probability $P(x)$ defining the probability of choosing the value x between x_{low} and x_{high} so that $\sum_{x_{\text{low}}}^{x_{\text{high}}} P(x) = 1$, we need the associated cumulative probability distribution defined as $C(x) = \sum_{x_{\text{low}}}^x P(x)$ – see figure E.1.

The cumulative distribution is defined so that $C(x_{\text{low}}) = 0$ and $C(x_{\text{high}}) = 1$.

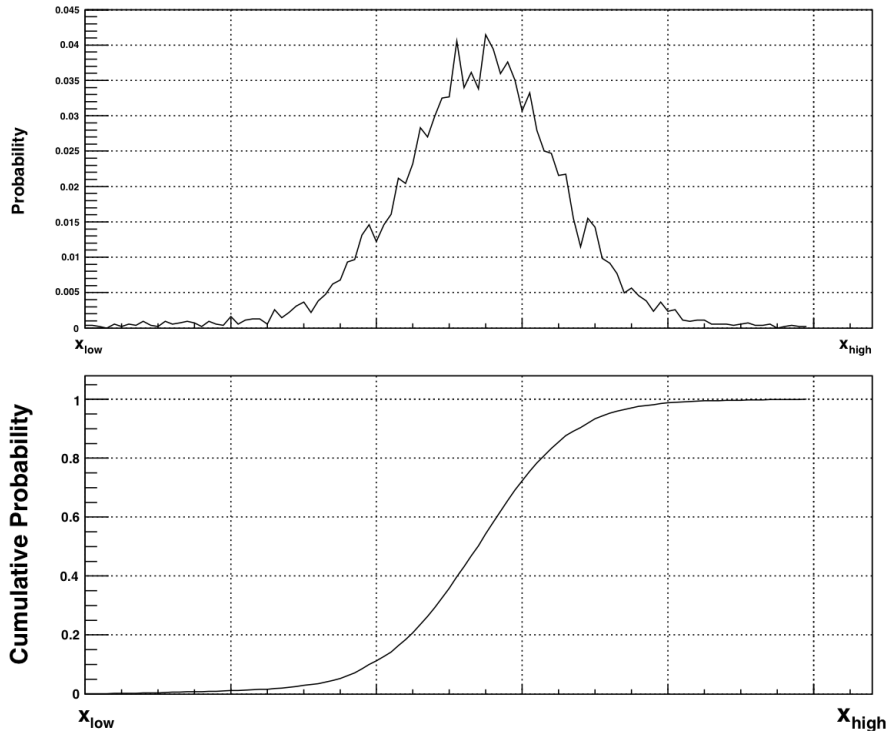


Figure E.1: Probability distribution (top) and the associated cumulative probability distribution (bottom).

E.2 Computer random number generator

The random selection of value relies on computer pseudo-random number generator that provides floating number in the interval $[0, 1[$. Each call to the appropriate function `random()` returns a new random number r – see example of samples in figure E.2.

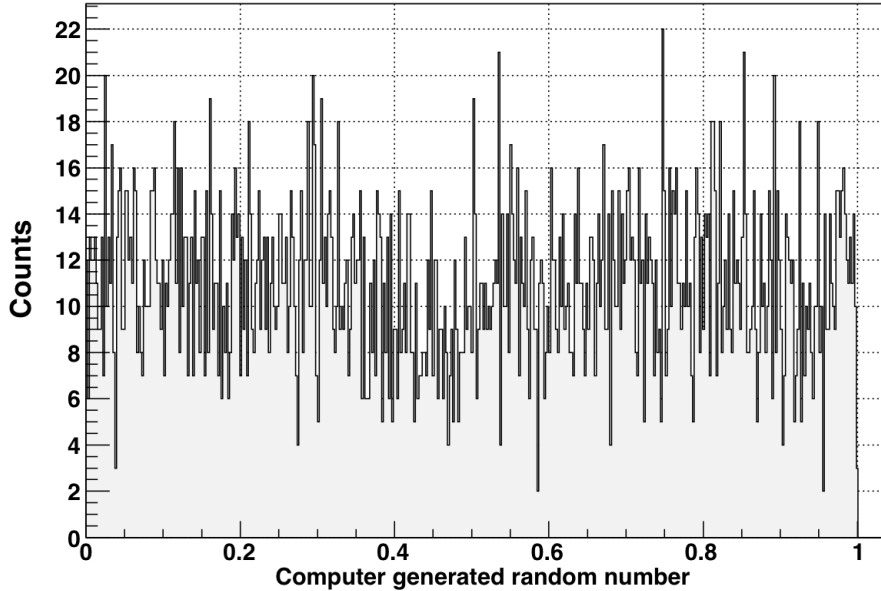


Figure E.2: Example of random generated numbers from a computer pseudo-random generator.

E.3 Choosing a value from the probability distribution

The cumulative probability distribution is used in conjunction with the random number generator according to the following procedure, shown on figure E.3:

1. A random number r is obtained from the generator.
2. The cumulative probability distribution is scanned by increasing x as long as $C(x) < r$.
3. The first x so that $C(x) \geq r$ is the selected value x_{found} .

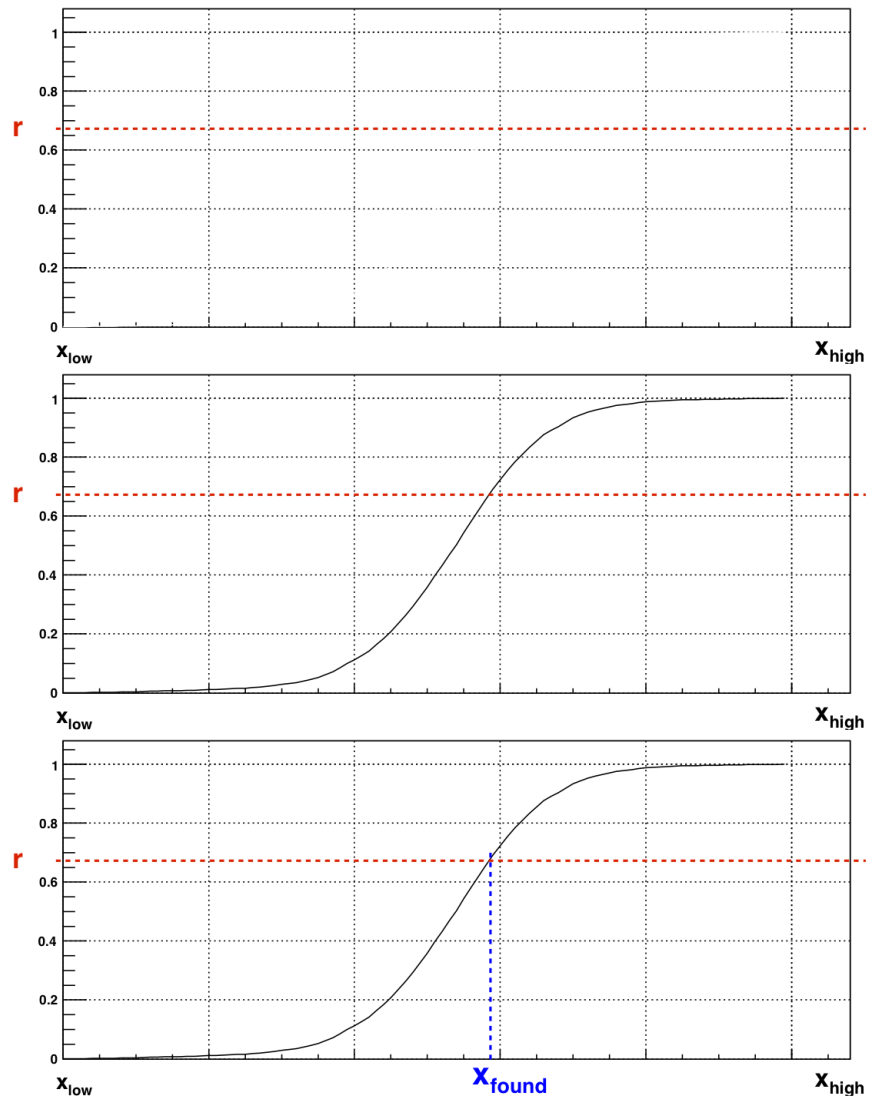


Figure E.3: Steps for choosing a random point according to a probability distribution.

Appendix F

Determining the half maximum point in a distribution

The analysis of the entry distribution relies on the half maximum point of the energy distribution at each spin. The value $E_{1/2}$ is then used to characterise the gamma / fission competition.

F.1 Procedure

The half maximum point is determined in the histogram by a simple interpolation of the bin population. The procedure goes as follows :

1. The bin containing the maximum number of counts is found (bin number noted B_{\max}), its content is A_{\max} , and its centre value (x_{\max}).
2. The half maximum value will be A_{half} .
3. Starting from x_{\max} and going up to the upper the limit of the histogram, the last bin with a number of counts above A_{half} is found. Its content is A_{above} , its bin number B_{above} and its bin centre x_{above} .
4. Starting from the upper limit of the histogram, down toward x_{\max} , the last bin with a number of counts below A_{half} is find. Its content is A_{below} , its bin number B_{below} and its bin centre x_{below} .

5. The bin counts can therefore be parametrized as a function of x between x_{above} and x_{below} with the function :

$$A = A_{\text{above}} + (A_{\text{below}} - A_{\text{above}}) \frac{x - x_{\text{above}}}{x_{\text{below}} - x_{\text{above}}}$$

6. The previous interpolation can be reversed and used to find x_{half} as :

$$x_{\text{half}} = x_{\text{above}} + (x_{\text{below}} - x_{\text{above}}) \frac{A_{\text{half}} - A_{\text{above}}}{A_{\text{below}} - A_{\text{above}}}$$

Figure F.1 shows examples of x_{half} determination for different distributions.

F.2 Uncertainty on $x_{1/2}$

F.2.1 Uncertainty from bin width

The uncertainty from the bin width ($\Delta_x^{\text{bin width}}$) applies for all x quantities : $\delta x = \Delta_x^{\text{bin width}}$. Therefore, $\delta x_{\text{half}}^{\text{bin width}} = \Delta_x^{\text{bin width}} \sqrt{1 + 2 \frac{A_{\text{half}} - A_{\text{above}}}{A_{\text{below}} - A_{\text{above}}} + 2 \left(\frac{A_{\text{half}} - A_{\text{above}}}{A_{\text{below}} - A_{\text{above}}} \right)^2}$

F.2.2 Uncertainty from bin count

Assuming a purely statistical uncertainty on the bin count, each A value is associated with an error \sqrt{A} that propagates to x_{half} :

- $\delta x_{\text{half}}^{A_{\text{max}}} = \frac{\sqrt{A_{\text{max}}}}{2} \frac{x_{\text{below}} - x_{\text{above}}}{A_{\text{below}} - A_{\text{above}}}$
- $\delta x_{\text{half}}^{A_{\text{above}}} = \sqrt{A_{\text{above}}} \frac{x_{\text{below}} - x_{\text{above}}}{A_{\text{below}} - A_{\text{above}}} \left(1 + \frac{1}{A_{\text{below}} - A_{\text{above}}} \right)$
- $\delta x_{\text{half}}^{A_{\text{below}}} = \sqrt{A_{\text{below}}} \frac{x_{\text{below}} - x_{\text{above}}}{A_{\text{below}} - A_{\text{above}}}^2$

The uncertainty expressions show that it is better to work on histogram with small bins and sharp fall around x_{half} (i.e. large $A_{\text{below}} - A_{\text{above}}$). In general, the dominant source of uncertainty is the bin width.

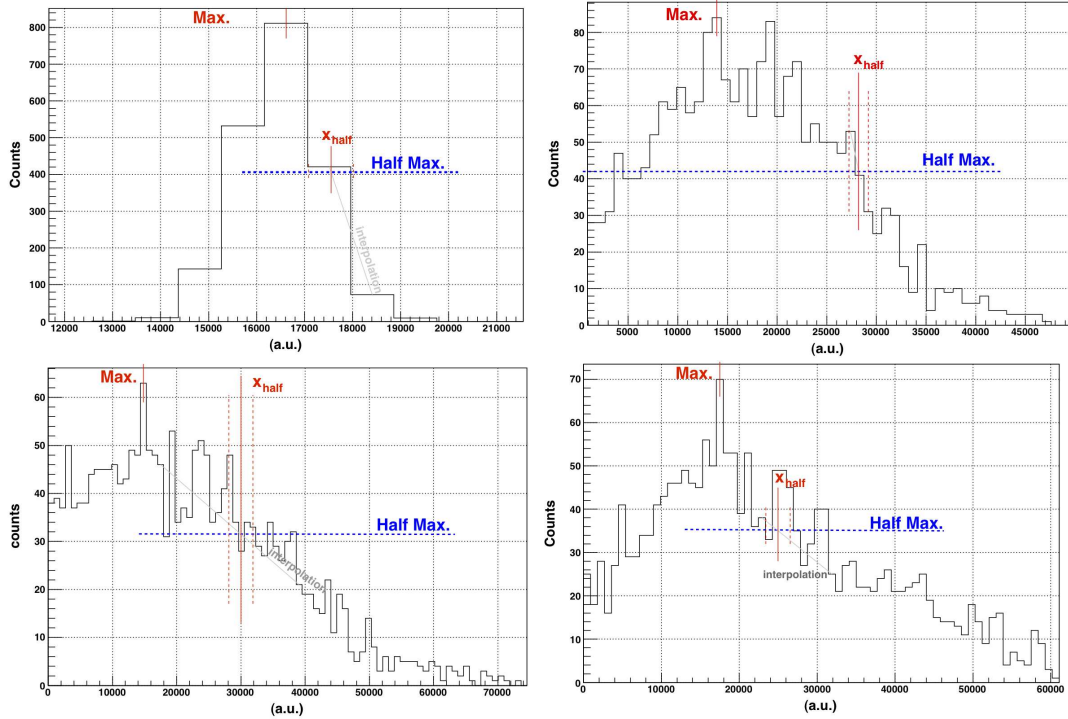


Figure F.1: Examples of half maximum finding. The top left shows a good determination with an uncertainty of the order of the bin width. The top right shows an example with a less ideal distribution, but still good determination. As the statistical fluctuations grow more important, or the distribution gets less clearly defined, the x_{half} determination is not as good, the uncertainties are larger.

F.3 Case of multiple half maxima

In cases of multiple maxima (or half maxima) – also in presence of large statistical fluctuations – the determination of a single half maximum becomes impossible. One has to choose which is the relevant one.

Bibliography

- [1] P. Möller, A. J. Sierk, T. Ichikawa, A. Iwamoto, R. Bengtsson, H. Uhrenholt, and S. Åberg, “Heavy-element fission barriers,” *Phys. Rev. C*, vol. 79, p. 064304, Jun 2009.
- [2] M. Kowal, P. Jachimowicz, and A. Sobiczewski, “Fission barriers for even-even superheavy nuclei,” *Phys. Rev. C*, vol. 82, p. 014303, Jul 2010.
- [3] J. L. Egido and L. M. Robledo, “Fission barriers at high angular momentum and the ground state rotational band of the nucleus ^{254}No ,” *Phys. Rev. Lett.*, vol. 85, pp. 1198–1201, Aug 2000.
- [4] L. Bonneau, P. Quentin, and D. Samsøen, “Fission barriers of heavy nuclei within a microscopic approach,” *The European Physical Journal A - Hadrons and Nuclei*, vol. 21, pp. 391–406, 2004. 10.1140/epja/i2003-10224-x.
- [5] T. Duguet, P. Bonche, and P.-H. Heenen, “Rotational properties of $^{252,253,254}\text{No}$: influence of pairing correlations,” *Nuclear Physics A*, vol. 679, no. 3–4, pp. 427 – 440, 2001.
- [6] B. B. Back, H. C. Britt, O. Hansen, B. Leroux, and J. D. Garrett, “Fission of odd-A and doubly odd actinide nuclei induced by direct reactions,” *Phys. Rev. C*, vol. 10, pp. 1948–1965, Nov 1974.
- [7] B. B. Back, O. Hansen, H. C. Britt, and J. D. Garrett, “Fission of doubly even actinide nuclei induced by direct reactions,” *Phys. Rev. C*, vol. 9, pp. 1924–1947, May 1974.
- [8] A. Marchix, *Etude de l'influence de l'énergie de correction de couches sur les réactions nucléaires menant à la région des noyaux superlourds*. PhD thesis, UNIVERSITÉ de CAEN/BASSE-NORMANDIE, 2007.
- [9] V. I. Zagrebaev, “Nrv code: <http://nrv.jinr.ru/nrv/>.”

- [10] W. Prout, “On the relation between the specific gravities of bodies in their gaseous state and the weights of their atoms.,” *Annals of Philosophy*, vol. 6, pp. 321–330, 1815.
- [11] W. Prout, “Correction of a mistake in the essay on the relation between the specific gravities of bodies in their gaseous state and the weights of their atoms.,” *Annals of Philosophy*, vol. 7, pp. 111–113, 1816.
- [12] D. Mendelejew, “über die beziehungen der eigenschaften zu den atomgewichten der elemente,” *Zeitschrift für Chemie*, pp. 405–406, 1869.
- [13] H. Becquerel, “Sur les radiations invisibles émises par les corps phosphorescents,” in *Comptes-rendus de l'Académie des sciences*, pp. 420–421, 501–502, 1896.
- [14] J. J. Thomson, “Cathode rays,” *Philosophical Magazine*, vol. 44, no. 293, 1897.
- [15] J. Thomson, “On the masses of the ions in gases at low pressures,” *Philosophical Magazine*, vol. 48, p. 547, December 1899.
- [16] E. Rutherford, “The scattering of α and β particles by matter and the structure of the atom,” *Philosophical Magazine*, vol. 21, p. 669, 1911.
- [17] M. G. Mayer, “Nuclear configurations in the spin-orbit coupling model. i. empirical evidence,” *Phys. Rev.*, vol. 78, pp. 16–21, Apr 1950.
- [18] M. H. L. Pryce, “Nuclear shell structure,” *Rep. Prog. Phys.*, vol. 17, p. 1, 1954.
- [19] W. Nörtershäuser, D. Tiedemann, M. Žáková, Z. Andjelkovic, K. Blaum, M. L. Bissell, R. Cazan, G. W. F. Drake, C. Geppert, M. Kowalska, J. Krämer, A. Krieger, R. Neugart, R. Sánchez, F. Schmidt-Kaler, Z.-C. Yan, D. T. Yordanov, and C. Zimmermann, “Nuclear charge radii of $^{7,9,10}\text{Be}$ and the one-neutron halo nucleus ^{11}Be ,” *Phys. Rev. Lett.*, vol. 102, p. 062503, Feb 2009.
- [20] X. Roca-Maza, M. Centelles, X. Viñas, and M. Warda, “Neutron skin of ^{208}Pb , nuclear symmetry energy, and the parity radius experiment,” *Phys. Rev. Lett.*, vol. 106, p. 252501, Jun 2011.
- [21] H. Iwasaki, T. Motobayashi, H. Akiyoshi, Y. Ando, N. Fukuda, H. Fujiwara, Z. Fülöp, K. I. Hahn, Y. Higurashi, M. Hirai, I. Hisanaga, N. Iwasa, T. Kijima, A. Mengoni, T. Minemura, T. Nakamura, M. Notani, S. Ozawa, H. Sagawa, H. Sakurai, S. Shimoura, S. Takeuchi, T. Teranishi, Y. Yanagisawa, and M. Ishihara, “Inelastic scattering on ^{12}Be and disappearance of the $n = 8$ magic number,” *The European Physical Journal A - Hadrons and Nuclei*, vol. 13, pp. 55–58, 2002. 10.1140/epja1339-29.

- [22] R. Kanungo, I. Tanihata, and A. Ozawa, “Observation of new neutron and proton magic numbers,” *Physics Letters B*, vol. 528, no. 1–2, pp. 58 – 64, 2002.
- [23] D. Ackermann, “Superheavy elements at GSI - present and future,” *Nuclear Physics A*, vol. 787, no. 1–4, pp. 353 – 362, 2007.
- [24] A. Sobiczewski and K. Pomorski, “Description of structure and properties of superheavy nuclei,” *Progress in Particle and Nuclear Physics*, vol. 58, no. 1, pp. 292 – 349, 2007.
- [25] P. Reiter, T. L. Khoo, C. J. Lister, D. Seweryniak, I. Ahmad, M. Alcorta, M. P. Carpenter, J. A. Cizewski, C. N. Davids, G. Gervais, J. P. Greene, W. F. Henning, R. V. F. Janssens, T. Lauritsen, S. Siem, A. A. Sonzogni, D. Sullivan, J. Uusitalo, I. Wiedenhöver, N. Amzal, P. A. Butler, A. J. Chewter, K. Y. Ding, N. Fotiades, J. D. Fox, P. T. Greenlees, R.-D. Herzberg, G. D. Jones, W. Korten, M. Leino, and K. Vetter, “Ground-state band and deformation of the $Z = 102$ isotope ^{254}no ,” *Phys. Rev. Lett.*, vol. 82, pp. 509–512, Jan 1999.
- [26] M. Leino, H. Kankaanpää, R.-D. Herzberg, A. Chewter, F. Heßberger, Y. Le Coz, F. Becker, P. Butler, J. Cocks, O. Dorvaux, K. Eskola, J. Gerl, P. Greenlees, K. Helariutta, M. Houry, G. Jones, P. Jones, R. Julin, S. Juutinen, H. Kettunen, T. Khoo, A. Kleinböhl, W. Korten, P. Kuusiniemi, R. Lucas, M. Muikku, P. Nieminen, R. Page, P. Rahkila, P. Reiter, A. Savelius, C. Schlegel, C. Theisen, W. Trzaska, and H.-J. Wollersheim, “In-beam study of ^{254}no ,” *The European Physical Journal A - Hadrons and Nuclei*, vol. 6, pp. 63–69, 1999. 10.1007/s100500050318.
- [27] M. G. Itkis, Y. T. Oganessian, and V. I. Zagrebaev, “Fission barriers of superheavy nuclei,” *Phys. Rev. C*, vol. 65, p. 044602, Mar 2002.
- [28] J. Rainwater, “Nuclear energy level argument for a spheroidal nuclear model,” *Phys. Rev.*, vol. 79, pp. 432–434, Aug 1950.
- [29] R. F. Casten, *Nuclear Structure from a Simple Perspective*. Oxford University Press, 2000.
- [30] S. G. Nilsson, “ ,” *Mat. Fys. Medd. Dan. Vid. Selsk.*, vol. 29, p. 16, 1955.
- [31] P. Greenlees. private communication.
- [32] V. Zagrebaev, “Fusion-fission dynamics of super-heavy element formation and decay,” *Nuclear Physics A*, vol. 734, no. 0, pp. 164 – 167, 2004. Proceedings of the Eighth International Conference On Nucleus-Nucleus Collisions.

- [33] A. P. Robinson, T. L. Khoo, I. Ahmad, S. K. Tandel, F. G. Kondev, T. Nakatsukasa, D. Seweryniak, M. Asai, B. B. Back, M. P. Carpenter, P. Chowdhury, C. N. Davids, S. Eeckhaudt, J. P. Greene, P. T. Greenlees, S. Gros, A. Heinz, R.-D. Herzberg, R. V. F. Janssens, G. D. Jones, T. Lauritsen, C. J. Lister, D. Peterson, J. Qian, U. S. Tandel, X. Wang, and S. Zhu, “ $K^\pi = 8^-$ isomers and $K^\pi = 2^-$ octupole vibrations in $n = 150$ shell-stabilized isotones,” *Phys. Rev. C*, vol. 78, p. 034308, Sep 2008.
- [34] T. Kibédi, T. Burrows, M. Trzhaskovskaya, P. Davidson, and J. C.W. Nestor, “BrIcc Conversion coefficient calculator.”
- [35] L. W. Alvarez, “Nuclear k electron capture,” *Phys. Rev.*, vol. 52, pp. 134–135, Jul 1937.
- [36] L. W. Alvarez, “The capture of orbital electrons by nuclei,” *Phys. Rev.*, vol. 54, pp. 486–497, Oct 1938.
- [37] I. Perlman, A. Ghiorso, and G. T. Seaborg, “Relation between half-life and energy in alpha-decay,” *Phys. Rev.*, vol. 75, pp. 1096–1097, Apr 1949.
- [38] Y. Hatsukawa, H. Nakahara, and D. C. Hoffman, “Systematics of alpha decay half-lives,” *Phys. Rev. C*, vol. 42, pp. 674–682, Aug 1990.
- [39] E. Cheifetz, R. C. Jared, E. R. Giusti, and S. G. Thompson, “Search for superheavy elements in nature,” *Phys. Rev. C*, vol. 6, pp. 1348–1361, Oct 1972.
- [40] S. K. Tandel, P. Chowdhury, S. Lakshmi, U. S. Tandel, I. Ahmad, M. P. Carpenter, S. Gros, R. V. F. Janssens, T. L. Khoo, F. G. Kondev, J. P. Greene, D. J. Hartley, T. Lauritsen, C. J. Lister, D. Peterson, A. Robinson, D. Seweryniak, and S. Zhu, “Rotational bands in odd- a cm and cf isotopes: Exploring the highest neutron orbitals,” *Phys. Rev. C*, vol. 82, p. 041301, Oct 2010.
- [41] R. Bass, “Fusion of heavy nuclei in a classical model,” *Nuclear Physics A*, vol. 231, no. 1, pp. 45 – 63, 1974.
- [42] R. Bass, “Nucleus-nucleus potential deduced from experimental fusion cross sections,” *Phys. Rev. Lett.*, vol. 39, pp. 265–268, Aug 1977.
- [43] P. D. Carlos A. Bertulani, *Introduction to Nuclear Reactions*. Institutue of Physics Publishing, 2004.
- [44] W. J. Swiatecki, K. Siwek-Wilczyńska, and J. Wilczyński, “Fusion by diffusion. ii. synthesis of transfermium elements in cold fusion reactions,” *Phys. Rev. C*, vol. 71, p. 014602, Jan 2005.

- [45] K. Hagino, N. Rowley, and A. Kruppa, “A program for coupled-channel calculations with all order couplings for heavy-ion fusion reactions,” *Computer Physics Communications*, vol. 123, no. 1–3, pp. 143 – 152, 1999.
- [46] N. Rowley. private communication.
- [47] V. Weisskopf, “Statistics and nuclear reactions,” *Phys. Rev.*, vol. 52, pp. 295–303, Aug 1937.
- [48] G. N. S. A. V. Ignatyuk and A. S. Tishin, “Phenomenological description of the energy dependence of the level density parameter,” *Soviet Journal of Nuclear Physics*, vol. 21, p. 255, 1975.
- [49] A. Gavron, “Statistical model calculations in heavy ion reactions,” *Phys. Rev. C*, vol. 21, pp. 230–236, Jan 1980.
- [50] V. I. Zagrebaev, Y. Aritomo, M. G. Itkis, Y. T. Oganessian, and M. Ohta, “Synthesis of superheavy nuclei: How accurately can we describe it and calculate the cross sections?”, *Phys. Rev. C*, vol. 65, p. 014607, Dec 2001.
- [51] A. S. Zubov, V. V. Sargsyan, G. G. Adamian, and N. V. Antonenko, “Population of ground-state rotational bands of superheavy nuclei produced in complete fusion reactions,” *Phys. Rev. C*, vol. 84, p. 044320, Oct 2011.
- [52] A. S. Zubov, G. G. Adamian, N. V. Antonenko, S. P. Ivanova, and W. Scheid, “Survival probability of superheavy nuclei,” *Phys. Rev. C*, vol. 65, p. 024308, Jan 2002.
- [53] A. Junghans, M. de Jong, H.-G. Clerc, A. Ignatyuk, G. Kudyaev, and K.-H. Schmidt, “Projectile-fragment yields as a probe for the collective enhancement in the nuclear level density,” *Nuclear Physics A*, vol. 629, no. 3–4, pp. 635 – 655, 1998.
- [54] A. V. Ignatyuk, M. G. Itkis, V. N. O. andgaa G. N. Smirenkin, and A. S. Tish, “Fission of pre-actinide nuclei. excitation functions for the (α , f) reaction,” *Soviet Journal of Nuclear Physics*, vol. 21, p. 612, 1975.
- [55] B. B. Back, H. C. Britt, J. D. Garrett, and O. Hansen, “Subbarrier fission resonances in Th isotopes,” *Phys. Rev. Lett.*, vol. 28, pp. 1707–1710, Jun 1972.
- [56] S. A. Karamian and A. B. Yakushev, “Formation of heavy compound nuclei, their survival, and correlation with longtime-scale fission,” *Physics of Atomic Nuclei*, vol. 70, no. 2, p. 205–214, 2007.

- [57] W. Hauser and H. Feshbach, “The inelastic scattering of neutrons,” *Phys. Rev.*, vol. 87, pp. 366–373, Jul 1952.
- [58] G. A. Leander, “Statistical E 1 and M 1 gamma strength functions from heavy-ion, $xn\gamma$ data,” *Phys. Rev. C*, vol. 38, pp. 728–736, Aug 1988.
- [59] D. Sarantites and B. Pate, “Angular momentum effects in the compound-statistical model for nuclear reactions: (i). monte carlo calculations of excitation functions,” *Nuclear Physics A*, vol. 93, no. 3, pp. 545 – 566, 1967.
- [60] W. Swiatecki, K. Siwek-Wilczyńska, and J. Wilczyński, “Ratios of disintegration rates for distinct decay modes of an excited nucleus,” *Phys. Rev. C*, vol. 78, p. 054604, Nov 2008.
- [61] A. Yeremin, A. Belozerov, M. Chelnokov, V. Chepigin, V. Gorshkov, A. Kabachenko, O. Malyshev, Y. Oganessian, A. Popeko, R. Sagaidak, A. Svirikhin, S. Hofmann, G. Berek, I. Brida, and S. Saro, “The upgrade of the kinematic separator vasilissa—experimental results and plans,” *Physics of Atomic Nuclei*, vol. 66, pp. 1042–1052, 2003. 10.1134/1.1586416.
- [62] H. Gäggeler, D. Jost, A. Türler, P. Armbruster, W. Brüchle, H. Folger, F. Heßberger, S. Hofmann, G. Münzenberg, V. Ninov, W. Reisdorf, M. Schädel, K. Sümmerer, J. Kratz, U. Scherer, and M. Leino, “Cold fusion reactions with ^{48}ca ,” *Nuclear Physics A*, vol. 502, no. 0, pp. 561 – 570, 1989.
- [63] Y. Oganessian, “Heaviest nuclei from ^{48}ca -induced reactions,” *J. Phys. G: Nucl. Part. Phys.*, vol. 34, 2007.
- [64] N. Bohr and J. A. Wheeler, “The mechanism of nuclear fission,” *Phys. Rev.*, vol. 56, pp. 426–450, Sep 1939.
- [65] P. Möller, A. J. Sierk, R. Bengtsson, H. Sagawa, and T. Ichikawa, “Global calculation of nuclear shape isomers,” *Phys. Rev. Lett.*, vol. 103, p. 212501, Nov 2009.
- [66] J. R. Nix and A. J. Sierk, “Dynamics of fission and heavy ion reactions,” *Nuclear Physics A*, vol. 428, no. 0, pp. 161 – 175, 1984.
- [67] A. J. Sierk, “Macroscopic model of rotating nuclei,” *Phys. Rev. C*, vol. 33, pp. 2039–2053, Jun 1986.
- [68] J. C. Pei, W. Nazarewicz, J. A. Sheikh, and A. K. Kerman, “Fission barriers of compound superheavy nuclei,” *Phys. Rev. Lett.*, vol. 102, p. 192501, May 2009.

- [69] A. Heinz, K.-H. Schmidt, and A. Junghans, “Shell stabilization and the survival of heavy compound nuclei,” *Nuclear Physics A*, vol. 746, no. 0, pp. 483 – 486, 2004. Proceedings of the Sixth International Conference on Radioactive Nuclear Beams (RNB6).
- [70] C. Schmitt, K.-H. Schmidt, A. Kelić, A. Heinz, B. Jurado, and P. N. Nadtochy, “Fragmentation of spherical radioactive heavy nuclei as a novel probe of transient effects in fission,” *Phys. Rev. C*, vol. 81, p. 064602, Jun 2010.
- [71] A. Heinz, T. Khoo, P. Reiter, I. Ahmad, P. Bhattacharyya, J. Caggiano, M. Carpenter, J. Cizewski, C. Davids, W. Henning, R. Janssens, G. Jones, R. Julin, F. Kondev, T. Lauritsen, C. Lister, D. Seweryniak, S. Siem, A. Sonzogni, J. Uusitalo, and I. Wiedenhöver, “Entry distribution of ^{220}Th : A method to determine the fission barrier of an unstable nucleus,” *Nuclear Physics A*, vol. 682, no. 1-4, pp. 458 – 463, 2001.
- [72] J. Péter, “Fission barriers of super-heavy nuclei obtained from experimental data,” *Nuclear Physics A*, vol. 734, no. 0, pp. 192 – 195, 2004. Proceedings of the Eighth International Conference On Nucleus-Nucleus Collisions.
- [73] F. Pühlhofer, “On the interpretation of evaporation residue mass distributions in heavy-ion induced fusion reactions,” *Nuclear Physics A*, vol. 280, no. 1, pp. 267 – 284, 1977.
- [74] V. Y. Denisov and S. Hofmann, “Formation of superheavy elements in cold fusion reactions,” *Phys. Rev. C*, vol. 61, p. 034606, Feb 2000.
- [75] J.-P. Delaroche, M. Girod, H. Goutte, and J. Libert, “Structure properties of even–even actinides at normal and super deformed shapes analysed using the gogny force,” *Nuclear Physics A*, vol. 771, no. 0, pp. 103 – 168, 2006.
- [76] N. G. Nicolis and J. R. Beene, “A multi-particle monte-carlo code intended to extend statistical-model calculations to the high-energy regime..”
- [77] M. Asai. private communication.
- [78] T. Lauritsen, P. Benet, T. L. Khoo, K. B. Beard, I. Ahmad, M. P. Carpenter, P. J. Daly, M. W. Drigert, U. Garg, P. B. Fernandez, R. V. F. Janssens, E. F. Moore, F. L. H. Wolfs, and D. Ye, “Feeding of superdeformed bands: The mechanism and constraints on band energies and the well depth,” *Phys. Rev. Lett.*, vol. 69, pp. 2479–2482, Oct 1992.

- [79] B. Bouriquet, Y. Abe, and D. Boilley, “Kewpie: A dynamical cascade code for decaying excited compound nuclei,” *Computer Physics Communications*, vol. 159, no. 1, pp. 1 – 18, 2004.
- [80] D. Boiley. private communication.
- [81] M. Itkis, Y. Oganessian, E. Kozulin, N. Kondratiev, L. Krupa, I. Pokrovsky, A. Polyakov, V. Ponomarenko, E. Prokhorova, B. Pustynnik, A. Rusanov, and V. Vakatov, “Fusion-fission of nuclei with $z \geq 100$ at low excitation energies,” *Il Nuovo Cimento A (1971-1996)*, vol. 111, pp. 783–790, 1998. 10.1007/BF03185349.
- [82] Y. T. Oganessian, V. K. Utyonkov, Y. V. Lobanov, F. S. Abdullin, A. N. Polyakov, I. V. Shirokovsky, Y. S. Tsyganova, A. N. Mezentsev, S. Iliev, V. G. Subbotin, A. M. Sukhov, K. Subotic, O. V. Ivanov, A. N. Voinov, V. I. Zagrebaev, K. J. Moody, J. F. Wild, N. J. Stoyer, M. A. Stoyer, and R. W. Lougheed, “Measurements of cross sections for the fusion-evaporation reactions $^{204,206,207,208}\text{Pb} + ^{48}\text{Ca}$ and $^{207}\text{Pb} + ^{34}\text{S}$: decay properties of the even-even nuclides ^{238}Cf and ^{250}No ,” *Phys. Rev. C*, vol. 64, p. 054606, Oct 2001.
- [83] F. Dechery. private communication.
- [84] I. Lee, “The gammasphere,” *Nuclear Physics A*, vol. 520, p. 641c, 1990.
- [85] M. Devlin, L. Sobotka, D. Sarantites, and D. LaFosse, “Simulated response characteristics of gammasphere,” *Nuclear Instruments and Methods in Physics Research Section A: Accelerators, Spectrometers, Detectors and Associated Equipment*, vol. 383, no. 2–3, pp. 506 – 512, 1996.
- [86] B. Back, D. Blumenthal, C. Davids, D. Henderson, R. Hermann, C. Jiang, H. Penttilä, and A. Wuosmaa, “Transport efficiency of the argonne fragment mass analyzer,” *Nuclear Instruments and Methods in Physics Research Section A: Accelerators, Spectrometers, Detectors and Associated Equipment*, vol. 379, no. 2, pp. 206 – 211, 1996.
- [87] C. Davids, B. Back, K. Bindra, D. Henderson, W. Kutschera, T. Lauritsen, Y. Nagame, P. Sugathan, A. Ramayya, and W. Walters, “Startup of the fragment mass analyzer at atlas,” *Nuclear Instruments and Methods in Physics Research Section B: Beam Interactions with Materials and Atoms*, vol. 70, no. 1–4, pp. 358 – 365, 1992.
- [88] J. Qian, *Commissioning of a New Focal Plane Detection System of SASSYER and Spectroscopy of 257Rf*. PhD thesis, Yale University, Graduate School of Art and Science, 2009.

- [89] T. Lauritsen, R. V. F. Janssens, T. L. Khoo, I. Ahmad, M. P. Carpenter, F. G. Kondev, C. J. Lister, E. F. Moore, D. Seweryniak, S. Zhu, T. Døssing, B. Herskind, A. Korichi, A. Lopez-Martens, R. M. Clark, P. Fallon, G. Lane, A. O. Macchiavelli, D. Ward, A. M. Heinz, D. G. Jenkins, A. J. Larabee, B. Meredith, J. Kozemczak, and P. Chowdhury, “Rotational damping, ridges, and the quasicontinuum of γ - rays in ^{152}Dy ,” *Phys. Rev. C*, vol. 75, p. 064309, Jun 2007.
- [90] D. Radford, “Radware software package.”
- [91] B. D. Mahapatra and P. Mukherjee, “ $^{108}\text{Ag}^m$ as a calibrating source for the absolute efficiency of Ge(Li) detectors,” *Nuclear Instruments and Methods*, vol. 107, no. 3, pp. 611 – 612, 1973.
- [92] I. Kim, C. Park, and H. Choi, “Absolute calibration of ^{60}Co by using sum-peak method and an hpge detector,” *Applied Radiation and Isotopes*, vol. 58, no. 2, pp. 227 – 233, 2003.
- [93] S. Ketelhut, *Rotational Structures and High-K Isomerism in $^{248,250}\text{Fm}$* . PhD thesis, University of Jyväskylä, 2010.
- [94] W. Reviol, C. J. Chiara, M. Montero, D. G. Sarantites, O. L. Pechenaya, M. P. Carpenter, R. V. F. Janssens, T. L. Khoo, T. Lauritsen, C. J. Lister, D. Seweryniak, S. Zhu, and S. G. Frauendorf, “Multiple octupole-type band structures in ^{220}Th : Reflection-asymmetric tidal waves?,” *Phys. Rev. C*, vol. 74, p. 044305, Oct 2006.
- [95] R. Clark, K. Gregorich, J. Berryman, M. Ali, J. Allmond, C. Beausang, M. Cromaz, M. Deleplanque, I. Dragojević, J. Dvorak, P. Ellison, P. Fallon, M. Garcia, J. Gates, S. Gros, H. Jeppesen, D. Kaji, I. Lee, A. Macchiavelli, K. Morimoto, H. Nitsche, S. Paschalis, M. Petri, L. Stavsetra, F. Stephens, H. Watanabe, and M. Wiedeking, “High-k multi-quasiparticle states in ^{254}No ,” *Physics Letters B*, vol. 690, no. 1, pp. 19 – 24, 2010.
- [96] S. Eeckhaudt, P. Greenlees, N. Amzal, J. Bastin, E. Bouchez, P. Butler, A. Chatillon, K. Eskola, J. Gerl, T. Grahn, A. Görgen, R. Herzberg, F. Hessberger, A. Hürstel, P. Ikin, G. Jones, P. Jones, R. Julin, S. Juutinen, H. Kettunen, T. Khoo, W. Korten, P. Kuusiniemi, Y. Le Coz, M. Leino, A. Leppänen, P. Nieminen, J. Pakarinen, J. Perkowski, A. Pritchard, P. Reiter, P. Rahkila, C. Scholey, C. Theisen, J. Uusitalo, K. Van de Vel, and J. Wilson, “Evidence for non-yrast states in ^{254}No ,” *The European Physical Journal A - Hadrons and Nuclei*, vol. 26, pp. 227–232, 2005. 10.1140/epja/i2005-10163-6.

- [97] F. Heßberger, S. Hofmann, D. Ackermann, S. Antalic, B. Kindler, I. Kojouharov, P. Kuusiniemi, M. Leino, B. Lommel, R. Mann, K. Nishio, A. Popeko, B. Sulignano, S. Saro, B. Streicher, M. Venhart, and A. Yeremin, “Alpha-gamma decay studies of ^{255}no ,” *The European Physical Journal A - Hadrons and Nuclei*, vol. 29, pp. 165–173, 2006. 10.1140/epja/i2006-10083-y.
- [98] P. Reiter, T. L. Khoo, T. Lauritsen, C. J. Lister, D. Seweryniak, A. A. Sonzogni, I. Ahmad, N. Amzal, P. Bhattacharyya, P. A. Butler, M. P. Carpenter, A. J. Chewter, J. A. Cizewski, C. N. Davids, K. Y. Ding, N. Fotiades, J. P. Greene, P. T. Greenlees, A. Heinz, W. F. Henning, R.-D. Herzberg, R. V. F. Janssens, G. D. Jones, F. G. Kondev, W. Korten, M. Leino, S. Siem, J. Uusitalo, K. Vetter, and I. Wiedenhöver, “Entry distribution, fission barrier, and formation mechanism of $^{254}_{102}\text{No}$,” *Phys. Rev. Lett.*, vol. 84, pp. 3542–3545, Apr 2000.
- [99] A. Lopez-Martens, K. Hauschild, A. Yeremin, O. Dorvaux, A. Belozerov, C. Brianson, M. Chelnokov, V. Chepigin, D. Curien, P. Désesquelles, B. Gall, V. Gorshkov, M. Guttormsen, F. Hanappe, A. Kabachenko, F. Khalfallah, A. Korichi, A. Larsen, O. Malyshev, A. Minkova, Y. Oganessian, A. Popeko, M. Rousseau, N. Rowley, R. Sagaidak, S. Sharov, A. Shutov, S. Siem, L. Stuttgé, A. Svirikhin, N. Syed, and C. Theisen, “Isomeric states in ^{253}no ,” *The European Physical Journal A - Hadrons and Nuclei*, vol. 32, pp. 245–250, 2007. 10.1140/epja/i2007-10391-8.
- [100] K. Schmidt, “A new test for random events of an exponential distribution,” *The European Physical Journal A - Hadrons and Nuclei*, vol. 8, pp. 141–145, 2000. 10.1007/s100500070129.
- [101] R.-D. Herzberg, P. T. Greenlees, P. A. Butler, G. D. Jones, M. Venhart, I. G. Darby, S. Eeckhaudt, K. Eskola, T. Grahn, C. Gray-Jones, F. P. Hessberger, P. Jones, R. Julin, S. Juutinen, S. Ketelhut, W. Korten, M. Leino, A.-P. Leppanen, S. Moon, M. Nyman, R. D. Page, J. Pakarinen, A. Pritchard, P. Rahkila, J. Saren, C. Scholay, A. Steer, Y. Sun, C. Theisen, and J. Uusitalo, “Nuclear isomers in superheavy elements as stepping stones towards the island of stability,” *Nature*, vol. 442, pp. 896–899, Aug 2006.
- [102] C. Theisen, A. Lopez-Martens, and C. Bonnelle, “Internal conversion and summing effects in heavy-nuclei spectroscopy,” *Nuclear Instruments and Methods in Physics Research Section A: Accelerators, Spectrometers, Detectors and Associated Equipment*, vol. 589, no. 2, pp. 230 – 242, 2008.
- [103] M. Jääskeläinen, D. Sarantites, R. Woodward, F. Dilmanian, J. Hood, R. Jääskeläinen, D. Hensley, M. Halbert, and J. Barker, “The spin spectrometer: Design, instru-

mentation and response characteristics of 4π γ -ray multidetector system," *Nuclear Instruments and Methods in Physics Research*, vol. 204, no. 2–3, pp. 385 – 405, 1983.

- [104] P. Benet, *Etude de l'émission de neutrons et distributions des moments angulaires du noyaux composé ^{156}Dy dans les voies de sorties*. PhD thesis, Université Louis Pasteur de Strasbourg, 1988.
- [105] S. Leoni, B. Herskind, T. Døssing, A. Ataç, I. Bearden, M. Bergstrom, C. Fahlander, G. Hagemann, A. Holm, D. Joss, M. Lipoglavsek, A. Maj, P. Nolan, J. Nyberg, M. Palacz, E. Paul, J. Persson, M. Piiparinens, N. Redon, A. Semple, G. Sletten, and J. Vivien, "Four independent decay properties in the super-deformed well of ^{143}Eu ," *Physics Letters B*, vol. 409, no. 1–4, pp. 71 – 76, 1997.
- [106] S. Eeckhaudt, *Spectroscopy in the transfermium region: probing rotational, non-yrast and isomeric structures in $^{253,254}\text{No}$* . PhD thesis, University of Jyväskylää, 2006.
- [107] L. Farris, *Gamma-ray Spectroscopy of ^{174}Hf at Low Angular Momentum*. Rutgers University, 1993.
- [108] S. K. Tandel, T. L. Khoo, D. Seweryniak, G. Mukherjee, and et al., " k isomers in ^{254}No : Probing single-particle energies and pairing strengths in the heaviest nuclei," *Phys. Rev. Lett.*, vol. 97, p. 082502, Aug 2006.
- [109] J. Blatt and V. F. Weisskopf, *Theoretical Nuclear Physics*. Dover Books on Physics Series, Dover Publications, 2010.
- [110] "<http://bugzilla-geant4.kek.jp/>."
- [111] P. A. Butler, R. D. Humphreys, P. T. Greenlees, R.-D. Herzberg, D. G. Jenkins, G. D. Jones, H. Kankaanpää, H. Kettunen, P. Rahkila, C. Scholey, J. Uusitalo, N. Amzal, J. E. Bastin, P. M. T. Brew, K. Eskola, J. Gerl, N. J. Hammond, K. Hauschild, K. Helariutta, F.-P. Heßberger, A. Hürstel, P. M. Jones, R. Julin, S. Juutinen, A. Keenan, T.-L. Khoo, W. Korten, P. Kuusiniemi, Y. Le Coz, M. Leino, A.-P. Leppänen, M. Muikku, P. Nieminen, S. W. Ødegård, T. Page, J. Pakarinen, P. Reiter, G. Sletten, C. Theisen, and H.-J. Wollersheim, "Conversion electron cascades in ^{254}No ," *Phys. Rev. Lett.*, vol. 89, p. 202501, Oct 2002.
- [112] E. Prokhorova, A. Bogachev, M. Itkis, I. Itkis, G. Knyazheva, N. Kondratiev, E. Kozulin, L. Krupa, Y. Oganessian, I. Pokrovsky, V. Pashkevich, and A. Rusanov, "The fusion-fission and quasi-fission processes in the reaction $^{48}\text{Ca} + ^{208}\text{Pb}$ at energies near the coulomb barrier," *Nuclear Physics A*, vol. 802, no. 1–4, pp. 45 – 66, 2008.

- [113] A. J. Pacheco, J. O. Fernández Niello, D. E. DiGregorio, M. di Tada, J. E. Testoni, Y. Chan, E. Chávez, S. Gazes, E. Plagnol, and R. G. Stokstad, “Capture reactions in the $^{40,48}\text{Ca} + ^{197}\text{Au}$ and $^{40,48}\text{Ca} + ^{208}\text{Pb}$ systems,” *Phys. Rev. C*, vol. 45, pp. 2861–2869, Jun 1992.
- [114] J. Randrup, C. Tsang, P. Möller, S. Nilsson, and S. Larsson, “Theoretical predictions of fission half-lives of elements with Z between 92 and 106,” *Nuclear Physics A*, vol. 217, no. 2, pp. 221 – 237, 1973.
- [115] S. Agostinelli, J. Allison, K. Amako, J. Apostolakis, H. Araujo, P. Arce, M. Asai, D. Axen, S. Banerjee, G. Barrand, F. Behner, L. Bellagamba, J. Boudreau, L. Broglia, A. Brunengo, H. Burkhardt, S. Chauvie, J. Chuma, R. Chytracek, G. Cooperman, G. Cosmo, P. Degtyarenko, A. Dell’Acqua, G. Depaola, D. Dietrich, R. Enami, A. Feliciello, C. Ferguson, H. Fesefeldt, G. Folger, F. Foppiano, A. Forti, S. Garelli, S. Gianni, R. Giannitrapani, D. Gibin, J. G. Cadenas, I. González, G. G. Abril, G. Greenbaum, W. Greiner, V. Grichine, A. Grossheim, S. Guatelli, P. Gumplinger, R. Hamatsu, K. Hashimoto, H. Hasui, A. Heikkinen, A. Howard, V. Ivanchenko, A. Johnson, F. Jones, J. Kallenbach, N. Kanaya, M. Kawabata, Y. Kawabata, M. Kawaguti, S. Kelner, P. Kent, A. Kimura, T. Kodama, R. Kokoulin, M. Kossov, H. Kurashige, E. Lamanna, T. Lampén, V. Lara, V. Lefebure, F. Lei, M. Liendl, W. Lockman, F. Longo, S. Magni, M. Maire, E. Medernach, K. Minamimoto, P. M. de Freitas, Y. Morita, K. Murakami, M. Nagamatu, R. Nartallo, P. Nieminen, T. Nishimura, K. Ohtsubo, M. Okamura, S. O’Neale, Y. Oohata, K. Paech, J. Perl, A. Pfeiffer, M. Pia, F. Ranjard, A. Rybin, S. Sadilov, E. D. Salvo, G. Santin, T. Sasaki, N. Savvas, Y. Sawada, S. Scherer, S. Sei, V. Sirotenko, D. Smith, N. Starkov, H. Stoecker, J. Sulkimo, M. Takahata, S. Tanaka, E. Tcherniaev, E. S. Tehrani, M. Tropeano, P. Truscott, H. Uno, L. Urban, P. Urban, M. Verderi, A. Walkden, W. Wander, H. Weber, J. Wellisch, T. Wenaus, D. Williams, D. Wright, T. Yamada, H. Yoshida, and D. Zschiesche, “Geant4 - a simulation toolkit,” *Nuclear Instruments and Methods in Physics Research Section A: Accelerators, Spectrometers, Detectors and Associated Equipment*, vol. 506, no. 3, pp. 250 – 303, 2003.
- [116] R. Holzmann, I. Ahmad, R. Janssens, T. Khoo, D. Radford, M. Drigert, and U. Garg, “A new method for measuring the neutron-induced background in bgo compton-suppressed ge detectors applied to in-beam gamma-ray studies,” *Nuclear Instruments and Methods in Physics Research Section A: Accelerators, Spectrometers, Detectors and Associated Equipment*, vol. 260, no. 1, pp. 153 – 156, 1987.
- [117] I. Lee, R. Clark, M. Cromaz, M. Deleplanque, M. Descovich, R. Diamond, P. Fallon, A. Macchiavelli, F. Stephens, and D. Ward, “Gretina: A gamma ray energy tracking array,” *Nuclear Physics A*, vol. 746, no. 0, pp. 255 – 259, 2004.

- [118] S. Akkoyun, A. Algora, B. Alikhani, F. Ameil, G. de Angelis, L. Arnold, A. Astier, A. Ataç, Y. Aubert, C. Aufranc, A. Austin, S. Aydin, F. Azaiez, S. Badoer, D. Balabanski, D. Barrientos, G. Baulieu, R. Baumann, D. Bazzacco, F. Beck, T. Beck, P. Bednarczyk, M. Bellato, M. Bentley, G. Benzoni, R. Berthier, L. Berti, R. Beunard, G. L. Bianco, B. Birkenbach, P. Bizzeti, A. Bizzeti-Sona, F. L. Blanc, J. Blasco, N. Blasi, D. Bloor, C. Boiano, M. Borsato, D. Bortolato, A. Boston, H. Boston, P. Bourgault, P. Boutachkov, A. Bouty, A. Bracco, S. Brambilla, I. Brawn, A. Brondi, S. Broussard, B. Bruyneel, D. Bucurescu, I. Burrows, A. Bürger, S. Cabaret, B. Cahan, E. Calore, F. Camera, A. Capsoni, F. Carrió, G. Casati, M. Castoldi, B. Cedervall, J.-L. Cercus, V. Chambert, M. E. Chambit, R. Chapman, L. Charles, J. Chavas, E. Clément, P. Cocconi, S. Coelli, P. Coleman-Smith, A. Colombo, S. Colosimo, C. Commeaux, D. Conventi, R. Cooper, A. Corsi, A. Cortesi, L. Costa, F. Crespi, J. Cresswell, D. Cullen, D. Curien, A. Czermak, D. Delbourg, R. Depalo, T. Descombes, P. Désesquelles, P. Detistov, C. Diarra, F. Didierjean, M. Dimmock, Q. Doan, C. Domingo-Pardo, M. Doncel, F. Dorangeville, N. Dosme, Y. Drouen, G. Duchêne, B. Dulny, J. Eberth, P. Edelbruck, J. Egea, T. Engert, M. Erduran, S. Ertürk, C. Fanin, S. Fantinel, E. Farnea, T. Faul, M. Filliger, F. Filmer, C. Finck, G. de France, A. Gadea, W. Gast, A. Geraci, J. Gerl, R. Gernhäuser, A. Giannatiempo, A. Giaz, L. Gibelin, A. Givechev, N. Goel, V. González, A. Gottardo, X. Grave, J. Grebosz, R. Griffiths, A. Grint, P. Gros, L. Guevara, M. Gulmini, A. Görgen, H. Ha, T. Habermann, L. Harkness, H. Harroch, K. Hauschild, C. He, A. Hernández-Prieto, B. Hervieu, H. Hess, T. Hüyük, E. Ince, R. Isocrate, G. Jaworski, A. Johnson, J. Jolie, P. Jones, B. Jonson, P. Joshi, D. Judson, A. Jungclaus, M. Kaci, N. Karkour, M. Karolak, A. Kaşkaş, M. Kebbiri, R. Kempley, A. Khaplanov, S. Klupp, M. Kogimtzis, I. Kojouharov, A. Korichi, W. Korten, T. Kröll, R. Krücken, N. Kurz, B. Ky, M. Labiche, X. Lafay, L. Lavergne, I. Lazarus, S. Leboutelier, F. Lefebvre, E. Legay, L. Legeard, F. Lelli, S. Lenzi, S. Leoni, A. Lermitage, D. Lersch, J. Leske, S. Letts, S. Lhenoret, R. Lieder, D. Linget, J. Ljungvall, A. Lopez-Martens, A. Lotodé, S. Lunardi, A. Maj, J. van der Marel, Y. Mariette, N. Marginean, R. Marginean, G. Maron, A. Mather, W. Meczyński, V. Mendéz, P. Medina, B. Melon, R. Menegazzo, D. Mengoni, E. Merchan, L. Mihailescu, C. Michelagnoli, J. Mierzejewski, L. Milechina, B. Million, K. Mitev, P. Molini, D. Montanari, S. Moon, F. Morbiducci, R. Moro, P. Morrall, O. Möller, A. Nannini, D. Napoli, L. Nelson, M. Nespolo, V. Ngo, M. Nicoletto, R. Nicolini, Y. L. Noa, P. Nolan, M. Norman, J. Nyberg, A. Obertelli, A. Olariu, R. Orlandi, D. Oxley, C. Özben, M. Ozille, C. Oziol, E. Pachoud, M. Palacz, J. Palin, J. Pancin, C. Parisel, P. Pariset, G. Pascoalici, R. Peghin, L. Pellegrini, A. Perego, S. Perrier, M. Petcu, P. Petkov, C. Petrache, E. Pierre, N. Pietralla, S. Pietri, M. Pignanelli, I. Piqueras, Z. Podolyak, P. L. Pouhalec, J. Pouthas, D. Pugnaire, V. Pucknell, A. Pul-

lia, B. Quintana, R. Raine, G. Rainovski, L. Ramina, G. Rampazzo, G. L. Rana, M. Rebeschini, F. Recchia, N. Redon, M. Reese, P. Reiter, P. Regan, S. Riboldi, M. Richer, M. Rigato, S. Rigby, G. Ripamonti, A. Robinson, J. Robin, J. Roccaz, J.-A. Ropert, B. Rossé, C. R. Alvarez, D. Rosso, B. Rubio, D. Rudolph, F. Saillant, E. Şahin, F. Salomon, M.-D. Salsac, J. Salt, G. Salvato, J. Sampson, E. Sanchis, C. Santos, H. Schaffner, M. Schlarb, D. Scraggs, D. Seddon, M. Şenyiğit, M.-H. Sigward, G. Simpson, J. Simpson, M. Slee, J. Smith, P. Sona, B. Sowicki, P. Spolaore, C. Stahl, T. Stanios, E. Stefanova, O. Stézowski, J. Strachan, G. Suliman, P.-A. Söderström, J. Tain, S. Tanguy, S. Tashenov, C. Theisen, J. Thornhill, F. Tomasi, N. Toniolo, R. Touzery, B. Travers, A. Triossi, M. Tripone, K. Tun-Lanoë, M. Turcato, C. Unsworth, C. Ur, J. Valiente-Dobon, V. Vandone, E. Vardaci, R. Venturelli, F. Veronese, C. Veyssiére, E. Viscione, R. Wadsworth, P. Walker, N. Warr, C. Weber, D. Weisshaar, D. Wells, O. Wieland, A. Wiens, G. Wittwer, H. Wollersheim, F. Zocca, N. Zamfir, M. Ziebliński, and A. Zucchiatti, “Agata—advanced gamma tracking array,” *Nuclear Instruments and Methods in Physics Research Section A: Accelerators, Spectrometers, Detectors and Associated Equipment*, vol. 668, no. 0, pp. 26 – 58, 2012.